ABSTRACT

Title of Document:	STUDY OF CATALYTIC GROWTH OF OLEFIN NANO FIBRILS AND CARBON NANO FIBRILS OVER SOLID SURFACE AND ITS APPLICATION
	Sangyool Lee, Doctor of Philosophy, 2015
Directed By:	Professor Kyu Yong Choi
	Department of Chemical and Biomolecular Engineering

In this dissertation, the catalytic growth of nano fibrils over solid surface of different geometric types is studied and their applications are also investigated.

The new experimental results on olefin polymerization with metallocene catalyst over silica supports of different geometries are presented. Flat surface silica, nano-sized spherical silica, straight cylindrical pore silica, macroporous silica, and conventional silica are used as support materials. The presence or absence of intraparticle monomer diffusion resistance and particle fragmentation has been shown to have significant effects on the catalytic activity. Also the effects of support geometry on the morphology of polymers and intrinsic catalytic activity are analyzed.

The catalytic growth of olefin nano fibrils are applied in micro/milli reactors. Unlike many conventional olefin reactors, the reaction temperature, heat transfer and bimodal distribution of polymer molecular weight can easily be controlled in the micro/milli reactor systems developed during this study.

The catalytic growth of carbon nano fibrils on silicon has been investigated for application as anode materials in Li-ion batteries. This research is aimed at developing a binder free silicon anode system that consists of a modified Cu foil (current collector), Si nanoparticles (SiNPs), and carbon nanotubes (CNTs). This anode system includes the nanostructured Cu surface layer as a hub for the Si nanoparticles that undergo deformation and fragmentation during the charge/discharge cycles. SiNPs are deposited with Fe-Co bimetallic catalyst and CNTs are grown *in situ* at the catalyst sites. The surface layer of the Cu is modified via an oxidation and reduction processes to have knife-like nanostructures with high void fractions. The SiNPs are deposited on/in to the nanostructured Cu foil without any binders. The CNTs growing at the surface of the SiNPs serve as the electron conductor and also holds the SiNP during the lithiation/delithiation cycles. Since Si/CNT particles are surrounded by thin protrusions on the surface of Cu current collector, the maximum connectivity between silicon and current collector can be obtained, and excellent cycle stability of the battery can be maintained without any binders.

STUDY OF CATALYTIC GROWTH OF OLEFIN NANO FIBRILS AND CARBON NANO FIBRILS OVER SOLID SURFACE AND ITS APPLICATION

By

Sangyool Lee

Dissertation submitted to the Faculty of the Graduate School of the
University of Maryland, College Park, in partial fulfillment
of the requirements for the degree of
Doctor of Philosophy
2015

Advisory Committee:
Professor Kyu Yong Choi, Chair
Professor Chunsheng Wang
Professor Dongxia Liu
Professor Amy J. Karlsson
Professor Sang Bok Lee

Dedication

I dedicate this work

To

My wife Sookyeong

My son Jun, My daughter Jia

And my parents

Acknowledgements

I would like to express my deep and sincere gratitude to my advisor, Professor Kyu Yong Choi, for his guidance, support, patience, and encouragement throughout my graduate study at the University of Maryland. His enthusiasm, creative ideas and fundamental understanding of the entire field of chemical engineering acted as a stimulus, helping me to solve many problems making it possible to move my research forward. I also would like to thank my advisory committee members, Profs. Chunsheng Wang, Dongxia Liu, Amy J. Karlsson, and Sang Bok Lee, for their valuable suggestions and advice regarding this project.

I would like to thank Prof. Jin Suk Chung at Ulsan University, South Korea for analyses of catalyst concentrations with ICP and specific surface areas with BET. I also thank Dr. Sungkyung Kim in Prof Sang Bok Lee's group for helping with the synthesis of silica nanotubes. Thanks go to Ms. Laleh Emdadi, my former lab mate, who helped measure the specific surface area of silica particles with BET in Prof. Dongxia Liu's Lab. I would like to thank LG Chem and Mr. Wonseok Hwang in Prof. Lawrence R. Sita's Lab for the high temperature GPC analysis. I would also like to thank Dr. Yang Wen and Dr. Mao in Prof. Chunsheng Wang's group for helping with battery cycle life tests.

I am truly thankful to my Korean friends, Inhak Baick, Moosoo Lee, Woojic Yang, Yunju Jung Kim, and Wonseok Hwang for their helpful suggestions and cherishable friendship. I am also truly thankful for Pho 75 which serves the most

delicious noodle soup and iced coffee in the world. I cannot even think about my life in the U. S. without this humble but comfortable restaurant.

Special thanks go to my parents for their endless support and encouragement. Finally, I would like to thank my wise and lovely wife, Sookyeong, who has understood the hard situations, encouraged me, and waited for this moment with patience during my study. Also I thank my son Jun and my daughter Jia who let me realize such special, inexplicable joy in my life.

Table of Contents

List of Tables

List of Figures

Chapter 1. Introduction

1.1. Background and Motivation

1.1.1. Heterogeneous Olefin Polymerization

In heterogeneously catalyzed polymerization of α-olefins, the characteristics of a solid support material impact the catalyst activity, polymer particle morphology, and resulting polymer properties. The presence or absence of intraparticle monomer diffusion resistance and particle fragmentation has also been shown to have significant effects on the catalytic activity. Silica is the most widely used support for metallocene catalysts in α-olefin polymerization processes because of its large surface area and favorable surface properties for catalyst anchoring. Understanding the kinetics of heterogeneous olefin polymerization over a solid-supported catalyst is often quite complicated because of mass transfer effects and catalyst particle fragmentation during the polymerization. Incomplete or premature fragmentation of support material results in a large fraction of catalyst sites left unavailable for the polymerization, causing some inconsistencies in the performance of the catalyst. Silica-supported metallocene catalysts for α-olefin polymerization are known to follow the layer-by-layer fragmentation mechanism where the fracture of the silica/polymer layer begins from the surface region of a silica particle and it gradually continues into the center of the particle as fragmentation is complete. High porosity and high surface area silica particles are the most widely used support materials for high activity metallocene catalysts for α-olefin polymerization. One of the important requirements for an effective catalyst support is its ability to disintegrate with the growth of polymers in a controlled manner. Premature or incomplete fragmentation may

cause severe diffusion resistance for monomer transport or blockage of catalyst sites for the monomer access [1-3]. It is not uncommon that only a small fraction of catalyst sites is actually used for the polymerization because of irregular or uncontrolled particle fragmentation, and the overall polymerization efficiency becomes quite low. It is also to be noted that the reproducibility of catalytic performance, polymer properties, and the resulting polymer particle morphology are dependent upon the particle fragmentation process [3, 4].

Unlike in Ziegler-Natta catalyzed polymerization processes where transition metal catalyst fragments disintegrated at the beginning of polymerization become the nuclei for primary polymer particles and subsequent macroparticle growth, the fragmentation of silica-supported metallocene catalysts in olefin polymerization is described by the layer-by-layer fragmentation mechanism [5-7]. According to this mechanism, the porous outer surface region of a silica particle is rapidly filled up with polymer at the beginning of polymerization, forming a dense polymer layer. This polymer layer causes a strong diffusion resistance for the monomer transport to the interior of a catalyst particle. Thus, the polymerization rate decreases as monomer experiences a strong intraparticle diffusion resistance. Eventually, as the polymer mass increases and the hydraulic force generated by the pore-filling polymer builds up, cracking of the silica/polymer layer occurs to allow the for the further diffusive penetration of monomer toward the particle core [5, 7]. The sequence of events of polymer formation - pore filling - cracking of silica/polymer layer repeatedly occurs until the entire silica particle disintegrates. During the fracture or fragmentation, the active catalytic sites present in the silica pore surface are partially exposed and allow for the polymerization to continue.

Since the catalyst/polymer particle fragmentation is a complicated process of chemical reaction and physical transport events, quantifying the heterogeneous reaction kinetics of

polymerization over silica-supported metallocene catalysts is a very difficult task. Furthermore, it is also of a practical interest to find a new way to improve the catalyst effectiveness by either having maximum active sites exposed to monomer early in the reaction process or minimizing intraparticle monomer diffusion limitations.

In this dissertation, the new experimental results on ethylene polymerization with *rac*-Et(indenyl)$_2$ZrCl$_2$/MAO catalyst using different geometric types of silica supports are presented. The effects of support geometry on intrinsic catalytic activity are analyzed. To that purpose, flat surface silica, nano-sized spherical silica, straight cylindrical pore silica, macroporous silica, and conventional silica are used as supports. **Error! Reference source not found.** schematically illustrates these silica supported catalyst where polymers grow as nanofibrils, and **Error! Reference source not found.** summarizes their qualitative aspects of physical characteristics. The flat surface silica represents the most idealistic surface condition for the heterogeneous catalyst because all the active sites are equally exposed to monomer. The monomer diffusion resistance to these catalytic sites is minimal or even absent. A silica nanoparticle of diameter c.a. 300 nm represents a spherical support with no internal pores and hence the active catalytic sites are present only at the exterior surface of the particle. The cylindrical tube of silica (silica nanotube) represents another well-defined support geometry. If both interior and exterior of a silica nanotube are deposited with the metallocene catalyst, polymer will grow inside and outside of the tube. The macroporous silica particle (pseudo inverse opal silica particle, PIOS [8]) represents open pore silica material and it shows much higher activity than the conventional silica-supported catalysts. Finally, porous micron-size silica represents a typical commercial grade support for a variety of high activity metallocene catalysts.

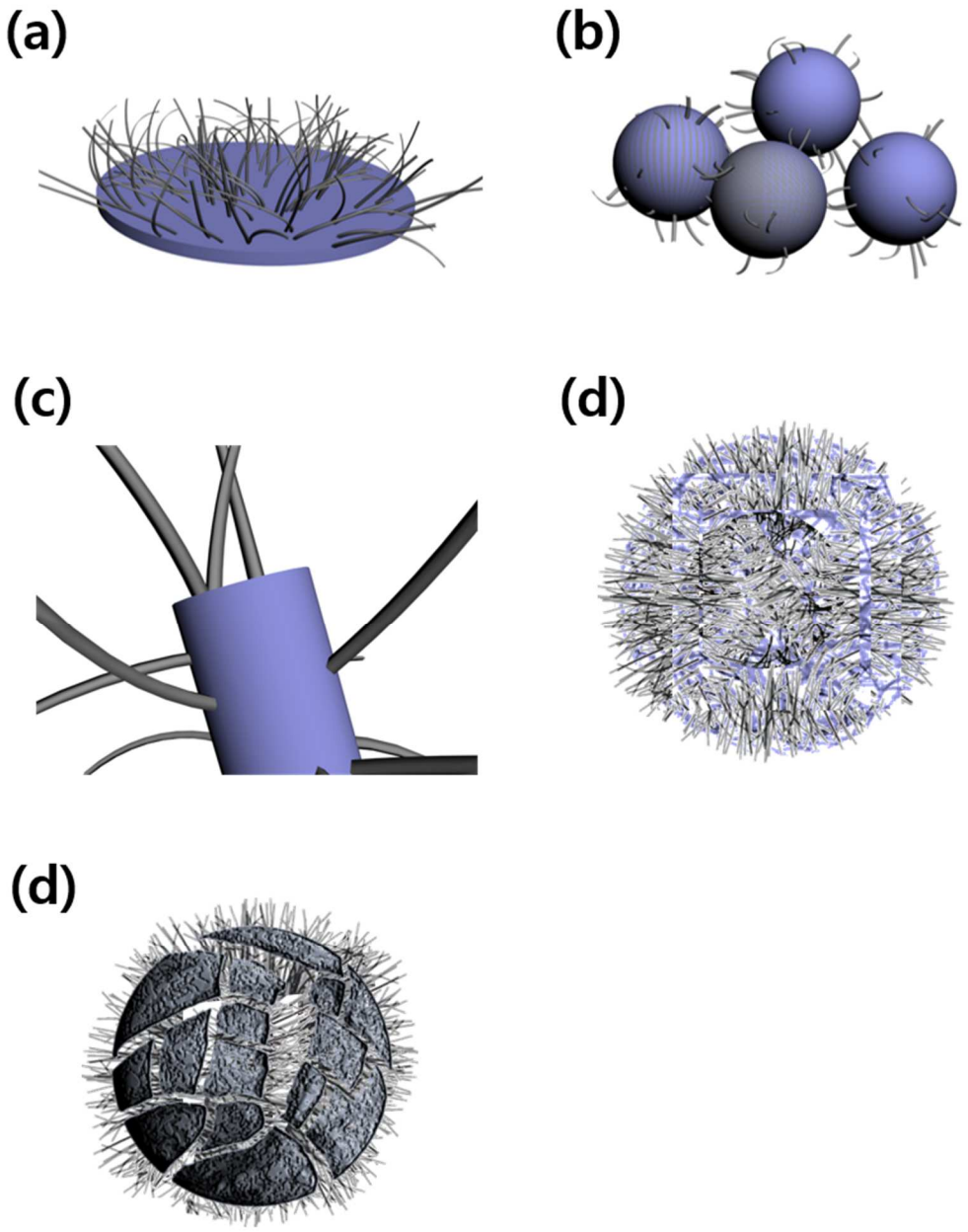

Figure 1-1. Schematics of different support geometries for a metallocene catalyst in ethylene polymerization: (a) flat surface, (b) silica nanoparticle, (c) silica nanotube, (d) macroporous silica, (e) silica microparticle.

Table 1-1. Characteristics of silica supports

	Fragmentation	Dynamics of fragmentation	Monomer diffusion resistance	Catalyst site usage
Flat surface	absent	n.a.	minimal	very high
Nonporous nano-size spherical particle	absent	n.a.	minimal	very high
Cylindrical nanotube	present	time dependent	low	high
Macroporous particle	present	time dependent	low	high
Porous micron-size spherical particle (conventional silica)	present	time dependent (gradual)	strong	low (fragmentation dependent)

1.1.2. Silicon Anode for Li-ion Battery

During the study on the silica-supported metallocene catalyst for the synthesis of ethylene and syndiotactic polystyrene, the polymer nanofibrils grown directly from the silica surface were observed. When the monomer conversion is controlled to a certain low level, the *in situ* silica-polymer composite can be easily prepared with polymer nanofibrils permanently and covalently attached to the silica surface [9-12]. This observation led to the idea of developing an *in situ* composite of silicon particles and CNTs because this process is also catalyst assisted and CNTs grow as nanofibrils when properly controlled. Collaboration with Prof. C.S. Wang who is directing the lithium battery research laboratory at the University of Maryland has been sought to test this idea. Furthermore, the test results indicated that the Si/CNT anode system was quite effective to maintain the anode stability.

Si has the highest-known theoretical charge capacity (~4200 mAh g^{-1}), but it is known to have limited applications as anode material for Li ion batteries because of the large volume change (about 400%; each Si atom can accommodate 4.4 Li atoms to form $Li_{22}Si_5$ alloy when it is fully lithiated) [13]. The volume change eventually leads to cracking and pulverization of the Si anode, thereby causing the loss of electrical contact and capacity fading [14]. The research presented in this thesis is aimed at developing a novel integrated system of silicon nano particles networked with carbon nanotubes that are grown directly at the silicon particle surfaces using bi-metallic catalyst. Through optimization of silicon particles and CNT dimensions, the highest possible anode capacity can be developed. The chemical and physical phenomena associated with the growth of CNTs on silicon particles and the lithiation and delithiation processes were investigated through experimentation.

Recognizing the potential of silicon as highest capacity anode material for Lithium ion batteries, many researchers have reported various techniques in the literature to mitigate the silicon fragmentation and rapid capacity decay problems and thereby to improve the cycling characteristics of the silicon based anode materials. One of the techniques involves the homogeneous dispersion of an electrochemically active phase within an electrochemically inactive matrix that provides the resistance to the mechanical stresses and strains by alloying and dealloying processes [13]. For example, composites of silicon and graphite have been attempted to obtain a stable capacity of 1000 $mAhg^{-1}$; however, the small amount of nanosized Si used in the composites resulted in low specific capacity. Carbon-coated Si nanocomposites have also been reported to show some improvement (1489 $mAhg^{-1}$, high coulombic efficiency for about 20 cycles) [15]. Cui et al. developed silicon nanowire anode-prepared by reductive decomposition of a silicon precursor in an alumina template and etching [16]. Other reported techniques include a Si film deposited on a Ni substrate. Although these reported techniques offer some improvements in Si anode performances, the development of an anode exhibiting a stable and reversible high capacity (e.g. > 1000 mAhg-1) is still a challenging technical problem.

Carbon nanotubes (CNTs) have been tested as Li insertion host materials (anode) in the past but a high irreversible loss and a large voltage hysteresis have greatly limited their use as anode material in Li ion batteries [17]. However, CNTs can be an excellent matrix material for Li-ion anodes because of their excellent mechanical strength (Young's modulus of 1.0 TPa) and electrical conductivity (resistivity < 10^{-4} Ω/cm). When CNTs and Si particles are mixed to form a composite structure, homogeneous distribution of Si particles within the CNTs is practically difficult, limiting the commercial potential of the composite anode.

The anode research in this dissertation is aimed at developing a stable Si anode materials that consist of Si particles on which CNTs of controlled dimension (length, thickness and surface population) are grown without any usage of binder. Nano Si particles are used and CNTs are grown using cobalt-iron bimetallic catalyst in a horizontal quartz tube reactor with acetylene as a carbon source. Figure 1-2(a) shows the concept of the CNT-loaded Si particles on a current collector plate. The CNTs emanating from Si particle surfaces can be entangled and they play a role of holding the Si particles during the lithiation and delithiation deformation processes as well as conducting electrons from the Si particles to the current collector. The population of CNTs on the Si particle surface should be controlled and optimized not to restrict the access and transport of lithium ions during the charge and discharge cycles.

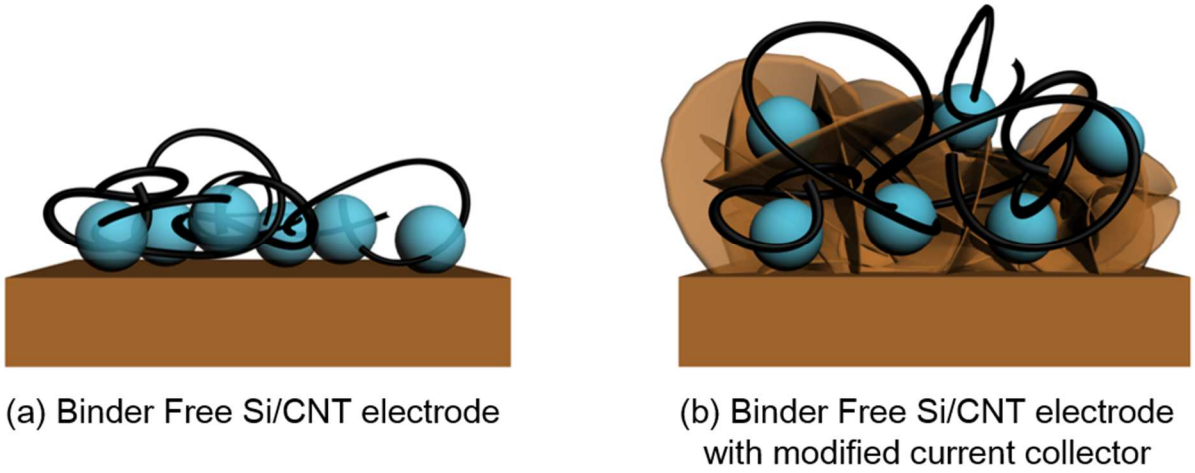

Figure 1-2. Concept of (a) binder free Si/CNT electrode, and (b) binder free Si/CNT electrode with surface modified current collector.

In this research, CNTs are used as an electron conducting material as well as a holder for Si particles during the service life of a Li-ion battery. Unlike in other researchers' attempt to

make Si-CNT composite by blending these two constituent materials, CNTs are grown directly at the surface of Si particles, thereby improving the electron transport ability during the lithiation/delithiation cycles. Another main difference between other researchers' and this work is that in this work, the binder free Si/CNT electrodes (Figure 1-2(a)) were successfully developed. Furthermore, the surface of current collector was modified to have a higher surface area to increase the contact area between active materials and current collector as illustrated in Figure 1-2(b) so the battery can have more stable cycle life.

The use of Si as anode material has excellent merits but the structural deformation of Si due to alloying and dealloying processes with Li ion is a problem in maintaining high specific capacity and long charge-discharge cycles. The developed technique will alleviate these critical technical problems.

1.2. Research Objectives

The major objectives of the dissertation are:

(1) To investigate the polymer morphology and kinetic behavior of ethylene and styrene polymerization over different geometries of silica support catalysts system;

(2) To develop a microreactor system for metallocene catalyst and olefin polymerization / copolymerization;

(3) To investigate a Si/CNT anode material for Li-ion battery and fabricate a stable binder free electrode;

For the successful development of a microreactor system for metallocene olefin polymerization, it is needed to investigate the morphological growth of polymer because it helps us to understand the polymerization mechanism and polymer properties. It is also needed to investigate the kinetic behavior of olefin polymerization to optimize the reaction conditions of microreactor. Similar to olefin polymerization, the morphological growth and kinetic behavior of CNT are needed to be investigated to control, optimize the Si/CNT ratio, so someone can customize and maximize the stability of Si/CNT electrode. Binder free electrode can reduce the use of organic solvent and increase the specific capacitance if the active materials are strongly attached on current collector. Therefore, it is expected that the current research reported in this dissertation will offer new concepts and valuable contributions to the olefin manufacturers and Li-ion battery technology.

Chapter 2. Kinetics and Growth of Polyethylene Nanofibrils over Metallocene Catalyst supported on Flat Silica and Spherical Nano-Silica Particles*

2.1. Abstract

The kinetics of ethylene polymerization and the growth of polymer nanofibrils for the *rac*-Et(indenyl)$_2$ZrCl$_2$/MAO catalyst supported on flat-surface silica and nonporous silica nanoparticles are presented. The polymerization rate per mol of Zr is highest for the flat silica supported catalyst due to maximum exposure of catalyst sites to cocatalyst and monomer. The SEM and AFM analysis show that large clusters of oxidized form of MAO are present at the surface, while nano-silica supported catalyst show less of such effects. The polyethylene grows as nanofibrils of 30–50 nm in diameter from the silica surface. No particle fragmentation is observed with nano-silica supported catalyst where polymer nanofibrils grow only from the external surface. Polymer properties are almost not affected by the support type.

---

* The materials presented in this chapter has been published :
Lee, S. Y.; Choi, K. Y. Kinetics and Growth of Polyethylene Nanofibrils over Metallocene Catalyst Supported on Flat Silica and Spherical Nano-Silica Particles. *Macromolecular Reaction Engineering* **2014,** *8* (11), 755-765.

2.2. Introduction

In heterogeneous polymerization of α-olefins over supported catalysts, the properties of support materials influence the polymerization activity, polymer morphology, and sometimes polymer properties such as molecular weight distribution. Highly porous micron-size silica particles having large specific surface area (e.g., 250-300 m^2/g), good mechanical properties, and surface silanol groups have been an important class of support materials for industrial α-olefin polymerization catalysts such as metallocene catalysts and chromium oxide catalysts (Phillips catalyst).

The properties of silica and the techniques of supporting metallocenes onto silica particles for olefin polymerization have been the subject of extensive studies in the past years. It is to be noted that many of the previous studies have focused on the development of improved understanding of (i) how a specific catalyst component is anchored onto a silica surface and complexed with cocatalyst such as methylaluminoxane (MAO) to form active catalytic sites, (ii) how the polymerization kinetics are affected by the nature of catalyst complex, (iii) what are the effects of mass and heat transfer limitations in a growing polymer particle, and (iv) how a silica-polymer particle disintegrates during the polymerization and influences the polymerization rate, polymer molecular weight distribution (MWD), and polymer particle morphology.

The morphological changes of a polymer particle during the polymerization in conventional silica-supported metallocene polyolefin processes are known to be different from those observed in $MgCl_2$-supported Ziegler-Natta catalyst processes for ethylene or propylene polymerization. For example, in the latter, micron size original catalyst support particles disintegrate in the early stage of polymerization into catalyst crystallites of about 5-17 nm and

they are dispersed within the polymer particle and act as individual polymerization nuclei. Each catalyst crystallite is encapsulated by the growing polymer primary particles of 100-350 nm and these primary particles agglomerate to about 1 μm sized polymer particles [18, 19]. This mechanism of particle fragmentation and growth has been modeled quite successfully using various types of polymer particle models such as multigrain model (MGM), polymeric flow model, solid-core multigrain model, and other variations [20-26]. Intraparticle and interfacial monomer diffusion and heat transfer limitations that affect the polymerization kinetics and polymer properties are also strongly related to catalyst fragmentation and particle morphology.

In silica-supported metallocene catalysts, active catalytic centers are formed at solid surfaces inside the pores of mean diameter of c.a. 30 nm. There are several different techniques to deposit a metallocene catalyst onto a silica surface. Although we do not intend to provide a comprehensive review of the catalyst supporting techniques in this paper, one of the most widely used methods is to treat a silica surface containing surface silanol groups with methylaluminoxane (MAO) before a metallocene catalyst is added to form a catalytic complex with the surface-anchored MAO [27]. The silica surface consists of a mixture of single silanols, hydrogen-bonded vicinal silanols, silanediol (geminals) and siloxane. The surface properties can be controlled to some extent by the calcination temperature. The complexity of the surface characteristics is also due to the fact that the commonly used cocatalyst, MAO, is not of a single or uniform structure but is often a mixture of clusters and cages [28]. Commercially available MAO solution also contains trimethylaluminum (TMA). To prepare a silica-supported catalyst, for example, silica particles are first treated with a solution containing methylaluminoxane (MAO). Then, the MAO treated silica particles are brought to contact with a solution containing metallocenes. The metallocenes diffuse into the pores and form active catalytic complexes with

MAO molecules that are anchored at the silica surface. It is not difficult to expect that the performance of the catalyst will be dependent upon how effectively these catalyst components are immobilized onto the silica surface inside the pores to form desired active catalytic sites.

Unlike Ziegler-Natta type catalysts, silica-supported metallocene catalysts are known to undergo a layer-by-layer fragmentation process [29]. According to this mechanism, a thin layer of porous external surface of a silica particle, upon exposure to monomer in a reactor, is quickly penetrated by the monomer as the polymerization begins. The polymerization in the surface layer rapidly fills up the silica pores, leading to the formation of a dense surface layer, which causes a strong diffusion resistance for the additional transport of monomer from the bulk fluid phase to the interior of the catalyst particle. As a result, the polymerization rate decreases during this period. As the polymer mass continues to increase in the pores, the hydraulic force rises by the pore-filling polymer and eventually leads to the disintegration of the silica layer, allowing for the further diffusion of ethylene toward the particle interior. Thus, polymerization leads to a gradual cracking and disintegration of the catalyst-loaded silica particle from the outer surface to the particle core. The fragmentation of silica exposes active catalytic sites present inside a particle to monomer to permit further polymerization reaction but these fragments are connected to each other by polymers. As a result of particle fragmentation and exposure of catalytic sites, the polymerization rate gradually increases with time. The size of the ultimate silica fragments in olefin polymerization has been reported to be about 20~100 nm. If the fragmentation is complete in the early stage of polymerization, the polymerization rate profile exhibits high reaction rate initially but followed by a gradual or sometimes rapid rate decrease, which is often called the decay type kinetics.

Due to the complexities associated with the preparation of silica supported metallocene catalysts, metallocene catalysts immobilized onto the silica surface exhibit catalytic performances (e.g. reaction rate, polymer properties, and particle morphologies) that are often quite difficult to reproduce consistently. As a result, direct comparison of catalyst activities or polymerization kinetics measured by different authors even for the same catalyst systems is often results in significant discrepancies. Therefore, to develop a fundamental understanding of the intrinsic polymerization kinetics over a heterogeneous metallocene catalyst, it would be desirable to eliminate some factors that may contribute to the uncertainties or variations in the final polymerization data. One of such factors that can be removed with a relative ease is the geometry of a support silica material. For example, flat-surface silica can be an ideal support geometry because it would be possible to uniformly disperse catalytic sites onto the geometrically well-defined silica surface. Also, since the flat-surface silica will not disintegrate during the polymerization, the physical and chemical effects of catalyst fragmentation in conventional silica supported catalyst systems can be completely eliminated. Another silica support geometry we can think of is a solid (non-porous) silica particle as a three-dimensional representation of a flat silica support. On such silica particle surface, the catalyst components can be deposited only onto the external surface of the particle and like in the flat surface silica supported catalyst, the maximum catalytic site efficiency can be attained without any fragmentation effects. Therefore, these two geometrically well-defined silica support materials are used in the present work to investigate the polymerization kinetics and the growth of polymer from the catalyst surfaces.

The preparation techniques for non-porous solid silica nanoparticles are well documented in the literature. Also, the use of nanometer size silica particles for catalytic olefin polymerization has been reported in recent literature [30-35]. There was a report that nanosilica

supported metallocene catalysts showed higher polymerization activities and slightly larger molecular weight than the micron-sized porous silica supported catalysts. For example, Amgoune et al. [30] used silica particles of about 50 nm-diameter as a support for modified salicylaldiminato-substituted titanium (IV) complexes incorporating a trimethoxysilane-terminated liner that were bound covalently to silica nanoparticles. These supported catalysts showed high ethylene polymerization activity as well as high polymer molecular weight. The titanium catalyst was anchored only onto the external surface of the silica nanoparticles; however, the authors reported that the fragmentation of silica nano particles occurred. According to the reported scanning electron microscopy and transmission electron microscopy data, the diameter of the polymer particles was about 200-500 nm (grown from 50 nm silica particles) and the fragmented silica nano-particles of about 8-12 nm were dispersed quite homogeneously within the polyethylene particles. No intact original nano-silica particles were reported to be present in the TEM images. The authors concluded that original silica nano-particles have fragmented during the polymerization. This report poses a puzzling question about the particle fragmentation because it has been well known that silica nano-particles synthesized by Stöber process are smooth and compact with no internal pores. If internal pores are not present, catalyst sites will be present only at the external particle surface and hence, polymers can grow only at the silica nano-particle surfaces where active catalyst sites are present. The surface area of 50 nm-diameter silica particles used by these authors was reported to be 239 m^2/g that is much larger than the external surface area (65 m^2/g). Such a high surface area is possible only if the silica particles are very porous as noted by the authors [30] Also, the average pore size in the silica nanoparticles was reported to be about 20 nm, which seems to be quite large for a particle of 50 nm-diameter. The authors suggested that these mesopores corresponded to interstices

between packed particles. The presence of much smaller pores less than 2 nm was also observed by BET measurements. Although, these authors showed that the silica nanoparticles fragmented during the polymerization, it leaves a question about the statement by the authors that the polymer layer at the particle surface can exert pressure for the spherical silica particle to disintegrate.

In this chapter, the experimental study of ethylene polymerization over metallocene catalyst deposited on a flat-surface silica as well as on the non-porous silica particles of 300~400 nm diameter with MAO as a cocatalyst has reported. The kinetics of polymerization as well as the morphology of polymer growing in these catalyst systems is discussed.

2.3. Experimental

2.3.1. Materials

A flat surface silica support was prepared using a 2 inch silicon wafer (University Wafer, P-type). Polymerization grade ethylene (Air products) was purified by passing through a stainless steel column packed with R3-11 Cu catalyst, 4Å molecular sieves, neutral alumina and activated carbon. Toluene (Aldrich) was used as a diluent and it was purified over sodium and benzophenone in nitrogen atmosphere. *Rac*-Et(1-indenyl)$_2$ZrCl$_2$ (EBI) was used as a main catalyst (Aldrich) and methylaluminoxane solution (MAO, Aldrich, 10 wt.% in toluene) was used as a cocatalyst.

2.3.2. Preparation of silica supports

To prepare a flat surface silica support, a silicon wafer surface was treated with a piranha solution and calcined at 250^{o}C in a furnace. Silica nano-particles were synthesized using a modified Stöber process. A solution of 0.124 moles of tetra ethyl ortho silicate (TEOS, Sigma Aldrich) in 50 mL ethanol was added to a solution of NH_4OH (6.34 mL), distilled water (11.3 mL), and ethanol (32.5 mL) slowly and the mixture was allowed to react for 1 h with agitation. Then, equal volume of HCl solution was added to neutralize the solution. The solution was filtered, washed with water several times, and dried in a high temperature oven. Figure 2-1 show the SEM images of silica nanoparticles. The synthesized silica particles had the following properties: density = 2.648 g/mL, average particle diameter ~ 400 nm.

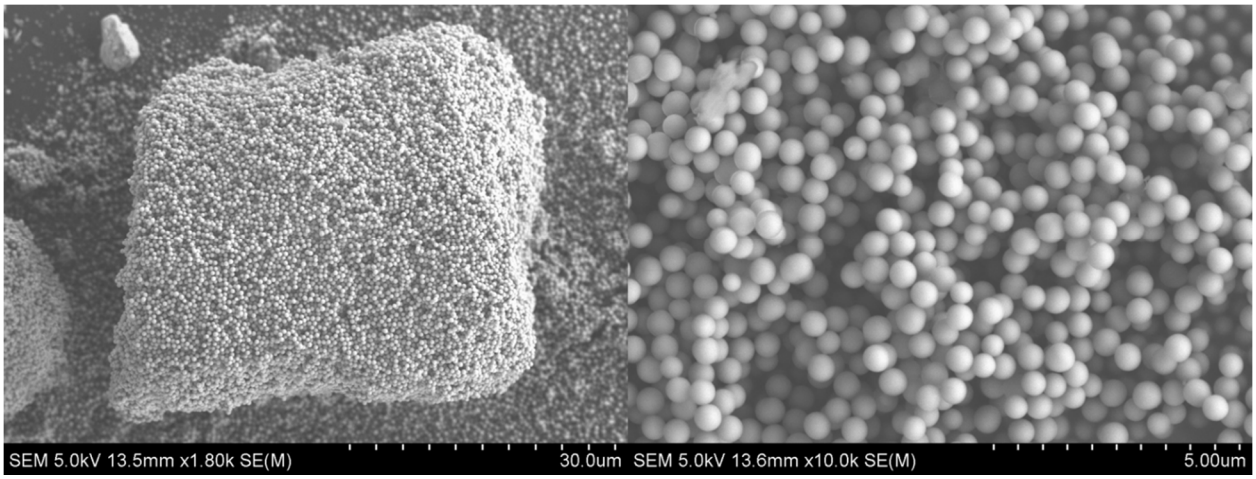

Figure 2-1. SEM image of nonporous silica nanoparticles.

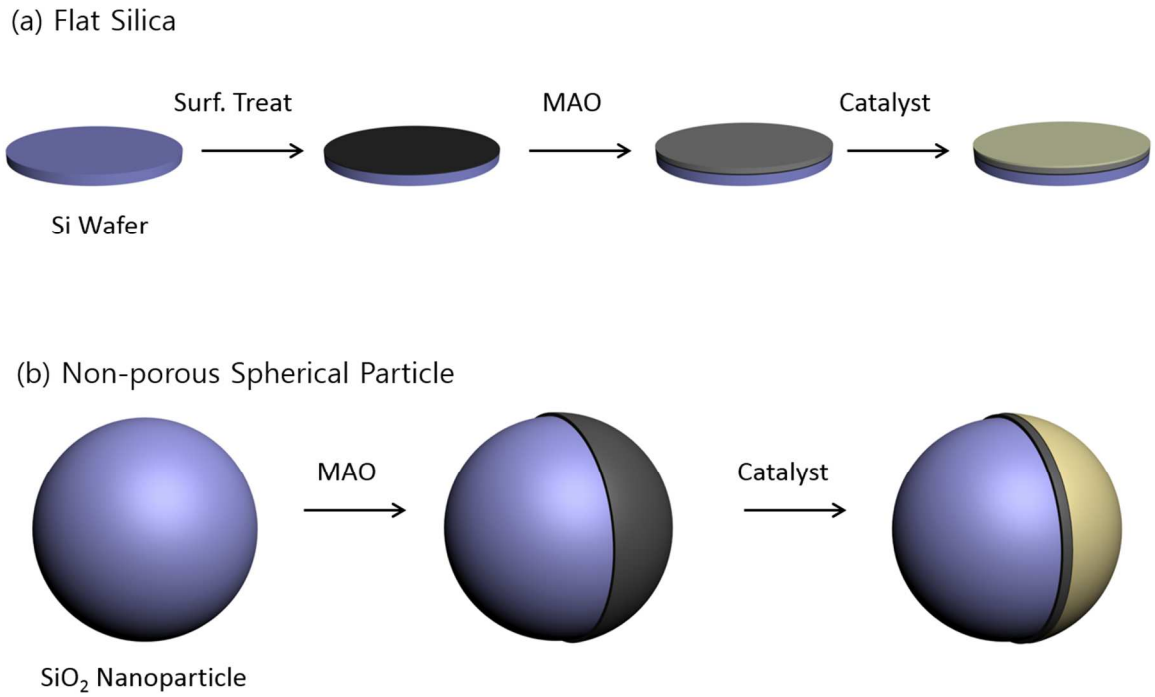

Figure 2-2. Schematic illustration of preparing flat-surface catalyst and solid silica supported catalyst.

2.3.3. Preparation of silica-supported catalysts

The procedure for the preparation of flat-silica and nano-silica supported catalysts are illustrated schematically in Figure 2-2. A known amount of nano-silica particles were first

calcined at 250oC for 24h (-OH group concentration at this temperature: 1.0-2.4 mmol/g) [36] and they were treated with a mixed acid solution (30% hydrogen peroxide and 70% sulfuric acid) for 30 min, washed with excess amount of deionized water, and then treated with an MAO solution (10 wt.% in toluene, Aldrich) at ambient temperature for 24 h. The MAO-treated silica support was washed with toluene several times, and dried in vacuo overnight. Then, it was immersed in the rac-Et(1-indenyl)$_2$ZrCl$_2$ (EBI) catalyst (Aldrich) in toluene solution for 24 hr, washed with toluene several times, and dried in vacuo overnight. The flat-surface catalyst was prepared using the same procedure. The Zr loadings were measured by inductively coupled plasma mass spectrometry (ICP-OES (ACTIVA, JY HORIVA))*. It is shown that the catalyst loading per unit surface area of the non-porous silica nanoparticles is much larger than the typical catalyst loading in conventional (commercial) porous micron-sized silica supported catalyst as illustrated in Table 2-1. According to the literature, the Zr loading on silica by impregnation method is about 1.8×10^{-7}mol Zr/m2 (0.4 wt.%) [37-39], which is consistent with the measured Zr loading in this work as shown in Table 2-1. It is also observed that the Zr loading (mol/m2) for the flat silica supported catalyst is about 3 times larger than for the nano-silica supported catalyst. The data in Table 2-1 indicates that although the zirconium loading per gram of silica for the nano-silica and commercial micron-sized porous silica supported catalysts is quite similar, the Zr loading per unit surface area on the commercially available silica supports is only 3.8~4.8% of that on the nano-silica support and 1.4~1.7% of that on the flat silica support. Therefore, these data suggest that forming active zirconium sites in conventional micron-sized porous silica support is very inefficient compared to other silica support materials. It is probably because the pore size distribution of conventional silica particles is broad and

* Measured by Prof. Jin Suk Chung at Ulsan University, South Korea.

despite of large specific surface area, a large fraction of silica surface may not be accessible by metallocenes and/or MAO.

Table 2-1. Properties of silica and silica-supported catalysts

Support Material	Diameter (μm)	Surface area (m^2/g-cat)	Zr (mol/g-cat)[b)]	Zr (mol/m^2)
Flat-silica	-	0.015	8.56×10^{-8}	5.71×10^{-6}
Nano-silica	0.4	16.0[a)]	3.17×10^{-5}	1.98×10^{-6}
Commercial silica[c)]	30 ~ 50	250~295.0	$(1.88\sim2.82)\times10^{-5}$	$(7.52\sim9.56)\times10^{-8}$

[a)] External surface area; [b)] by ICP; [c)] Davisil 643® and Sylopol 948®

2.3.4. Polymerization

Ethylene polymerization experiments were carried out using a 500 mL glass reactor equipped with a two-blade mechanical agitator. Predetermined amounts of solvent (toluene), MAO solution, and supported catalyst were charged into the reactor in an argon-filled glove box. The concentration of aluminum ([Al]) in the liquid phase was 6.03×10^{-3} mol/L in all the experiments. The charged reactor assembly was removed from the glove box and was installed in a fume hood. The reactor was immersed in a constant temperature bath at 70°C. After the reactor temperature was stabilized at its target temperature, ethylene supply valve was open and the

reactor pressure was kept constant at 2.07 bar and the reactor temperature was controlled at 70 ± 2°C throughout the polymerization. The ethylene concentration in the liquid phase at given temperature is calculated by Henry-Gesetz equation [40], which is developed to calculate the ethylene solubility in toluene:

Equation 2-1

$$[E] = P_E H_0 \exp\left(\frac{\Delta H_L}{R \cdot T}\right)$$

where P_E is ethylene pressure (bar), H_0 = 0.00175 (mol/L.bar), and ΔH_L = 10,742 (J/mol).

According to Equation 2-1 the ethylene concentration dissolved in toluene is 0.157 mol/L. The reactor temperature, pressure, and ethylene supply rate were monitored on-line using a data acquisition computer (Figure 2-3(b)). The recorded ethylene supply rate (polymerization rate) was integrated over reaction time to calculate the polymer yield data. The calculated and experimentally measured polymer yield data agreed well (within ± 7 ~ 9 % of scatter range. After polymerization, the reaction mixture was filtered, washed with an excess amount of acidified methanol and vacuum dried.

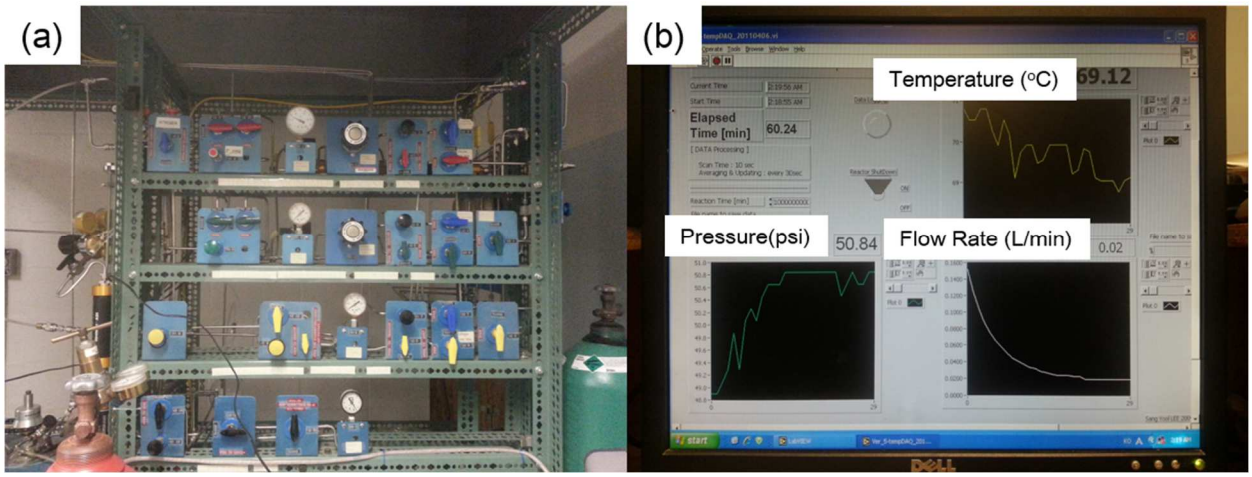

Figure 2-3. (a) Actual experimental plant, (b) data acquisition program.

2.3.5. Polymer analysis

The morphologies of polyethylene synthesized over silica-supported catalyst were analyzed by scanning electron microscopy (SEM, Hitachi S-4700). The sample particles were coated with carbon layers in a Denton DV-503 vacuum evaporator. The atomic force microscopy (AFM) analysis was carried out using Bruker Dimension 3000 with a normal Si 40-50 nm radius probe. Si cantilever tip (Veeco) with a resonance frequency 334 kHz, force constant 40 N/m was used. The molecular weight distribution was measured by gel permeation chromatography (Polymer Laboratories) using 1,2,3-trichlorobenzene at 160°C with PLgel® 10 μm MIXED-B and PLgel® 10 μm GUARD columns*.

* LG Chemical., Daejeon, South Korea.

2.4. Results and Discussion

2.4.1. Catalyst activity

The polymerization rate is estimated by converting the ethylene consumption rate measured by an in-line mass flow meter. Figure 2-4 shows the catalyst activity (i.e., polymerization rate) data for the flat silica and nano silica supported catalysts. Also shown in Figure 2-4 are the polymerization data (in Kg/mmol-Zr.min) obtained using conventional commercial-grade porous silica particles (Davisil® 643 and Sylopol® 948, W.R. Grace & Co.). We can observe that the flat silica supported catalyst shows the highest activity, followed by the nano-silica supported catalyst and the two conventional micron-size silica supported catalysts.

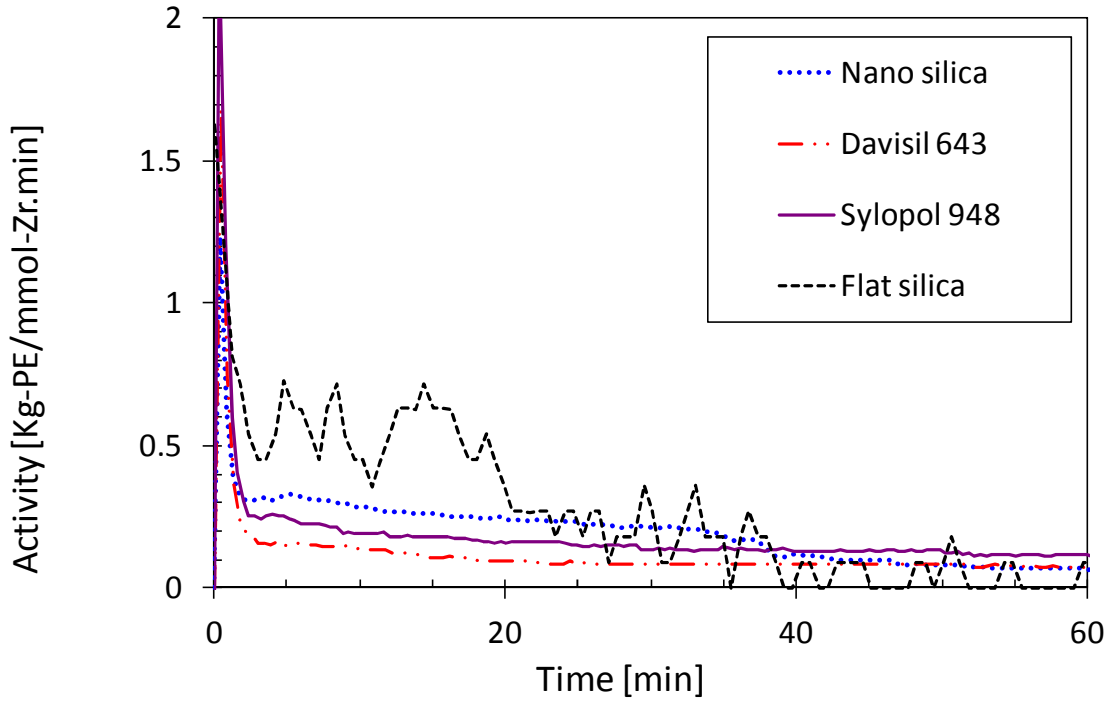

Figure 2-4. Polymerization activity profiles of flat silica, nano-silica, and two commercial silica supported catalysts.

Since the original polymerization rate data (i.e., ethylene consumption rate) shown in Figure 2-4 are noisy, time-averaged polymerization rate will be used in the following discussion. To discuss the catalytic activities of the supported catalysts used in this study, we first define the polymerization rate in Kg-polymer/g-cat .min as follows:

Equation 2-2

$$\tilde{R}_p = k_p[\mathrm{Zr}][M]w_m \quad \text{(Kg/g-cat.min)}$$

where k_p is the propagation rate constant (L/mol.min), [Zr] is the active catalyst site concentration (mol/g-silica), [M] is the monomer concentration (mol/L), and w_m is the molecular weight of ethylene (Kg/mol). Here, it is assumed that g-cat ≈ g-silica. Assuming that an active zirconium site decays following the first order kinetics, we can reduce the Equation 2-2 to $\tilde{R}_p = k_p[\mathrm{Zr}]_0 e^{-k_d t}[M]w_m$. The polymerization rate (R_p) can also be expressed in Kg/mmol.Zr.min by the following equation:

Equation 2-3

$$R_p \equiv \frac{\tilde{R}_p}{[\mathrm{Zr}]_0} = k_p e^{-k_d t}[M]w_m$$

In this formulation, we assume that the total amount of zirconium in silica ($[\mathrm{Zr}]_0$), measured by ICP, is catalytically active. The polymerization rate constant and the deactivation parameter can be determined by plotting the polymerization rate vs. reaction time expressed by the following equation:

Equation 2-4

$$\ln R_p = \ln\left(\frac{\tilde{R}_p}{[\mathrm{Zr}]_0}\right) = \ln\left(k_p[M]w_m\right) - k_d t$$

Figure 2-5 shows the test of this equation for the four supported catalysts used in our experiments and it is seen that Equation 2-4 fits the data quite well.

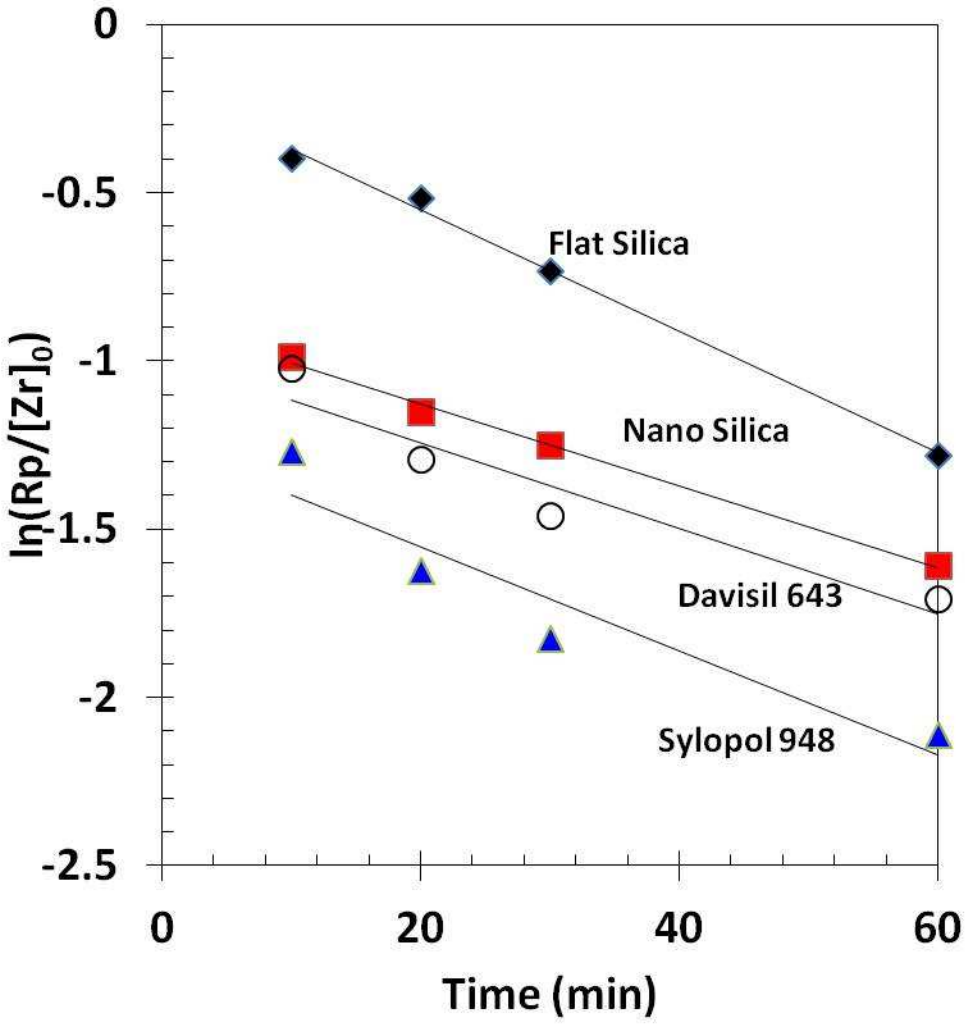

Figure 2-5. Polymerization rate analysis.

Table 2-2 summarizes the results obtained by analyzing the data in Figure 2-5. The polymerization rate at t = 0 (third column in Table 2-2) for each catalyst system was obtained by extrapolating the linear regression line in Figure 4 to time zero. The polymerization rate data in Table 2-2 show that all four supported catalysts exhibit similar catalytic activities per molar site

of zirconium, although flat silica supported catalyst is about 2~3 times larger activity than the other three supported catalysts.

Table 2-2. Analysis of polymerization data*

Catalyst	R_p (Kg/mmol Zr.min) time averaged for 20 min	$-\ln\frac{\tilde{R}_p}{[Zr]_0}$ at t = 0	$k_p[M]w_m$	$\frac{k_p}{k_{p,flat}}$	k_d
Flat-silica	0.600	0.1897	0.827	1.0	0.0181
Nano-silica	0.316	0.886	0.412	0.498	0.0121
Davisil 643	0.198	0.988	0.372	0.450	0.0127
Sylopol 948	0.275	1.242	0.289	0.349	0.0155

* [Zr] in mmol/g-cat, [M] in mol/L, k_d in min^{-1}, $k_{p,flat}$ = propagation rate constant for flat silica supported catalyst (L/mmol.min)

For the flat silica catalyst, the propagation rate constant at 70 ^oC estimated from the data in Table 2-2 is k_p = 188.1 L/mmol.min. Although both the flat surface catalyst and the nano-silica supported catalyst are believed to have active catalytic sites only on the external surface of silica that is fully exposed to monomer, Table 2-2 indicates that the propagation rate constant for the solid nano-silica supported catalyst is 50% smaller than for the flat-silica catalyst. Also, the propagation rate constants for the conventional porous silica supported catalyst are about 35~45 % of that for the flat-silica supported catalyst. The reasons for smaller rate constants may include incomplete active site formation inside catalyst pores and incomplete fragmentation of silica particles (Davisil 643 and Sylopol 948).

2.4.2. Catalyst surface characterization

We have analyzed the surface characteristics of a flat-silica supported catalyst using the energy-dispersive X-ray spectroscopy (EDX/EDS, EDAX (Ametek) attached to AMRAY-1610). The flat-silica supported catalyst sample was prepared by first oxidizing a silicon wafer surface and treat it with an MAO solution (0.9~1.7 wt.% in toluene) at room temperature for 24 h. Then, the sample was washed with toluene, and dried in vacuo overnight. The MAO treated sample was immersed in a toluene solution containing $Et(indenyl)_2ZrCl_2$ catalyst for 24 h, washed with toluene, and dried in vacuo overnight. Figure 2-6 shows the EDX images of the catalyst surface. (Note: Since the catalyst was exposed to air and oxidized, the image shown in Figure 2-6 may not represent the true surface characteristics of the supported catalyst under actual polymerization conditions). We can observe that the silica surface is covered with a layer of MAO-Zr and it is seen that the layer is not a uniform thin layer but it consists of clusters or aggregates of MAO in certain regions of the silica surface. From EDX and ICP data, Al/Zr (mol/mol) ratio of 27.0 was obtained.

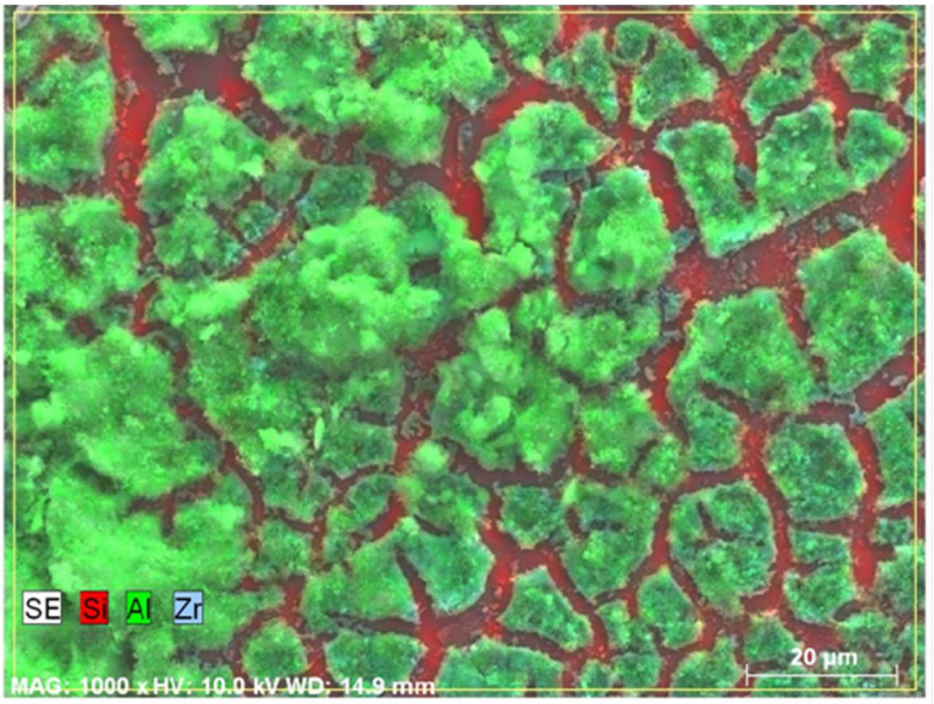

Figure 2-6. EDX scan image of a flat-silica supported catalyst.

The catalyst surface was also analyzed by Atomic Force Microscopy (AFM) using a high resolution diamond-like tip (Hk'RES-C14, MicroMasch) with scan rate of 1 line/sec and scan size of 5 µm. Figure 2-7 shows the three-dimensional AFM image of the flat-silica catalyst and Figure 2-8 is the height measurement. It is seen that the MAO-catalyst sites are distributed on the solid surface as clusters of size ranging from about 130 nm to 350 nm. Some clusters appear to be the aggregates of small clusters (base length: 130-400 nm) that are about 50 nm high. The distance between non-aggregated clusters varies from about 50~70 nm to as large as 700 nm. The large aggregate of clusters in the center of the AFM image in Figure 2-8 is 197 nm high. The AFM images suggest that when a silica surface was treated with an MAO solution, the surface was not uniformly deposited with MAO molecules that were immobilized onto the surface by the reaction with surface hydroxyl groups.

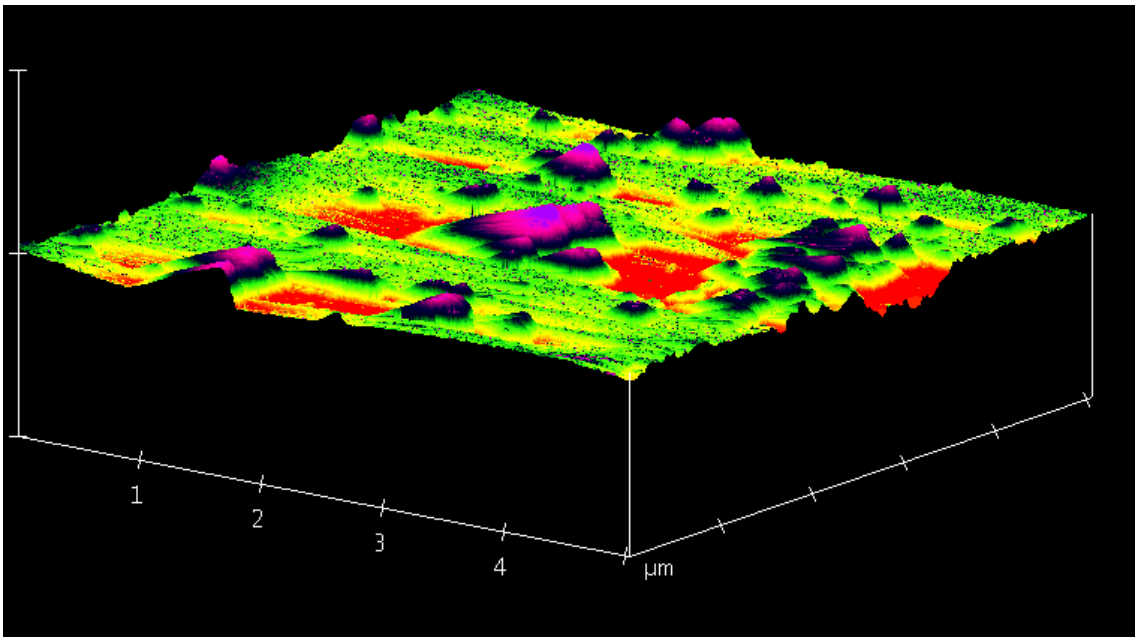

Figure 2-7. Three dimensional image of the AFM scan image of the flat-silica supported catalyst.

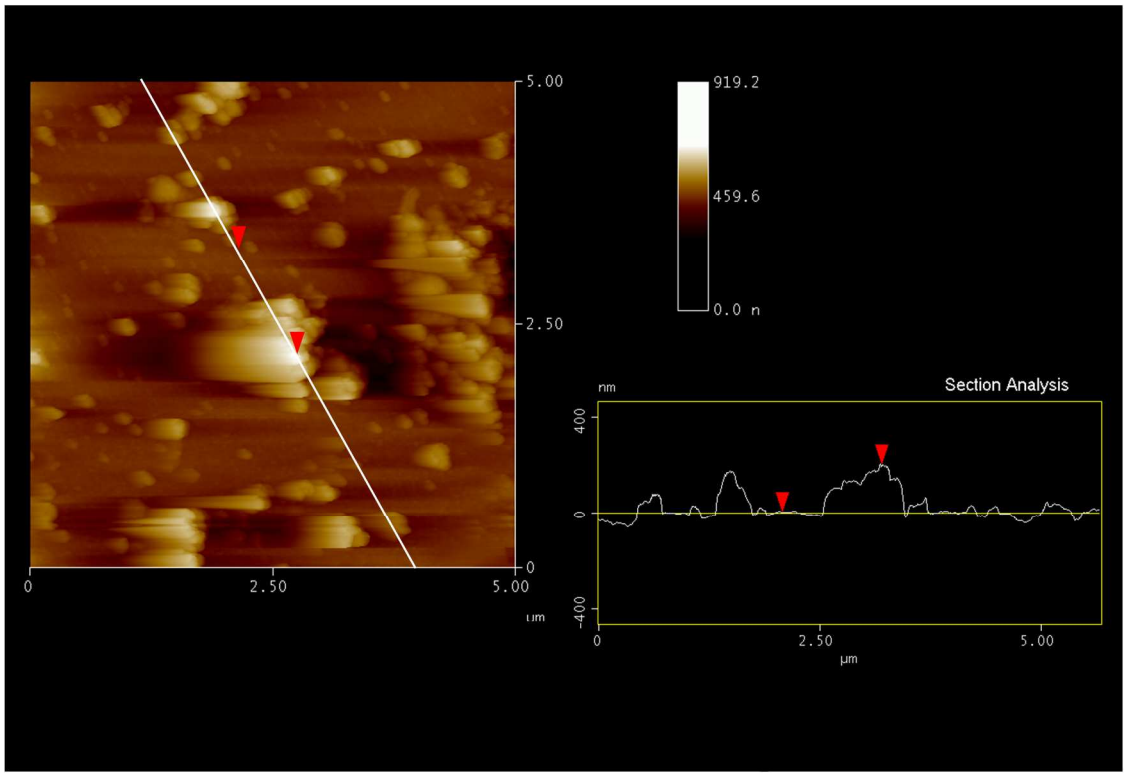

Figure 2-8. AFM images of a MAO-catalyst deposited flat surface silica surface.

2.4.3. Morphology of polymer growing from catalyst surfaces

The growth of polyethylene at the solid catalyst surface has been an interesting and important subject of study for many years. The flat-silica supported catalyst and the nano-silica supported catalyst offer unique opportunities to directly observe the nascent morphology of polymers growing from the active metal sites at the catalyst surface.

2.4.3.1. Flat surface catalyst

When a flat-silica supported catalyst was used for ethylene polymerization, a 2 inch-diameter catalyst wafer was broken into small pieces so that they can be inserted into a glass reactor bottle in the glove box. For the visual observation of the polymer growth at the flat catalyst surface, the pieces of flat catalyst were placed at the bottom of the reactor and the liquid phase was not stirred. Figure 2-9 shows the pictures of polymerization reactor at different reaction times. These pictures clearly show that as polymers are formed at the flat-surface catalyst, they grow in fibrillar shape and disperse into the liquid phase (toluene). As reaction continues with time, the entire glass reactor is filled with polymer.

Figure 2-10 shows the SEM images of polyethylene formed at the surface of flat-silica deposited catalyst. First of all, we observe that polyethylene nanofibrils of diameter 30-40 nm were growing from the silica surface. Also, we can see some MAO/catalyst clusters from which a multitude of polymer nanofibrils are growing, suggesting that active catalytic sites are also present in the cluster aggregates. At the silica surface, there are many round shaped blobs of diameter 50-100 nm that seem to be the polymers growing from prematurely dead active sites. In 1968, Guttman and Guillet [41] reported that when propylene was polymerized on single crystals of α-$TiCl_3$ catalyst, the polymer growth starts with a globular shape with a diameter of 30-50

nm, spaced relatively uniformly along the lateral faces or at crystal dislocations, but as growth continued, these globules elongated into fibrils of approximately same diameter. Although the catalyst and the polymer (polypropylene) were different from our system (silica supported metallocene, polyethylene), the qualitative aspects of polymer nanofibrils they observed are strikingly similar to what we have observed in this work. The anchoring of MAO onto the silica surface is dependent upon the concentration of surface hydroxyl groups. Fully hydroxylated silica contains 4.6 OH/nm^2, which is independent of silica type and structural characteristics [36]. The OH-group concentration on a typical silica support (Sylopol 948) calcined at 250^{o}C is 2.4 mmol/g.

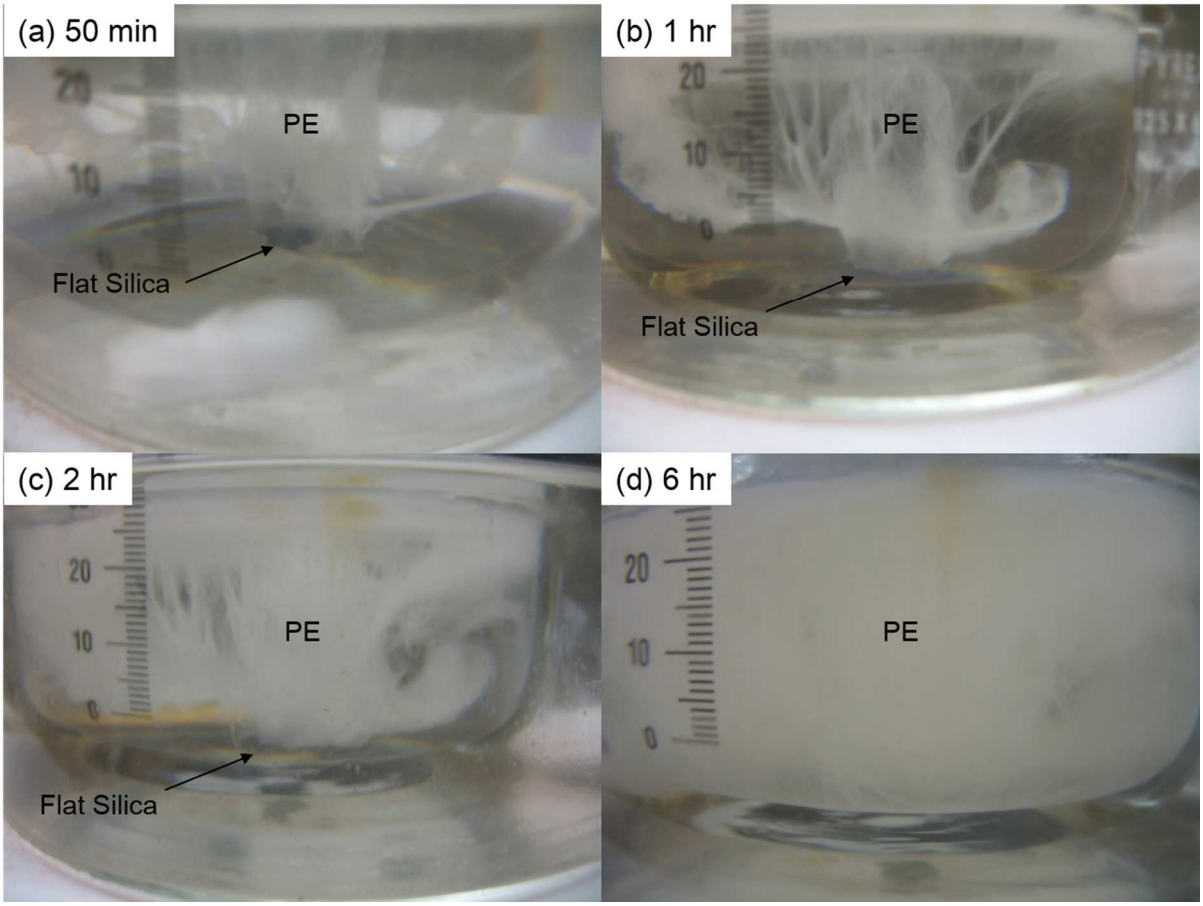

Figure 2-9. Macroscopic morphology of polyethylene growing at the surface of flat surface catalyst.

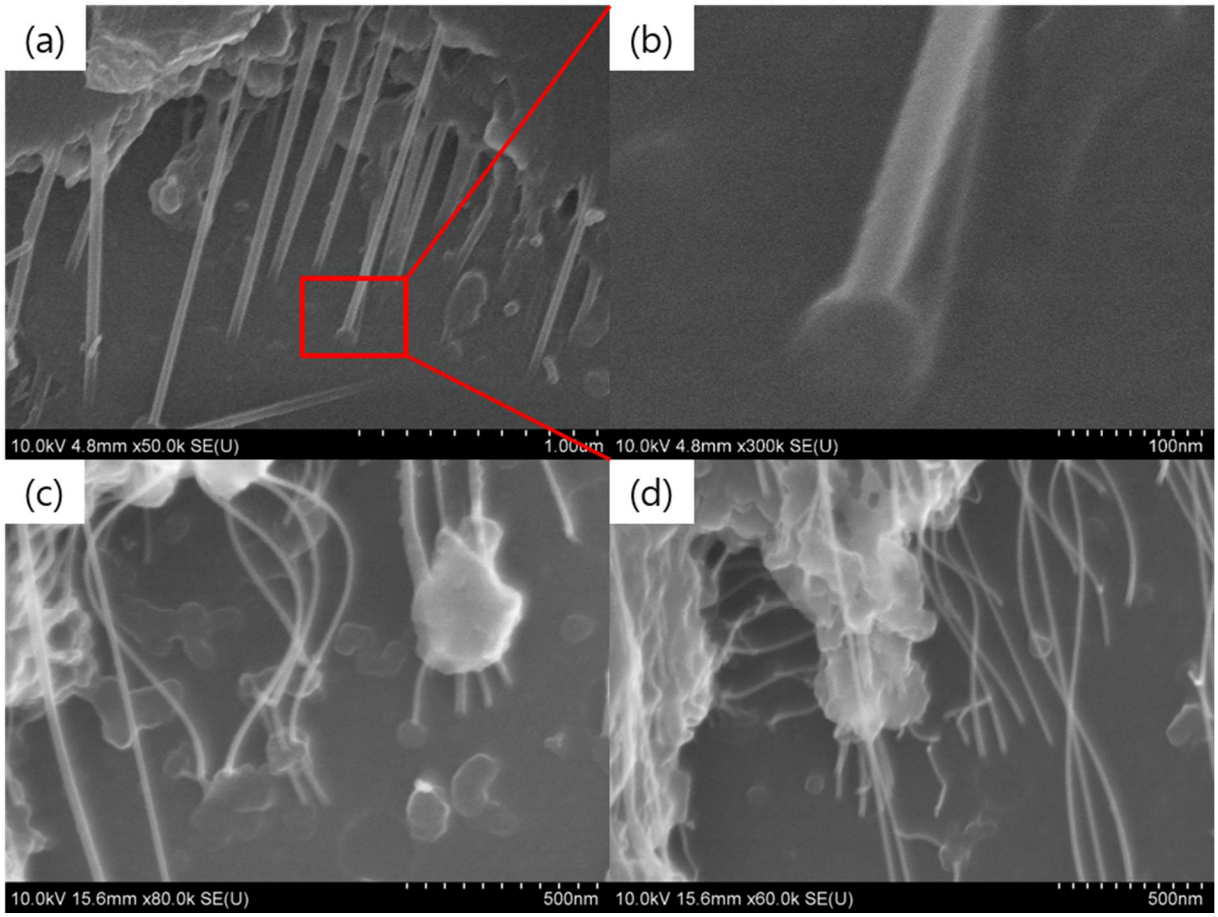

Figure 2-10. SEM images of polymer nanofibrils growing from the flat silica supported catalyst surface.

2.4.3.2. Nano-silica supported catalyst

The metallocene catalyst supported on nonporous nano-silica particles is expected to show the catalytic polymerization behavior similar to that of the flat silica supported catalyst. The morphology of polyethylene growing from the nano-silica supported catalyst is illustrated in Figure 2-11. In the early period of reaction (e.g., 1~5 min), polyethylene nanofibrils of diameter 30-50 nm emanate from the silica surface. The shape of the nano-silica particles with polymer nanofibrils growing from their surfaces resembles the shape of nattos (Japanese fermented soybeans). These nanofibrils tangle up as the polymer yield increases. Since the silica particle surface is also covered with polymer, it is thought that many polymer nanofibrils collapse onto

the silica surface and fuse together as they contact each other. At 20 min of reaction, the entanglement of polymer nanofibrils growing from neighboring silica particles is quite significant and as the reaction continues, these nanofibrils fuse together and form a rather smooth polymer layer, although some discrete silica nanoparticles with polymer nanofibrils are still visible.

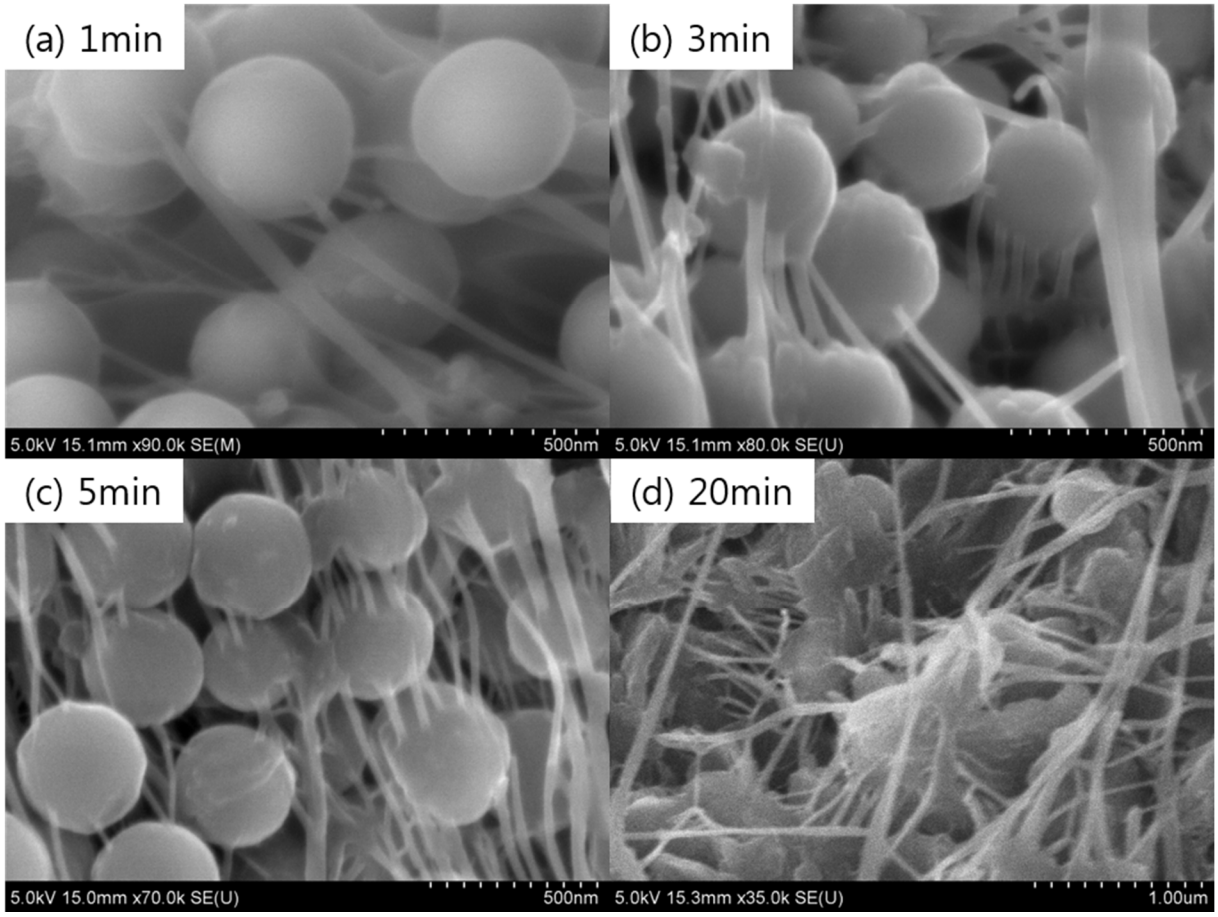

Figure 2-11. SEM images of polymer morphologies with nano-silica supported catalyst with different reaction time.

From the BET surface area measurement, it was confirmed that the silica nano particles used in our study were solid particles with no internal porosity. We have calcined the polymer particles at 700 ^{o}C in a furnace to remove the polymer and investigated the morphology of the remaining silica by SEM and TEM.

Figure 2-12 (a) is the SEM image of neat nano silica particle. Figure 2-12 (b) shows that the silica particles maintained original shape and dimension after removing the polymer by calcination. In other words, silica nanoparticles used as catalyst support did not disintegrate during the polymerization. The neat nano-silica particles, catalyst loaded nano-silica particles, and calcined catalyst particles have also been analyzed by transmission electron microscopy and Figure 2-13 shows the results. It is also interesting to observe that the surface of a nano-silica particle after calcination have aluminum oxide clusters (derived from MAO after exposure to air) of about 7~15 nm in diameter that are relatively uniformly distributed on the external particle surface.

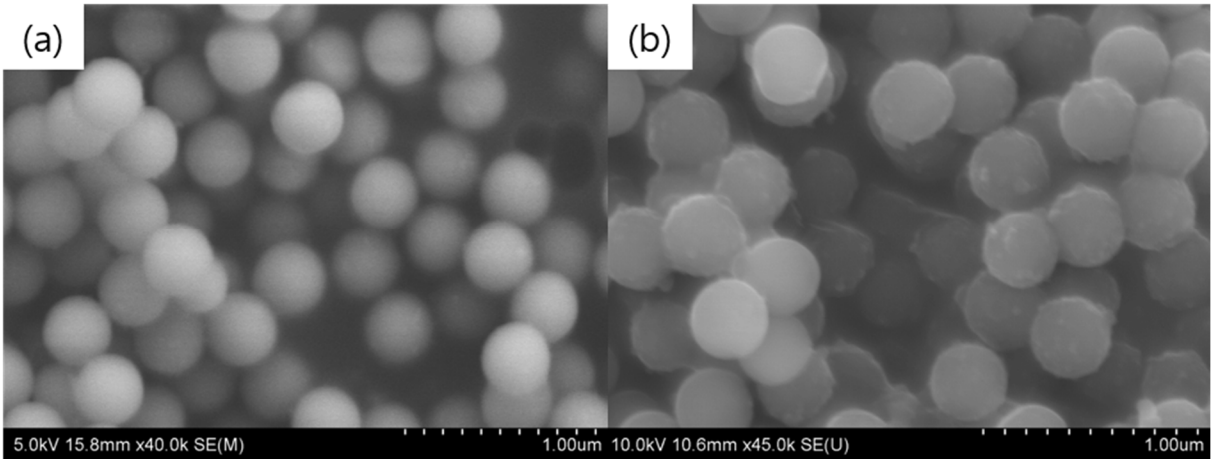

Figure 2-12. (a) Neat SiO2, (b) Nano silica particles after removing polymer by calcinations.

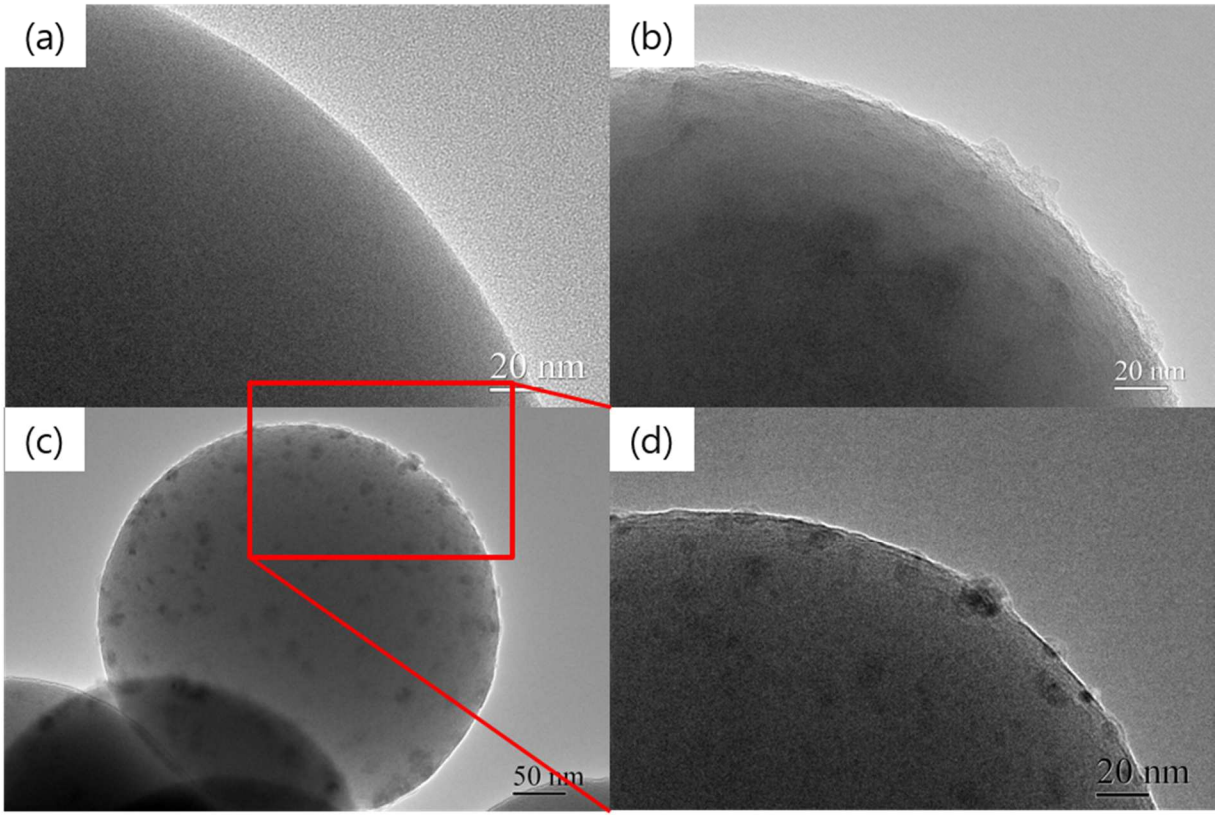

Figure 2-13. TEM images of nano-silica supported catalyst: (a) neat silica, (b) after MAO and catalyst deposition, (c),(d) after calcinations at 700 oC,

2.4.3.3. Polymer molecular weight and crystallinity

The molecular weight distribution (MWD) of polyethylene synthesized over the nano-silica supported catalyst at 70ºC is shown in Figure 2-14. Also the MWDs of polyethylene obtained using the same catalyst but on commercial micron-sized porous silica particles that are widely used industrially are shown. Table 2-3 shows the molecular weight averages of these polyethylene samples. We observe that these three different silica supported catalysts yield almost identical MWDs with the polydispersity values slightly larger than 2.0 because of heterogeneous nature of the catalyst. Considering the fact that the nano-silica supported catalyst provides minimum monomer diffusion resistance to the active catalytic sites on the silica

support, it can be concluded that any mass transfer resistances, if present, had little impact on the polymer MWDs for the experimental conditions used in this work.

Table 2-3. Molecular weight averages and polydispersities of polyethylenes synthesized over different silica support materials at 70oC

	Mn (g/mol)	Mw (g/mol)	PD
Nano-silica	41,500	109,300	2.63
Davisil 643	42,200	109,000	2.58
Sylopol 948	45,900	107,400	2.34

Figure 2-15 shows the wide-angle X-ray diffraction (XRD) of the polyethylenes produced with four different silica supported catalysts. All these patterns show (110) and (200) diffraction peaks (with slight shifts) of polyethylene at 21.6 and 24.0^{o}, indicating that they have orthorhombic crystal structure. The degree of crystallinity of polyethylene determined from the XRD data indicated that all four polyethylene samples synthesized over different silica supported catalysts have same degrees of crystallinity (77.7% (flat-silica), 77.3% (nano-silica), 77.4 %(Davisil 643), and 77.8 %(Sylopol 948)).

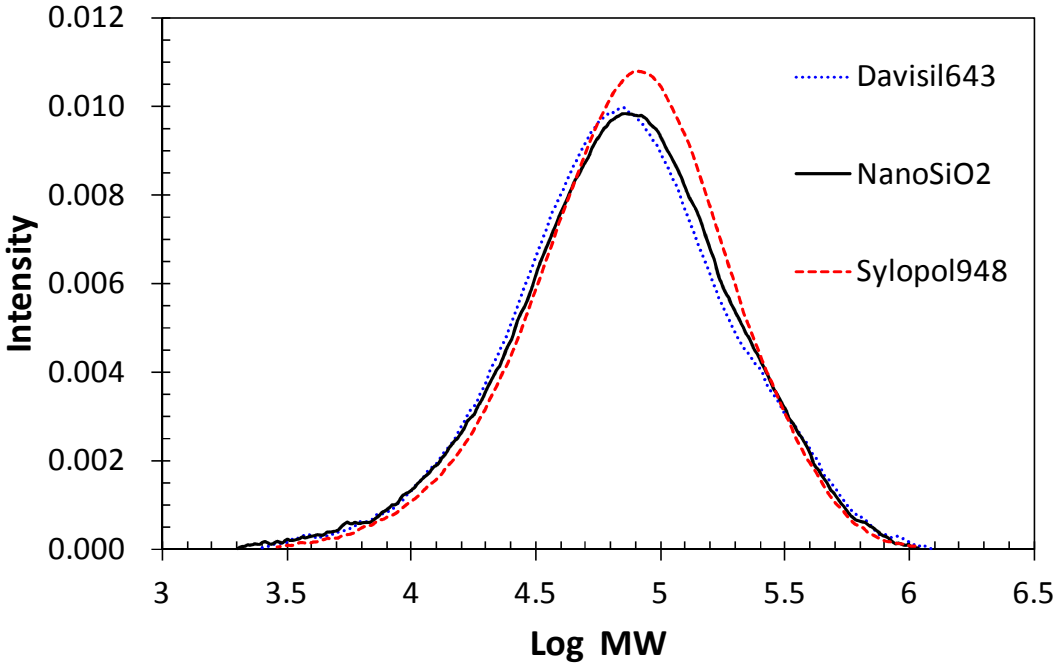

Figure 2-14. Molecular weight distributions of polyethylene.

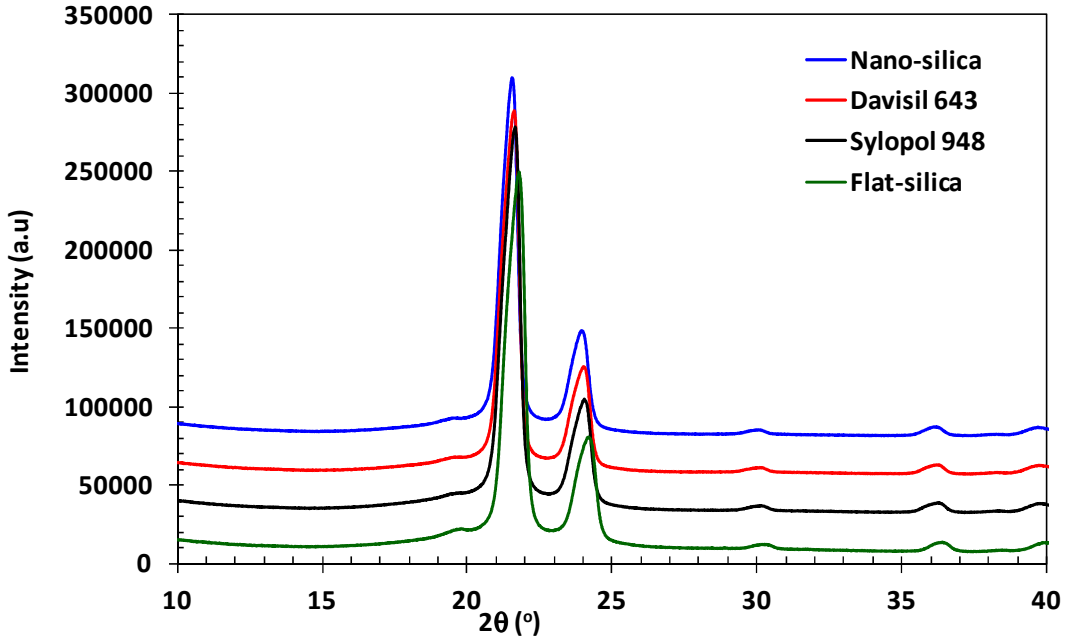

Figure 2-15. X-ray diffraction analysis of polyethylene samples.

2.5. Conclusions

In this chapter, the kinetic behavior and the polymer morphology with flat-silica and nano-silica particle supported metallocene catalysts for ethylene polymerization have reported. The polymerization results obtained with conventional micro-porous silica particles have also been presented for comparison. The polymerization rate per mol of Zr was highest for the flat-silica supported catalyst, and the conventional silica-supported catalysts exhibited the activities that were 55-65% lower than the flat-silica supported catalyst. Although non-porous nano-silica supported catalyst was expected to show quite similar activity as flat-surface catalyst, its activity was about 50% of the flat-surface catalyst. Since the catalyst compounds are deposited only at the particle surface, the usage of the catalyst was more effective than the conventional silica-supported catalyst. The SEM and AFM images of the flat-silica catalyst showed that large clusters of MAO were present at the surface, while nano-silica supported catalyst showed less of such effects. We have also observed that polyethylene grew as nanofibrils of 30-50 nm in diameter from the silica surface. With nano-silica supported catalyst used in our study, we have observed that particle fragmentation did not occur. It was also observed that both the molecular weight distribution and polymer crystallinity were almost not affected by the geometrical shape and dimension of the silica support materials.

Chapter 3. Growth of Polyethylene Nanofibrils Over rac-Et(Indenyl)$_2$ZrCl$_2$/MAO Catalyst Supported on Silica Nanotubes*

3.1. Abstract

The growth phenomena of polyethylene synthesized over *rac*-Et(indenyl)$_2$ZrCl$_2$/MAO catalyst supported on silica in cylindrical nano-channels of anodized aluminum oxide (AAO) template and on liberated silica nanotubes have been studied. In the presence of a liquid diluent, a catalyst deposited silica nanotube is quickly filled up with polyethylene and the polymer extrude out to the bulk liquid phase in the form of nanofibrils of about 30-35 nm diameter. The nanofibrils move toward the tube outlet in the direction of tube axis as polymer continues to be made at the silica surface inside the silica nanotube. When silica nanotubes are liberated from the AAO template and deposited with catalysts, polyethylene nanofibrils grow in both inside and outside the silica nanotubes. The polyethylene nanofibrils formed at the outer surface of the liberated silica nanotubes also grow as 30~35 nm diameter fibrils and they quickly entangle to form a mass of polymers in the liquid phase. The liberated silica nanotube reactors showed much higher ethylene polymerization activity per gram of silica support than the micro silica particle-supported catalyst because of higher Zr loading and less mass transfer resistance for the monomer.

---

* The materials presented in this chapter has been submitted :
Lee, S.; Choi, K. Y. Growth of Polyethylene Nanofibrils Over rac-Et(Indenyl)2ZrCl2/MAO Catalyst Supported on Silica Nanotubes. *Macromolecular Reaction Engineering* **2015,** *Submitted*.

3.2. Introduction

The catalytic polymerization of α-olefins over silica-supported metallocene catalyst is an important class of industrial polymerization processes. Commercially available silica micro-particles are highly porous with large specific surface area (e.g., 250-500 m^2/g) containing surface silanols for the covalently anchoring active catalyst compounds to the silica surface through a cocatalyst such as methylaluminoxane (MAO). Due to the heterogeneous nature of the silica-supported catalysts, some physical effects associated with silica disintegration or fragmentation, intraparticle and interfacial mass and heat transfer resistances affect the catalyst activity and polymer particle morphology. When titanium-based Ziegler-Natta catalysts are used in conjunction with electron donors and aluminum alkyl cocatalyst, catalyst particles disintegrate early in the reaction stage and they grow to large polymer particles. The morphological changes and overall heterogeneous reaction kinetic behaviors of Ziegler-Natta catalysts and some supported metallocene catalysts can be modeled by the well-known multigrain model framework where it is assumed that the original catalyst particles breakup at the beginning of polymerization and the polymer grows around each catalyst fragment [20, 22, 24, 26, 42]. In the transmission electron microscopic study of propylene polymerization over Ziegler-Natta catalyst, Kakugo et al observed that polymer grows around a fragmented transition metal crystallite, forming a rather continuous polymer matrix [18, 19, 43]. However, not much has been reported on how individual polymer chains actually form a continuous polymer layer around the catalyst fragment.

The catalyst fragmentation and polymer growth phenomena over porous silica-supported high activity metallocene catalysts are often represented by a layer-by-layer fragmentation morphology. According to this catalyst fragmentation mechanism, catalyst breakup does not occur instantly but gradually: catalyst particle disintegration starts from the outer layer of the

particles and the polymerization front moves from the outer surface of the particle into the silica particle core as the catalyst-deposited silica fragmentation occurs gradually as dense polymer/silica layer is formed from the outer region of the catalyst particle. The typical polymerization rate profile shows an initial rise of the rate followed by an induction period before the reaction rate increases again after the catalyst particle fragmentation is nearly complete [44]. If the fragmentation is very rapid, then the overall catalyst/polymer particle behavior can be described by the multigrain model and the overall polymerization rate profiles follow that of decay type. The morphological development of polymer particles depends upon the properties of silica particles as well as catalyst activity or polymerization rate.

In general, commercially available silica micro-particles consist of macro-pores and micro-pores of average pore diameter of about 20-30 nm where most of the catalyst sites are present. These pores are large enough for the diffusion of MAO and catalyst molecules. For example, the most frequently observed oligomeric MAO-12 ($[AlOMe]_{12}$) structure has a dimension of about 0.96 nm [9]. But the pores are quite tortuous and it is quite possible that some fraction of pores or surfaces may not be fully accessible by monomer and cocatalyst (MAO) molecules if silica fragmentation is incomplete to expose the entire active sites available for polymerization. During the typical catalyst preparation process, silica particles are impregnated in a solution containing MAO that diffuses into the pores of various diameters and lengths. MAO molecules are immobilized onto the silica surface by reacting with surface silanol groups. Then, the MAO-loaded silica particles are treated by a solution containing a metallocene catalyst component, which diffuses into the catalyst pores to form active catalytic sites by complexation with MAO molecules. To obtain high catalyst activity, MAO is often added to a slurry phase as a cocatalyst during the polymerization. Then, it diffuses into the pores to activate

the supported metallocene catalyst. Understanding the details of how polymer grows inside a catalyst pore and how actual fragmentation occurs is very important to optimally design a silica-supported metallocene catalyst. Although some qualitative observations and analysis have been studied through scanning electron microscopy, the catalyst (silica) fragmentation and the resulting polymer morphology are not fully understood.

The formation, growth and transport of polymers inside silica-supported catalyst pores are also complex but important subjects of study in olefin polymerization. For example, as polymer chains are formed at the silica support surface, the movements of these polymer chains through the pores and the way they accumulate and exert hydraulic pressure for silica fragmentation have not been well investigated.

Recently, mesoporous silica was used as a support for metallocene catalyst for ethylene polymerization and some interesting polymer morphologies have been observed [45-49]. For example, Aida and coworkers [47] observed that extremely high molecular weight polyethylene was produced as the polymer extruded out from the mesopores of mesoporous silica fiber (MSF) as cocoon-like nanofiber bundles with diameters of ca. 30-50 μm which were comprised of ultrathin extended-chain crystal fibers of 30~50 nm in diameter.

Commercially available silica micro-particles for catalyst impregnation have both micro- and mesopores that are responsible for the large specific surface for catalyst deposition. However, the pore structure of conventional silica microparticles is very complex and difficult to quantify. For example, spray-dried silica gel particles consist of small primary particles of about 10 nm that agglomerate to clusters of 80~120 nm or up to about 500 nm [44]. The pores are the interstitial volumes of void space between these agglomerates and hence, the exact shape characteristics of the pores are hard to observe or characterize. Also, the exact locations of

catalyst sites are not precisely known except for the fact that the catalyst sites are formed at the silica surfaces within the pores where monomer is accessible. The growth and movement of polymer in the catalyst pores are not well known. It is not also certain what fraction of catalyst sites are exposed to monomer by the particle fragmentation, although it is generally well accepted that some catalyst sites may never be accessed by monomer due to improper particle fragmentation. As a result, the effectiveness of the catalyst for polymerization decreases.

If a catalyst support with a geometrically well-defined pore structure can be used, the growth of polymer in a porous catalyst can be better observed. For that purpose, in this study, we used silicananotubes (SNTs) as a support material for metallocene catalyst for ethylene polymerization. Unlike mesoporous silica particles, silica nanotubes (SNTs) of diameter 50-200 nm derived from an anodized aluminum oxide film (AAO) used as a template offer well-defined channels or pore structures of straight cylindrical shape. For the polymerizatioln of ethylene, a metallocene catalyst can be supported onto the surface of silica inside the nanochannels of an AAO film. The thickness of a typical silica layer inside a silica nanotube surface is about 10-15 nm, which is about the same dimension of the smallest unit of the silica gels synthesized by sol-gel techniques for industrial silica microparticles [44]. When SNTs are loaded with active metallocene catalyst, olefin polymers can be synthesized inside the nanochannels. Although the channel diameter of a SNT is larger than that of mesoporous silica, they offers some unique advantages such that direct observation of polymers inside the nanochannels is possible through transmission electron microscopy (TEM) analysis of a single SNT. The silica-coated SNTs can also be liberated from the template by dissolving the alumina matrix with NaOH. If the liberated SNTs are treated with MAO and metallocene catalyst solution, both inside and outside of the SNTs can be deposited with active catalyst sites that are available for polymerization. Figure 3-1

illustrates the preparation procedure we used in this study to make SNTs as catalytic reactor arrays in an AAO matrix (SNT/AAO) and SNTs liberated from the AAO film by dissolving the AAO matrix with NaOH.

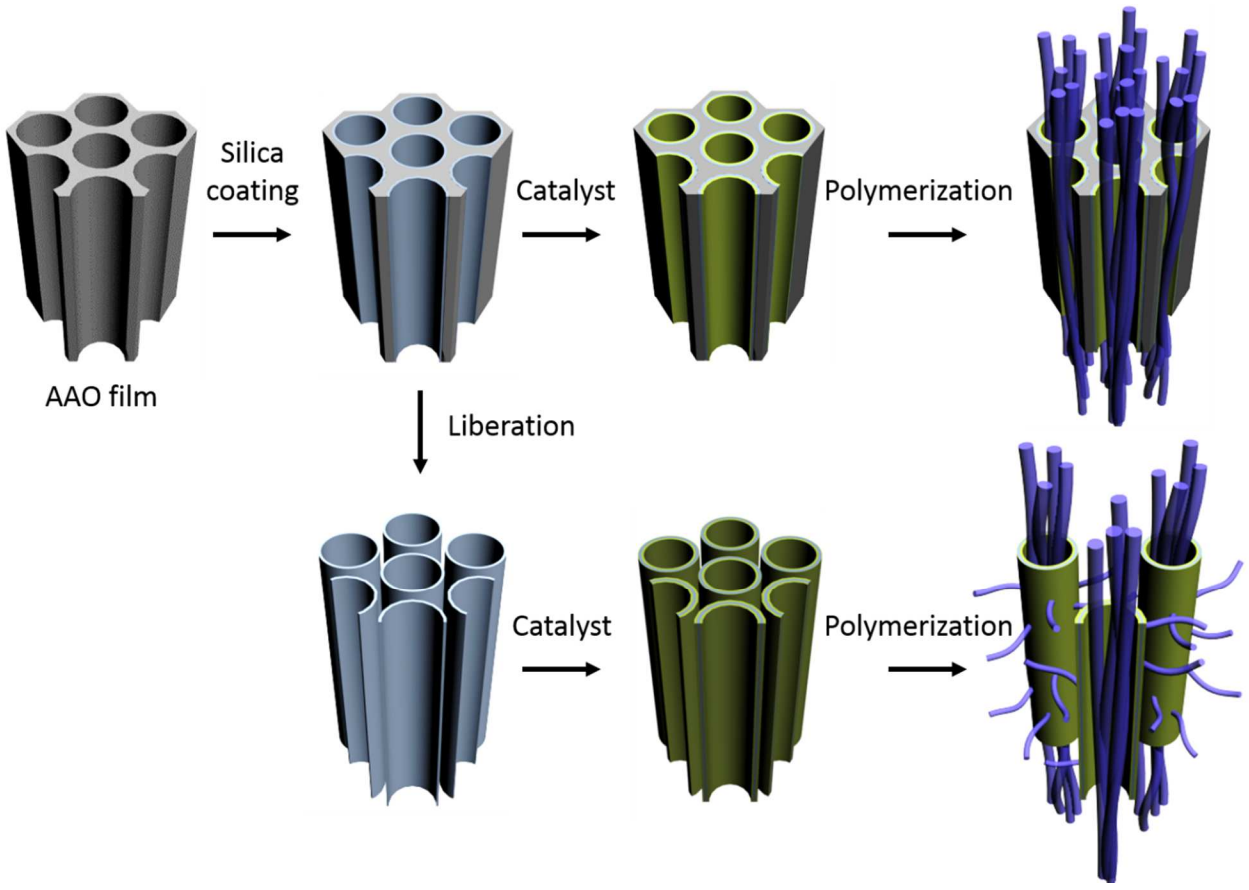

Figure 3-1. Scheme of preparation of silica nanotube reactors and ethylene polymerization.

3.3. Experimental

3.3.1. Materials

The metallocene catalyst, *rac*-Et(indenyl)$_2$ZrCl$_2$ (EBI) (Strem Chemicals) and methylaluminoxane (MAO, Aldrich, 10% in toluene, 4.55 wt.% Al content) were used without further purification. The solvents, toluene (Aldrich) and hexane (Aldrich) were used after they were demoisturized using molecular sieves.

3.3.2. Preparation of Silica nanotubes

An anodized aluminum oxide (AAO) porous film was used as a template for the silica nanotube reactors. The AAO porous films with 200 nm pores were purchased from Whattman® and the AAO films with 60 nm pores were synthesized in our (SBL) laboratory using the previously reported method [9]. Two types of silica nanotubes were used for the polymerization experiments:

(1) Type 1-nanotubes in the AAO template (SNT/AAO),

(2) Type 2-nanotubes liberated from the AAO template (SNT).

To prepare type (1) silica nanotubes, the pore walls of these AAO films were coated with silica by surface sol-gel (SSG) method: An AAO film was first soaked in $SiCl_4$ (99.8%) solution and then it was quickly immersed and washed with fresh hexane for 4 times to remove unabsorbed $SiCl_4$. The top surface of the AAO film was gently polished mechanically and the AAO film was placed in methanol/hexane (1:1 v/v) and ethanol mixture before drying in nitrogen flow. Finally, the film was placed in a deionized water bath, washed with methanol and

dried. This procedure was repeated five to ten times to obtain *ca.*10 nm thick layer of silica at the pore surfaces.

The type (2) silica nanotubes were obtained by dissolving aluminum oxide portion of the silica-coated AAO template (1) with NaOH. Figure 3-2 shows the transmission electron microscopic (TEM) and energy dispersive X-ray (EDX) scan images of a liberated silica naoutube. We can confirm the formation of silica layer thickness of about 25 nm inside a 200 nm (OD) silica nanotube. In our analysis, we observed a small fraction of silica nanotubes that were filled with silica, i.e., silica nanorods, but most of the silica nanotubes prepared in this study had quite uniform layer thickness. The length of 200 nm SNTs was about 60 μm. Figure 3-3 shows the SEM image of the silica nanotubes liberated from the AAO film by dissolving the AAO matrix with NaOH solution.

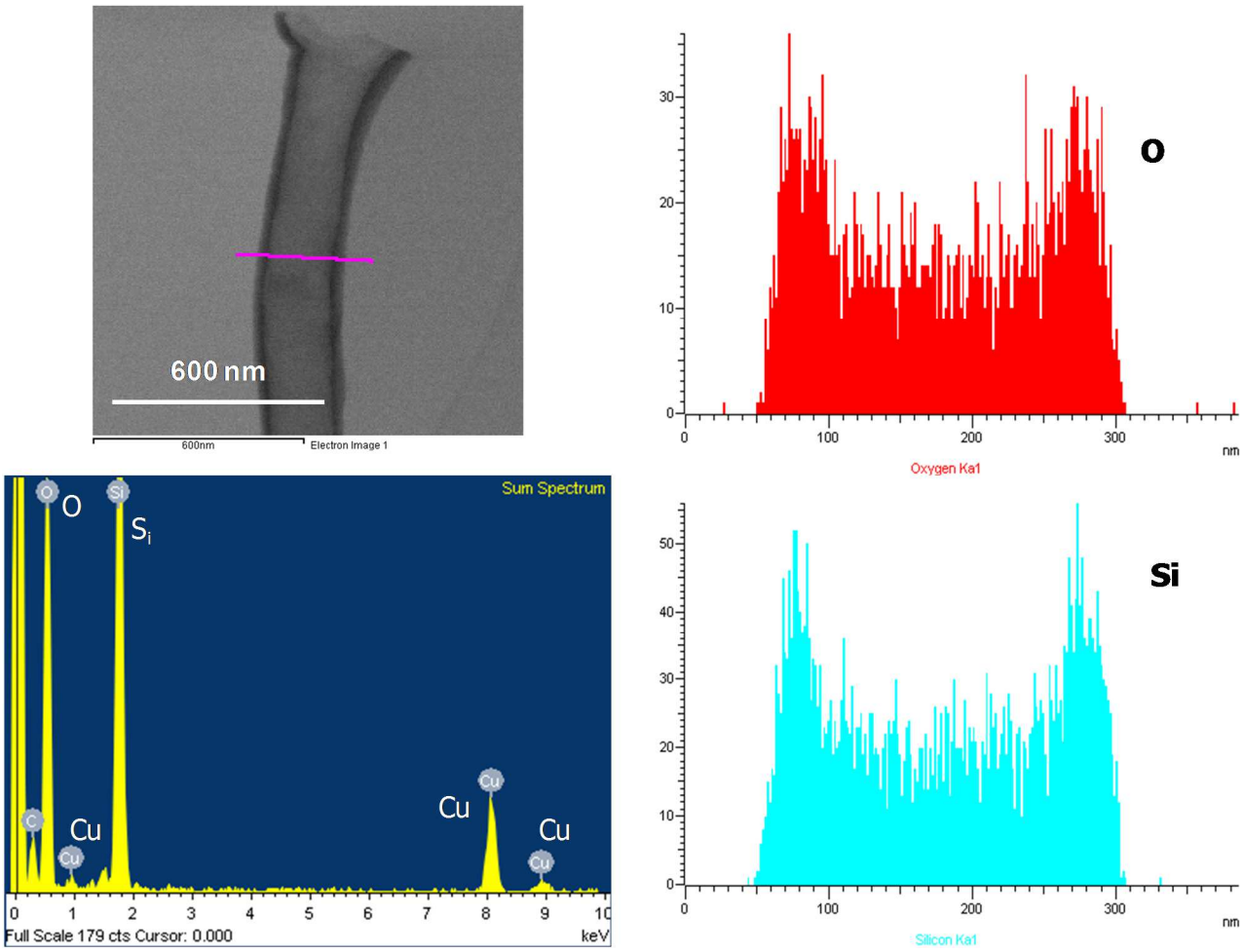

Figure 3-2. TEM and EDX scan images of a liberated silica nanotube.

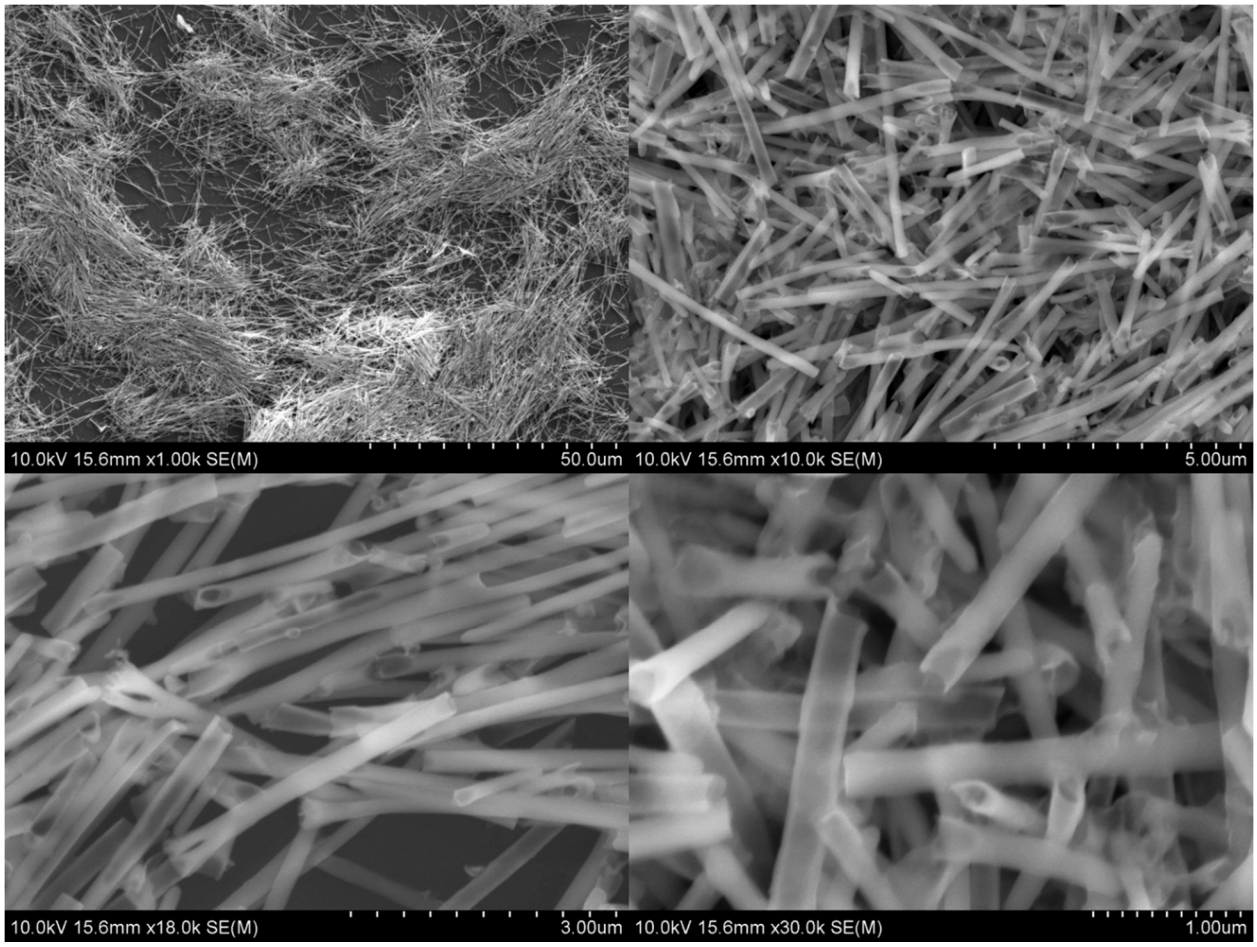

Figure 3-3. SEM image of liberated silica nanotubes.

3.3.3. Catalyst preparation

To support a metallocene catalyst (EBI) onto the inner walls of a type (1) silica nanotube (SNT/AAO), we treated a silica nanotube film with a MAO solution in toluene (7.5 vol%) at ambient temperature for 24 hr. Then, the treated silica nanotubes were washed with toluene, and dried in vacuo overnight. This treatment process was repeated twice. The prepared SNT/AAO film was mixed with an EBI catalyst solution in toluene at ambient temperature for 24 hr, washed with toluene, and dried in vacuo. To limit the polymer chain growth inside the nano channel of the silica nanotubes, the top and bottom surfaces of the SNT/AAO film were mechanically

polished and the catalyst deposited on these surfaces was completely removed. Type (2) silica nanotubes (SNT) were prepared similarly but the liberated nanotubes were treated with the catalyst solution and hence, both inside and outside of the nanotubes were deposited with the catalyst.

3.3.4. Polymerization

To polymerize ethylene, the silica nanotube films (SNT/AAO) or liberated silica nanotubes (SNT) loaded with EBI catalyst were placed in a 500 mL glass bottle containing toluene in a glove box. Polymerization grade ethylene (Air Products) was purified by passing through a stainless steel catalyst column packed with R3-11 Cu catalyst, 4 Å molecular sieves, neutral alumina, and activated carbon. The glass bottle was pressurized to 50 psig by adding ethylene gas and the liquid phase was saturated with ethylene at 70 ^{o}C. The glass reactor was placed in a constant temperature bath. All experiments were carried out at 70±1 ^{o}C at constant ethylene partial pressure. The polymerization rate or ethylene consumption rate was measured using an on-line mass flowmeter connected to a data acquisition computer. The polymerization time was varied from 0 to 60 min. After polymerization, the reactor was vented and the reaction mixture was removed, washed with excess amount of acidified methanol, and dried in vacuo.

3.3.5. Polymer Morphology

The morphology of polyethylene was analyzed by scanning electron microscopy (SEM, Hitachi S-4700) and transmission electron microscopy (TEM). For the SEM analysis, dried silica nanotube -polyethylene samples were coated with AuPd layer in a Denton DV-503 vacuum

evaporator and analyzed by scanning electron microscopy. TEM analysis was carried out using Zeiss EM10CA. To characterize the thermal properties, differential scanning calorimetry (DSC) was used at a heating rate of 20^{o}C/min under nitrogen atmosphere using Q1000 (TA Instruments). The molecular weights of polyethylene samples were measured by high temperature gel permeation chromatography (PL GPC 220, Polymer Laboratories) with trichlorobenzene (TCB) at 160^{o}C. X-ray diffraction (XRD) analysis was performed on Bruker D8 Advanced powder diffractometer using CuK-alpha radiation and LynxEye position sensitive detector.

3.4. Results and Discussion

In this study, the first aim was to observe the morphology of polyethylene growing inside a nanotube (STN/AAO). Figure 3-4(a) shows a vertical cross-sectional view of the fractured SNT/AAO-PE sample from the nanochannels of diameter 200 nm. Notice in Figure 3-4(a) that the top of the SNT arrays is covered with a thick layer of polymer extruded out from the nanochannels. Apparently, these extruded polymers collapsed onto the SNT array and formed a fused polymer layer. Recall that the top surface was mechanically polished to remove the catalyst and hence no polymer could have grown directly from the AAO film surface. Figure 3-4(b) shows a close-up view of the vertical cross-section shown in Figure 3-4(a). Figure 3-4(c) and (d) show the images of the horizontal cross-section of the fractured nanochannel of 60 nm diameter (the inner diameter is about 30-40 nm). It appears that each nanochannel is filled with a single polymer nanofibril. After the breakup of the AAO film during the sample preparation and subsequent SEM analysis, some of these nanofibrils seem to have fused together into larger diameter fibrils (Figure 3-4(d)). Figure 3-5 shows the TEM image of a silica nanotube (200 nm OD) separated from the template matrix after polymerization by dissolving the AAO film matrix with NaOH solution. Notice that 200 nm silica nanotube is filled with several straight polyethylene nanofibrils of diameter 30-40 nm. It is also seen that each nanofibril is oriented in the axial direction of the tube, suggesting that they were moving out of the nanochannel as more polymer is produced inside the channel. These nanofibrils do not seem to have fused together inside the channel; instead they were independently extruded out from the channel interior to the SNT exits.

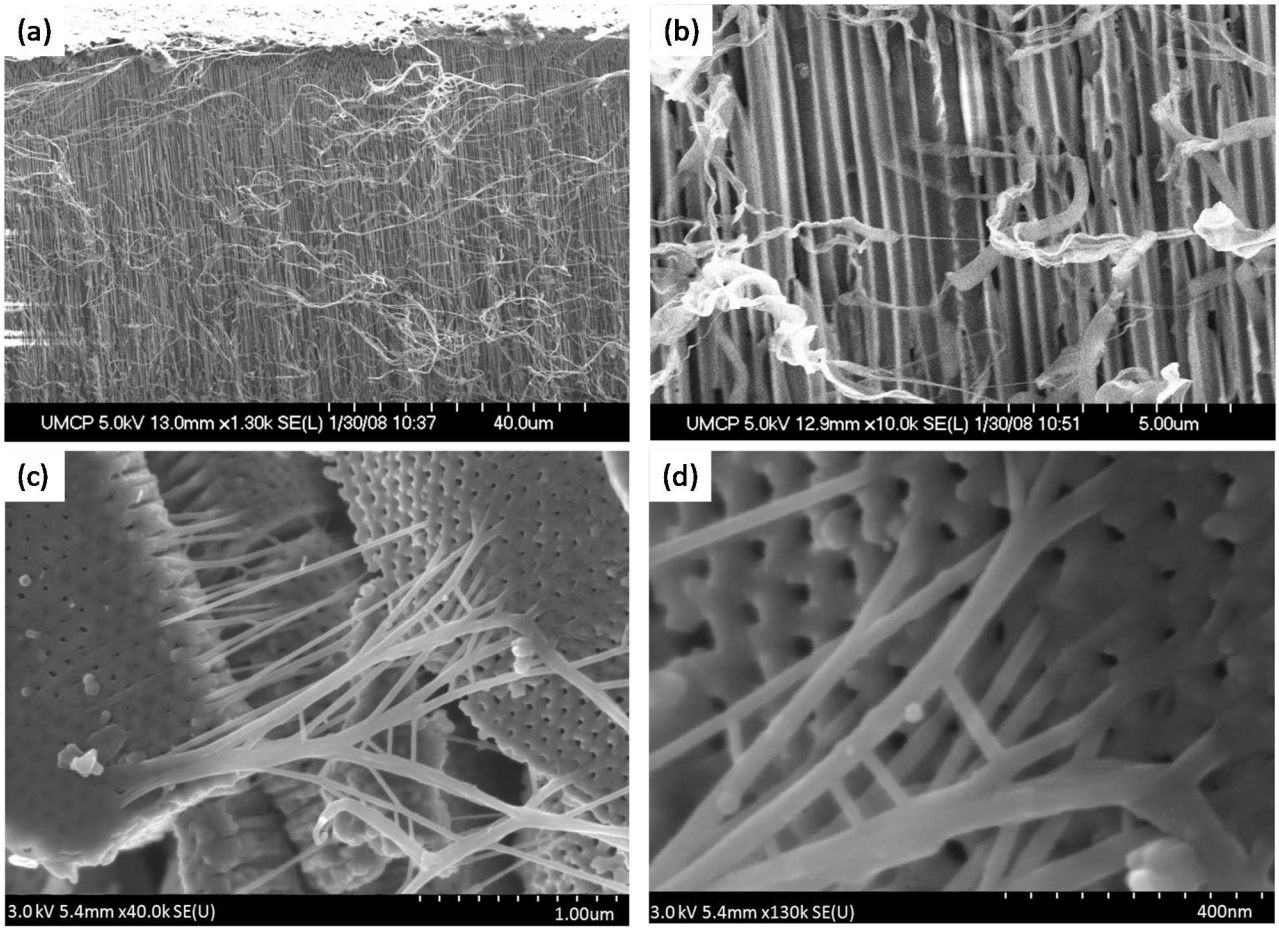

Figure 3-4*[50]. (a), (b) polyethylene nanofibrils in 200 nm diameter SNTRs; (c), (d) polyethylene nanofibrils in fractured SNTRs of 65 nm diameter.

* This work has done by Joong Jin Han:
Han, J. J. Kinetics and morphology of metallocene catalyzed syndiospecific polymerization of styrene in homogeneous and heterogeneous reaction systems. Univerisity of Maryland, College Park, 2008.

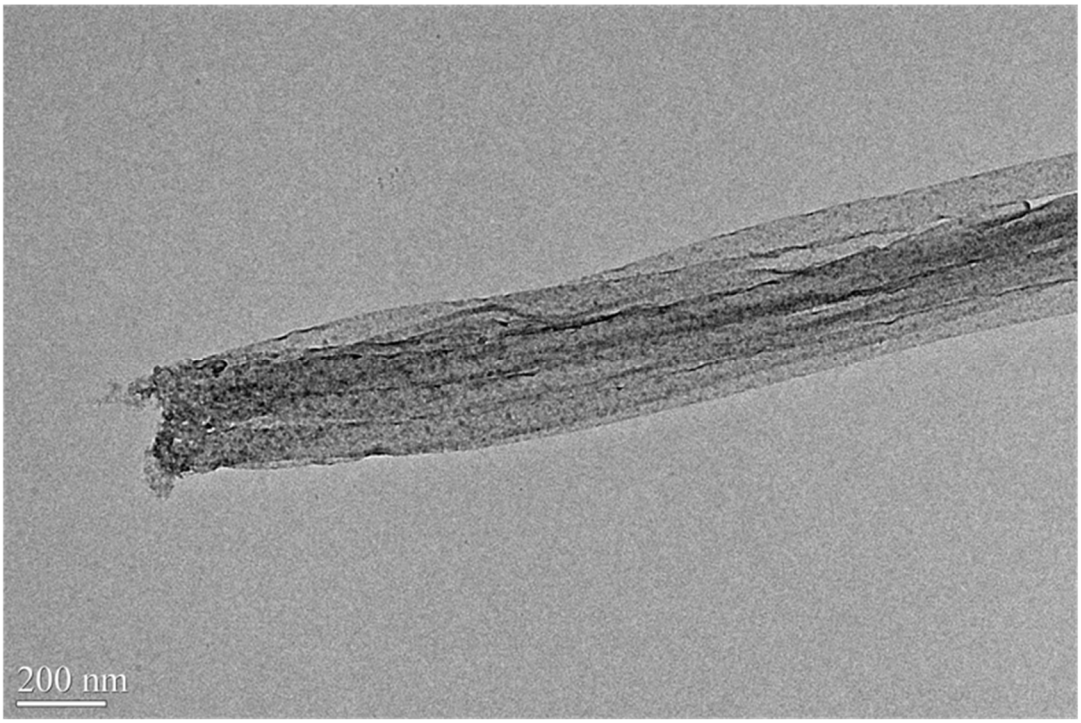

Figure 3-5*. TEM image of a silica nanotube (200 nm) filled with polymer nanofibrils.

The polymers accumulated on the top of the AAO film showed some interesting sructures. Figure 3-6 shows the SEM micrographs of the polymer at the top of the 60 nm SNT/AAO film. The thick surface layer of polyethylene was formed by the accumulation of polymers extruded out from the nano channels during the polymerization. These images show nanofibrils, fiber aggregates, and floccules, but shish-kebab type polymer crystals are also seen [51]. The average diameter of the outer kebab is about 300 nm, which is very similar to that reported in the literature for ultrahigh molecular weight polyethylene. It is also seen in Figure 5(b) and (b‘) that the adjacent kebabs are interconnected by several shish aligned parallel to each

* This work has done by Joong Jin Han:
Han, J. J. Kinetics and morphology of metallocene catalyzed syndiospecific polymerization of styrene in homogeneous and heterogeneous reaction systems. Univerisity of Maryland, College Park, 2008.

other. The shish-kebab type polyethylene crystalline morphology has been known to be formed in dilute polymer solutions undergoing extensional flow at high extension rates [52]. It was not possible to measure the polymer extrusion rate from the nano channels, but it can be hypothesized that during the initial reaction period, the polymer nanofibrils extruding out from the nanochannels are exposed to a solvent (dilute conditions) and the high polymerization rate during the early reaction period might have caused high extensional flow of the polymer moving and exiting the nanochannels. In particular, the stress accumulated inside the nano channels might have been released rapidly to the liquid phase. For a 65 nm-diameter and 10 μm long SNT/AAO (inner diameter after silica layer deposit ≈ 40 nm) with the polymerization rate of 10-100 g/g-silica.min, the polyethylene extrusionr ate is about 2.3~23 μm/sec (with Zr loading of 4 x 10-4 mol/g-silica). Many nano fibrils observed in Figure 3-6(a) are very similar to those observed when mesoporous silica such as MCM-41 or SBA-15 were used as a support for metallocene catalysts for ethylene polymerization [48, 53].

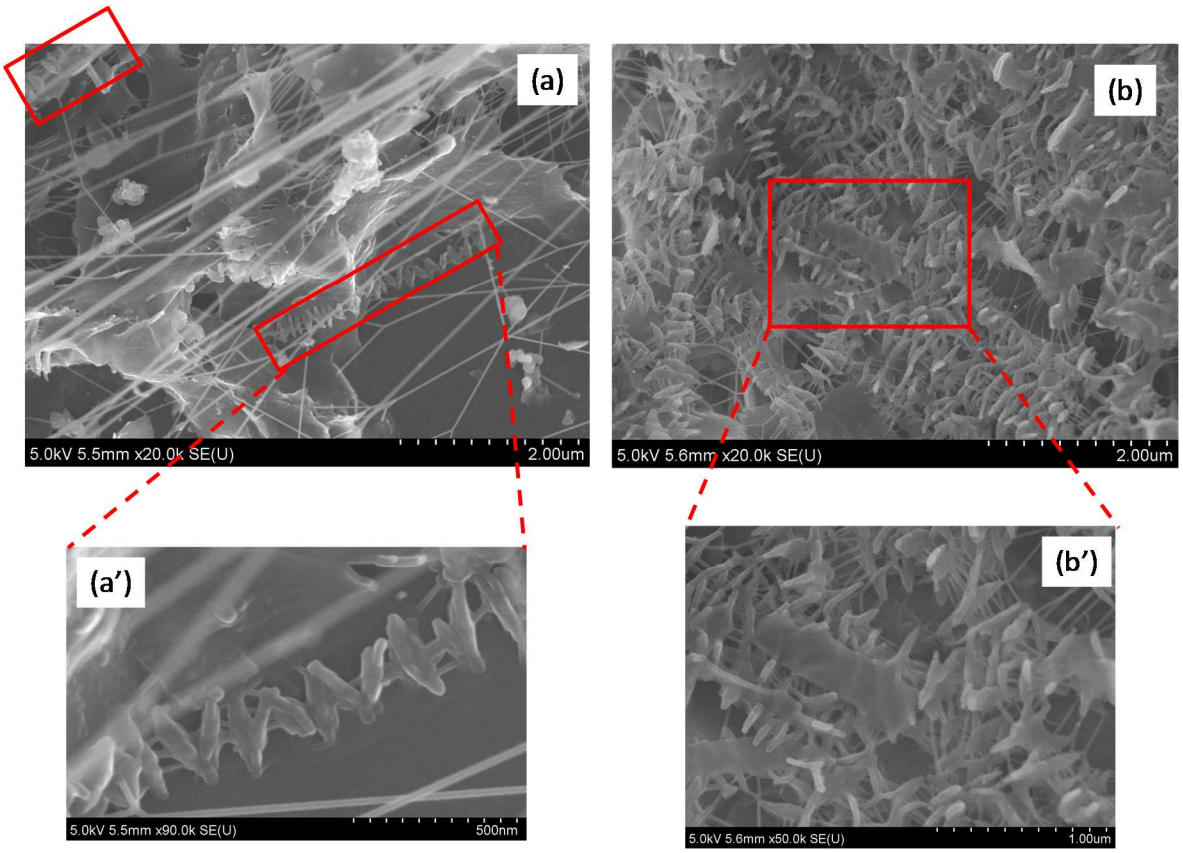

Figure 3-6*. Crystallized polyethylene synthesized over SNT/AAO-supported catalyst

Figure 3-7 shows the SEM images of the polymer when silica nanotubes (SNT) of diameter 200 nm liberated from the AAO film were used for polymerization. Since the catalyst was deposited on both the exterior and the interior of the silica nanotubes, polymers grow from both sides. Figure 3-7(a) shows a 200 nm (O.D.) liberated SNT with polyethylene nanofibrils of 30-35 nm diameter growing from the exterior surface. Apparently, some of these nanofibriles are heavily entangled. Figure 3-7(b) shows the view of a partially broken silica nanotube. Here, we can observe the densely packed polyethylene nanofibril bundles inside a silica nanotube. The

* This work done by Joong Jin Han:
Han, J. J. Kinetics and morphology of metallocene catalyzed syndiospecific polymerization of styrene in homogeneous and heterogeneous reaction systems. Univerisity of Maryland, College Park, 2008.

polymer nanofibrils inside the silica nanotube are all oriented in the direction of tube axis and they are of the nearly uniform diameter of about 35 nm, which is quite consistent with the TEM image shown in Figure 3-5. Figure 3-7(c) and (d) show that polymerization occured quite extensively at the SNT surfaces. The silica nanotubes of diameter 200 nm are deposited with polyethylene nanofibrils of 20-40 nm to about 800 nm diameter (i.e., the polymer layer thickness is 300 nm). It is interesting to note that the diameter of polymer nanofibrils inside and outside the silica nanotube is almost identical, indicating that the basic dimension of the polyethylene growing from the silica-supported catalyst is nanofibrils of about 30-35 nm in diameter.

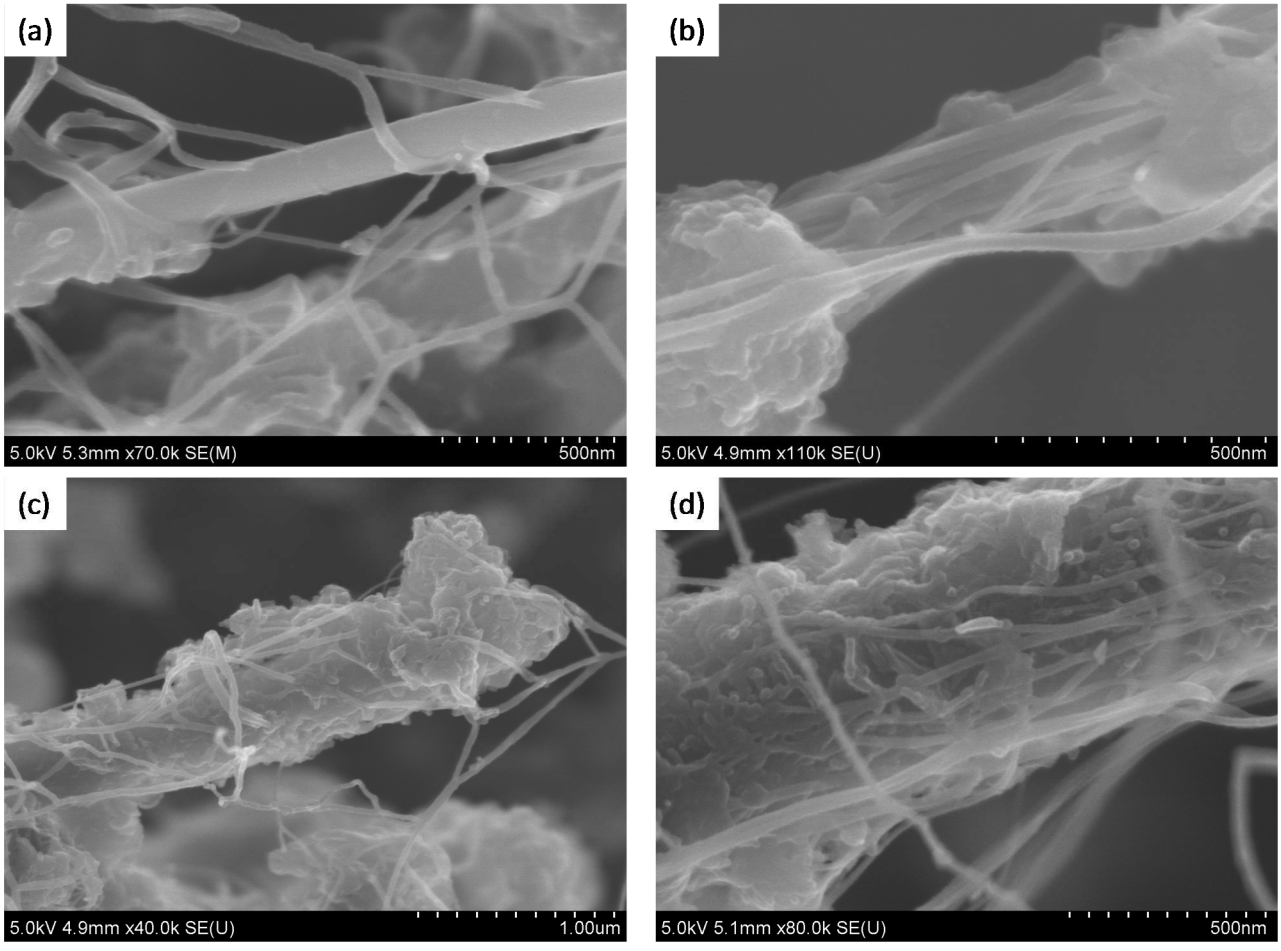

Figure 3-7. Polyethylene nano fibrils inside and outside of silica nanotube reactors (at 30 oC, 30 min).

It is also to be noted that the dimension of polyethylene nanofibrils observed in Figure 3-7(b) is very similar to that of polypropylene short nanofibrils reported by Guttman and Guillet [41]: In the gas phase polymerization of propylene over single crystals of α-$TiCl_3/Al(CH_4)_3$, they reported that the polymer grew as nanofibrils of about 1.5 μm length (much shorter than the polyethylene nanofibrils observed in our work perhaps because the catalyst had low activity and the monomer concentration was very low) at the active sites, primarily on lateral edges and surface defects of catalyst crystals. In their study, they showed that polypropylene initially grew at the catalyst site region in a globular form with a diameter of 20-50 nm before these globules are elongated into fibrils of about the same diameter as the reaction continued. They also observed the striations approximately perpendicular to the nanofibril axis in the polypropylene nanofibrils. The striations in the fibrils were with a periodicity of about 10-15 nm and they proposed that the polypropylene nanofibrils were composed of highly crystalline polypropylene lamellae without extended chain crystallization [54]. They further proposed that (i) polymerization of propylene was faster than crystallization to yield a hemispherical mass of amorphous polymers; (ii) the reaction continued to increase the hemispherical globule size with decreasing polymerization rate due to diffusion resistance for monomer to reach active catalytic sites through the amorphous polymer phase; (iii) crystallization occurred at the apex of the polymer globule in the form of folded-chain lamellae. The crystallization rate of polyethylene is much slower than the crystallization rate of polypropylene.

Figure 3-8 shows a schematic summary of how polymer chains formed at the solid silica surfaces assemble to polymer nanofibrils with SNT/AAO and SNT. Scheme 2(A) illustrates that polymer chains grown inside a nanochannel of SNT/AAO forms a nanofibril or its assembly that moves toward the nanochannel exit. When mesoporous silica materials were used as catalyst

supports, similar movement of polymers as a bundle of nanofibrils was reported by Kageyama et al. and this phenomenon was called the extrusion polymerization [47]. In the SNT/AAO, each nanochannel is separated by the AAO matrix phase and the polymer nanofibril moves along the nanochannel direction, and the force acting on the channel surface is not large enough to cause the breakage of the AAO matrix phase. Thus, no breakage of nanochannels occurs.

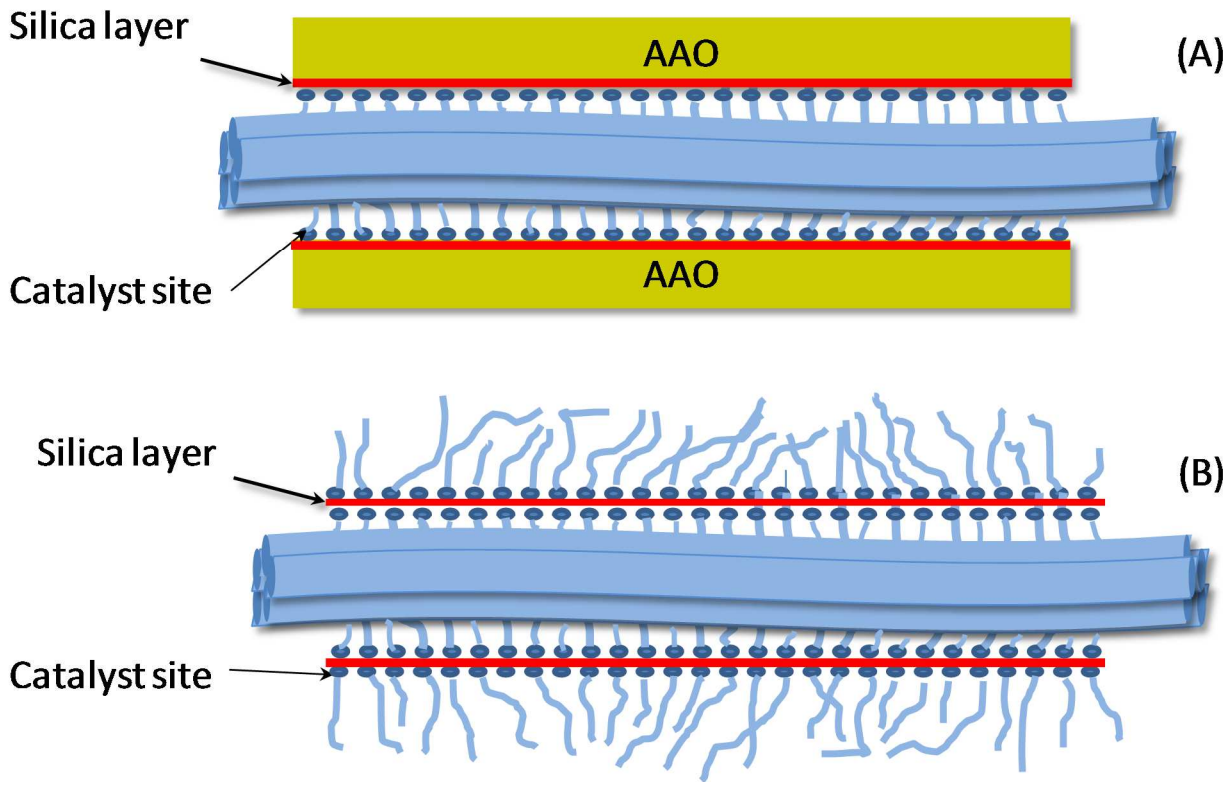

Figure 3-8. Scheme of polymer nanofibrils' groth inside and outside silica nanotubes.

Mechanism of axial movement of polyethylene nanofibril inside the nanochannel is an intriguing subject. Initially, the silica nanotube is filled (or wetted) with a solvent only. As monomer diffuses into a nanochannel interior, polymers are rapidly formed. For a single cylindrical nanochannel of 40 nm inner diameter (typical channel diameter of 65 nm OD SNT after silica deposition) and 60 μm long with the catalyst activity of 100 g/gcat.min, the time to

fill up the nanochannel is about 0.4 sec. As the nanochannel is filled up with polymer nanofibrils, the solvent is squeezed out from the channel. The flow of the solvent induces the orientation of the polymer nanofibrils in the tube's axial direction because the shear force is applied onto the nanofibril surface. If the steady flow of solvent is established in the annular space between the nanofibril and the silica nanotube wall, the shear force acting on the nanofibril surface will drive the nanofibrils move toward the nanochannel outlet.

The differencial scanning calorimetry (DSC) thermograms for the SNT/AAO (200 nm)-PE and and the polyethylene produced over nonsupported catalyst (homogeneous catalyst, HOMO-PE) are shown in Figure 3-9 (a) and (b), respectively. The melting peak of SNT/AAO-PE shows a slightly lower melting peak in the first heating cycle than in the second heating cycle (Figure 3-9 (a)) with the heat of fusion (ΔH_m) of 185.2 J/g and 169.0 J/g, respectively. The heat of fusion data suggest that the crystallinity is 63.9% (based on ΔH_m = 290 J/g for a perfect polyethylene crystal [19]). The HOMO-PE sample shows much lower melting temperatures at 110~114 ^{o}C (Figure 3-9 (b)) and the melting peak itself is quite broad. The heat of fusion ΔH_m values are 28.69 J/g and 14.53 J/g for the first and the second heating cycles, respectively. The crystallinity of the nascent HOMO-PE is only 10.0%.

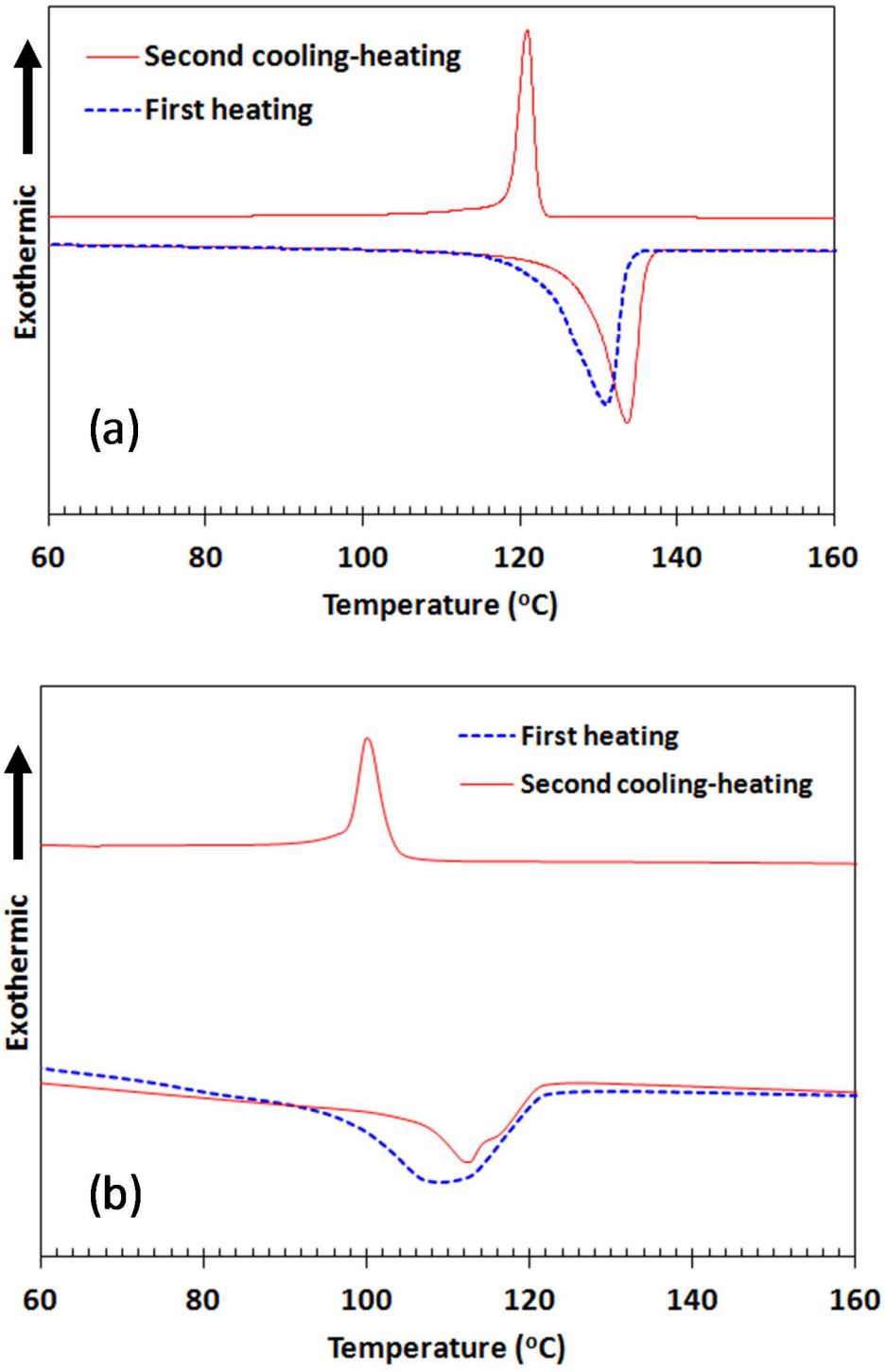

Figure 3-9. DSC thermograms of polyethylene prepared with (a) SNT-supported EBI catalyst (inside AAO nanochannel, SNT/AAO-PE) and (b) homogeneous EBI catalyst (HOMO-PE).

The XRD patterns of the polyethylenes synthesized over silica nanotubes (SNT (200 nm, 65 nm)/AAO-PE) and homogeneous catalyst (HOMO-PE) are shown in Figure 3-10. The spectra for all three samples show [110] and [200] diffraction peaks at 21.5 and 24°, respectively. The spectrum for the polyethylene sample produced over homogeneous catalyst shows a small amorphous halo around 19.4° but it is negligible for the SNT/AAO-PEs.

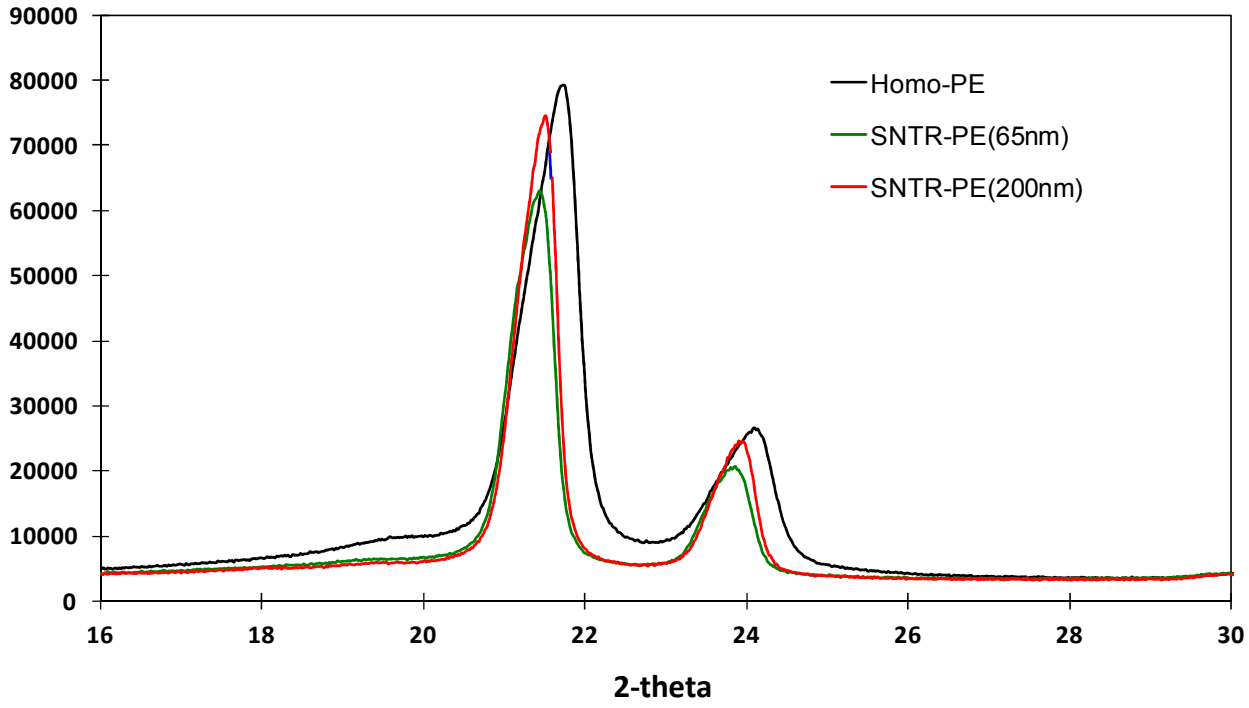

Figure 3-10. XRD patterns of polyethylene samples.

Table 3-1. Molecular weights of polyethylenes

	$\bar{M}_n$	$\bar{M}_w$	PD ($\bar{M}_w / \bar{M}_n$)
PE (homogeneous)	25,732	76,011	3.11
PE(SNTR, 65 nm)	23,266	68,548	2.95
PE (SNTR, 200 nm)	31,164	71,090	2.28

The molecular weight data for three polyethylene samples are shown in Table 3-1. It is seen that the highest weight average molecular weight was obtained with homogeneous catalyst (non-suppported catalyst), although the difference between the samples is not quite significant. We observe a general trend of decreasing polydispersity when ethylene is polymerized in SNTs.

Figure 3-11 shows the polymerization rate profiles for the EBI catalyst supported on the liberated silica nanotubes (200 nm diameter) and conventional silica microparticles (average diameter = 35 μm Sylopol 948®, WR Grace). The Zr contents in the silica supported catalysts were measured by inductively coupled plasma mass spectrometry (ICP-OES, ACTIVA, JY HORICA) and they were 1.88×10^{-5} mol-Zr/g for commercial micro-silica particles (Sylopol 948®) and 4.0×10^{-4} mol-Zr/g for silica nanotubes, indicating that catalyst can be more effectively deposited onto silica nanotubes than commercial micro-silica particles. Figure 3-11 shows that the silica nanotube-supported catalyst exhibit much higher catalytic activity per g-catalyst (silica) basis than the micro-silica particle supported catalyst because the Zr loading per gram of silica is far larger for the silica nanotubes (about 20 times larger). For the 200 nm SNTs, both MAO and EBI catalyst can more readily access to the silica surface to form active catalyst

sites. Moreover, the monomer diffusion resistance for the SNTs will be much smaller, contributing to high polymerization rate. However, the reaction rates per mole of Zr look quite similar (inset), indicating that the intrinsic catalyst activity is quite comparable regardless of the support type.

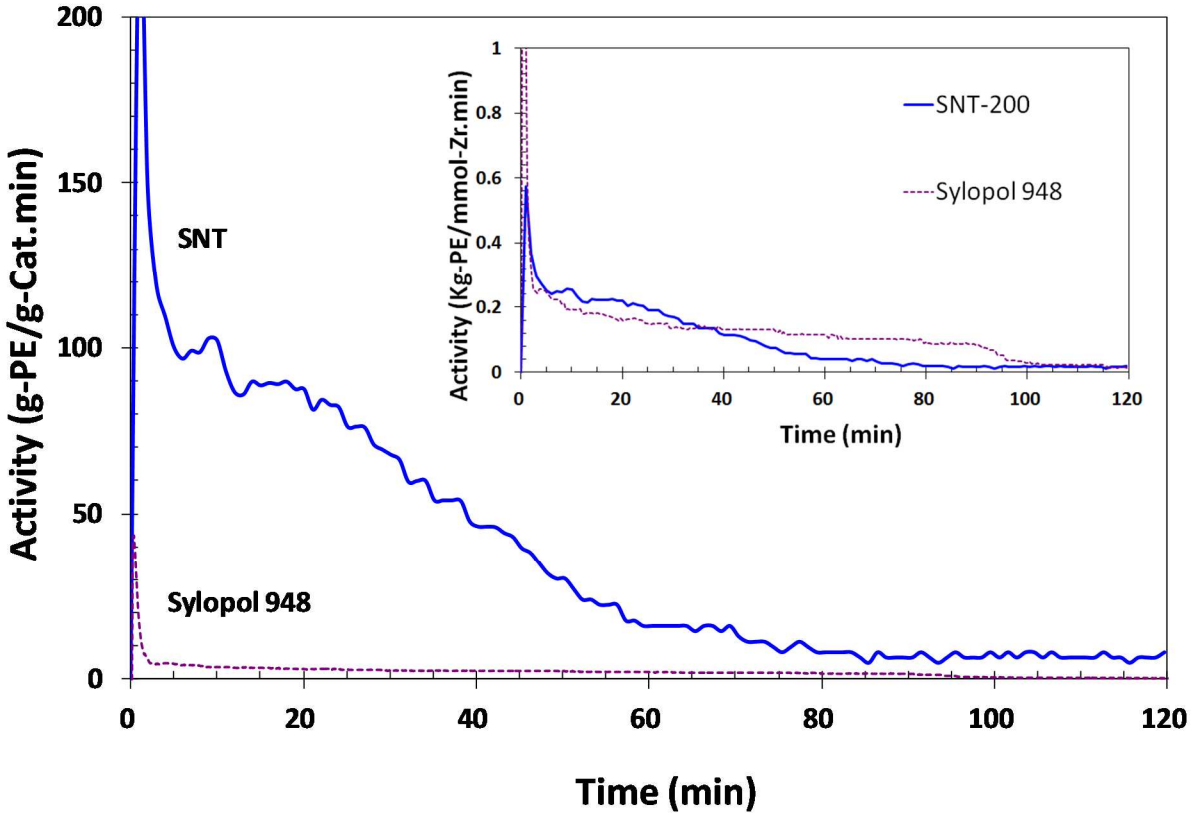

Figure 3-11. Catalyst activity for ethylene polymerization with Silica nanotube-supported catalyst and micro-silica particle supported catalyst.

3.5. Conclusions

The growth of polyethylene inside a porous silica particle has been the subject of study in the past years because the particle fragmentation, polymer growth, polymer particle morphology, and catalyst activity influence each other and all these phenomena impact the quality of process operation as well as product polyethylene properties. From the recent study of ethylene polymerization over flat silica surface and nonporous nanosilica particle supported metallocene catalysts, it has been confirmed that the basic morphological unit of the polymer is a long nanofibril of diameter 30-40 nm [10]. In this chapter, silica nanotubes were used as a support material for the metallocene catalyst and found that polyethylene nanofibrils of diameter 30-40 nm are the basic polymer morphology, which is consistent with the results observed over flat and nonporous silica nanoparticle supported metallocene catalyst. It has been observed that polyethylene nanofibrils grew in the axial direction inside the silica nanotube as a bundle of nanofibrils whereas polyethylene grew from the exterior nanotube surface perpendicular to the surface and they entangled and collapsed onto the silica nanotube surfaces. The intrinsic activity of the silica nanotube-supported catalyst and that of conventional micron size silica particle supported catalyst showed similar activities and yielded polyethylene of similar molecular weight properties, indicating that the intrinsic activity of the catalyst was quite similar. However, the 20-fold increase in the amount of deposited catalyst with silica nanotubes over conventional silica micro particles suggests that it can be an interesting option as a new silica support to boost the productivity of a catalytic ethylene polymerization process.

Chapter 4. Polymerization of Ethylene over rac-Et(1-indenyl)$_2$ZrCl$_2$/MAO Catalyst Supported on Pseudo-Inverse Opal Silica Particles*

4.1. Abstract

The polymerization of ethylene with *rac*-Et(1-indenyl)$_2$ZrCl$_2$/MAO catalyst supported on ultraporous and spherical pseudo-inverse opal silica (PIOS) particles is reported. The novel silica particles with an inverse opal-like structure provide offer wide-open pore and surface structures favorable for the catalyst deposit and monomer access with minimal intraparticle diffusion resistance. The metallocene catalyst supported on the PIOS support exhibited very high initial catalyst activity and long catalyst life time. The effects of support geometry on the catalytic activity, catalyst particle fragmentation, polymer particle morphology, and polymer molecular weight distribution in ethylene polymerization are presented.

* The materials presented in this chapter has been published :
Lee, S. Y.; Choi, K. Y. Polymerization of Ethylene over rac-Et(1-indenyl)2ZrCl2/MAO Catalyst Supported on Pseudo-Inverse Opal Silica Particles. *Industrial & Engineering Chemistry Research* **2012,** *51* (29), 9742-9749.

4.2. Introduction

Porous silica particles with large surface areas are widely used in polyolefins industry to support high activity chromium oxide catalysts for high-density polyethylene or metallocene catalysts for α-olefin polymerization in liquid slurry or gas phase polymerization processes. The performance of olefin polymerization catalysts represented by high catalyst activity and the controllability of particle morphology and polymer properties is critical for the competitiveness of industrial polymerization processes. The effectiveness of heterogeneous olefin polymerization catalysts depends upon several factors such as chemical composition and structure of a catalyst itself, chemical and physical properties of a support material, and supported catalyst formulation procedure.

One of the intriguing issues concerning silica-supported metallocene catalysts in olefin polymerization is the role of a silica support that is the most widely employed support material. For example, the properties of a silica particle surface influence the formation of various types of active sites of different catalytic activity when active metallocene compounds are immobilized with or without methylaluminoxane (MAO). The morphology and physical properties of silica can also affect the performance of a silica-supported metallocene catalyst. Commercially available silica gel is comprised of randomly linked spherical polymerized primary particles. These primary particles grow to sizes over 4-5 nm before they coagulate to form the aggregated clusters. The properties of silica gels are influenced by the size and state of aggregation of the primary particles and their surface chemistry. Porous silica-supported metallocene catalysts usually undergo complex particle fragmentation and growth process as polymerization progresses. It is generally believed that the initial particle fragmentation affects the catalyst activity as well as the final morphology of a polymer particle. Although catalyst/polymer particle

fragmentation is a critical phenomenon in both heterogeneous Ziegler-Natta and metallocene catalyst systems in olefin polymerization, the morphological changes in silica-supported metallocene polyolefin processes during the polymerization are quite different from those observed in $MgCl_2$-supported Zigler-Natta catalyst processes. In $MgCl_2$-supported Ziegler-Natta processes, the original catalyst particles of tens of microns in diameter disintegrate in the early stage of polymerization into catalyst crystallites of about 10-20 nm that become the polymerization nuclei dispersed uniformly within the polymer particle [19]. As the polymerization proceeds, each catalyst crystallite is encapsulated by the polymer that grows to ca. 1 μm polymer globule. The entire polymer particle becomes the agglomerate of these primary polymer particles. The overall polymer particle morphology is known to follow the multigrain model (MGM) and there has been a quite substantial amount of publications on the modeling of polymer particle growth with Ziegler-Natta catalysts [20-22, 24, 55-57]. In particular, the effects of monomer diffusion and heat transfer resistances on the polymerization rate and molecular weight distribution (MWD) have been extensively studied.

In contrast to the multigrain model type morphological development in Ziegler-Natta processes, the morphology of polyethylene or polypropylene polymerized over silica-supported catalysts is known to follow the layer-by-layer fragmentation mechanism [2, 29, 42, 58-62]. When exposed to monomer at the beginning of polymerization, the porous outer surface layer of a silica particle is quickly penetrated by the monomer that polymerizes to form a dense surface layer, which poses a significant diffusion resistance to the supply of monomer to active catalytic sites. The formation of this dense surface layer causes a strong diffusion resistance for the transport of monomer from the bulk fluid phase to the interior of the catalyst particle. The polymerization rate decreases during this period and it is called the induction period. Eventually,

as the polymer mass increases in the pores, the hydraulic force generated by the pore-filling polymer increases and causes the silica layer to disintegrate, allowing for the further diffusive penetration of ethylene toward the particle core. Thus, polymerization leads to a gradual cracking and disintegration of the catalyst-loaded silica particle from the surface, which results in the additional exposure of active catalytic sites present in the silica pore surface. As a result, the polymerization rate gradually increases with time [29, 61]. Often, the silica fragmentation is incomplete or irregular and a large fraction of catalyst sites are buried in the silica fragments and unavailable for the polymerization [9]. Therefore, overall polymerization activity of the silica-supported catalysts is strongly dependent on the particle fragmentation progress. For homogeneous fragmentation of the silica support, it is required that active catalytic sites are distributed uniformly on the support surface within micro-pores and that pore size and structure are optimally designed. The catalyst activity data reported in the literature by different authors are often inconsistent even for a chemically identical metallocene catalyst. It is thought that such discrepancies might be due to the variations in the actual amount of active transition metal deposited on a support material as well as particle disintegration patterns that affect the availability of the catalyst sites for polymerization [27, 63-66].

In this chapter, I present the experimental study of ethylene polymerization over *rac*-Et(1-indenyl)$_2$ZrCl$_2$/MAO (methylaluminoxane) (EBI) catalyst supported on a nonconventional silica support called the pseudo inverse opal silica (PIOS) that has been developed recently in our laboratory. The performance of this unique PIOS-supported catalyst is compared with conventional silica-supported catalysts.

4.3. Experimental

4.3.1. Materials

Polymerization grade ethylene (Air products) was purified by passing through a stainless steel column packed with R3-11 Cu catalyst, 4Å molecular sieves, neutral alumina and activated carbon. Toluene (Aldrich) was purified by being refluxed over sodium and benzophenone in nitrogen atmosphere. *Rac*-Et(1-indenyl)$_2$ZrCl$_2$ catalyst (EBI, Aldrich) and methylaluminoxane solution (MAO, Aldrich, 10 wt.% in toluene) were used without further purification. There are many different silica gels commercially available for supporting metallocene catalysts. These commercial silicas offer different pore structure, surface area, and particle size distribution. In this work, we have used two commercial silica supports (Davisil 643 (BET surface area 272.17 m^2/g), Sylopol 948 (BET surface area 295.0 m^2/g), W.R. Grace) that are widely used to support metallocene catalysts for α-olefin polymerization. The main silica support material used in this study is the pseudo-inverse opal silica (PIOS) (BET surface area 523.86 m^2/g) prepared in our laboratory. Note that the surface area of the PIOS particles is about 78-93% larger than the two commercial silica samples employed in this study.

4.3.2. Preparation of PIOS particles

Inverse opals are the three-dimensionally ordered macro porous materials and they are inverse replicates of opals consisting of regularly arranged and uniformly sized spherical void spaces of a few hundred nanometers in diameter surrounded by thin solid walls. Micrometer-sized (30-100 μm) spherical silica particles (PIOS particles) that have a pseudo-inverse opal structure have unique morphological characteristics. Here, each PIOS micro-particle is packed

with 0.5-1.5 μm-diameter “hollow” silica sub-particles that resemble the aggregates of egg shells. These silica sub-particles are packed densely and interconnected. However, they not packed in a geometrically perfect hexagonal array and hence, it is called the *pseudo* inverse opal silica. PIOS particles are synthesized using pomegranate-like poly(methyl methacrylate) (PMMA) particles as a template [8]. The template polymer particles can be synthesized by a modified suspension polymerization called micro-dispersive suspension polymerization where sub-particle nucleation and growth are induced by controlling the thermodynamic solution conditions within suspended monomer/solvent droplets. The procedure to make PIOS particles has been reported in the literature [67]. The typical synthesis process for PIOS particles is illustrated in Figure 4-1(a). Here, the three step preparation procedure involves (i) the synthesis of unique pomegranate-like micro-particle templates encapsulating a silica precursor ($SiC_8H_{20}O_4$, tetraethyl orthosilicate; TEOS), (ii) the impregnation of the polymer particles with a sol-gel catalyst to induce the hydrolysis/condensation of TEOS within polymer micro-particles, and (iii) the selective removal of the polymer by pyrolysis to obtain PIOS particles. The synthesis of template microparticles is briefly summarized as follows: an organic phase containing 48 wt % of monomer (MMA), 20.0 wt % of nhexane, 30.0 wt % of TEOS, 0.7 wt % of methacryloxypropylterminated polydimethyl siloxane (PDMS), and 1.3 wt % of lauroyl peroxide was suspended in an aqueous phase by mechanical agitation. The organic droplets (10−150 μm) werestabilized by a small amount of partially hydrolyzed poly(vinylalcohol) dissolved in the aqueous phase (89% hydrolyzed, MW= 85 000−124 000 g/mol). The initial composition of MMA−n-hexane mixture is chosen such that the PMMA produced precipitates in the liquid phase within suspended droplets [67]. During the polymerization, polymer particles precipitate out from the liquid phase within suspended droplets. The final polymer particle of 20−50 μm

with a pericellular membrane (“skin”) packed with 1−2 μm subparticles has a morphology resembling a pomegranate.

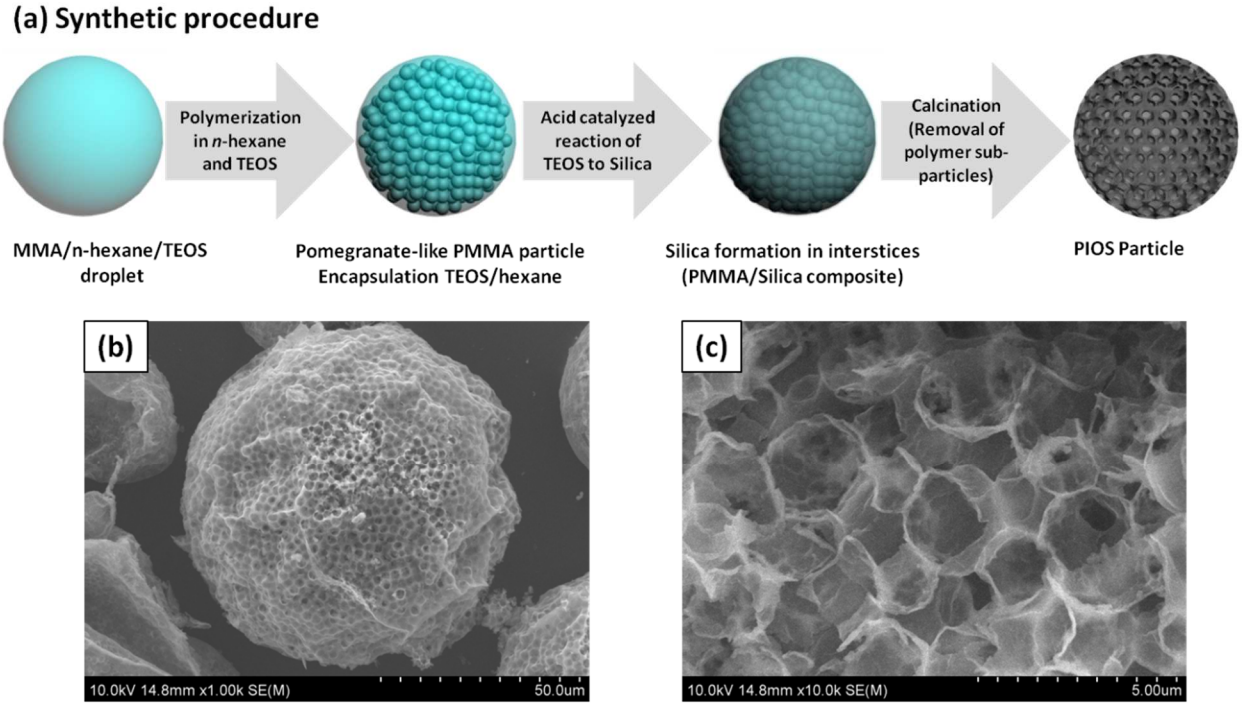

Figure 4-1. (a) Synthetic procedure of PIOS particles using pomegranate-like PMMA particles as templates, (b), (c) SEM images of PIOS particles.

Figure 4-1(b) and (c) show the scanning electron microscopic (SEM, Hitachi S-4700) images of the PIOS particle morphologies prepared by the three-stage process. The thin transparent surface layer in Figure 4-1(b) is the silica present in the shell section of a polymer template particle. From the magnified view of the PIOS particle as shown in Figure 4-1(c), we can clearly see that the PIOS resembles the aggregates of *egg shell*-like pseudo inverse opals. The BET surface area was measured using Micrometrics ASAP2020 apparatus at 77K and the pore size distribution was measured using the Barrett-Joyner-Halenda (BJH) method. The surface area of the PIOS particles is about 78−93% larger than the two commercial silica samples employed in this study. The PIOS particles as well as commercial silica particles were completely amorphous as confirmed by the X-ray diffraction (XRD) patterns [67].

4.3.3. Preparation of supported catalysts

Silica supported EBI catalysts were prepared as follows. A known amount of silica support particles were calcined at 250^{o}C before they were soaked in a piranha solution (30% hydrogen peroxide and 70% sulfuric acid) for 30 min, washed with excess amount of deionized water, and then treated with an MAO solution (10 wt.% in toluene) at ambient temperature for 24 h. The treated silica particles were washed with toluene, and dried in vacuo overnight. The MAO treated silica support was immersed in the catalyst/toluene solution for 24 hr, washed with toluene several times, and dried in vacuo overnight.

4.3.4. Polymerization

A liquid slurry ethylene polymerization was carried out in a 500 mL glass reactor equipped with a mechanical agitator. Predetermined amounts of toluene (300 mL), MAO solution (4 mL), and silica-supported EBI catalyst (40-50 mg) were charged into a reactor assembly in an argon-filled glove box. The concentration of MAO in the reactor was 0.02 mol/L in all the experiments. The reactor assembly was removed from the glove box and was immersed in a constant temperature bath at 70^{o}C and connected to an ethylene supply line. The reactor pressure was raised and set at 2.07 bar by pure ethylene gas. The equilibrium ethylene concentration in toluene calculated by Henry-Gesetz equation was 0.0157 mol/L. The reactor pressure (i.e., ethylene pressure) was kept constant by supplying ethylene on demand automatically with a pressure controller. The ethylene flow rate to the reactor (mL/min), which corresponds to the polymerization rate for a given mass of supported catalyst, was monitored by an in-line mass flow meter during the polymerization experiment. The ethylene mass flow rate, reactor temperature, and reactor pressure data were recorded onto an on-line data acquisition computer. The recorded polymerization rate (i.e., ethylene flow rate) was numerically integrated with time to obtain the polymer yield data. The calculated yield and actually measured yield values agreed quite well within $\pm 7 \sim 9\%$. Some loss of very fine samples might have occurred during the sample collection process (separation and drying). After polymerization, the reaction mixture was filtered, washed with acidified methanol and dried in vacuo overnight. The morphology of polymer particles and support silica materials were analyzed by scanning electron microscopy (SEM, Hitachi S-4700). The sample particles were coated with carbon layers in a Denton DV-503 vacuum evaporator. The molecular weight distribution was measured by gel

permeation chromatography (Polymer Laboratories) using 1,2,3-trichlorobenzene at 160ºC with PLgel® 10 μm MIXED-B and PLgel® 10 μm GUARD columns.

4.4. Results and Discussion

4.4.1. Silica properties and catalyst distribution

The Zr contents in the supported EBI catalyst were measured by inductively coupled plasma (ICP-OES, ACTIVA, JY HORIVA) and they were: 6.40×10^{-5} mol-Zr/g for PIOS, 2.82×10^{-5} mol-Zr/g for Davisil 643, and 1.88×10^{-5} mol-Zr/g for Sylopol 948. High concentration of Zr per gram of PIOS is due to its large specific surface area that is approximately twice that of typical commercial silica. The Zr contents per unit surface area for each catalyst were very similar: 1.22×10^{-7} mol-Zr/m^2 for PIOS/EBI catalyst, 1.037×10^{-7} mol-Zr/m^2 for Davisil 643/EBI catalyst, and 0.637×10^{-7} mol-Zr/m^2 for Sylopol 948/EBI catalyst. Davisil 643 silica particles are irregularly shaped with particle size of 35-70 μm and Sylopol 948 silica particles are spherical with average particle size of 60 μm. The average diameter of PIOS particles is about 50 μm. In each experiment, 6.03 mmole of Al (MAO) was used in 300 mL toluene solution. The area distribution of EBI catalyst components on PIOS particles was measured by energy-dispersive X-ray spectroscopic analysis (EDX/EDS, EDAX (Ametek) attached to AMRAY-1610). Figure 4-2 (a.1) and (a.2) show the EDX element mapping images of the PIOS supported EBI catalyst surface. It is shown that both zirconium and aluminum (lighter parts in the photos) are quite homogeneously dispersed in the PIOS particle (Zr, 6.97 atom %; Al, 21.38 atom %; Cl, 5.55 atom %; Si, 65.49 atom %). The EDX element mapping images of the Davisil 643-supported EBI catalyst surface illustrated in Figure 4-2(b.1) and (b.2) also show that both zirconium and aluminum are uniformly dispersed. It is interesting to observe that the availability of larger open surface of PIOS particles than conventional silica particles for

catalyst deposition can be seen by higher density of deposited metal atoms indicated by higher contrast intensities in panels a.1 and a.2 than in panels b.1 and b.2.

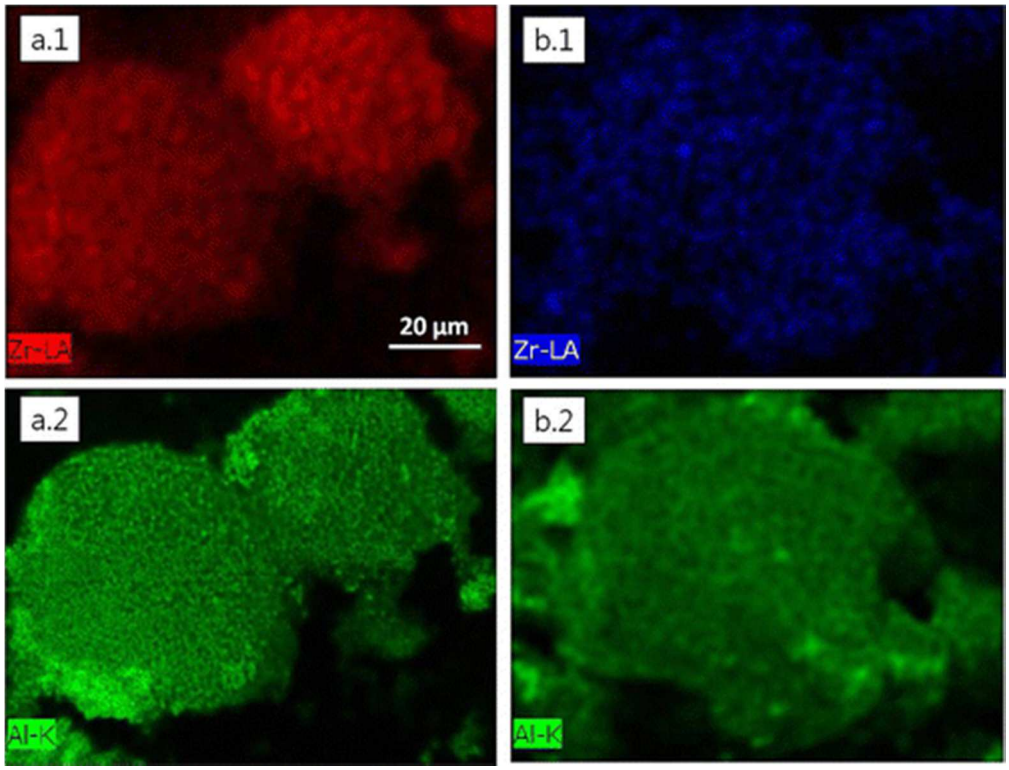

Figure 4-2. EDX element mappings (zirconium and aluminum) of EBI catalyst supported on PIOS particles (a.1 and a.2) and Davisil 643 particles (b.1 and b.2) (lighter parts indicate metal atoms) (scale bar applies to all images).

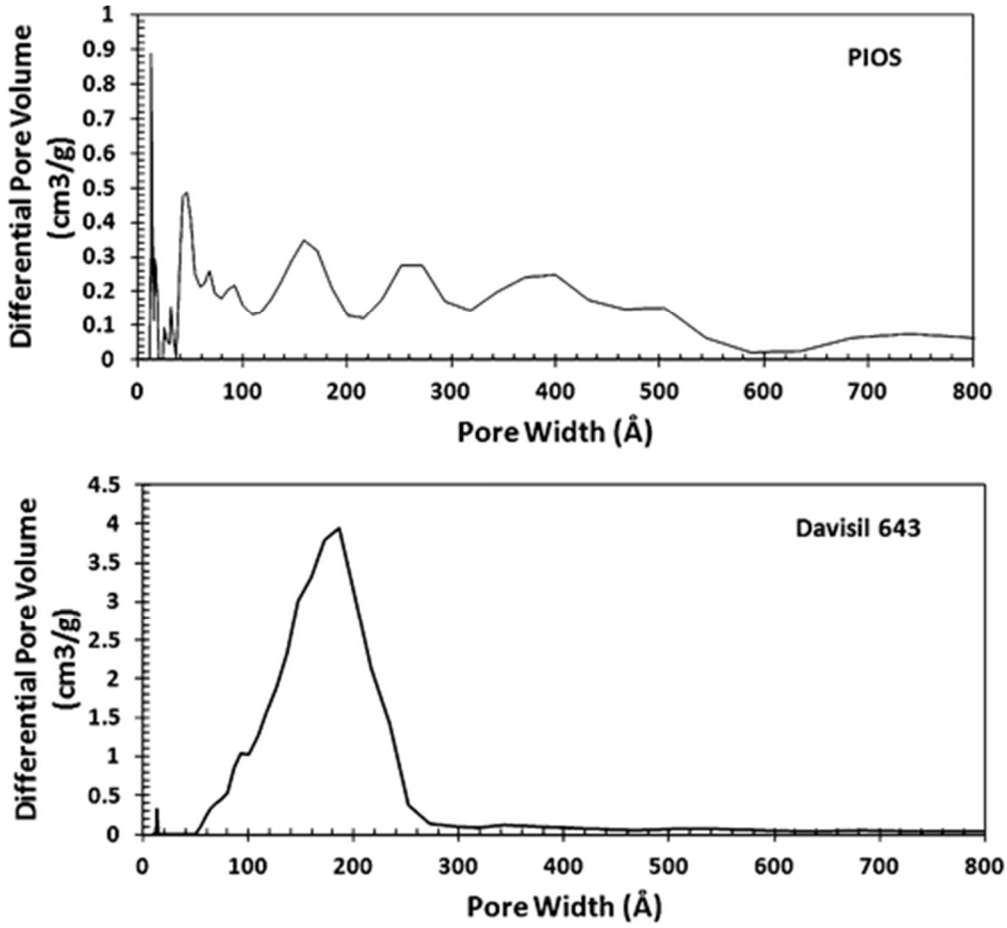

Figure 4-3. Pore size distributions of PIOS and conventional silica particles (Davisil 643).

The pore size distributions, obtained from the adsorption-desorption data using the Barrett-Joyner-Halenda (BJH) procedure, are shown in Figure 4-3 for PIOS and conventional silica particles (Davisil 643). In general, internal surface of a porous silica particle comprises the walls of all cracks, pores and cavities. The pore size distribution of PIOS particles shown in Figure 4-3 indicates that PIOS particles contain mesopores as well as larger macropores that are quite broadly distributed from about 10 nm to about 80 nm whereas conventional commercial silica particles have a narrow pore size distribution between 5 ~ 28 nm.

In the synthesis of commercial silica particles, 10-50 nm-diameter spheroids or primary particles are first formed during the polymerization of silicic acid solution. These spheroids aggregate to 0.2-0.5 μm-diameter clusters and the channels between the primary particles and those between the clusters are void pores [9]. In the PIOS, silica is formed at the surface of sub-polymer particles and in the interstices between these sub-particles formed within a suspended monomer/solvent droplet. The void space is formed as the polymer sub-particles are removed by pyrolysis. The difference in the pore-forming mechanisms between PIOS and conventional silica particles is the primary reason for the difference in pore size distributions that are illustrated in Figure 4-3.

4.4.2. Catalyst activity

Catalyst activity or polymerization rate (g/g-cat.min or g/mol-Zr.min) is the most important performance measure of a polymerization catalyst. Here, we note that, in most of the literature, the reported catalyst activity is usually a time-averaged polymerization rate obtained by dividing a polymer yield by reaction time. If a catalyst exhibits rapid activity decay with time, the calculated value of time-averaged polymerization rate becomes strongly dependent on the reaction time that is used to divide the overall polymer yield. The choice of reaction time for the calculation of average reaction rate using polymer yield data can be arbitrary and this could be one of the reasons why some inconsistent average activity data are often reported in literature for a same catalyst compound. In our study, we have measured complete time-dependent polymerization rate profiles or instantaneous ethylene consumption rate profiles (i.e., ethylene polymerization rates) using an in-line mass flow meter with an on-line data acquisition system for each supported EBI catalyst system.

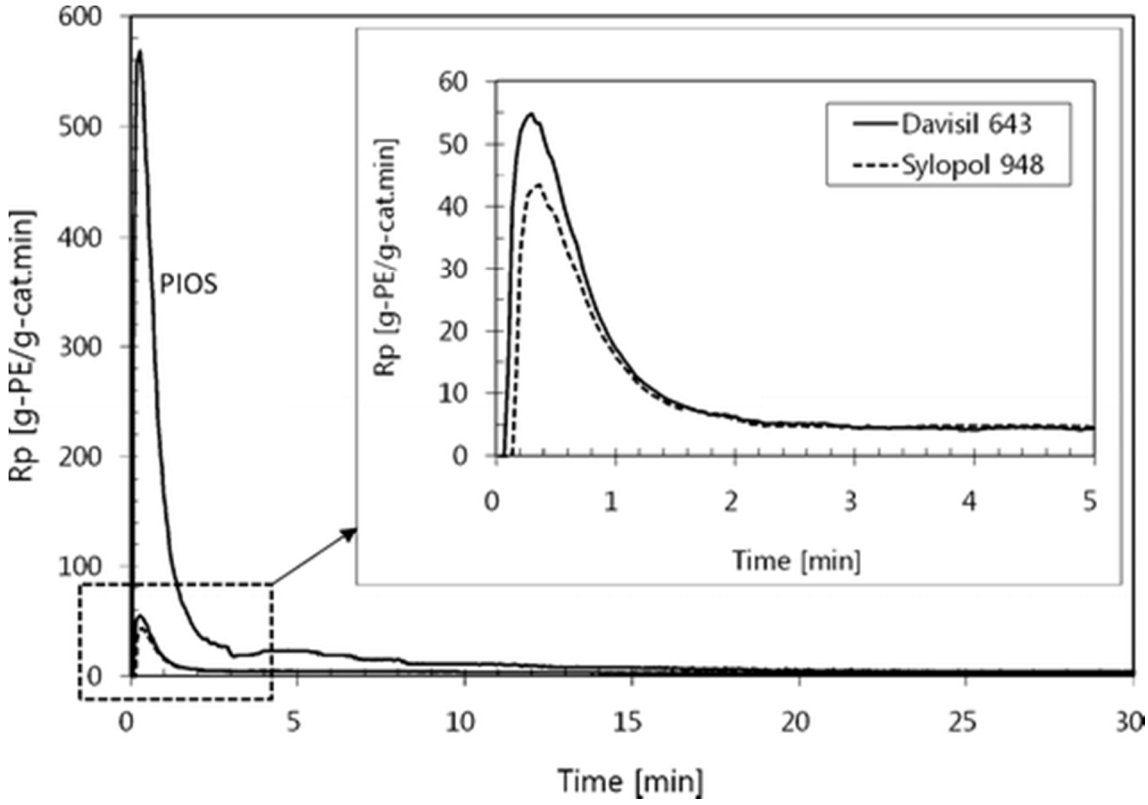

Figure 4-4. Polymerization rate profiles for three different silica-supported catalysts at 70 °C and 2.07 bar.

Figure 4-4 shows the ethylene polymerization rate profiles directly measured for three different silica-supported EBI catalysts at 70°C and 2.07 bar of ethylene partial pressure. First of all, we observe that all three supported catalysts exhibit decay-type kinetic profiles where the polymerization rate rises rapidly to a maximum and then declines with reaction time. In many silica-supported metallocene or chromium oxide catalysts for ethylene polymerization, it has been frequently reported that polymerization rate profiles can exhibit induction period, followed by a gradual rate increase with time.[29, 61] In such cases, the induction period was attributed to the formation of dense outer layer of polymer that severely hinders the diffusion of monomer until dense silica-polymer layer disintegrates to permit the penetration of monomer into the

particle interior. Secondly, the initial maximum polymerization rate with PIOS-supported catalyst is about 10 times higher than the two conventional silica-supported catalysts that show almost identical kinetic profiles. Also, it is interesting to observe that the polymerization activity of the PIOS-supported catalyst maintains its steady rate after about 3 min and its level of activity is much higher than the silica-supported catalysts. The stationary activity for the silica-supported catalysts (inset) corresponds to about 70 kg/mol-Zr.min, which is quite comparable to the reported values [64].

The polymer yields per gram of catalyst with reaction time for these catalysts are shown in Figure 4-5. The yield data were obtained by integrating the polymerization rate (ethylene consumption rate) vs. time profiles (Figure 4-4). The symbols indicate actual yield measurements. A Figure 4-5 show that the cumulative yield of polyethylene (g-PE/g-cat) obtained with PIOS-supported EBI catalyst is several times higher than the commercial silica-supported catalyst. The performances of the two commercial silica-supported catalysts (dotted lines) show similar yield profiles. It is also seen that the yield reaches a stationary value at about 90 -120 min for commercial silica systems whereas the PIOS-supported catalyst system shows continuous increase in polymer yield. It was observed that the high initial reaction rates illustrated in Figure 4-4 did not cause significant exotherms and constant temperature conditions were well maintained. Figure 4-6 illustrates the actual reactor temperature profiles during the polymerization. It is seen that some deviations from the target reaction temperature of 70 ^{o}C are present but not to a significant level to affect the measured polymerization rate.

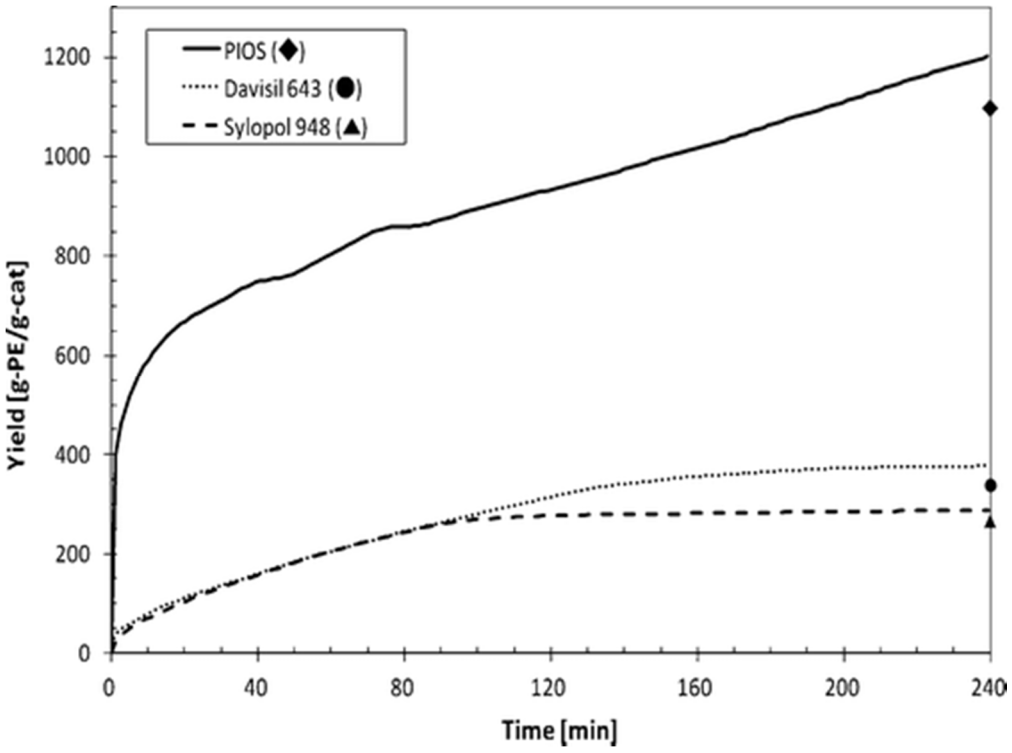

Figure 4-5. Ethylene polymerization at 70 °C and 2.07 bar with EBI catalyst on three different silica supports. Symbols represent actual yield measurements.

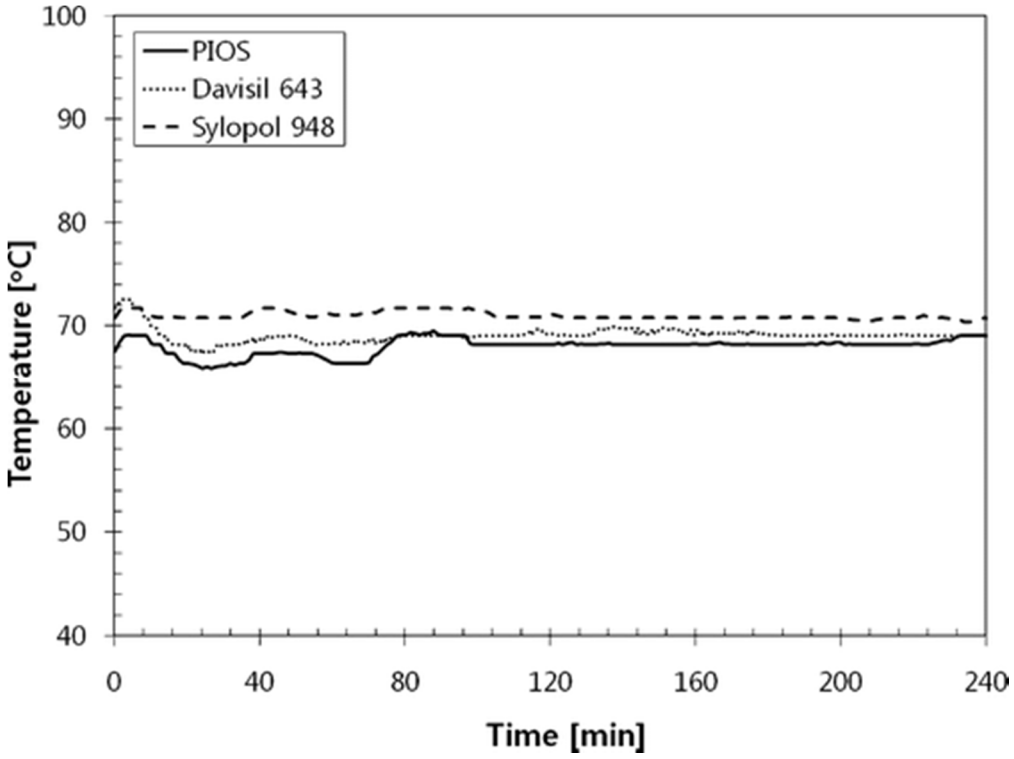

Figure 4-6. Reaction temperature profiles in semibatch ethylene polymerization experiments in a 500-mL agitated reactor.

4.4.3. Polymerization rate analysis

In Figure 4-4 and Figure 4-5, we have illustrated that the catalytic performance of the PIOS-supported EBI catalyst differs from that of silica particle-supported catalysts. For further analysis of the observed polymerization kinetics, we consider the polymerization rate $\tilde{R}_p$ (g/gcat.min) that can be expressed in a general form as:

Equation 4-1

$$\tilde{R}_p = k_p [M]_p f([Zr]) w_m$$

where k_p is the propagation rate constant (L/mol·min), $[M]_p$ is the monomer concentration (mol/L) at the catalytic site, w_m is the molecular weight of monomer (g/mol), $[Zr]$ is the active catalyst site concentration (mol-Zr/g-cat). Here, the concentration of active catalytic sites that are available for the polymerization is dependent on many factors such as catalyst preparation procedure, uniformity of complexation of zirconium site with MAO, silica morphology, pore surface properties of silica, particle disintegration, etc. Because of such empirical factors, it is practically difficult to know exact concentration of catalyst sites available for polymerization. Thus, in Equation 4-1, the active catalyst site concentration is expressed in a functional form (i.e., $f([Zr])$). The intrinsic catalyst activity is also affected by catalytic site deactivation and monomer diffusion resistance because of the heterogeneous nature of the polymerization. The monomer concentration in the solid phase, $[M]_p$, is generally affected by intraparticle diffusion resistance and it can be approximated as $[M]_p = \eta [M]_b$ where $[M]_b$ is the bulk phase monomer concentration and η is the effectiveness factor ($\eta \leq 1.0$) that represents the monomer diffusion effect in the particle. Since not all the zirconium sites may be catalytically active for ethylene polymerization and also the activity may change with time, we define a new parameter called the catalyst activity parameter (ψ) to account for the catalyst efficiency with the initial zirconium

loading as a basis. For example, we assume that the site activity function is approximated by $f([Zr]) = \psi[Zr]_0$ where $[Zr]_0$ is the initial zirconium concentration on the silica support surface. If ψ = 1.0, then all the initial zirconium sites will be available for polymerization. In practice, the exact value of this parameter will be difficult to measure but it will be reasonable to assume that ψ value is smaller than 1.0 due to poisoning by impurities, incomplete complexation with MAO, etc. Here, we note that both η and ψ are the empirical parameters because they are difficult to directly measure experimentally. Then, Equation 4-1 can be recast into the following form using these new parameters:

Equation 4-2

$$\tilde{R}_p = k_p \left(\eta[M]_b\right)\left(\psi[Zr]_0\right) w_m$$

The exact cause of catalytic activity decay is not fully understood but it is generally modeled by the first-order decay kinetics. Then, Equation 4-2 can be written as:

Equation 4-3

$$\tilde{R}_p = k_p \left(\eta[M]_b\right)\left(\psi_0[Zr]_0 e^{-k_d t}\right) w_m$$

where k_d is the deactivation rate constant and ψ_0 is the initial catalyst activity parameter.

The polymerization rate can also be expressed in g/mol-Ti·min (i.e., $R_p = \tilde{R}_p / [Ti]_0$). Then, from Equation 4-3 the initial polymerization rate (i.e., at t = 0) in g/mol-Ti·min can be expressed as:

Equation 4-4

$$R_{p0} \equiv \frac{\tilde{R}_{p0}}{[Zr]_0} = \eta_0 \psi_0 k_p [M]_b w_m$$

where η_0 is the initial effectiveness factor (i.e., $\eta_0 = \lim_{t \to 0} \eta$). For the experimental conditions used in this study, the monomer concentration remains nearly constant because ethylene partial pressure was kept constant during the polymerization. If we normalize the polymerization rate (g/mol-Ti·min) in Equation 4-4 with initial polymerization rate, we obtain the following equation:

Equation 4-5

$$\frac{R_p}{R_{p0}} = \frac{\eta\psi}{\eta_0\psi_0}\exp(-k_d t) \equiv \frac{\eta'}{\eta_0'}\exp(-k_d t)$$

where $\eta'(=\eta\psi)$ and $\eta_0'(=\eta_0\psi_0)$ represent the overall effectiveness factors at time t and time zero. Equation 4-5 can be rearranged to:

Equation 4-6

$$-\ln\frac{R_p}{R_{p0}} = \ln\frac{\eta_0'}{\eta'} + k_d t$$

Figure 4-7 shows the plots of Equation 4-6 for three supported catalyst systems over the first 15~16 min reaction time. For both conventional silica-supported catalysts, the rate data are well fitted by Equation 4-6 and from the intercept we obtain $\eta'/\eta_0' = 0.828$. This value indicates that the mass transfer resistance and/or unavailability of all the catalytic sites might have affected the polymerization from the beginning of polymerization. On the other hand, the PIOS-supported catalyst shows that the intercept is zero (i.e., $\eta' \approx \eta_0'$), which suggests that the effects of particle fragmentation and physical transport resistance on the reaction kinetics were minimal. The deactivation parameter values (k_d) estimated from the slope of each straight line in Figure 4-7 are 0.04 min^{-1} for the two conventional silica-supported EBI catalysts and 0.112 min^{-1} for the PIOS-supported catalyst. The decay constant for the PIOS supported catalyst is larger

than the conventional catalysts but as seen in Figure 4-4, the polymerization rate over PIOS-supported catalyst maintained much higher value than the conventional silica-supported catalysts over extended period of reaction time.

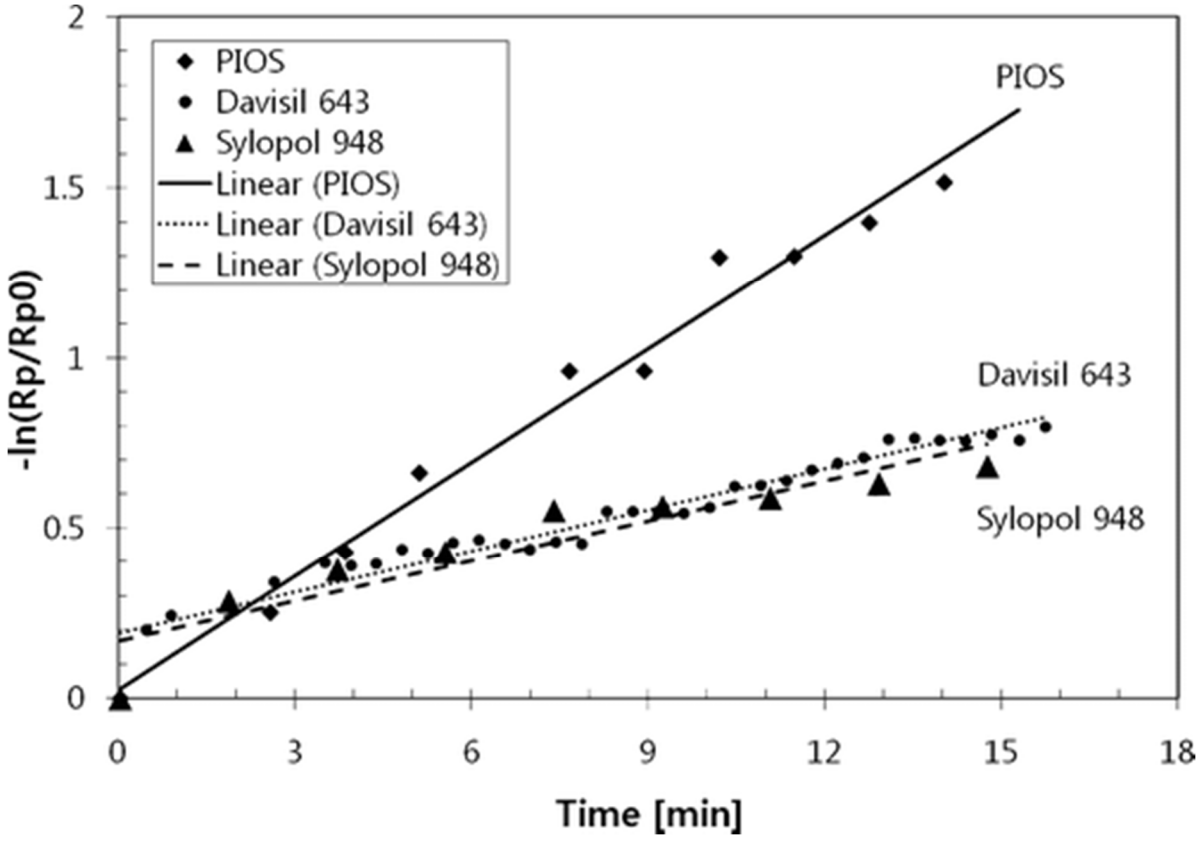

Figure 4-7. Plot of Equation 4-6.

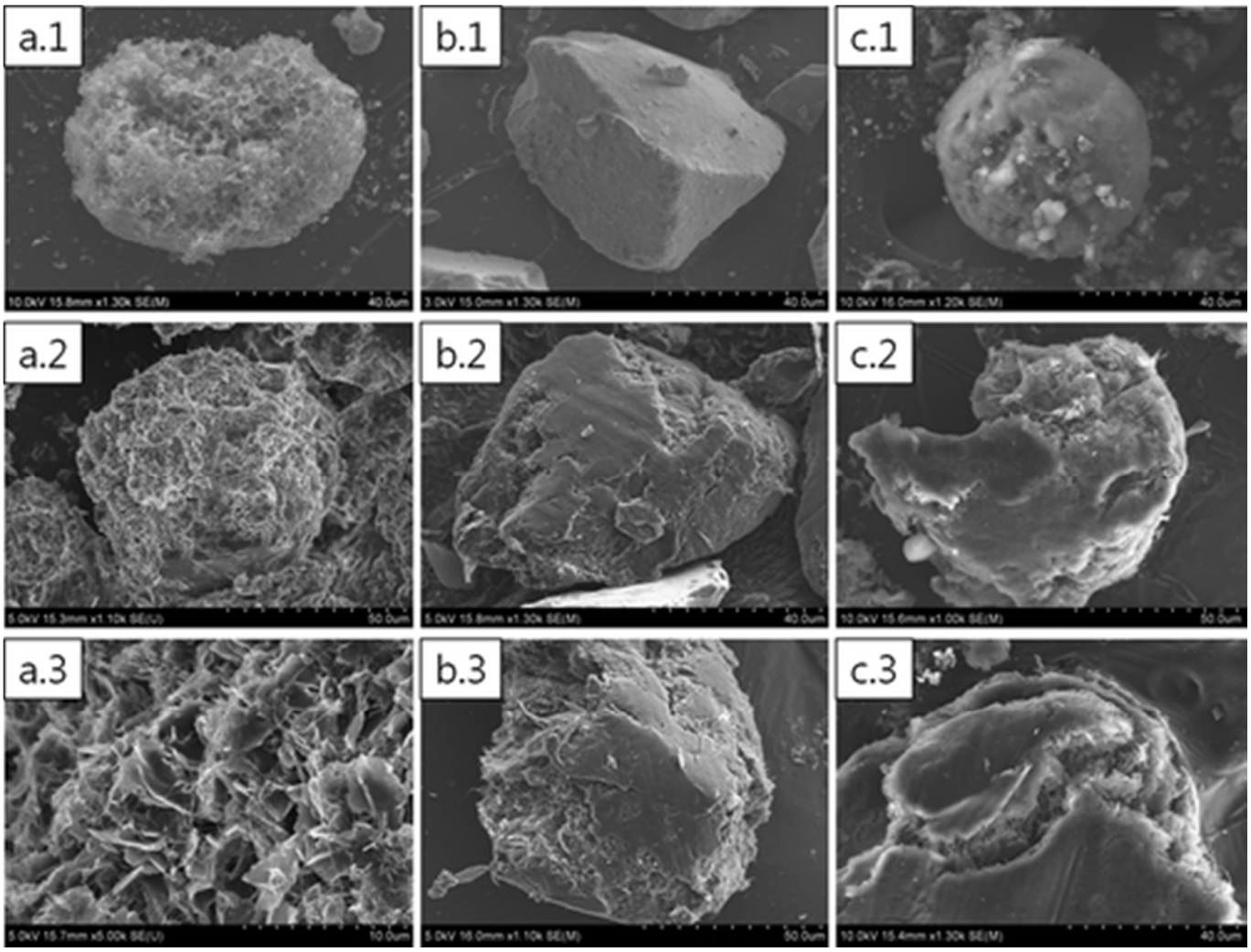

Figure 4-8. Polyethylene particle morphologies: (a.1) catalyst-impregnated PIOS particle before polymerization, (a.2) polymer with PIOS-support catalyst after 7 min, (a.3) details of (a.2); (b.1) catalyst-impregnated Davisil 643 particle before polymerization, (b.2) polymer with Davisil 643 at 10 min, (b.3) polymer with Davisil 643 at 20 min; (c.1) catalyst-impregnated Sylopol 948 particle before polymerization, (c.2) polymer with Sylopol 948 at 10 min, (c.3) polymer with Sylopol 948 at 20 min.

4.4.4. Polymer particle morphology

The analysis of polymer particle morphology during the early period of polymerization provides useful information about the differences in catalytic activity observed for the supported catalyst systems tested in this study. Figure 4-8 shows the SEM images of polyethylene particles obtained using PIOS-supported catalyst and commercial silica-supported catalyst (Davisil 643 and Sylopol 948). The panels (a.1), (b.1) and (c.1) in Figure 4-8 show the catalyst-loaded PIOS and silica particles before polymerization. The morphologies of polymer particles after 7min with PIOS particles are shown in (a.2) and (a.3). Notice that polymerization has already progressed in the entire PIOS-supported particle. In contrast, only partial fragmentation is observed with Davisil 643 and Sylopol 948-supported catalyst after 10-20 min (b.2 and b.3; c.2 and c.3), indicating that commercial silica particles are quite resistant to fragmentation whereas the PIOS-supported particle shows a nearly full fragmentation from the beginning of polymerization. It is believed that this difference in the particle morphology during the polymerization is the primary reason for the difference in catalytic activity as illustrated in Figures 4-7. In other words, the PIOS-supported catalyst starts the polymerization with its wide open structure from the beginning of polymerization with minimal resistance to silica fragmentation as polymerization progresses. The bulk densities of polymer recovered after 4 h of reaction were 0.156 g/cm3 for a PIOS-supported catalyst and 0.168−0.186 g/cm3 for commercial silica-supported catalysts.

4.4.5. Polymer molecular weight distribution

It has been generally accepted that any mass transfer limitations in porous heterogeneous olefin polymerization catalysts have minimal effect on polymer molecular weight distribution whereas the catalytic activity is more influenced by the intraparticle monomer mass transfer limitations. Therefore, as expected, the molecular weight properties of polyethylene obtained by PIOS-supported catalyst and commercial silica-supported catalyst were almost identical as illustrated in Table 4-1and Figure 4-9. It is believed that both polymerization rate and chain transfer rate that dictate the polymer chain length development are enhanced with PIOS-supported catalyst to result in the average molecular weight similar to that of conventional silica-supported catalyst systems. The polydispersity (PDI) values for both supported catalysts indicate some departure from 2.0. The molecular weight broadening (i.e., departure from the theoretical value of 2.0 for a perfectly single site catalyst) is mostly due to the interactions between the metallocene and the support. For example, a silica support material with surface heterogeneity in hydroxyl group types and concentration may lead to the formation of active sites differing in electronic and steric character.[64] Considering the difficulty in the experimental measurements of MWD by high temperature gel permeation chromatography, The differences in polydispersity values in Table 4-1 for the tested catalysts seem to be practically insignificant.

Table 4-1. Molecular Weight Distributions of Polyethylene

Catalyst Support	Mn (g/mol)	Mw (g/mol)	PDI
PIOS	41,600	95,000	2.28
Davisil 643	42,200	109,000	2.58
Sylopol 948	45,900	107,400	2.34

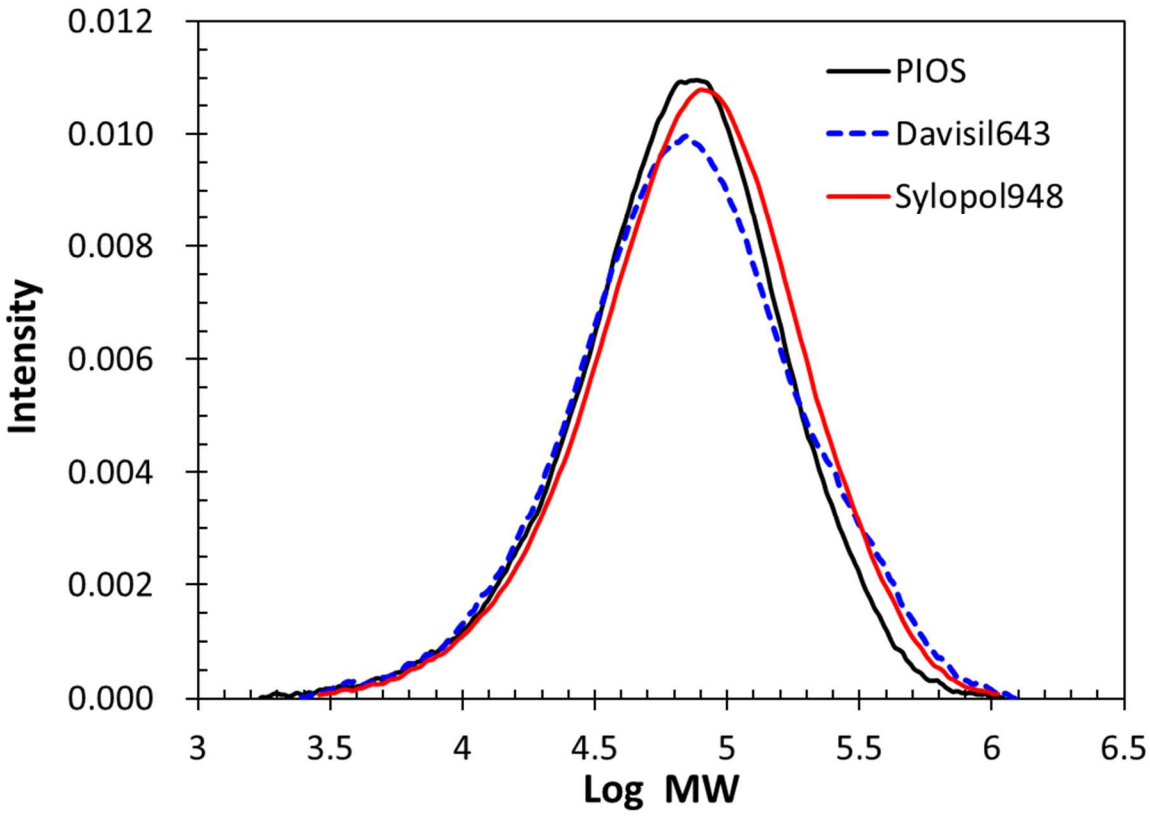

Figure 4-9. Molecular weight distributions of polyethylenes with PIOS-supported catalyst, and conventional silica-supported catalyst.

4.5. Conclusions

In this chapter, the experimental results of ethylene polymerization with novel PIOS-supported metallocene catalyst have presented. The comparison of the catalyst performance was made with commercially available silica particle-supported catalyst. Although the choice of these commercial silica particles may not be considered as most representative of available silica support materials, the experimental results obtained using identical catalyst preparation and polymerization conditions indicate that the unique morphological structure of PIOS particles yield clear difference in catalytic activity or kinetic profiles. The wide open structure of the PIOS support materials seems to present little fragmentation resistance as polymer is formed in the solid phase, which is quite different from the layer-by-layer fragmentation mechanism in typical silica-supported olefin polymerization. The initial catalyst activity with PIOS-supported catalyst is much higher than the conventional silica-supported catalysts where layer-by-layer fragmentation mechanism delays the monomer penetration and prohibits effective exposure of active catalytic sites in the support material. The polymer molecular weight distributions by PIOS and silica-supported catalysts are very similar, indicating that in both catalyst systems, the chemical natures of the active sites are practically identical. This work suggests that the catalytic activity can be significantly enhanced by the support geometry.

Chapter 5: Kinetics of Styrene Polymerization to Syndiotactic Polystyrene over Metallocene Catalyst on Flat Surface, Silica Nanotube Reactors and Porous Silica Particles*

5.1. Abstract

The geometry of a catalyst support has a strong influence on the catalytic activity of heterogeneous metallocene catalysts for polymerization of α-olefins and styrene. In this study, the catalytic activities of Cp*Ti$(OCH_3)_3$/MAO catalyst for styrene polymerization to syndiotactic polystyrene (sPS) have been investigated using three different types of support materials with different geometries: flat surface derived from silicon wafer, cylindrical pores in silica nanotube reactor arrays, and random tortuous and interconnected pores in porous silica particles. With the same catalyst immobilization technique applied to these support materials, the highest titanium loading per unit solid surface area has been obtained with a flat surface catalyst whereas porous silica particles of 15 nm average pore size has the lowest titanium loading. The metallocene catalyst supported on a flat silica surface also exhibited the highest catalyst activity per mole of titanium among different types of support materials investigated. The flat surface catalyst renders minimal mass transfer resistance for the catalytic components as well as monomer and all the active sites are fully exposed to monomer and available for polymerization. The low catalyst activity of silica particle supported catalyst is mainly attributed to the limited exposure of active

* The materials presented in this chapter has been published :
Lee, S. Y.; Kim, S.-K.; Nguyen, T. M.; Chung, J. S.; Lee, S. B.; Choi, K. Y. Kinetics of Styrene Polymerization to Syndiotactic Polystyrene over Metallocene Catalyst on Flat Surface, Silica Nanotube Reactors and Porous Silica Particles. *Macromolecules* **2011,** *44* (6), 1385-1392.

sites to monomer because of geometric obstructions. The catalyst deactivation kinetics for the different types of supported catalysts was very similar and fitted well by the first order deactivation kinetics. The sPS synthesize with all these supported catalysts show nanofibrillar structures of about 30 nm in diameter.

5.2. Introduction

Supported metallocene catalysts are widely used for the polymerization of α-olefins because the catalyst immobilized on a solid support can preserve the catalytic activity and provide desired polymer particle morphology. In industrial α-olefin polymerization processes, supported catalysts are used for slurry and gas phase polymerizations in stirred reactors, loop reactors, and fluidized bed reactors. Silica-supported metallocene catalysts used for olefin polymerization are interesting in that the silica fragmentation occurs during the polymerization and the characteristics of the fragmentation have a big impact on the catalyst activity, and resulting polymer properties and polymer particle morphology. Therefore, understanding the role of silica in supported metallocene and Ziegler-Natta catalysts is an important technical issue to design superior polymerization catalysts. Besides α-olefins, vinyl monomers such as styrene can also be polymerized over silica supported metallocene catalysts to syndiotactic polystyrene (sPS) with high syndiospecificity and high crystallinity. The polymerization of sPS with supported metallocene catalyts are advantageous over homogeneous catalyst systems in that the global gelation of sPS can be prevented by controlling the reaction rate and polymer morphology [68, 69]. Syndiotactic polystyrene is an industrially important semicrystalline engineering polymer with strong chemical resistance, low dielectric constant, and high heat resistance suitable for harsh engineering applications in automotive, electrical, and electronics industries [70, 71].

One of the important issues in heterogeneously catalyzed polymerization processes is concerned with the characterization of catalytic activities for the design and optimization of industrial polymerization conditions and polymer properties control. However, the quantification of the intrinsic polymerization kinetics is known to be complex and difficult because of the presence of site heterogeneity and physical transport effects between the bulk fluid phase and the

solid phase where active catalytic sites reside. The effects of support properties on the polymerization kinetics are not completely understood, either. The formation of active catalytic complex at the surface of the support material such as silica gel is influenced by many factors such as local concentrations of the catalyst forming precursors, the structure and dimension of pores, and the structure of surface functional groups. For example, the presence of hydroxyl groups on the silica surface has a strong effect on the formation of active sites. Moreover, catalyst/polymer particle disintegration, interfacial and intraparticle mass and heat transfer effects can strongly affect the catalyst activity and the monomer composition in a heterogeneous catalyst particle.

The morphological development of polymer particles during the polymerization is also of great practical importance. The cracking and fragmentation of catalyst support materials with a buildup of polymers in the catalyst pores and subsequent polymer particle growth are the major mechanisms of complex morphological developments of polymer particles. For example, in silica-supported metallocene catalysts for ethylene polymerization, the buildup of hydraulic forces occurs within the pores at the beginning of polymerization, leading to the disintegration of silica particles that are loosely connected by polymers.

The catalytic activity is also strongly dependent on the catalyst preparation procedure that determines the chemical and physical states of the catalyst. Quite often, different catalytic performances are reported in the literature for the polymerization of α-olefins with the same or similar catalysts by different authors and direct comparison of catalyst performances is sometimes difficult. Therefore, interpretation of kinetic data obtained with a certain heterogeneous catalyst becomes catalyst specific. Even for the same catalyst constituents, the nature of the heterogeneous catalyst material and the way the active catalyst components are

anchored and activated at the solid surface can dramatically change the catalytic behavior, often resulting in inconsistent kinetic behaviors and varying polymer properties (e.g., molecular weight distribution, copolymer composition, particle morphology, and density). The three most representative methods to support metallocene catalysts on to a silica are: (i) direct immobilization of metallocene on a pretreated silica; (ii) reaction of MAO cocatalyst with the hydroxyl surface groups of the silica, and subsequent impregnation with a metallocene catalyst; (iii) immobilization of preactivated MAO/metallocene complex on a porous silica support [44]. The resulting catalyst activity is strongly affected by the catalyst preparation process.

The characterization of active catalytic species is also difficult because of heterogeneous nature of the catalyst. For example, the exact amount of transition metal sites active for polymerization is very hard to measure and hence, the determination of intrinsic kinetic parameter values such as propagation rate constant and chain transfer constants is difficult.

Recently, some new approaches to synthesize supported catalysts have been reported for olefin and styrene polymerizations in the literature using non-conventional forms of silica materials [72]. Choi et al. used silica nanotube reactor arrays with a well-defined straight cyclindrical nanopores to polymerize styrene to sPS using $Cp^*Ti(OCH_3)_3$/MAO catalyst. They discovered that sPS grows as a bundle of nanofibrils through intertwining inside nanopores and surprisingly high molecular weight sPS was also obtained[73]. A flat silicon substrate covered by amorphous silica was also used to study the catalytic reaction and polymer morphology with chromium oxide catalyst for ethylene polymerization [74-78].

Here, the kinetics of heterogeneous polymerization using three different types of silica support geometries are discussed. To this purpose, the syndiospecific polymerization of styrene as a model system, and three well-defined catalyst support configurations were used: a

hydroxylated silicon wafer (flat-surface catalyst), a silica nanotube reactor (cylindrical reaction tube), and a granular silica particle (3-dimensional support). A catalytic pore or channel in a silica nanotube reactor is straight whereas the pores in a silica particle are tortuous and pore size is not uniform. The flat surface catalyst and silica nanotube reactors are resistant to fragmentation whereas porous silica particle-supported catalyst with small pore diameters (~15 nm) undergo particle fragmentation in the early stage of polymerization [69, 79].

5.3. Experimental

5.3.1. Materials

For the catalytic polymerization of styrene to syndiotactic polystyrene (sPS), styrene (Aldrich) monomer was vacuum distilled over calcium hydride, and activated alumina was used to remove inhibitors from the monomer. *N*-heptane (Fisher Scientific) was used as a diluent, and it was purified by being refluxed over sodium and benzophenone in nitrogen atmosphere. Trimethoxy (pentamethylcyclopentadienyl) titanium(IV) ($Cp^*Ti(OCH_3)_3$, Strem Chemicals, min 97%) and methylaluminoxane solution (MAO, Aldrich, 10 wt.% in toluene) were used as catalyst and co-catalyst, respectively without further purification. Silicon wafer (University Wafer, P-type (100)), silica-coated anodized aluminum oxide films (SNTR200: Silica Nanotube Reactor, Anodisc 47, 200 nm pore diameter, Whatman; SNTR60: 60 nm pore diameter, prepared in the laboratory (Prof. Sang Bok Lee)), and silica particles (Davisil, Grade 643) were used as catalyst support materials.

5.3.2. Preparation of supported catalysts

5.3.2.1. Preparation of Flat-Surface Catalyst

The metallocene catalyst was supported on a flat surface using the following procedure. First, a silicon wafer was calcined at 250^{o}C for 24 hr and then it was treated for 30 min in a solution of 30 vol.% of hydrogen peroxide (Fisher, 30%) and 70 vol.% of sulfuric acid (Fisher, +95%) to form hydroxyl groups on the surface, and it was washed with excess amount of deionized water. The acid-treated wafer was immersed in an MAO/toluene solution for 24 hr, washed with toluene three times, and dried. The wafer was then immersed in a $Cp^*Ti(OCH_3)_3$

solution for another 24 hr, washed with toluene, and finally dried in vacuo overnight. It was used as a flat-surface catalyst. The same procedure was used to support the catalyst onto silica particles.

5.3.2.2. Preparation of Silica Nano Tube Reactor

Two different diameters of anodized aluminum oxide (AAO) films were used as a template to prepare silica nanotube reactor. The AAO film with 200 nm pore was purchased from Whatman Co., and 60 nm pore was electrochemically fabricated at Prof. Sang Bok Lee's group. Two-step anodization process was applied. The first step was processed in 0.4 M oxalic acid solution with constant voltage of 40 V at 15 ^{o}C. Then it was chemically etched in acid solution (mixture of phosphoric acid ~ 6 wt.% and chromic acid ~ 1.5 wt.%) for high ordering of alumina pores. The second anodization step was conducted under the same conditions until the current flow in the reaction cell reached to zero. Table 5-1 shows the basic properties of commercial and homemade AAO films.

Table 5-1. Main features of AAO templates for SNTR-200 and SNTR-60

	Commercial (SNTR-200)	Homemade (SNTR-60)
Pore Diameter	200 nm	60 nm
Membrane Thickness	60 μm	5 μm
Pore Density	10^{9} pores/cm^{2}	2.1×10^{10} pores/cm^{2}
Pore Surface Area	3.77×10^{-7} cm^{2}/pore	9.42×10^{-9} cm^{2}/pore
Specific Surface Area	2.3 m^{2}/g	23 m^{2}/g
Pore Volume	1.88×10^{-12} cm^{3}	8.48×10^{-14} cm^{3}

For the preparation of catalytic silica nanotube reactors (SNTRs), AAO films with 200 nm and 60nm diameter pores (SNTR-200 and SNTR-60) were treated as follows [80]. The nano-pore surfaces of AAO films were coated with silica by surface sol-gel (SSG) method where an AAO film was first soaked in $SiCl_4$ (99.8%) solution [81-89]. They were then quickly immersed and washed with fresh hexane for 4 times to remove unabsorbed $SiCl_4$. The top surface of the AAO film was gently polished mechanically, and the AAO films were placed in a methanol/hexane (1:1 v/v) mixture, washed and dried with nitrogen gas. This procedure was repeated several times to obtain 3-7 nm thick layer of silica at the pore surfaces.

Figure 5-1 is transmission electron miscroscopic (TEM) image of SNTR-200 after removing AAO film. The EDX spectrum and line scan images of SNTR-200 are also presented. Figure 5-1 (c), and (d) is the EDX line scan spectrum of silicon and oxygen, respectively. The spectrum is the typical shape of tube. Figure 5-2(a) shows the scanning electron microscopic (SEM) image of an AAO film with 60 nm diameter pores of length 8μm and Figure 5-2(b) is the TEM image of the silica-coated nanotubes liberated from the AAO film after dissolving the alumina matrix. It is clearly seen that the inner surface of the pores are uniformly coated with silica.

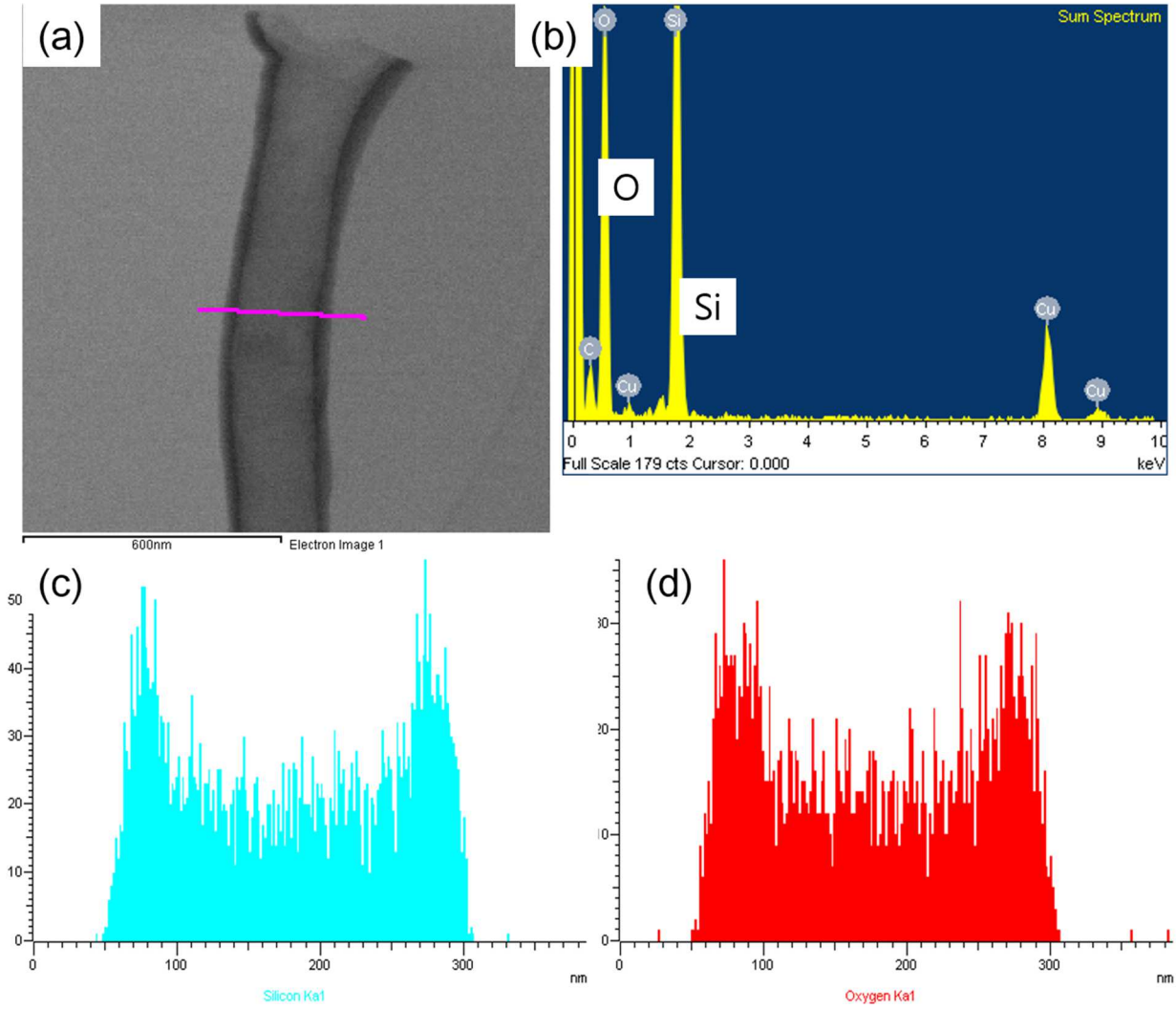

Figure 5-1. (a) TEM image of SNTR-200 after liberated from AAO film, (b) EDX spectrum, (c) EDX line scanning for silicon, (d) EDX line scanning for oxygen

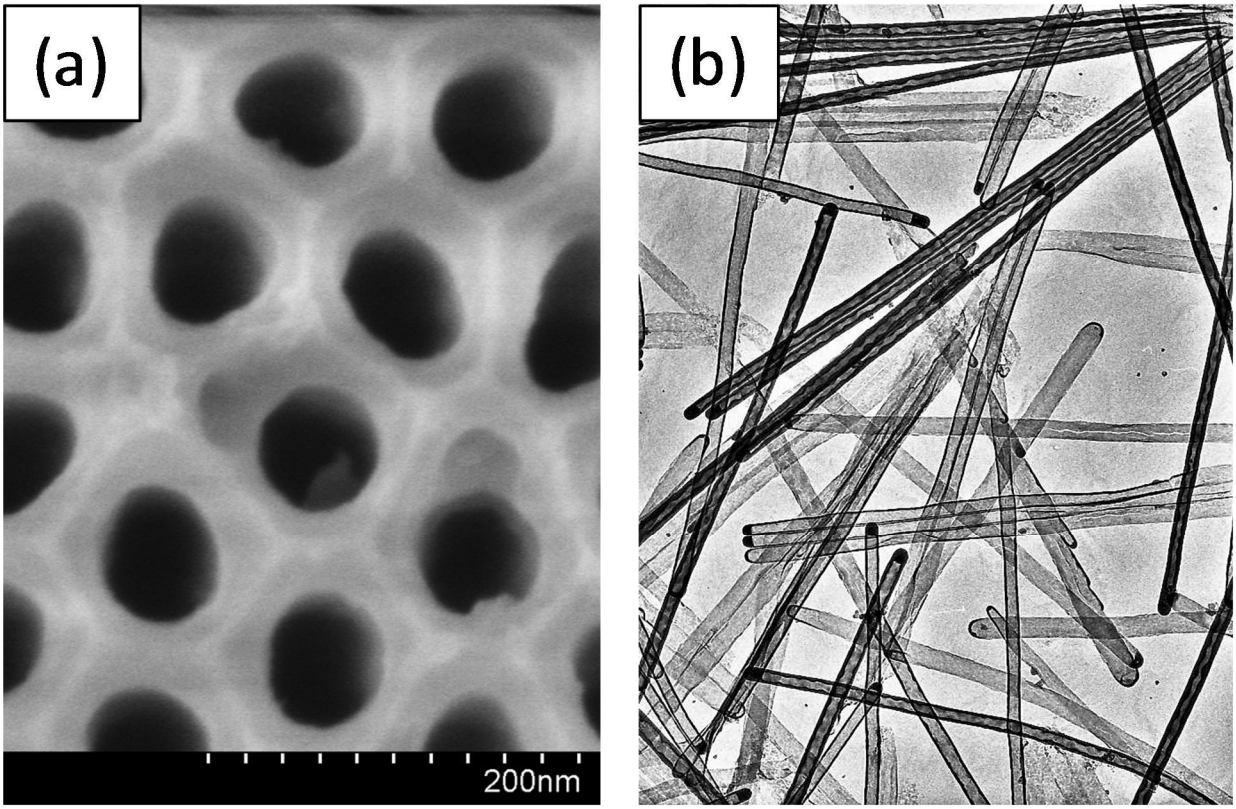

Figure 5-2. (a) AAO film (60 nm), (b) silica-coated nanotubes.

Before supporting metallocene catalyst onto the inner pore walls of an SNTR, the SNTR films were treated twice with MAO solution in toluene at ambient temperature for 24 h, washed with toluene, and dried in vacuo. To deposit the catalyst, MAO pretreated SNTR films were mixed with a catalyst solution in toluene at ambient temperature for 24 h, washed with toluene, and dried in vacuo. To remove the metallocene catalyst exposed to the bulk liquid phase, the top and bottom surfaces of the SNTR film were mechanically polished. This procedure ensures that the polymerization occurs only in the nanopores in the SNTRs. $Cp^*Ti(OCH_3)_3$ catalyst has been anchored onto the MAO-treated SNTRs and silica particles using the same procedure used for the flat surface catalyst. The titanium loading on each supported catalyst was measured by inductively coupled plasma optical emission spectrometry (ICP-OES(ACTIVA, JY HORIVA)). The specific surface area and pore size were measured using BET method (Micromeritics, ASAP 2020) at 78 K (or at the liquid nitrogen temperature) using nitrogen as an adsorption gas. Before the measurement, the samples were degassed at 150 ^oC for 4 h to reach a final pressure of 10^{-4} torr. The properties of these three supported metallocene catalysts are shown in Table 5-2. For SNTRs, the top surface of the film was mechanically polished to remove the catalyst. And hence, the specific surface areas for the SNTRs in Table 5-2 represent the net pore surface areas where the catalyst is deposited.

Table 5-2. Properties of supported catalysts (a) assumed to be same as SNTR-200)

Catalyst System	[Ti] loading (mol-Ti/g-support)	Specific Surface Area (m^2/g)	[Ti] loading (mol-Ti/m^2)	Avg. pore Size (nm)
Flat Surface catalyst	1.10×10^{-7}	1.464×10^{-3}	7.53×10^{-5}	n/a
SNTR (200 nm)	5.01×10^{-5}	2.3	2.18×10^{-5}	200
SNTR (60 nm)	1.42×10^{-4}	6.53	[a)] 2.18×10^{-5}	60
Silica particles	4.33×10^{-4}	300	1.44×10^{-6}	15

The titanium loading on the silica particles (1.44×10^{-6} mol-Ti/m^2) used in this study is quite comparable to those reported in the literature for $Ti(OBu)_4/MAO/SiO_2$ catalyst ($1.76x10^{-6}$ mol/m^2)[79]. Table 5-2 indicates that titanium loading per surface area available for the catalyst deposition is largest for the flat-surface catalyst whereas the silica particles have the smallest surface loading of Ti. It is probably because the silica particle consists of very narrow pores distributed from 1 to 20 nm and small pores may restrict the access of MAO and catalyst. The pores of smaller than 10 nm in the silica particles used in this study (Davisil 643) account for about 20% of its total pore volume.

Although the characterization of dormant and active species in a heterogeneous metallocene catalyzed polymerization is very difficult, if not impossible, it is well known that high activity of metallocene catalysts are imparted by MAO that forms a complex with the catalyst. Thus, it is important to have a heterogeneous catalyst structure that allows for the resistance-free transport of MAO molecules from the fluid phase to the catalytic site in narrow pores of a support material. MAO has a three dimensional cage structure with four-coordinate aluminum centers bridged by three-coordinate oxygen atoms.[28] In general, MAO is present in oligomeric forms ($[AlOMe]_n$) of different size. The most stable structure in the temperature range between 198.15K and 598.15K is known to be MAO-12.[28] Figure 5-3(a) shows the structure of MAO-12 and Figure 5-3(b) is the MAO-12 structural image obtained using Accelrys® Materials Studio Visualizer. The top view of MAO-12 shown in Figure 5-3(c) indicates that the largest dimension of the MAO-12 oligomer is 0.96 nm. The molecular structure and dimension of the catalyst ($Cp^*Ti(OCH_3)_3$) is shown in Figure 5-3(d), (e), and (f). Figure 5-3(f) show that the catalyst dimension is about 0.82 nm. The structural dimension of the catalyst and MAO-12 suggests that the dimension of the catalyst-MAO complex will be large and also,

the fraction of pores in silica particles might not be large enough for the MAO oligomers to diffuse from the bulk liquid phase into small pores and complex with $Cp^*Ti(OCH_3)_3$ catalyst at the pore surface.

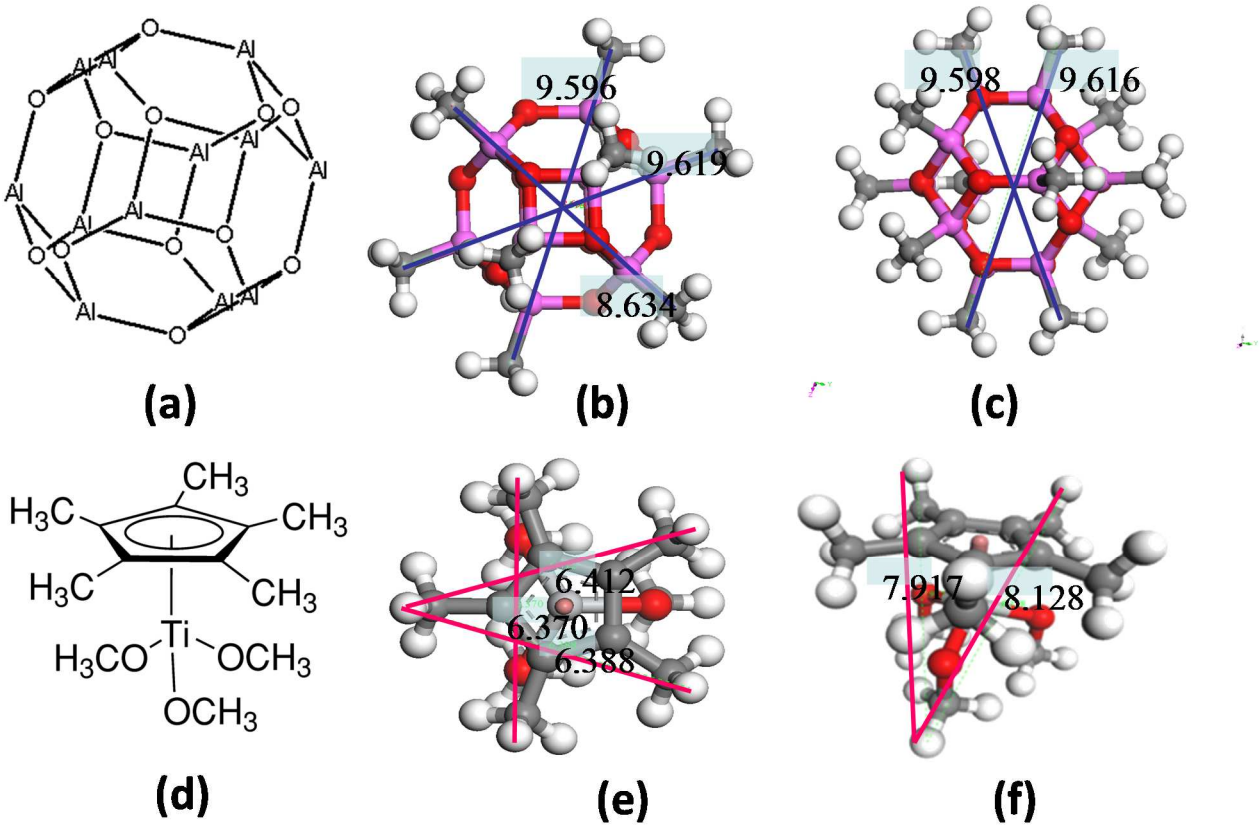

Figure 5-3. (a) MAO-12, (b) top view of MAO-12, (c) side view of MAO-12, (d) Cp*Ti(OCH3)3 catalyst, (e) top view of Cp*Ti(OCH3)3 catalyst, (f) side view of of Cp*Ti(OCH3)3 catalyst (units in Å).

When MAO is immobilized on a silica calcined at 250°C, the average pore diameter decreases by18-35%, indicating that the reduced pore size due to MAO deposition can obstruct the access of metallocene catalyst and additional MAO or alkyls that are needed to activate the supported catalyst [28]. If we assume that a monolayer of MAO-12 and $Cp^*Ti(OCH_3)_3$ complex is formed on silica surface and that the molecular dimensions of MAO-12 and catalyst shown in Figure 5-3 are used, the calculated pore diameter of silica decreases from 15 nm to about 11nm,

which is 27% decrease from the size of untreated silica pores. This approximate calculation result agrees well with the literature report of 18-35% reduction in pore size after MAO treatment [90]. Moreover, if we consider the possibility of a multilayer adsorption of MAO, it is expected that some silica pores can be blocked more than 27%, severely limiting the diffusional access of catalyst and cocatalyst components. All these effects are expected to contribute to low titanium loadings per surface area and reduced catalytic activity in porous silica. In particular, the reduced access of bulky MAO cocatalyst can have a significantly adverse effect on the catalyst activation. In other words, the large surface area of silica may not be fully utilized for catalyst support and not all the titanium sites may not be catalytically active for the subsequent polymerization.

It is also possible that more surface silanol groups are left unused in the small diameter pores of silica particles after MAO is grafted onto the pore surface. When silica is calcined at 250 ºC, the surface hydroxyl group concentration is about 2.4~3.2 mmol/g and the silica surface consists of mostly germinal and vicinal groups and some isolated silanol groups [90]. A relatively large concentration of silanol groups in the promixity can promote the formation of inactive catalytic sites.[72] It is also interesting to note that the titanium loading (mol-Ti/m^2) for three-dimensional silica particles is only 1.9 % of the titanium loading for a flat surface catalyst, suggesting that the efficiency of metallocene immobilization onto a silica support is quite low for the silica particles.

5.3.3. Polymerization of styrene

Polymerization of styrene to sPS with each supported catalyst was carried out using small glass reactors at 70℃. The reaction vessel was charged with desired amounts of purified

monomer and *n*-heptane, supported Cp*Ti(OCH_3)$_3$ catalyst, and MAO in an argon filled glove box. The MAO concentration in a liquid phase was kept constant at 5.0 wt.% (0.072 mol/L) in all the experiments with flat-surface catalyst and SNTRs. The MAO concentration was slightly higher for silica-supported catalysts (7.87 wt.% or 0.112 mol/L). The charged reaction vessel was immersed in a constant temperature bath and the polymerization was carried out at 70℃ for 15 ~ 240 minutes. After polymerization, the mixture was washed with an acidified methanol solution (10% hydrochloric acid) to remove MAO residue, then washed again with excess amount of methanol, and finally dried in vacuo. Figure 3 illustrates the schematics of the flat-supported catalyst, silica nanotube reactors, and conventional silica particle supported catalyst for syndiospecific styrene polymerization. The syndiotacticity of sPS measured by extraction with boiling methyl ethyl ketone (MEK) or ^{13}C NMR spectroscopy was 95-100 % for the tested catalysts. The sPS analysis data of syndiotacticity and molecular weight distribution with Cp*Ti(OCH_3)$_3$ /MAO catalyst system have been reported previously in detail elsewhere [73, 91, 92].

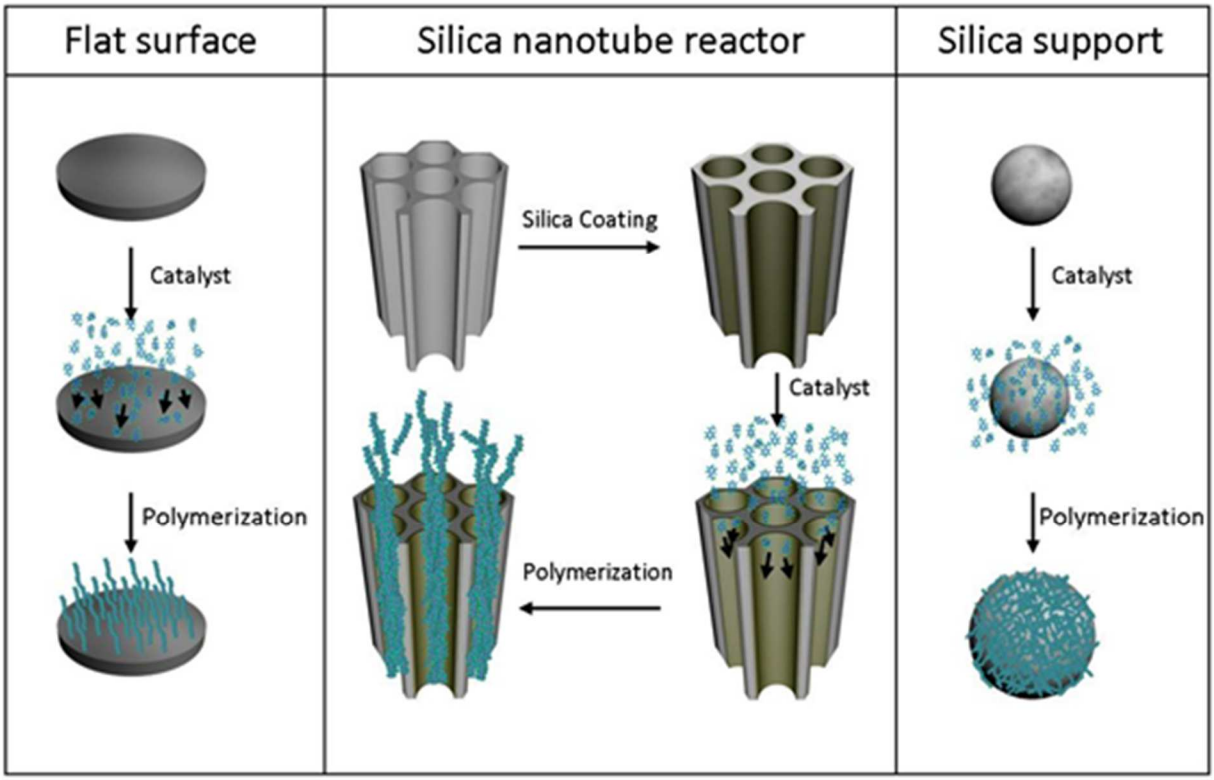

Figure 5-4 Polymerization of styrene over supported catalysts of three different geometries.

5.4. Results and Discussion

5.4.1. Catalyst Activity

For the three supported catalyst systems of different geometry used in this study, polymer yield (g-sPS/g-support) vs. reaction time data are shown in Figure 5-4. Each data point represents an independent polymerization experiment. Since the specific surface area (m^2/g) of a flat surface catalyst is the smallest of the three different support geometry, the polymer yield per gram of support is smallest for the flat-surface supported catalyst. It is observed that the polymer yield with small pore silica nanotube reactor (SNTR-60) is quite comparable to that of silica particle-supported catalyst (average pore diameter = 15 nm) up to about 40 min.

From the polymer yield data shown in Figure 4, the instantaneous polymerization rates in kg-polymer/mol-Ti·min were calculated using numerical differentiation technique and the results are shown in Figure 5. Notice that the catalyst activity is now the highest for the flat-surface catalyst and the lowest for the three-dimensional silica particle-supported catalyst. The activities of the silica nanotube reactors (SNTR-200 and SNTR-60) are quite similar and they lie between those for the two other catalyst geometries. The initial activity of the flat-surface catalyst is nearly 550 kg/mol-Ti·min (inset) is about 70 times larger than that of the silica particle-supported catalyst. The reduced activity of the flat surface catalyst after 60 min of reaction is still far higher than those for other supported catalysts. Figure 5-5 suggests that the more open structure of the catalyst support is, the higher the specific catalyst activity or polymerization rate becomes. In other words, the geometry of a catalyst support is an important factor that affects the catalytic activity for sPS polymerization.

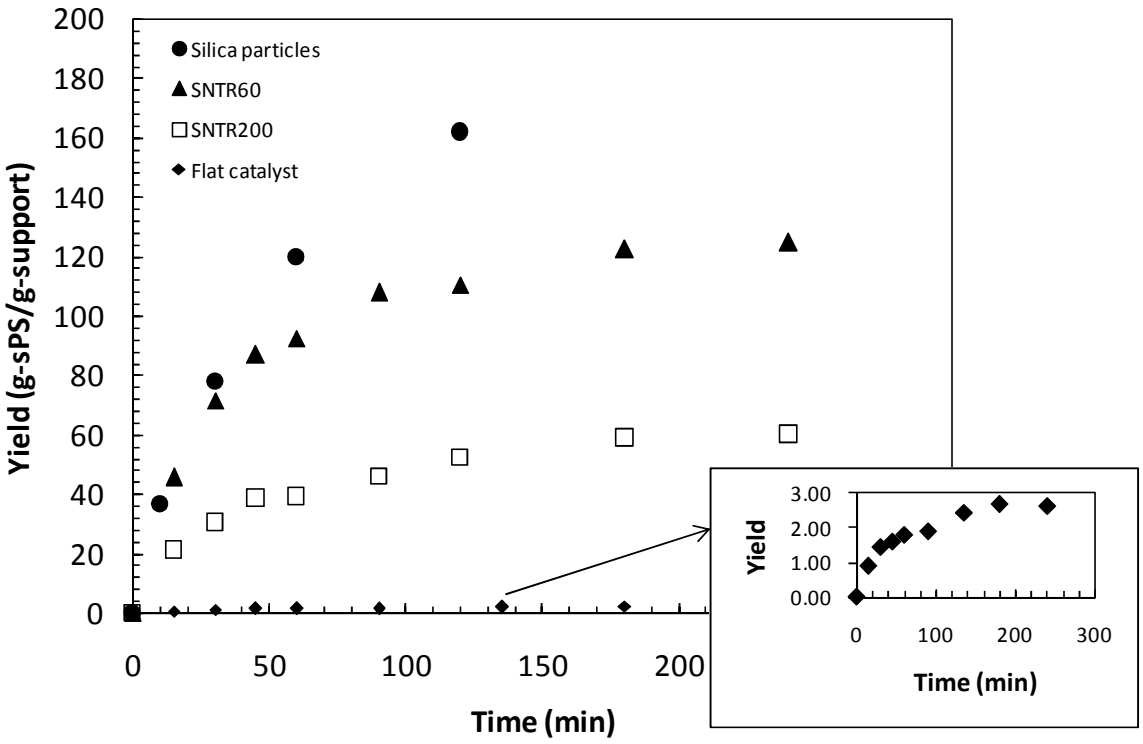

Figure 5-5. Polymer yield vs. reaction time with three different supported catalysts.

Figure 5-6 also shows that all these supported catalyst systems used in our study exhibit decay type kinetic profiles. Such kinetic profiles have been commonly observed in heterogeneous metallocene or Ziegler-Natta catalyzed polymerization of α-olefins and styrene. The exact mechanisms of gradual decline of catalytic activity in these systems is not completely understood but it is generally attributed to the catalyst deactivation caused by, for example, the loss of active sites by impurities, the interaction with support surfaces, spontaneous site deactivation, and the restrictions of the monomer access to the active sites via mass transfer limitations.

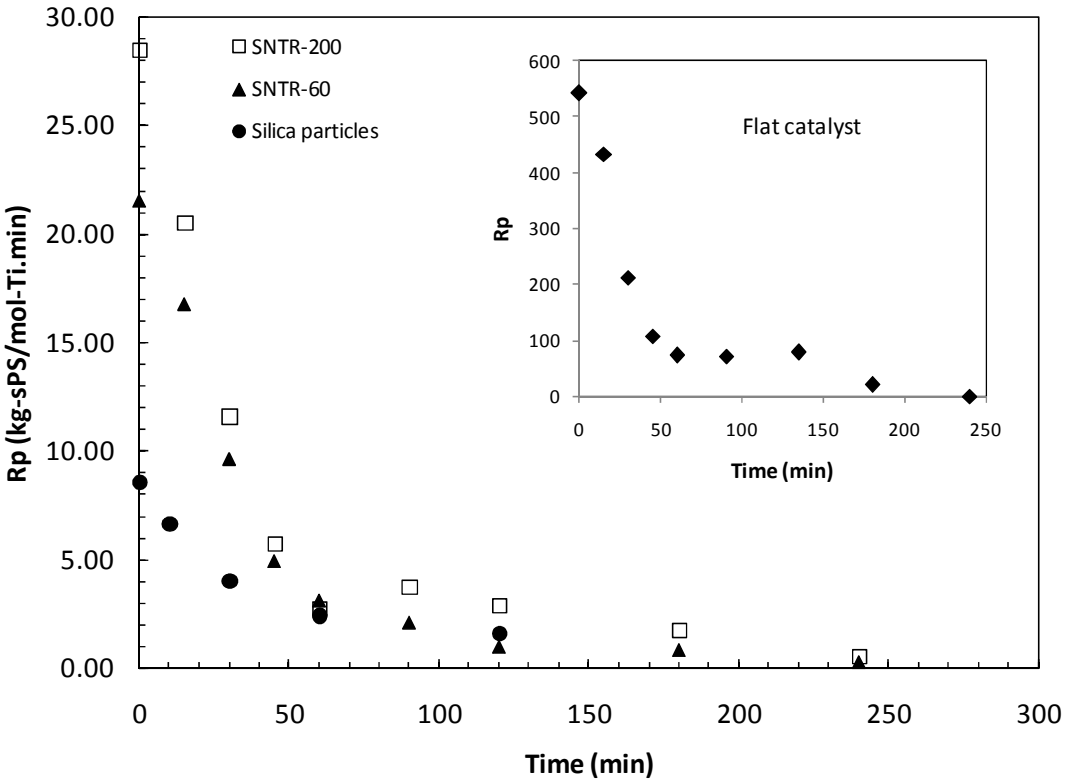

Figure 5-6. Catalyst activities for styrene polymerization for different supported catalysts.

In Figure 5-6, we also observe that the initial catalyst activities for the four supported catalyst systems show quite significant differences. In our experiments, the first data points in the yield measurements were taken at t = 15 min because it was very difficult to take the samples earlier than 15 min and secure sufficient amount of polymer sample for analysis. Table 5-3 summarizes the initial polymerization rate data.

Table 5-3. Initial catalyst activities

	$\tilde{R}_{p0}$ (g/gcat·min)	R_{p0} (g/mol-Ti·min)	$[M]_b$ (mol/L)	$\eta_0\psi_0 k_p$ (L/mol·min)	$(\eta_0\psi_0)/(\eta_0\psi_0)_{flat}$
Flat catalyst	0.0594	5.40×10^5	4.99	1.04×10^3	1.0
SNTR (200 nm)	1.423	2.84×10^4	4.99	54.70	0.053
SNTR (60 nm)	3.056	2.15×10^4	4.99	41.43	0.040
Silica particle	3.672	8.48×10^3	4.85	16.81	0.016

To understand the observed rate phenomena for the supported catalyst systems, let us consider the polymerization rate (g/gcat·min) that can be expressed as

Equation 5-1

$$\tilde{R}_p = k_p[M]_p f([Ti]) w_m$$

where k_p is the propagation rate constant (L/mol·min), $[M]_p$ is the monomer concentration (mol/L) at the catalytic site, w_m is the molecular weight of monomer (g/mol), $[Ti]$ is the active catalyst site concentration (mol-Ti/g-cat). The dependence of the polymerization rate on the catalyst site concentration is expressed as a functional form in Equation 5-1 because not every titanium site may not be catalytically active. The intrinsic catalyst activity represented by Equation 5-1 is affected by catalytic site deactivation and monomer diffusion resistance because of the heterogeneous nature of the polymerization.

To account for the monomer mass transfer resistance to active catalytic sites through a polymer, we introduce a parameter η as the effectiveness factor, i.e., $[M]_p = \eta[M]_b$ where $[M]_b$ is the bulk phase monomer concentration. It is expected that monomer diffusion effect is minimal for a flat-surface catalyst system whereas the silica-supported catalyst can have larger

pore diffusion resistance for styrene monomer because the pore diameter is very small, tortuous, interconnected, and buried deep inside a particle covered with polymer. For the flat-surface catalyst, all the active sites are likely to be fully exposed to monomer and we expect that the polymerization would takes place at almost every titanium site immobilized on the support surface. It is also expected that silica particles will undergo particle fragmentation during the polymerization [68, 69] whereas no such fragmentation is expected in SNTRs because the long cylindrical pores are fairly far separated by alumina matrix.

Since not all the titanium sites may be catalytically active for styrene polymerization and the activity may also change with time, we define a new catalyst activity parameter (ψ) that accounts for the catalytic efficiency of the initial titanium loading for polymerizaton. In other words, $\psi[Ti]_0$ represents the catalyst site efficiency based on the initial titanium concentration on the support surface. Both η and ψ are difficult to measure experimentally. Then, Equation 5-1 can be recast into the following form using these newly defined parameters:

Equation 5-2

$$\tilde{R}_p = k_p \left(\eta[M]_b\right)\left(\psi[Ti]_0\right) w_m$$

If we assume that the loss of catalyst activity (deactivation) occurs with time and that it can be modeled by the first-order decay kinetics, Equation 5-2 can be written as

Equation 5-3

$$\tilde{R}_p = k_p \left(\eta[M]_b\right)\left(\psi_0[Ti]_0 e^{-k_d t}\right) w_m$$

where k_d is the deactivation rate constant and ψ_0 is the initial catalyst activity parameter.

Here, the polymerization rate can also be conveniently expressed in g/mol-Ti·min (i.e., $R_p = \tilde{R}_p / [Ti]_0$). Then, from Equation 5-3, the initial polymerization rate in g/mol-Ti·min can be expressed as

Equation 5-4

$$R_{p0} \equiv \frac{\tilde{R}_{p0}}{[Ti]_0} = \eta_0 \psi_0 k_p [M]_b w_m$$

where η_0 is the initial effectiveness factor. For the experimental conditions used in this study, the monomer concentration remains nearly constant because the total polymer yield was very low (i.e., $[M]_b \approx$ constant). If we normalize the polymerization rate (g/mol-Ti·min) with initial polymerization rate, we obtain the following equation:

Equation 5-5

$$\frac{R_p}{R_{p0}} = \frac{\eta}{\eta_0} \exp(-k_d t)$$

In Figure 5-6, we observe that catalyst activities decline rapidly to very low values after about 60 min. In this experiments, the accuracy of measurements of polymerization rates was much higher during the early period of polymerization (e.g., 0 < t < 60 min) where polymer yield change with reaction time was quite large (Recall that the catalyst activity was determined by numerically differentiating the polymer yield data with respect to time.). Therefore, to test the validity of Equation 5-5, we used the rate data for the first 60 min of reaction. Figure 5-7 shows a plot of $-\ln\left(R_p / R_{p0}\right)$ vs. reaction time (t) (Equation 5-5) for all the catalysts used in our study. It is quite interesting that the entire rate data for four different supported catalysts are well fitted by a single straight line, suggesting that the first-order deactivation model is justifiable. The deactivation parameter (k_d) estimated from the slope of the straight line in Figure 5-7 is 0.033

min^{-1} and the corresponding catalyst half-life is about 20 min. Also, we find that the value of η / η_0 is 1.09, indicating that the effectiveness factor is practically constant during the course of polymerization.

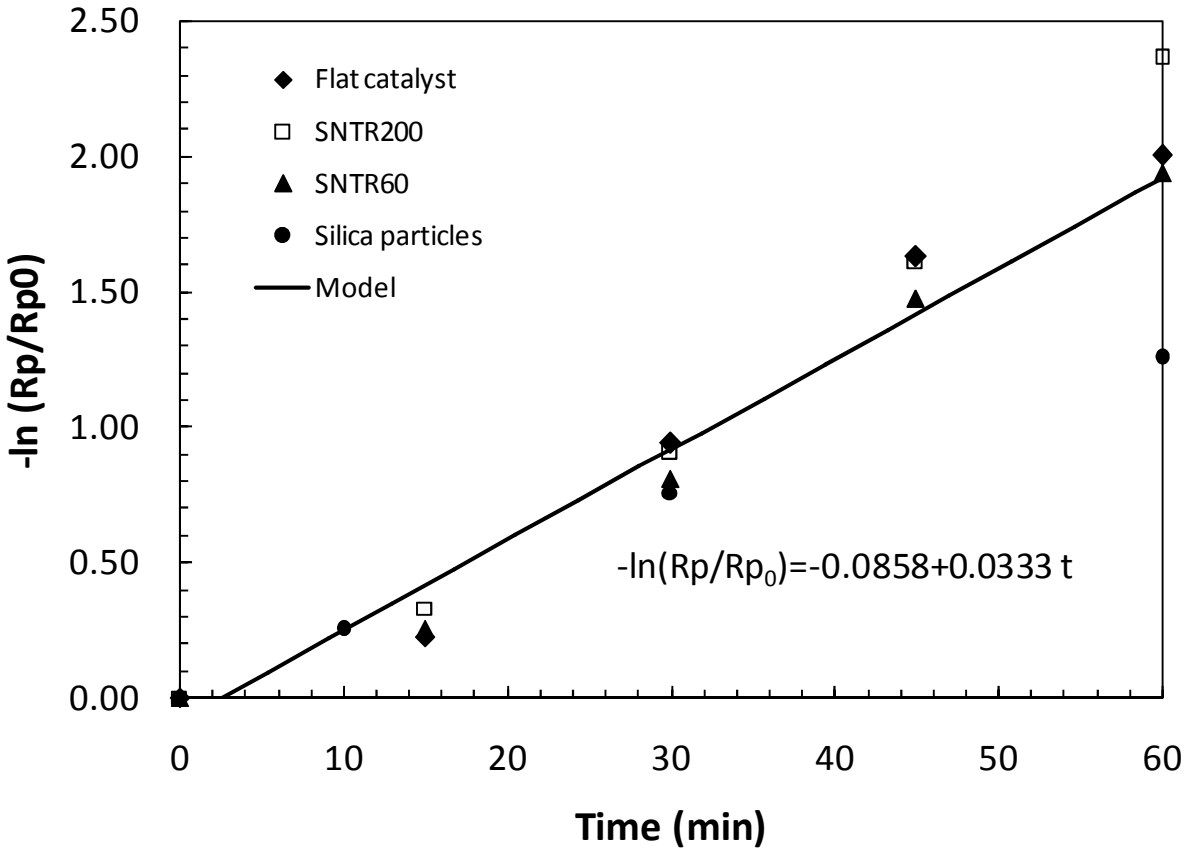

Figure 5-7. Test of first order catalyst deactivation model.

At this point, let us go to Table 5-3 again to further analyze the experimentally observed initial polymerization rate data for different types of supported catalysts. The last column in Table 5-3 shows the ratio of the catalyst efficiency parameters for the SNTRs and silica-supported catalyst with respect to that of flat-surface catalyst. This simple analysis indicates that the catalyst efficiency factors for SNTRs and silica particles are only about 1.6~5.3% of the flat surface catalyst. Since $\eta / \eta_0 \approx 1.0$, we can say that $\psi / \psi_0 = 0.016 \sim 0.053$ for the SNTRs and silica particles. In other words, if we assume that extent of monomer diffusion resistance in each supported catalyst is similar, then this ratio can be approximated as the ratio of the fraction of active sites effective for the polymerization. The geometrically constrained pores in SNTRs and silica particles have substantially low usage of titanium catalyst deposited onto the pore surfaces. It is possible that surface properties and the geometrical constraints in the SNTRs and silica particles might have influenced the formation of active titanium catalyst sites. As mentioned earlier, the diffusion of MAO into the pores during the catalyst preparation (for anchoring the catalyst) and during the polymerization (as cocatalyst) might have been very ineffective, resulting in the low usage of metallocene catalyst. When a silica-supported chromium oxide catalyst (Phillips-type catalyst) is used for ethylene polymerization, typically less than 10% of the chromium atoms are believed to be active [77]. This results suggest that the use of flat surface catalysts offers a new technique to measure the intrinsic kinetics of catalytic polymerization and to help design better support materials.

5.4.2. Polymer morphology

sPS is known to grow in nanofibrillar morphology with silica-supported metallocene catalysts [69, 73]. Figure 5-8. SEM images of sPS nanofibrils: a1-a2, flat surface catalyst; b1-b2, SNTR 200 and SNTR60; c1-c2, porous silica particle catalyst. shows the SEM images of sPS growing from three different supported catalysts. All these SEM photos show that indeed sPS grows as nanofibrils regardless of the support type. For the flatsurface catalyst, sPS nanofibrils of about 30 nm-diameter grow in a direction normal to the catalytic surface.

Figure 5-8(a1) shows the top view of the sPS nanofibrils grown on the flat surface catalyst. In the SNTRs, the sPS extruded out from nano pores. Parts b1 and b2 of Figure 5-8 show that the top surface of SNTRs is covered with 30-50 nm sPS nanofibrils extruded out from the pores. Similar sPS nanofibrils are also seen in the polymer particles from silica-supported catalysts (Figure 5-8, parts c1 and c2). Polymerization of olefins with silica-supported metallocene catalyst are well-known to exhibit a gradual fragmentation of catalyst/polymer particles and particle shape-replication phenomena. The fragmentation of a silica-supported catalyst particle starts in the surface region which is quickly covered with polymer layer, causing a diffusion barrier for monomer. As monomers diffuse and polymerize inside the particle, the silica core gradually disintegrates and expose catalytic sites [29, 44]. Similar catalyst fragmentation and shape replication phenomena occur in sPS polymerization with $Cp^*Ti(OCH_3)_3$/MAO/silica catalyst [69]. Figure 5-8(c1) shows a residue of a relatively large unfragmented silica particle of about 5 μm size embedded in the matrix of sPS nanofibrils. It is likely that titanium sites buried in this incompletely fragmented silica particle were not accessible by monomer and hence not used for polymerization. The stress fibrils are also visible in Figure 5-8(c1), clearly indicating that they were formed by the disintegration of silica particles

during the polymerization. Figure 5-9 is the TEM image of sPS, which confirms and shows the crystalline nanofibrils that has a diameter about 30~40nm.

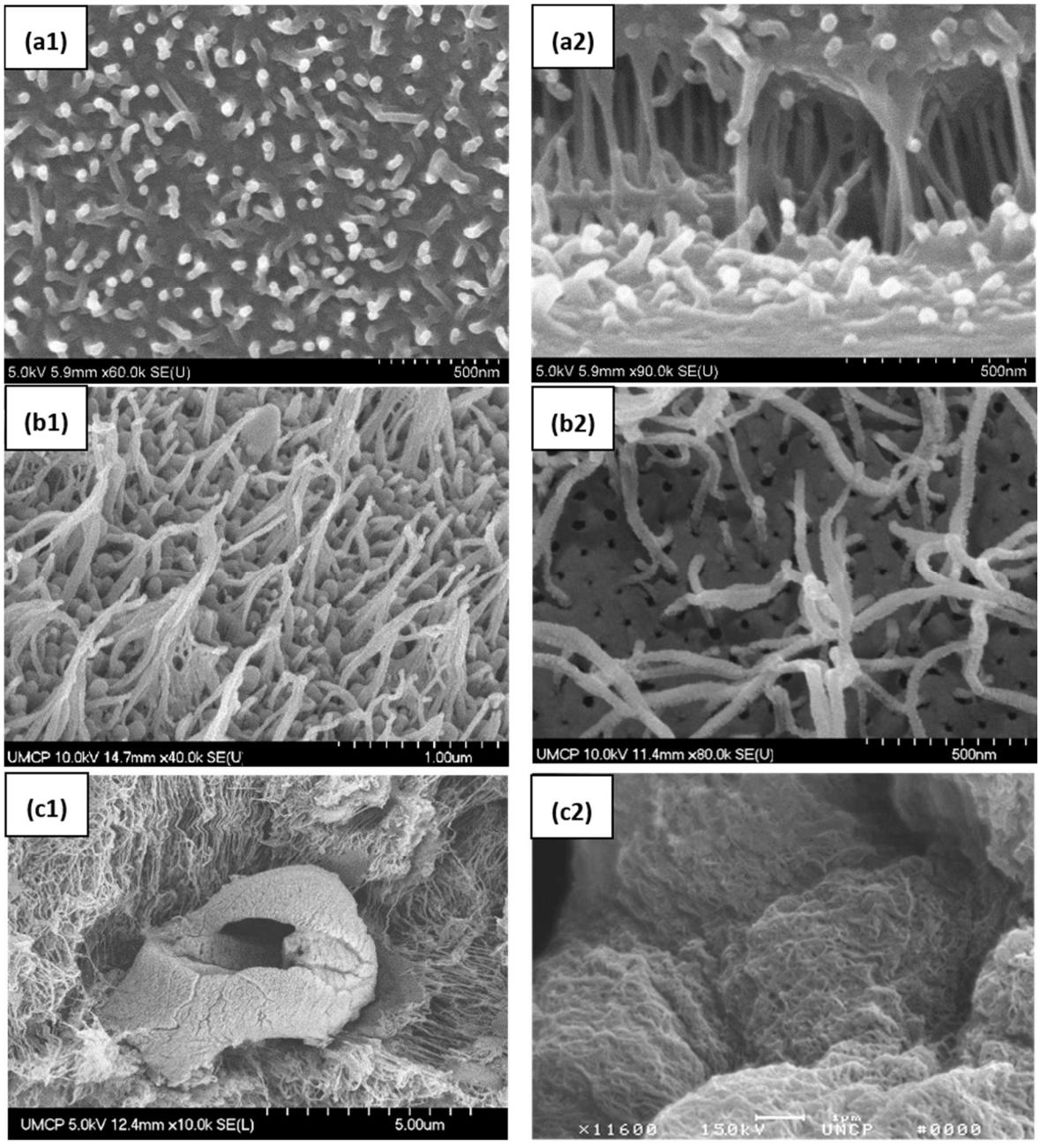

Figure 5-8. SEM images of sPS nanofibrils: a1-a2, flat surface catalyst; b1-b2, SNTR 200 and SNTR60; c1-c2, porous silica particle catalyst.

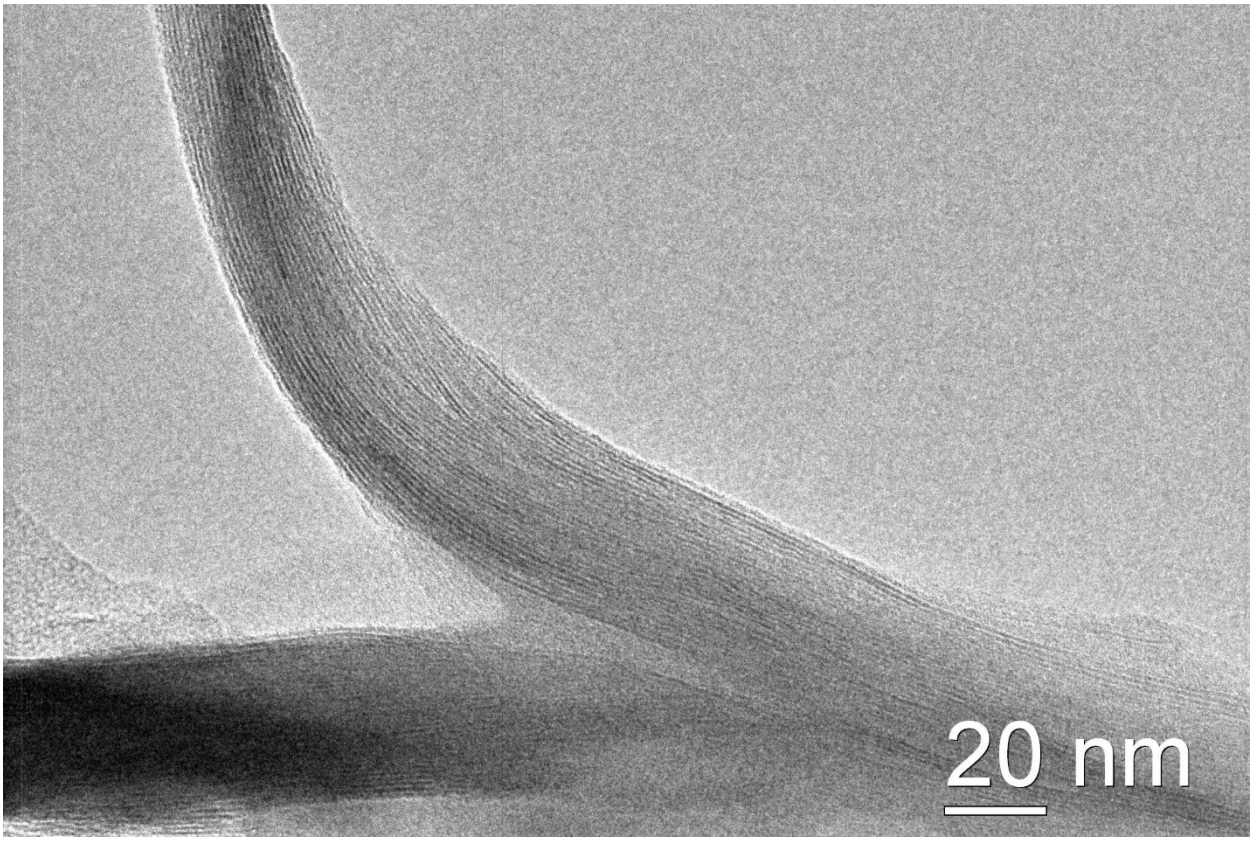

Figure 5-9. TEM images of sPS nanofibrils: crystalline fibrils diameter 30~40nm.

5.5. Conclusions

The kinetics of catalytic polymerization of styrene to syndiotactic polystyrene has been investigated using flat wafer, anodized alumina film, and porous silica gel particle as support materials for $Cp^*Ti(OCH_3)_3$/MAO catalyst. The same catalyst supporting technique was used for the comparison of resulting catalytic performances. The catalyst loading per support surface area and the corresponding catalyst activity are strongly influenced by the geometries of support materials. The flat-surface catalyst has been found to have the largest titanium loading per area and the highest catalyst activity per mole of titanium. A kinetic model analysis indicates that the active titanium sites for the SNTRs and silica particles is less than 10% of those for the flat-surface catalyst. It implies that the pore dimensions and support characteristics have a significant impact on the catalyst performce for sPS polymerization. The deactivation kinetics for these supported catalyst systems were well fitted by the decay type kinetic model. All these supported catalysts yield sPS as nanofibrils of about 30~40 nm-diameter. Finally, similar support effects are expected in α-olefin polymerization and our forthcoming paper will report the experimental results.

Chapter 6. Application of Nanosilica-Supported Metallocene Catalyst to Ethylene Polymerization in Micro/Milli Reactors: Preliminary Feasibility Study

6.1. Introduction

In Chapter 2, a detailed kinetic study of ethylene polymerization over solid nanosilica-supported metallocene catalyst has been presented. It was shown that polymer grew as nanofibrils of about 30-50 nm-diameter at the nanosilica particle surfaces. Inspired by the experimental results in Chapter 2, we investigated the feasibility of applying the nanosilica-supported metallocene catalyst to micro- or milli-reactors for heterogeneous ethylene polymerization. In this chapter, we shall present the experimental system developed and some preliminary results to illustrate the feasibility and potential of the micro/milli reactors as a new tubular reactor system that can be used to design molecular structure of ethylene polymers.

Micro or milli reactors have been of interest to both academic and industrial researchers because their excellent heat transfer efficiencies and plug-flow reactor profiles are very attractive in handling highly exothermic and fast reactions. There are some literature on the use of micro/milli reactors for polymerization [93-97] but very few literature is available on the use of such reactors in olefin polymerization.

Micro/milli reactors offer some unique merits over conventional stirred tank type reactors as follows:

(A) A plug flow fluid profile can be easily established in micro-milli reactors and hence, the micro/milli reactors can be regarded as an extension of batch reactors to a continuous mode;

(B) Many of olefin polymerization catalysts exhibit rapid catalyst deactivation. If a micro/milli reactor is used, the initial high catalyst activity during the short reaction time can be utilized to maximize the polymer yield

(C) Due to the high surface area/volume ratio of the micro-reactor, the heat transfer efficiency is excellent and heat removal problems can be minimized;

(D) An isothermal reaction condition can be well established along the reactor length or even the tube reactor temperature profile can be designed without much difficulty;

(E) The tubular reactor nature of the micro/milli reactor can be advantageous in changing the reaction conditions along the reactor. For example, comonomers or catalyst or any additives (e.g., hydrogen) can be injected along the reactor tubes to modify the molecular architecture of the polymers.

6.1.1. Technical challenges of micro/milli polymerization reactors

To use a micro/milli reactor for ethylene polymerization with a heterogeneous catalyst, some technical challenges should be resolved:

(A) Establishment of stable flow profiles: In conventional polyolefin processes, 30-50 μm size micro silica-supported catalysts are used. They grow to several hundred micron size polymer particles. In a micro/milli reactor of very small diameter, it is thus necessary to use much smaller catalyst particles and to ensure the flow stability without clogging of the tube by growing polymer particles;

(B) Mass transfer: Effective injection of diluents, catalyst, monomer, comonomer, and hydrogen is also a critical technical issue in designing and operating a micro/milli polymerization reactor. If ethylene is supplied to the reactor as a gas, it can be dissolved into the

liquid diluents phase or it can be forced to flow as gas bubbles in the reactor. If ethylene gas bubbles are present in the reactor, the mass transfer from the gas bubble to the liquid phase may become a rate controlling process;

(C) Heat transfer: With a single micro-reactor tube, it will not be very difficult to remove excess heat or to maintain a desired reaction temperature. However, in an industrial or manufacturing setting, tens or hundreds of shell-and-tube type micro-reactor tubes will be packaged into a reactor system and efficiently removing excess heat will be a very important issue;

In this study, we shall examine some of these problems through experimentation.

6.1.2. Literature Review – polymerization in micro reactors

There is a large pool of literature on micro reactors but there is a lack of literature on the micro/milli reactors for olefin polymerization. Miller et. al. [98] (Dow Chemical Co.) constructed a millireactor system using HPLC grade stainless steel tubes (1.59mm O.D. × 1.27mm I.D.). They polymerized ethylene using a homogeneous catalyst in a solution polymerization process. Figure 6-1 is a flow diagram showing their high temperature micro polyethylene reaction process. In this set-up, HPLC grade stainless steel with an outer diameter of 1.59mm is used.

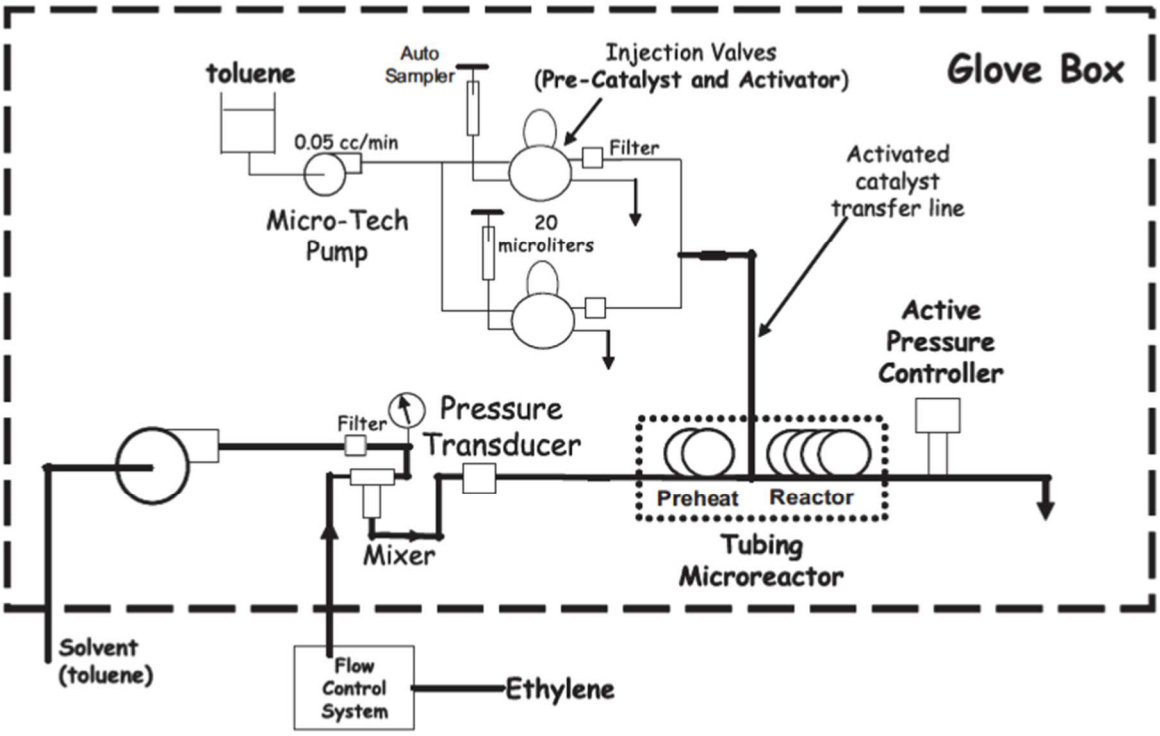

Figure 6-1. Reactor components and flow schematic diagram for tubing microreactor [99].

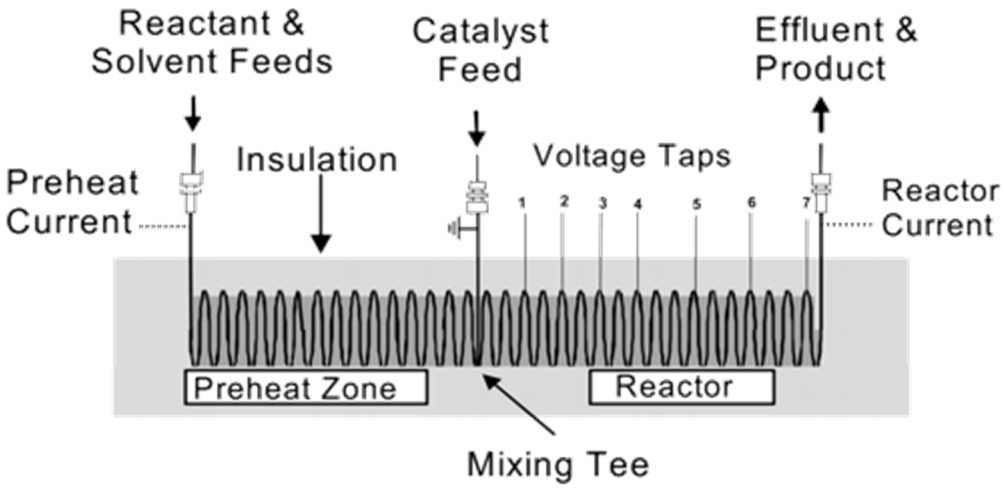

Figure 6-2. construction details for non-isothermal tubing microreactor [99].

The tubular reaction section is split up into 2 sections (Figure 6-2), the preheat zone and the reactor zone, and after the reactant/solvent mixture is brought up to the reaction temperature, the catalyst solution is injected into the main reaction zone and the reaction proceeds quickly.

The catalysts used in this system are Dow's CGC-cyclopentadienyl and CGC-indenyl catalysts. Figure 6-3 shows how the reaction temperature changes with time in each reactor zone.

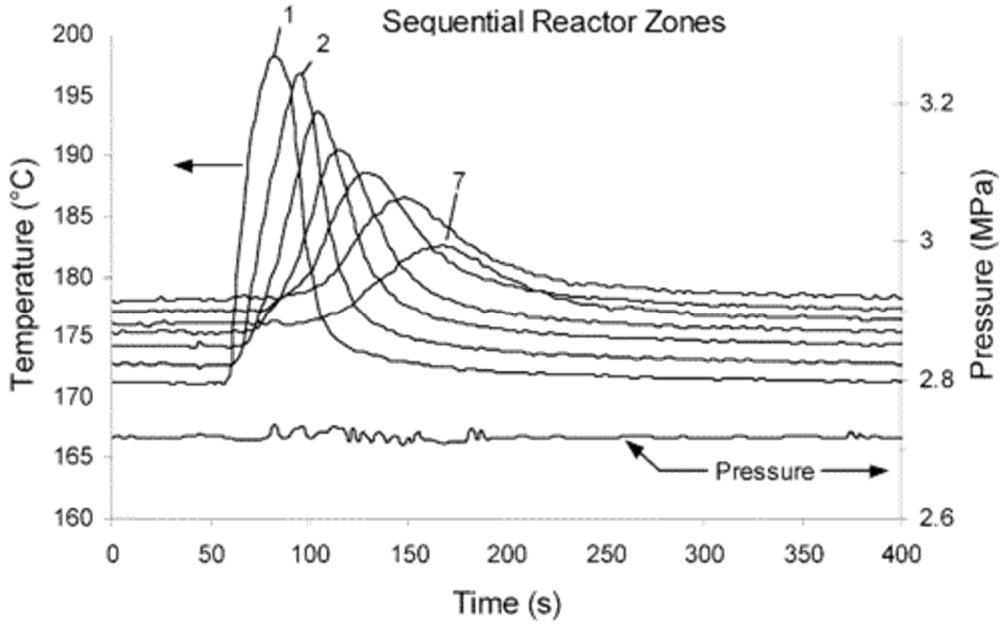

Figure 6-3. example of nonisothermal reaction temperature profile at different zones [98].

Figure 6-3 shows that the high temperature solution polymerization process exhibits significant nonisothermal temperature profiles in the microreactor. However, the important point here is that, unlike CSTRs, microreactors are capable of dealing with these types of temperature excursions. The ethylene polymerization study using a milli-reactor and homogeneous (soluble) catalysts illustrates that micro or milli-reactors offer some unique advantages. However, the use of homogeneous catalysts limit the utility of the micro/milli reactors because not many catalysts can endure high reaction temperatures without losing catalyst activity.

6.2. Experimental

6.2.1. Micro/Milli Reactor System

In this work, we investigated the feasibility of using a micro/milli reactor for heterogeneous polymerization of ethylene. The EBI catalyst used in our earlier work was chosen as a base catalyst system and silica nanoparticles of less than one micrometer were used as a catalyst support.

Figure 6-4 shows the schematic diagram of the initial micro-reactor experimental setup. Ethylene from the gas cylinder is supplied through the flow controller to the reactor, and the catalyst and solvent are added to the reactor using a syringe pump. As the catalyst (EBI) is very sensitive to air, the catalyst and solvent were loaded into the syringe in a glove box. The reactor system was designed so that the end of the needle on the syringe would be inserted into a tube filled with argon gas so that the catalyst would not be exposed to air. The ethylene gas and the catalyst/solvent from the syringe pump meet at a T-junction and then the mixture flows into the micro-channel reactor. The reactor temperature was fixed at 70°C. After the reaction, acidic methanol (10/90 vol %) was added to the flask where the polymer is collected in order to remove the residual MAO. The results from this initial experiment showed that the ethylene gas and the solvent in the micro-channel were not well mixed, resulting in a low ethylene concentration in the solvent which ultimately lead to a minute amount of polymer being produced. The reaction conditions could have been altered so that more polymer was produced, but any changes to the reaction conditions would not solve the fundamental problem of the inefficient mixing of the ethylene gas and solvent.

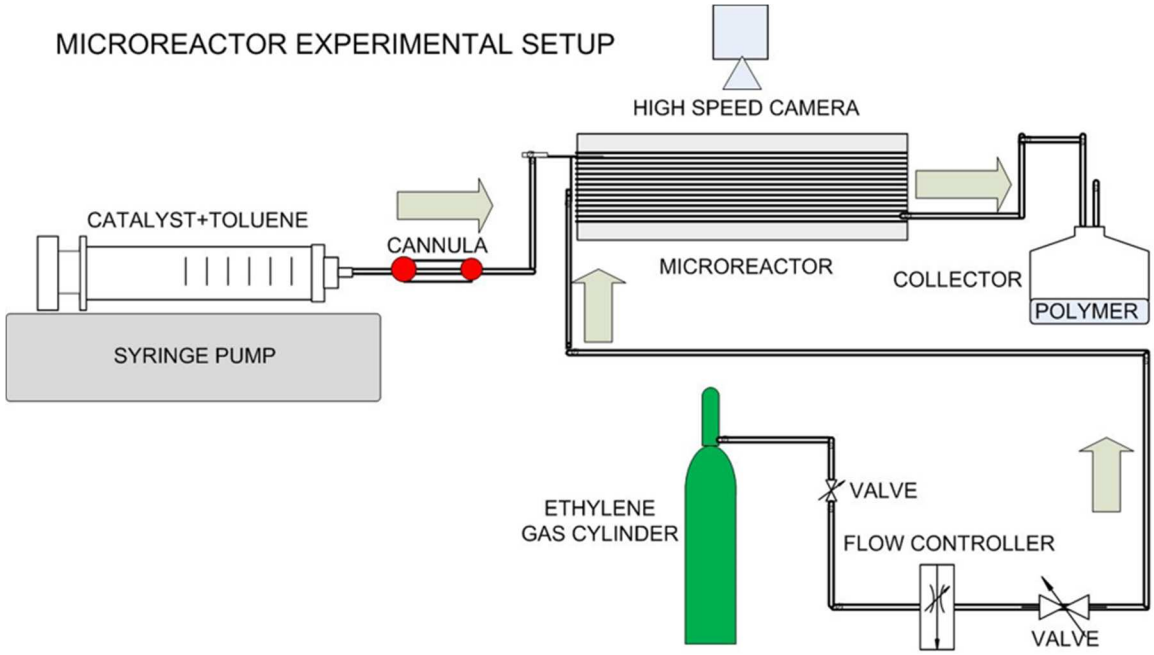

Figure 6-4. Schematic diagram of the initial micro/milli reactor

Figure 6-5 shows the changes made to the initial micro-channel reactor system. An absorbing section was added in between the ethylene cylinder and the micro-channel so that the ethylene gas could be dissolved in the solvent prior to the micro-channel.

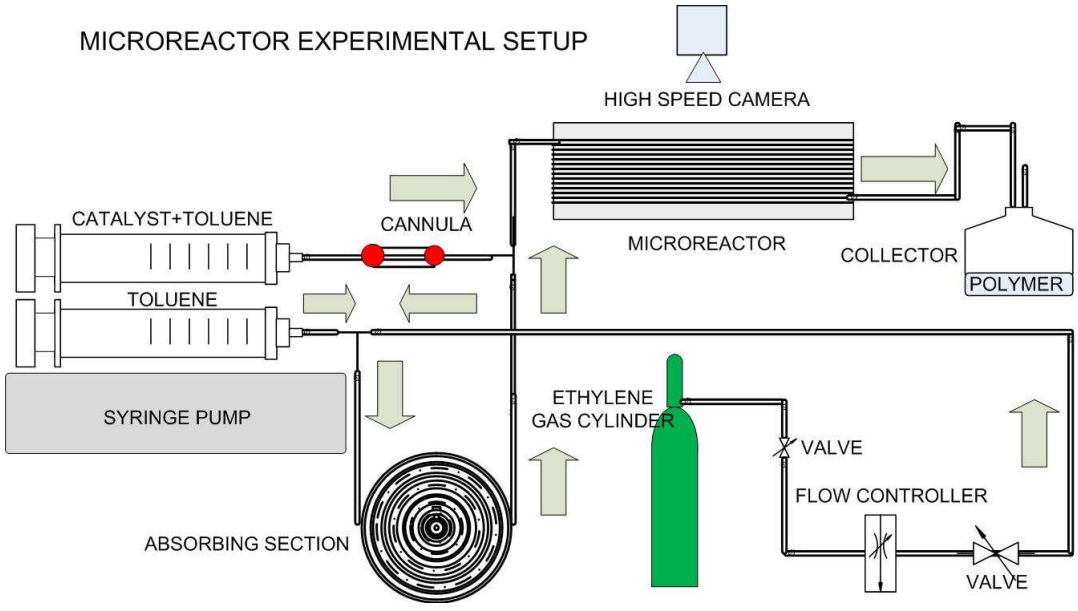

Figure 6-5. Modification of initial reactor set up; ethylene gas / toluene mixing zone was added.

6.2.1.1. Ethylene Polymerization in Microreactor

Ethylene polymerization was performed with the modified reactor illustrated in Figure 6-5 to check the feasibility of its use as a polymerization reactor. The reaction test conditions were:

- Temperature: 70ºC
- Pressure: 25 psig
- Catalyst / MAO / toluene flow rate: 0.1 ml/min
- Toluene flow rate: 0.1 ml/min
- Ethylene flow rate: 2.8 ml/min
- Length of reactor : 2.2 m
- Reactor material: Teflon tube
- Diameter of reactor : 630 μm

The first test of the reactor system shown in Figure 6-5 was only a partial success because although we were able to obtain polymer particles some clogging occurred and the particle morphology was not very well controlled. Figure 6-6 shows the SEM images of synthesized PE in the microreactor, and Figure 6-7 is the picture of the clogged PE in microchannel.

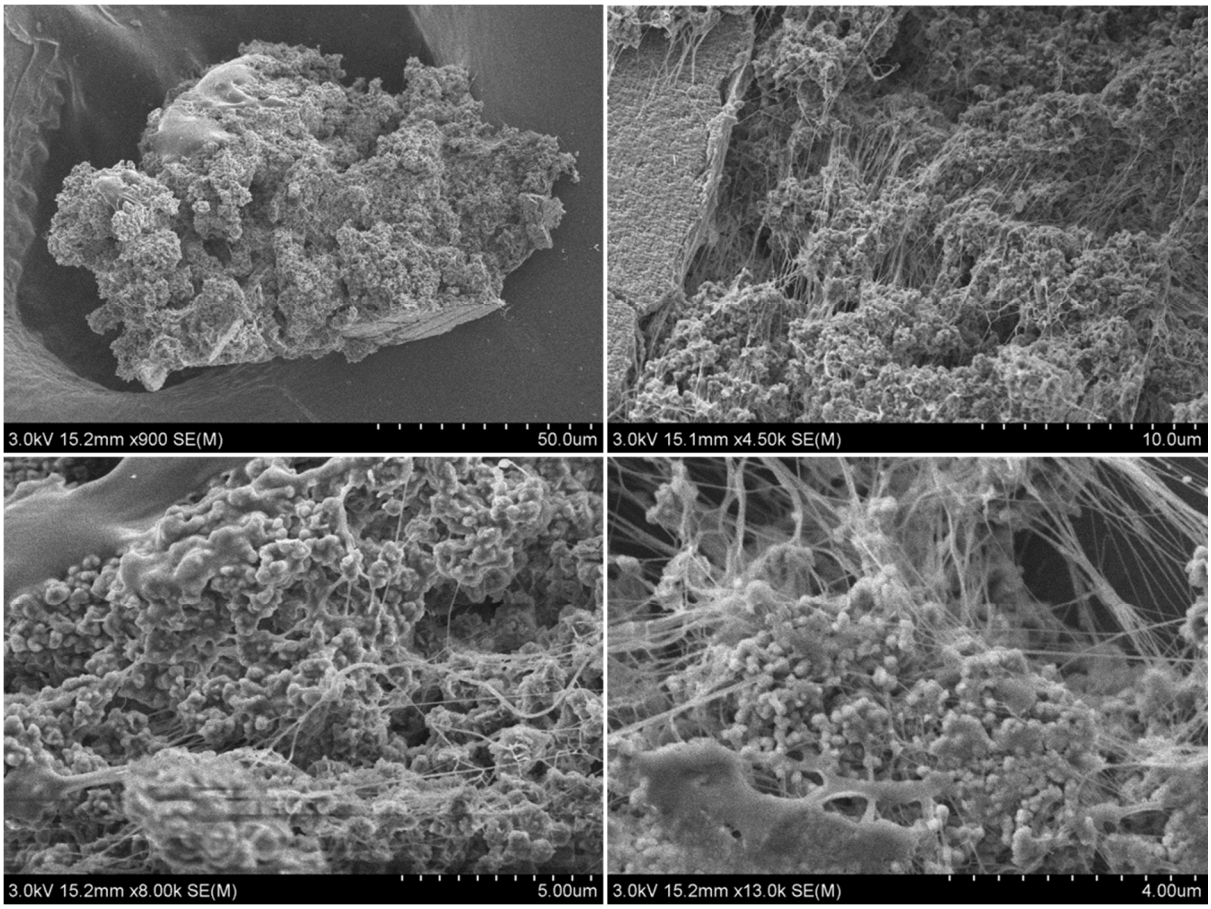

Figure 6-6. Polyethylene synthesized in microreactor with NanoSiO_2/EBI support catalyst.

Figure 6-7. Polyethylene residue that clogged in the micro channel.

6.2.2. Micro/Milli reactor design for comonomer sequential injection

One of the advantages of microreactors is that several comonomers can be injected at any point along the reactor. Thus, the micro/milli reactor was modified to accommodate the side injection of comonomer. Figure 6-8 depicts the schematic diagram of a system of this type. One more comonomer can be added if an additional reactor unit is added

A 3 mm PTFE tube was adopted as the reactor channel. In the feeding tank, ethylene is dissolved in the solvent (toluene). Then, the toluene/ethylene mixture is fed into the reactor using the ethylene pressure as the driving force. A back pressure line was installed between the feeding tank and the collector so that the pressure in the micro-channel is maintained. Otherwise, with a pressure drop, the dissolved ethylene would form ethylene bubbles in the micro-channel. The catalyst solution was prepared and loaded into a syringe and a syringe pump was used to inject the catalyst into the reactor.

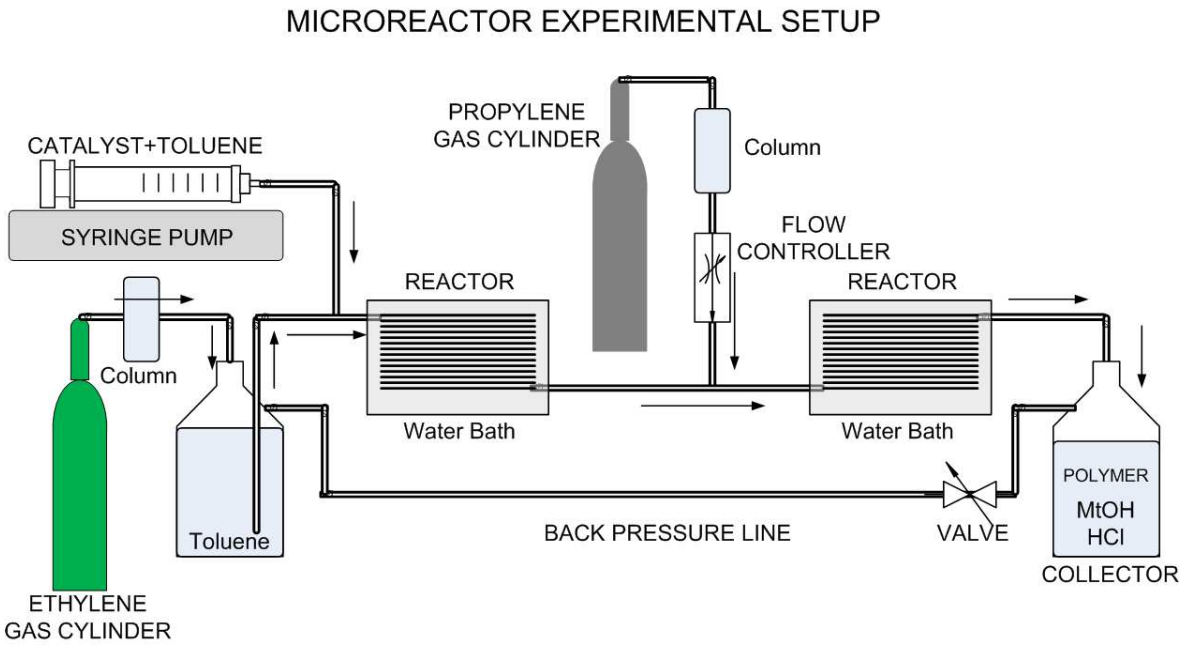

Figure 6-8. Schematic diagram of a modified micro reactor for comonomer sequential injection.

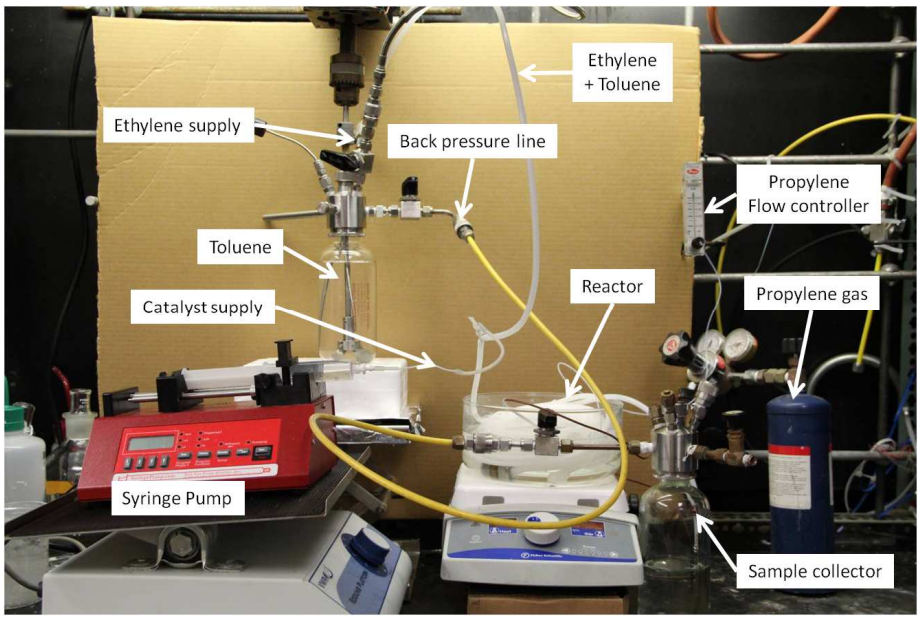

Figure 6-9. Picture for comonomer sequential injection system.

To use the side injection system, we need to know the right injection point that will allow for the onset of copolymerization to change the copolymer molecular architecture (e.g., bimodal polymers of different density, MWD, composition, etc.).

6.2.2.1. Hydrogen Injection System and MWD prediction.

Hydrogen gas can be introduced to the reactor as a MWD modifier. Figure 6-10 shows the modified reactor system with a hydrogen injection capability. As the concentration of hydrogen gas increases, chain transfer to hydrogen (k_{tH}) occurs more frequently, and finally the molecular weight of the polymer decreases. If hydrogen gas is introduced after Zone 1, the lower molecular weight polymer will be synthesized at Zone 2. So a bimodal molecular weight distribution (MWD) can be obtained in this system.

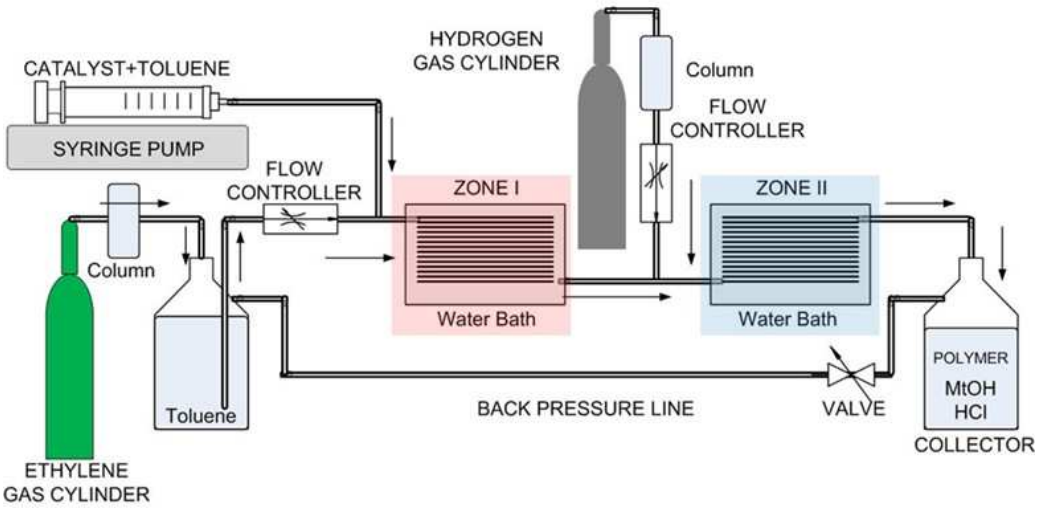

Figure 6-10. Scheme of hydrogen injection system.

To illustrate the function of hydrogen in the continuous micro/milli reactor process, we consider a simple mathematical model to calculate the polymer molecular weight distribution. Here, we shall consider the Flory's most probable distribution that is applied to a single-site metallocene catalyst. The weight chain length distribution w(r) is expressed in Equation 6-1.

Equation 6-1

$$w(r) = r\tau^2 \exp(-r\tau)$$

where *r*,is the chain length, and τ is the ratio of all chain transfer rate to propagation rate. τ is defined as:

Equation 6-2

$$\tau = \frac{k_{tM} M + k_{\beta} + k_{tH} H_2 + k_{tAl} Al}{k_p M}$$

where, k_{tM} is the rate constant for the chain transfer to monomer, k_{β} is for the beta-hydride chain transfer, k_{tH} is for the chain transfer to hydrogen, and k_{tAl} is for the chain transfer to comonomer

kinetic constants. In a continuous steady state reactor, the concentrations of monomer (*M*), hydrogen (H_2), and aluminum alkyl (*Al*) are constant and hence constant value of τ is used.

When there is no hydrogen gas in the reactor and the amount of cocatalyst is small enough, Equation 6-2 can be simplified as:

Equation 6-3

$$\tau = \frac{k_{tM}M + k_{\beta} + k_{tH}H_2 + k_{tAl}Al}{k_pM} \approx \frac{k_{tM}M}{k_pM} = \frac{k_{tM}}{k_p}$$

Similarly, if hydrogen gas is applied to the reactor, and the chain transfer is dominated by the hydrogen chain transfer reaction, Equation 6-2 becomes:

Equation 6-4

$$\tau = \frac{k_{tM}M + k_{\beta} + k_{tH}H_2 + k_{tAl}Al}{k_pM} \approx \frac{k_{tH}H_2}{k_pM}$$

Furthermore, the mathematical expression of the bimodal MWD can be obtained by the weighted superposition of two Flory's most probable distributions.

Equation 6-5

$$w(r) = m_1 w_1(r) + (1 - m_1) w_2(r)$$

$w(r)$: weight chain length distribution for chain length *r*.

m_1 : mass fraction of polymer made in Zone 1

$w_1(r)$: weight chain length distribution made in Zone 1 for chain length *r*.

$w_2(r)$: weight chain length distribution made in Zone 2 for chain length *r*.

The MWD of Zone 1 and Zone 2 can be predicted by Flory's most probable distribution (Equation 6-1). Zone 1, where hydrogen gas is not applied, will follow Equation 6-3, and Zone 2, where hydrogen gas is applied, will follow Equation 6-4. In addition, the monomer concentration profile can be calculated using steady state model of plug flow reactor.

Equation 6-6

$$v\frac{dC_A}{dV} = r_A = -k_p \cdot [C_A] \cdot [Cat]$$

The amount of polymer formed at each zone (m_1, m_2) can also be calculated by the integration of the monomer concentration profile in Equation 6-6.

By combining Equation 6-1, Equation 6-5, and Equation 6-6, the bimodal MWD can be calculated as shown in Figure 6-11. The exact kinetic constants are required for accurate modeling. As expected, Zone 2 shows an overall lower MWD than Zone 1 due to the hydrogen gas.

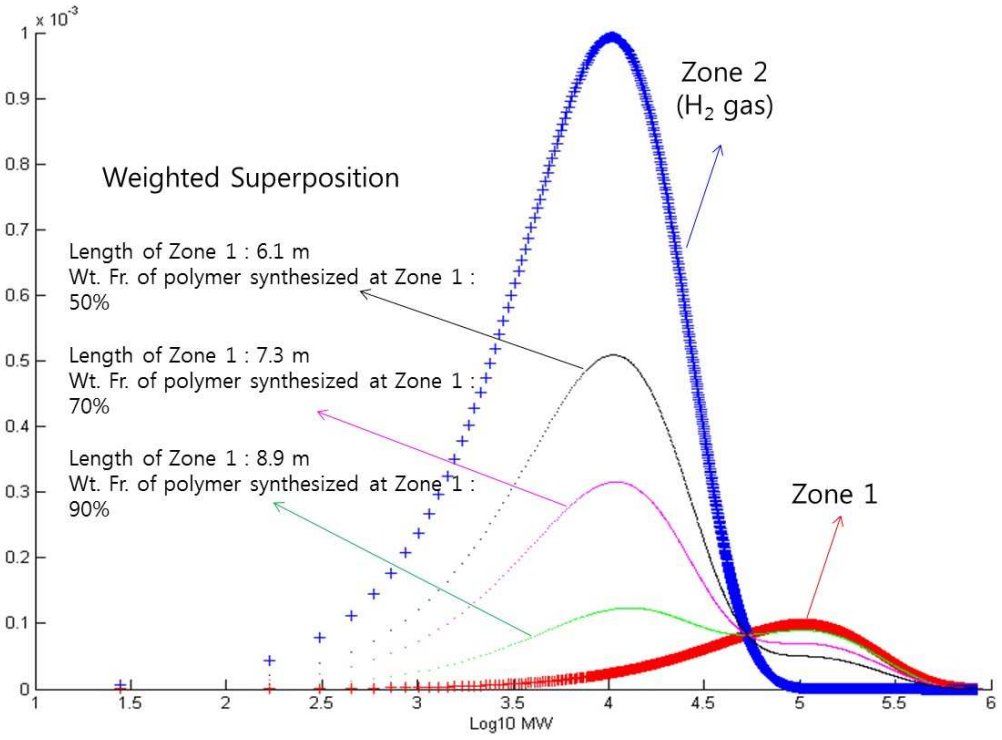

Figure 6-11. Estimated MWD of polymers obtained with a hydrogen injection system

6.2.3. Micro/Milli reactor design for Flow Rate Control

Figure 6-12 is the schematic diagram of the microreactor designed for better flow control. Since the overall flow of the reactor is driven by the pressure difference, the pressure in the

collector bottle must be monitored and controlled for the constant flow in the reactor. Inside a reservoir, ethylene gas is dissolved in toluene first. At the same time, the pressure of the whole system is almost maintained constant by a backpressure line. If the pressure in the reservoir is much higher than that in the collector, the flow rate increases. For higher yield of polymer, longer reaction time (residence time) is required, which means a slow flow rate yields a higher amount of polymer.

The flow rate of the main stream can be controlled by controlling the pressure of the sample collector with a controller, and the pressure is monitored by a pressure sensor. Finally, the ethylene/toluene mixture is transported into the reactor, and the catalyst/toluene mixture is introduced separately by a syringe pump.

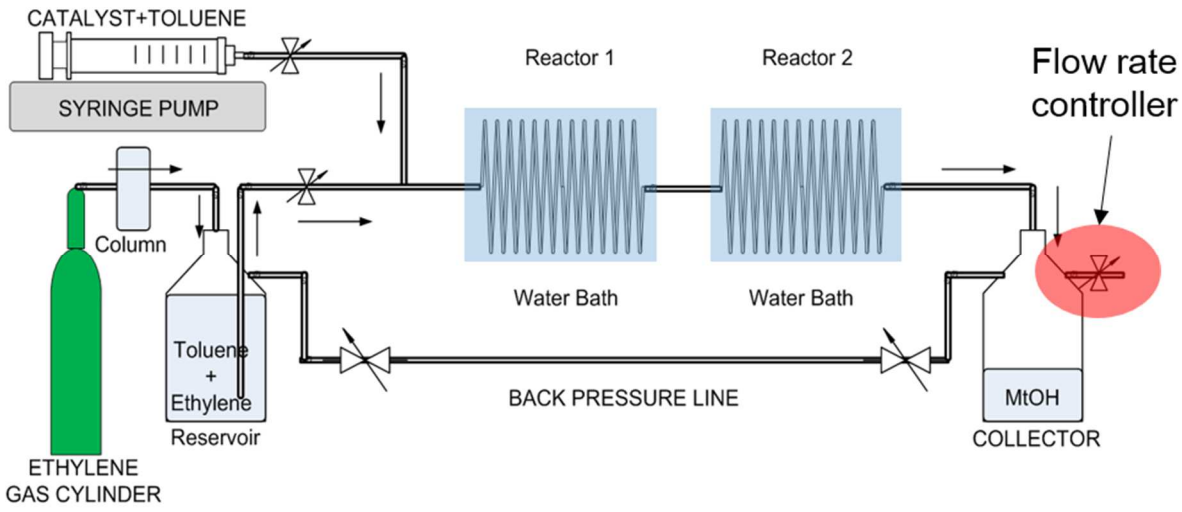

Figure 6-12. Scheme of microreactor setup

Before this reactor set up, we used a 1/4 inch O.D. × 1/16 inch wall-thickness PTFE tube (I.D. $\phi \sim 3$ mm) to check if the reactor functioned properly. After confirming that polymerization can be performed by several test experiments, we changed the PTFE tube to stainless steel tube.

Figure 6-13 (left bottom) shows an inside image of the stainless steel microreactor used for the experiments. We used a 1/8 inch O.D. × 0.016 inch wall-thickness stainless steel tube (I.D. $\phi \sim$ 2.4 mm). The length of the reactor is 43 m, and total volume is around 210 ml. This reactor is not actually micron-sized since we had to apply a high pressure and temperature for the experiments, and had to consider the possibility of clogging. During polymerization, the polymer size increase and large polymer particles can plug the tube if the diameter is not big enough. At high pressures and temperatures, clogging of the tube can cause serious safety problems. For these reasons, a millimeter-sized tube was chosen instead of a narrower micrometer sized PTEF tubes.

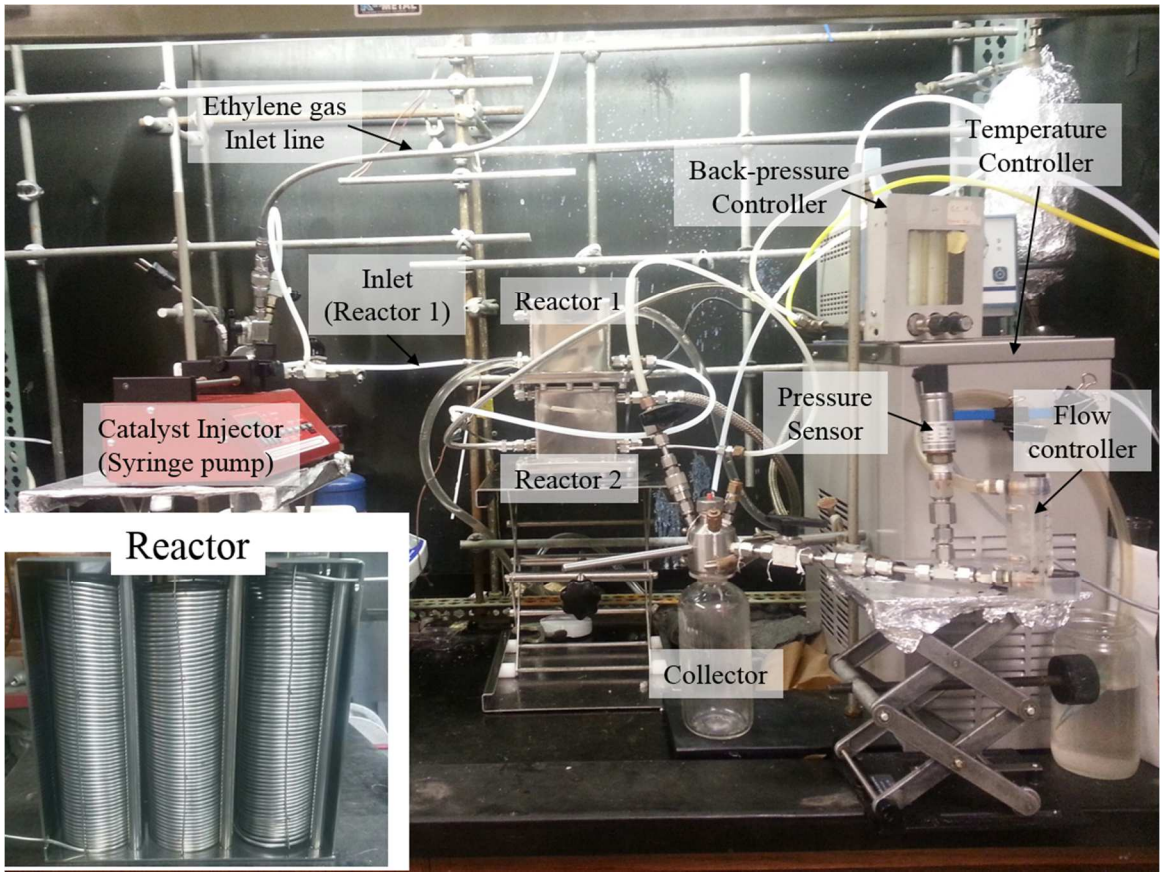

Figure 6-13. Picture of the reactor setup and stainless steel millireactor used for the experiments.

6.2.3.1. Multi-Zone Temperature System and MWD prediction

The mechanical and thermal properties and the molecular weight properties of the polymers depend on the reaction temperature. One of the advantages of the tubular microreactor is that it is easy to setup the reactor with different temperature zones along the axial direction. Conventional highly exothermic olefin polymerization reactors such as batch/semi batch and continuous reactors present significant challenges in precisely controlling the reaction temperature. Due to the high surface area to volume ratio and efficient heat transfer, microreactor offers a unique advantage of nonisothermal operation. Figure 6-14 shows a schematic of the multi-zone temperature microreactor system that has been set up in our laboratory. If needed, more temperature zones can be installed to this system by adding another tubular micro reactor to the Zone 2 unit.

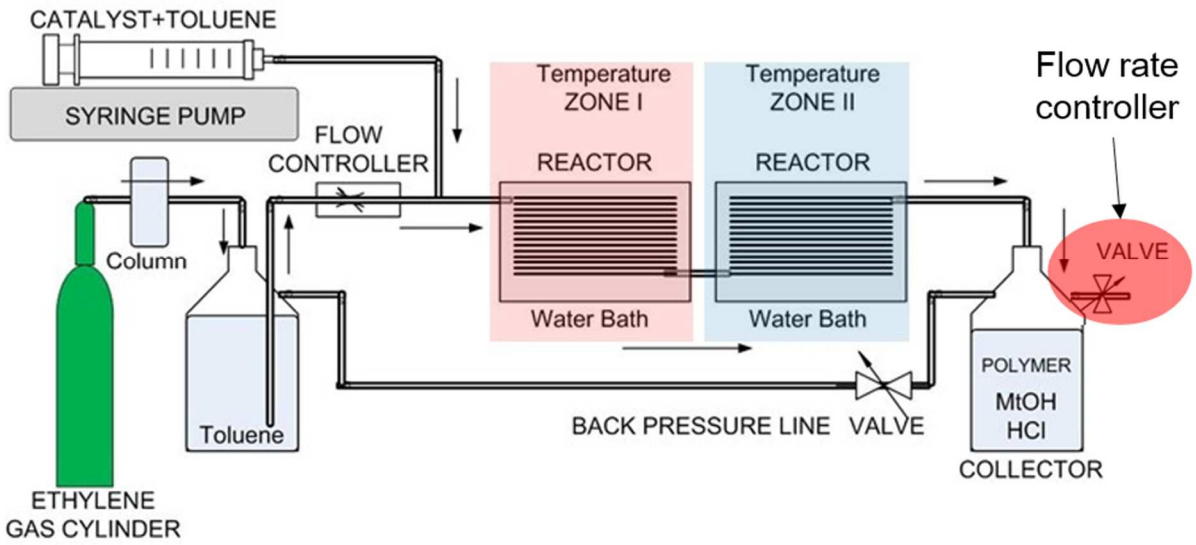

Figure 6-14. Scheme of multi-zone temperature system.

Similar to the hydrogen injection system illustrated in Figure 6-10, the micro reactor can be operated at different temperatures to modify the resulting polymer molecular weight distribution. Usually the molecular weight of polymer decreases as the reaction temperature is

increased because the kinetic constants of k_{tM} (chain transfer to monomer), k_{β} (beta-hydride chain transfer), k_{tH} (chain transfer to hydrogen) and k_{tAl} (chain transfer to comonomer) all increase as reaction temperature is increased.

If the temperature difference is large enough in two different reaction zones, bimodal MWD can be achieved if the amounts of polymers produced in different reaction zones are comparable. Figure 6-15 illustrates the estimated MWD with 2-zone temperature system. Much like in the hydrogen side feeding system, the Flory equation is used. Figure 6-15 illustrates that the overall molecular weight distribution profile depends on the length of Zone 1 (low temperature) or the amount of high molecular weight polymer fraction.

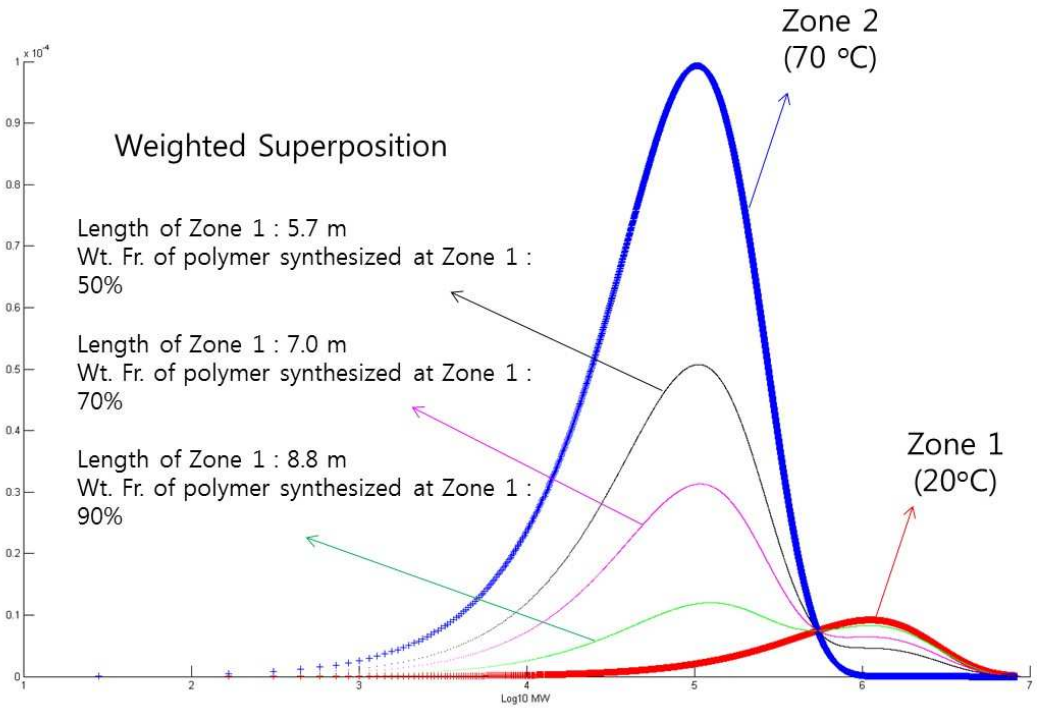

Figure 6-15. Estimated MWD of polymers obtained with a multi-zone temperature system.

6.2.4. Micro/Milli reactor design with a High Pressure HPLC Pump.

One of the main issues with the previous reactor set-up was controlling the reactor flow rate. Even if the flow ~~rate~~ controller can be used to vary the flow rate, it was not accurate or stable because the driving force for the flow was the pressure difference between the monomer/solvent reservoir and the product collector vessel. In other words, the collector pressure had to be monitored and the flow controller valve had to be adjusted manually during the polymerization. To solve this problem, an HPLC pump was installed right after the ethylene/toluene reservoir to control the flow rate directly.

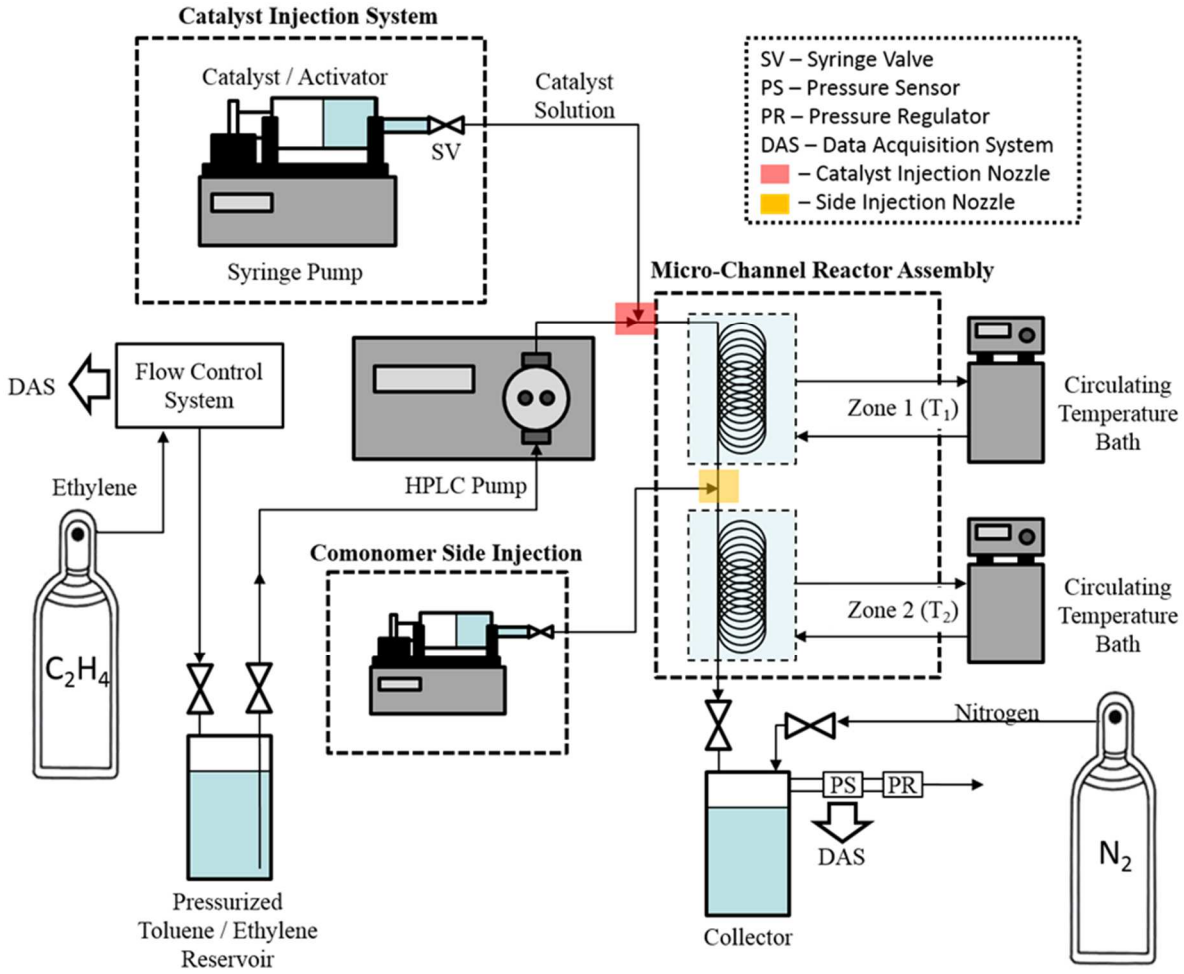

Figure 6-16. Schematic diagram of micro/milli reactor set up with HPLC pump.

Figure 6-16 shows the final reactor set up with HPLC pump. Unlike the previous reactor systems, the HPLC pump can directly supply the liquid stream to the reactor at a constant flow rate. Also, the minimum flow rate can be decreased to 0.5 ml/min (minimum was 10 ml/min for previous reactor set up) and hence, the reactor can be operated with longer residence times.

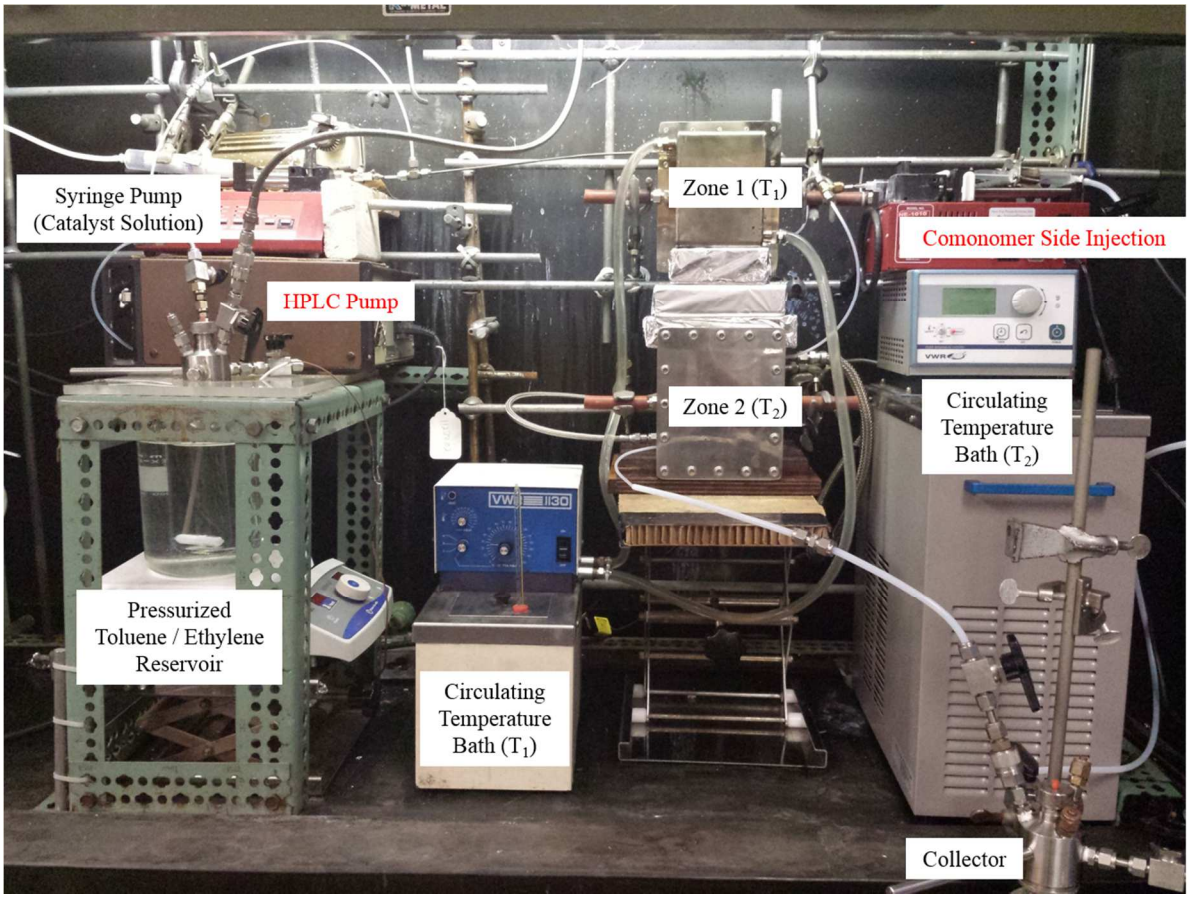

Figure 6-17. Picture micro/milli reactor with HPLC pump.

Figure 6-17 shows the actual reactor set up with HPLC pump. The HPLC pump was installed right after the monomer/solvent reservoir and it supplies the main stream into the microreactor with constant/controllable flow rate automatically. The catalyst solution was injected separately after the outlet of HPLC pump. Zone 1 and Zone 2 temperatures were controlled using circulating temperature baths. Furthermore, the comonomer side injection device was installed between Zone 1 and Zone 2 reactor for sequential injection of comonomer.

6.2.4.1. Solving a Plugging Problems

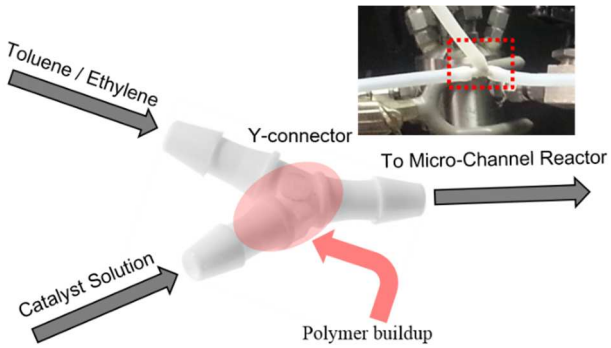

Figure 6-18. Y-connector used in this reactor system.

Figure 6-18 shows the Y-connector, where the monomer/solvent and catalyst streams are mixed. Before using HPLC pump, the flow rate was controlled manually by using the pressure drop between the inlet and outlet of the reactor. In that case the minimum flow rate was 10 ml/min, and the plugging problem was not detected. However, when HPLC pump was used to control the flow rate of monomer/solvent solution, the relatively low flow rate (minimum 0.2 ml/min) was used to extend the reaction time but a buildup of polymer inside of the Y-connector occurred and eventually it led to plugging.

In order to solve the plugging problem, the catalyst-monomer mixing junction needed a modification. Figure 6-19 shows the modified catalyst injection nozzles. After the Y-connector, a PTFE tube was used as a connector as shown in Figure 6-19. A needle was inserted into the PTFE tube such that the catalyst solution can flow through. The tube was connected to a stainless steel tube.

When Design #2 was used (Figure 6-19(a)), there was no plugging during the initial stages of the reaction. However, after about an hour, the polymer/catalyst started to build up where the PTFE tube and stainless steel tube were connected. Design #3 shows the reaming of the stainless steel tube which helped with the plugging problem.

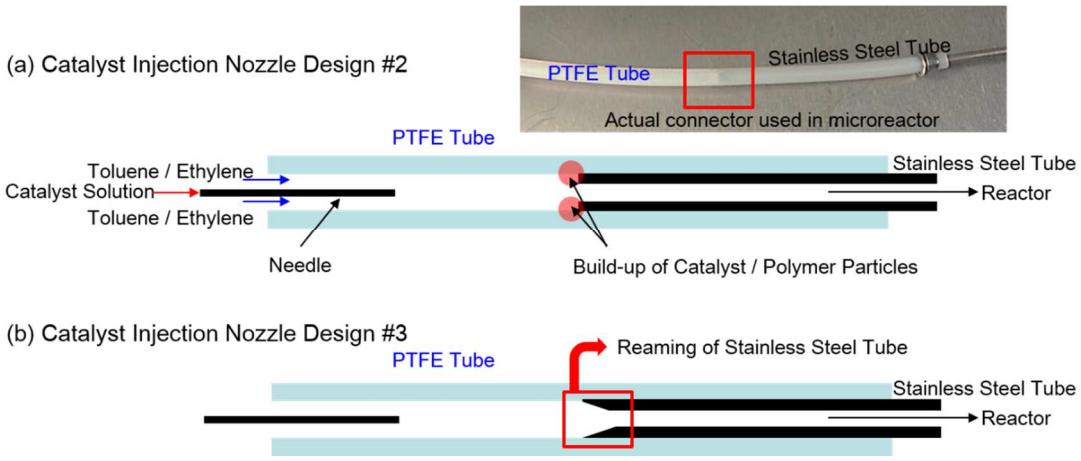

Figure 6-19. Catalyst injection nozzle designs

Figure 6-20 depicts the final design of the catalyst injection nozzle. The PTFE tube from previous design was removed, and instead, a connection, such that the catalyst needle goes directly into the stainless steel tube, was developed.

Additionally, in between the syringe and the needle, a syringe valve was installed to prevent the diffusion of ethylene into the catalyst syringe. Also, the syringe valve added flexibility by making it possible to replace a catalyst syringe during the reaction or add another type of catalyst without having to shut down the reactor.

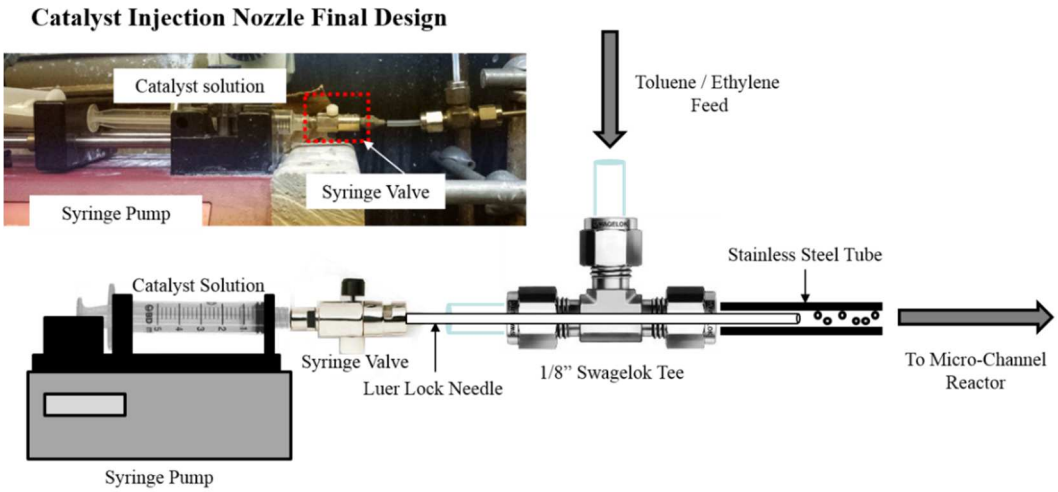

Figure 6-20. Final design of catalyst injection nozzle

6.2.4.2. Polymerization with micro/milli reactor.

After installing the HPLC pump to maintain a constant flow rate and solving the plugging problem, polyethylene polymerization was performed. The total pressure of the reactor was 35psig, T_1 and T_2 were 30 and 70°C, respectively, 3.2 mg_{SiO2}/ml catalyst solution was injected into the reactor at 56µl/min. The total flow rate was 2ml/min. Also before incorporating a comonomer side feed in the micro/milli reactor for copolymerization, 1-Hexene was added to the toluene/ethylene mixture to make a random copolymer. The reaction condition was same as ethylene polymerization.

Copolymers were produced using a micro/milli reactor with a side feed of the comonomer. The 1-hexane/toluene mixture was fed between Zone 1 and Zone 2 at 50 µl/min.

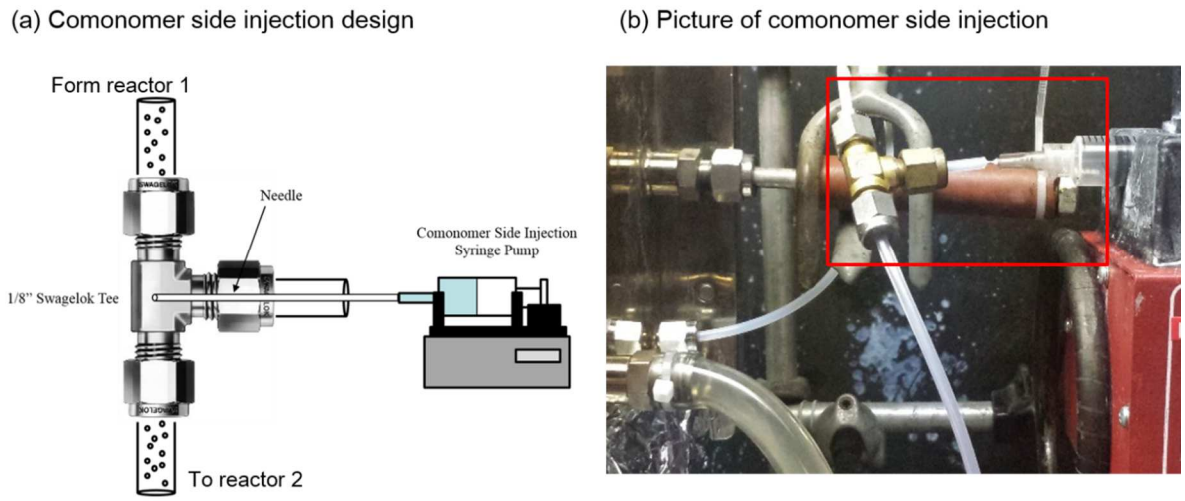

Figure 6-21. Comonomer side injection diagram (a) and image of that nozzle used in this system (b).

6.3. Results and discussion

6.3.1. Bimodal MWD Polymer for Li-ion Battery Separator.

In this work, we have researched a method to produce polyethylenes with a bimodal or multimodal MWD using a micro-reactor. As discussed in the foregoing, the modal MWD can be accomplished by varying the reaction conditions along the axial direction of the tubular reactor. There are many applications of bimodal polyethylenes; however, in our experimental work, we shall explore the possibility of using MWD polyethylenes as a Lithium ion battery separator. For example, the low molecular weight regions of a bimodal MWD resin can act as a shutdown films in case of excessive temperature rise to prevent the short circuit in the battery. The high molecular weight region provides strong mechanical properties. Figure 6-22 illustrates the concept of the bimodal polyethylene resin as a Li ion battery separator.

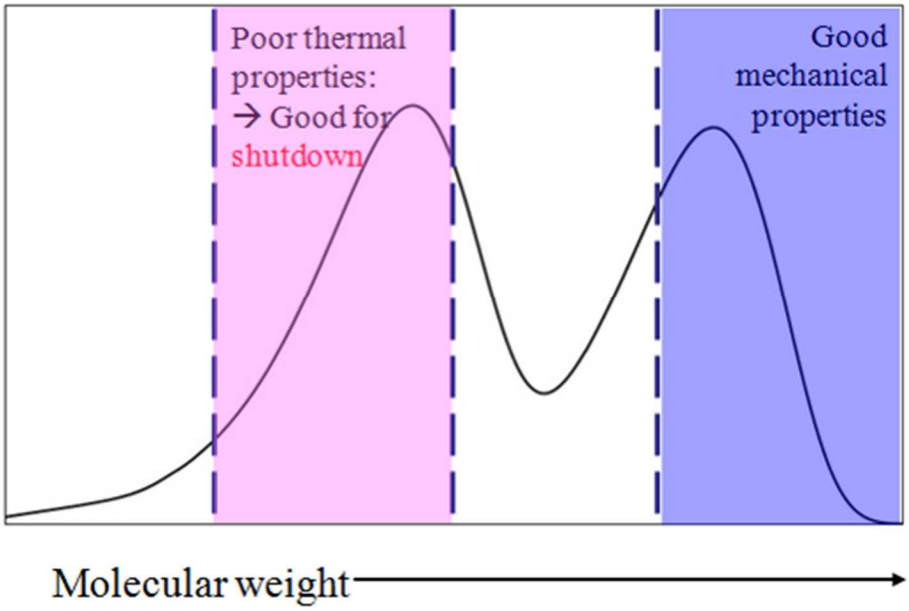

Figure 6-22. Concept of bimodal MWD for battery separator.

6.3.1.1. Requirements of material properties for battery separator.

The target polyethylene in this micro/milli reactor system has been set for the Li ion battery applications as a separator film. Table 6-1 summarizes the requirements of a battery separator. There are many properties that must be fulfilled to be used as battery separators.

Table 6-1. Requirements of material properties for battery separator [100, 101]

Property	Requirements	Comments	Value to study in Micro/Milli reactor
Chemical stability	Must be chemically stable.	PE, PP is stable	N/A
Thickness	Standard thickness ~25.4 μm, Uniform thickness is critical.	Depends on the separator process	N/A
Porosity / Permeability	Typically, porosity of 40% is required	Depends on the separator process	N/A
Pore size	Must be smaller than electrode components. Uniform distribution of the pores are highly desirable.	Depends on the separator process	N/A
Mechanical strength	Must withstand during winding operation. Minimum requirements: Mechanical strength : 1000kg/cm2, puncture strength : 300g	Depends on the polymer grade	Many grades of polymer can be polymerized in MR
Wettability	Should wet easily and retain the electrolyte permanently	Hydrophilic is good	Contents of SiO_2 in PE is manageable
Dimensional stability	Should remain stable in dimensions over wide temperature range	Depends on the polymer property	Contents of SiO_2 in PE is manageable
Thermal shrinkage	Shrinkage no more than 5% at 90ºC, 60min	Depends on the polymer property	Contents of SiO_2 in PE is manageable
shutdown	Must be shut down before the thermal runaway occurs	Depends on the polymer property	PE melts before the thermal runaway temperature

Materials commonly used for battery separators are HDPE and PP-HDPE-PP because they are chemically very stable against the electrolyte. The standard thickness of the separator is about 25.4 μm, and the uniform thickness is critical for long cycle life because even penetration of electrolyte through the separator should be warranted. The typical porosity of Li-ion battery separator is 40%. It is necessary to hold right amount of the electrolyte. If the porosity is too high, it will not work for shutdown performance, and it will shrink as it melts. The pore size must be smaller than the size of electrode materials. These properties are decided during the separator fabrication process.

However some of the requirements listed in Table 6-1 strongly depend on the polymer material's properties. The mechanical strength must be strong in the machine direction, and must hold the tension during battery assembly. The minimum requirements of mechanical and puncture strengths is 1000 kg/cm^2 and 300g, respectively. The separator should wet easily in the electrolyte and retain it permanently for better battery assembly and cycle life. Also the separator should maintain dimensional stability over a wide range of temperature. The thermal shrinkage of the separator should be less than 5% after 60 min at 90^{o}C. Beside these properties, the capability of shutdown performance below the temperature where thermal runaway occurs is the most important properties because it is directly related with the safety problems.

6.3.2. Fabrication of Polyethylene for Battery Separator in Micro/Milli Reactor.

The polyethylene was synthesized in micro/milli reactor and several properties have been measured to check the feasibility of the PE synthesized over silica nanoparticle-supported catalyst as battery separator. The total pressure (ethylene partial pressure) of the reactor was 35psig, the temperature of each zone (T_1, T_2) in Figure 6-17 were set to 30 and 70°C,

respectively, and 3.2 mg_{SiO2}/ml catalyst solution was injected into the reactor with different flow rate for different contents of SiO_2. The total flow rate was set to 2ml/min.

6.3.2.1. The class of PE synthesized in micro/milli reactor

Battery separator plays important role in Li-ion batteries because they prevent thermal runaway. If the battery separator is not working properly, the electrodes could come into direct contact and the resulting chemical reactions can cause a thermal runaway. So they must be capable of shutting the battery down at temperatures lower than where thermal runaway occurs. One of the main materials of battery separators is HDPE because the melting temperature of HDPE is around 135°C~140°C, which is below the thermal runaway temperature.

Figure 6-23 shows the XRD results of polyethylene film fabricated using the polyethylene synthesized in our micro/milli reactor system. The results show that the polyethylene polymerized with EBI catalyst in this system is HDPE, which is a main material of battery separators.

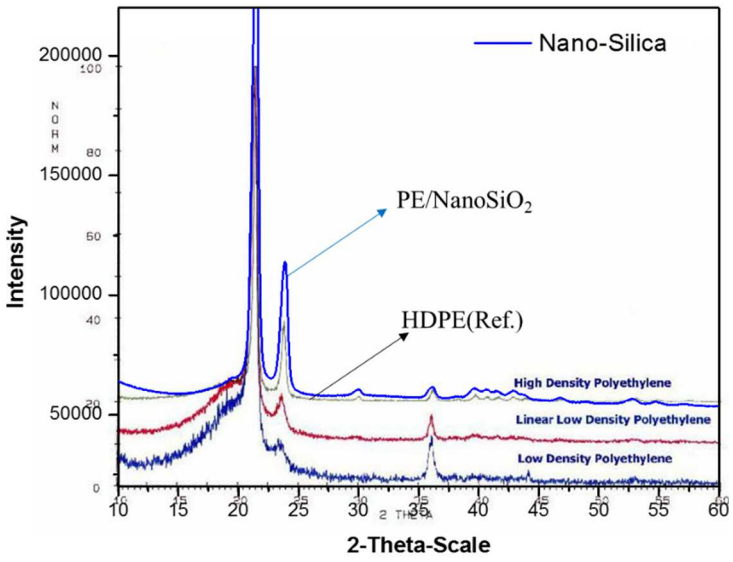

Figure 6-23. XRD spectrum of HDPE polymerized in this system and reference data.

6.3.2.2. Test of Mechanical Strength

By controlling the injection speed of the nano-silica catalyst, the amount of SiO_2 particles in the polymer is adjustable. Since the initial amount of SiO_2 and the amount of final product are known, the content of SiO_2 in each polymer can be calculated. In the micro/milli reactor, polyethylene with four different SiO_2 contents (0.3, 0.5, 2.2, 8.0 wt.%) were synthesized. The SiO_2 free PE was fabricated by dissolving the SiO_2 particles in PE with HF solution. Each of the polymers were melt pressed at 145^{o}C and cut into dog bone shape specimen. The mechanical strength test was performed using universal tensile machine (UTM) at a pulling rate of 2 mm/min in Dr. Sita's Lab, department of chemistry, University of Maryland.

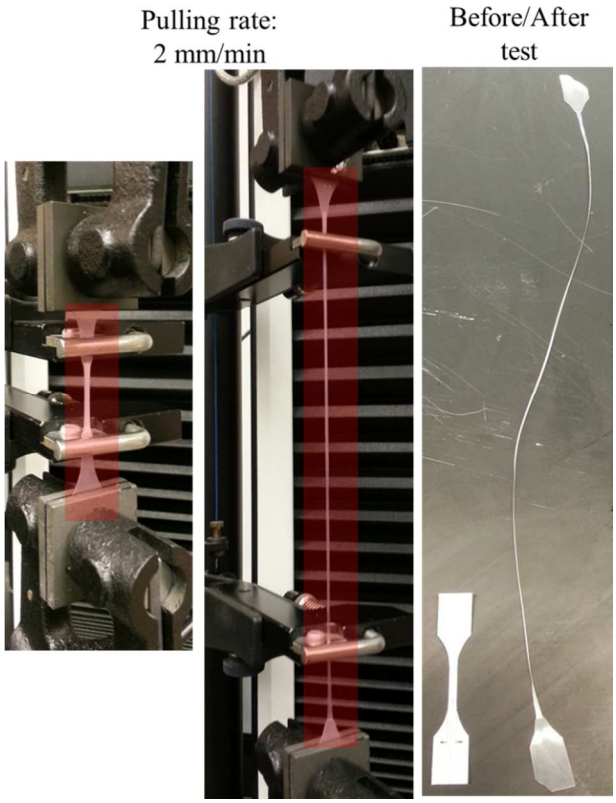

Figure 6-24. Mechanical strength test.

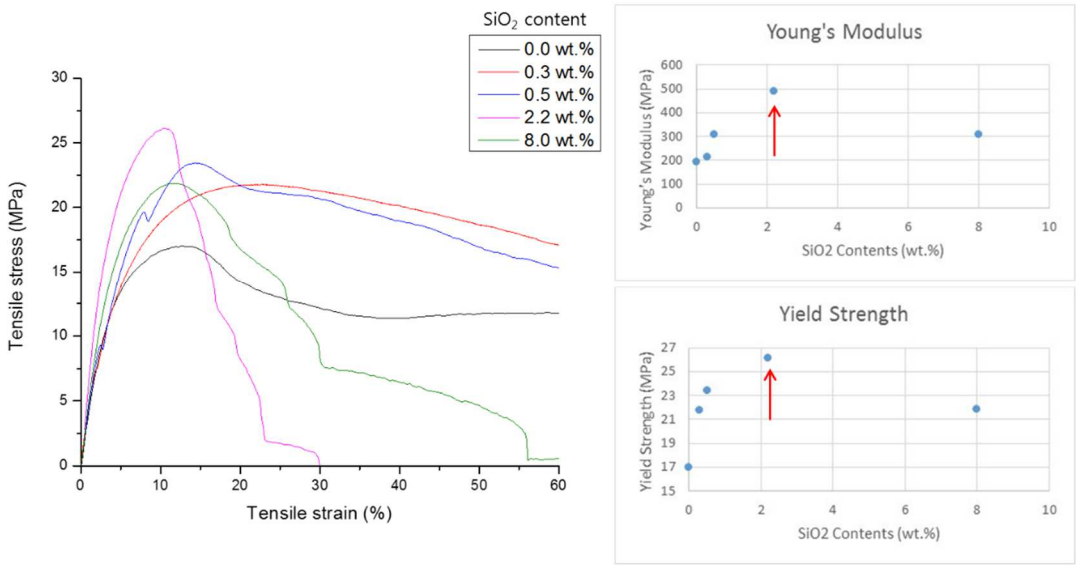

Figure 6-25. Stress-strain curve obtained after the mechanical strength test.

Analyzing the effect of SiO_2 content on the Young's modulus, we have seen that all five PE samples exhibit values that are above the required 1000 kg/cm^2(~100MPa). The value of Young's Modulus and the yield strength increases as the SiO_2 content increases, and the maximum was observed when the SiO_2 content is around 2.2 wt.% and the value decreases at 8.0 wt.%. It seems that SiO_2 functions as a reinforcement agent up to 2.2 wt.%, however it rather act as impurity at 8.0 wt.%

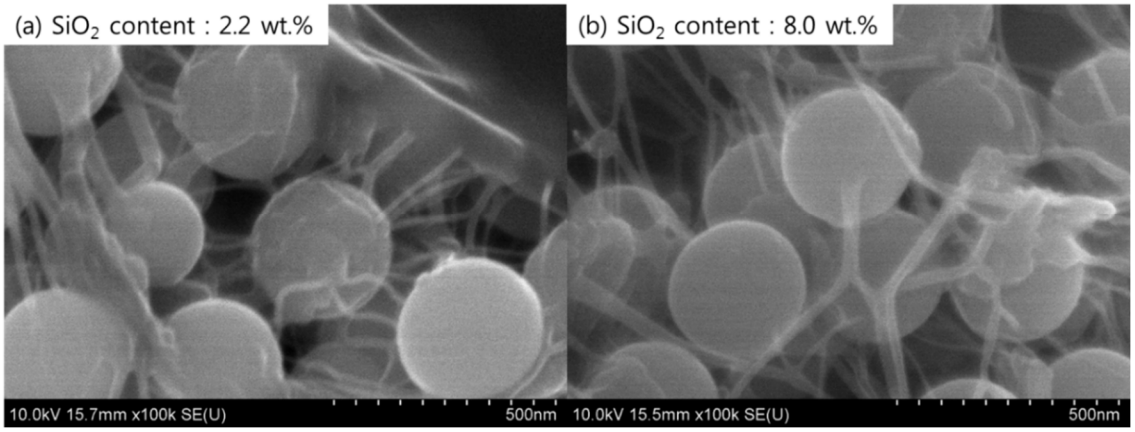

Figure 6-26. SEM image of PE with different contents of SiO_2 (a) 2.2 wt.% and (b) 8.0 wt.%.

Figure 6-26 shows the SEM image of polyethylene with different contents of SiO_2. In both images, it is clearly shown that the PE fibers grow from the surface of SiO_2 particles. Thus, this material cannot be obtained simply by physically blending the 2 components. The increase in Young's modulus when SiO_2 is present can be due to the bonding between the polymer and SiO_2 particles. Compare to 2.2 wt.% sample (Figure 6-26(a)), 8.0 wt.% sample (Figure 6-26(b)) has fewer PE fibers on the surface of SiO_2 particles When the SiO_2 content is 8.0 wt%, instead of acting as a reinforcement agent, it acts as an impurity. The SiO_2 in 8.0 wt.% sample affects the entanglement and crystallinity of the polymer chains and decreases Young's modulus.

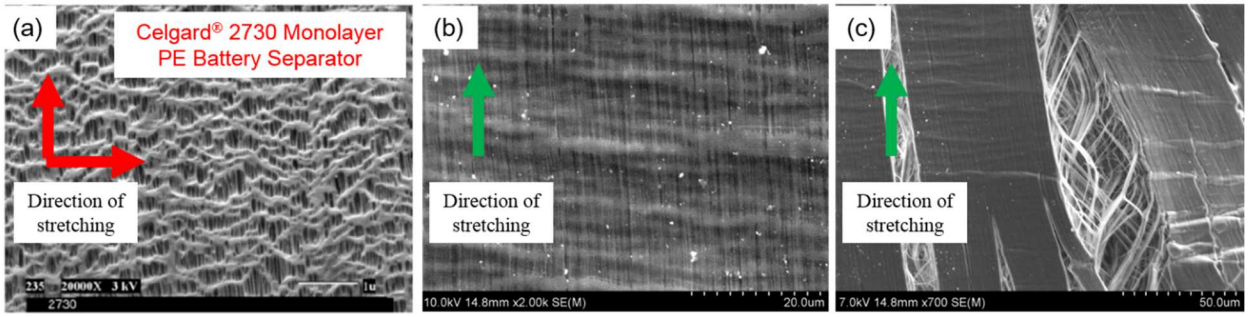

Figure 6-27. SEM image of (a) commercial PE separator (Celgard® 2730), (b), and (c) PE/SiO2 film after UTM test.

Figure 6-27(a) is the commercially available PE separator from Celgard® (2730 monolayer). And Figure 6-27(b), (c) show the PE/SiO_2 film that was obtained through UTM test. Compared to the commonly used Celgard separator, it can be seen that the PE/NanoSiO_2 film has a similar morphology with Celgard. By controlling the horizontal/vertical elongation, the separator thickness, porosity and pore size can be controlled.

6.3.2.3. Test of Wettability

The battery separator must be hydrophilic in order to quickly absorb the electrolyte. There is a lot of work being done to adhere SiO_2 to the surface of PE or PP separators to increase the hydrophilicity of the material. Tsai's group coated the PE separator with silica nanoparticles to enhance the cycle stability [101]. Lee et. al., used polydopamine and diatom to coat the surface of PE separators [102]. Park's group coated thin silica film on the PE separator with PDMS and ultraviolet ozone (UVO) [103]. However, in most of these work~~s,~~ only the surface of the PE separator was coated. In our micro/milli reactor system, SiO_2 is used as catalyst support and polymer grows from the SiO_2 surfaces. Thus, when such polyethylene is fabricated to thin separator films, silica nanoparticles are uniformly distributed in the PE matrix.

Figure 6-28 is the SEM images of PE/SiO_2 films, and more SiO_2 particles (white dots) are detected on the surface of PE as the SiO_2 content increases. At 0.3 and 0.5 wt%, the SiO_2 content is low and is hard to see, but at 8.0 wt%, the NanoSiO_2 particles can easily be seen. The crystalline features of the polymer that can be seen at 0.0 wt% decrease with the increase of SiO_2 content. When the film is made using a hot press, the NanoSiO_2 particles decrease the mobility of the polymer and disrupts the formation of crystalline structures. At 2.2 and 8.0 wt%, the contact angle decreases as the film becomes more hydrophilic (Figure 6-29). Figure 6-30 is the cross sectional view of PE-SiO_2 samples. At 0, and 0.3 wt.% samples show nothing, however at 2.2 wt.% and 8.0 wt.% samples, it was confirmed that the NanoSiO_2 is dispersed well not only on the surface but also in the middle of the film.

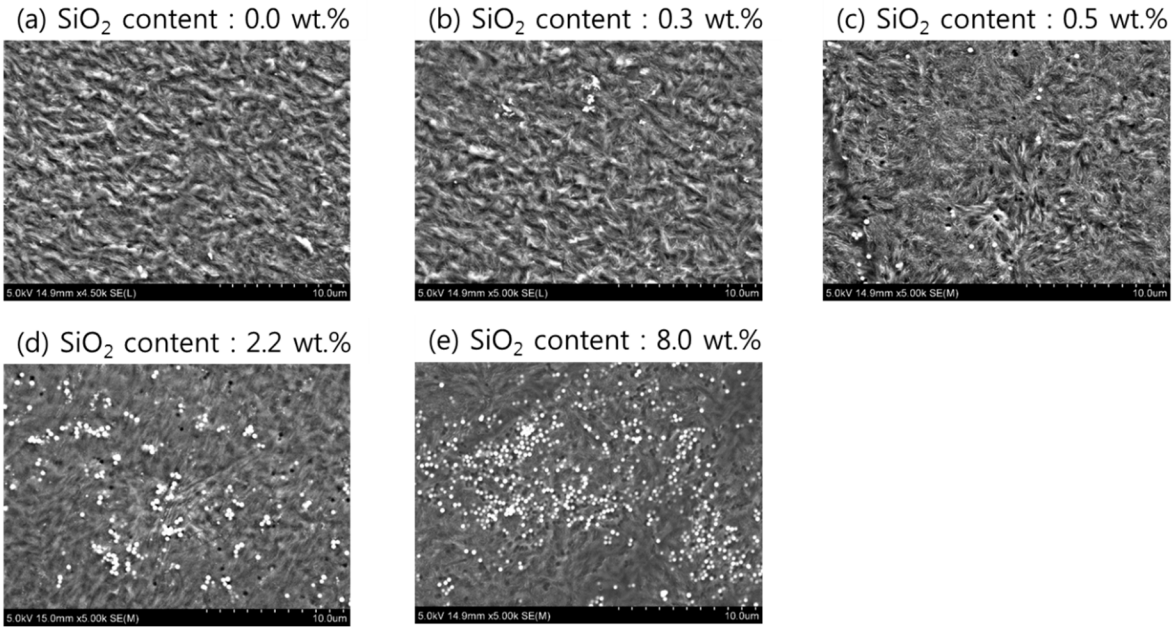

Figure 6-28. SEM images of PE surface with different contents of SiO_2 particles: (a) 0 wt.%, (b) 0.3 wt.%, (c) 0.5 wt.%, (d) 2.2 wt.%, and (e) 8.0 wt.%.

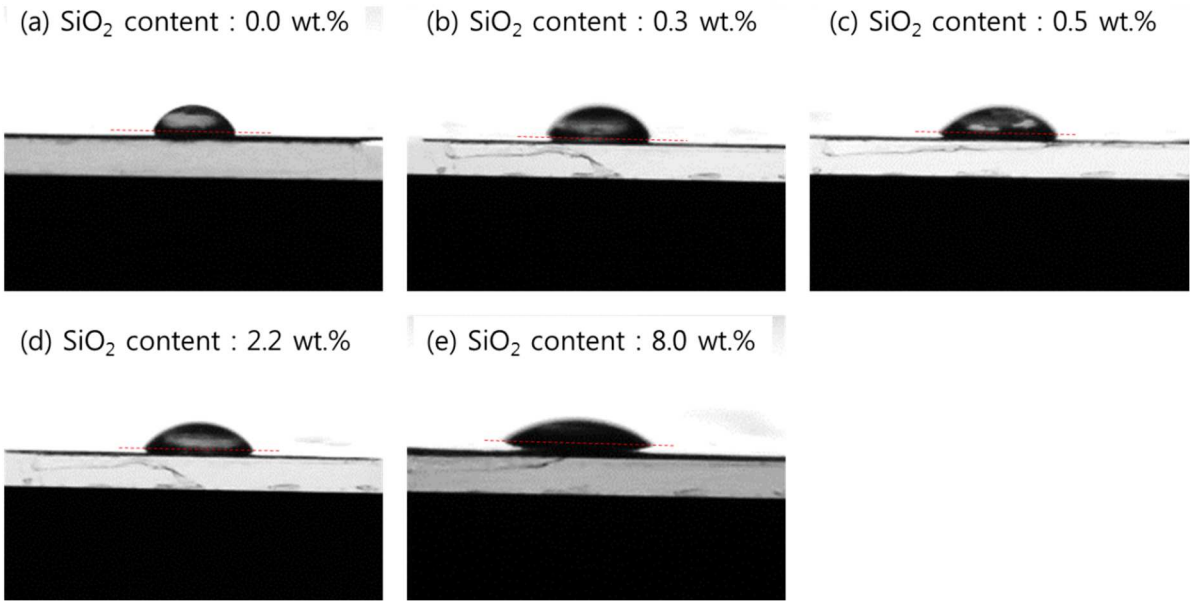

Figure 6-29. Contact angles of water on PE surface with different contents of SiO_2 particles: (a) 0 wt.%, (b) 0.3 wt.%, (c) 0.5 wt.%, (d) 2.2 wt.%, and (e) 8.0 wt.%.

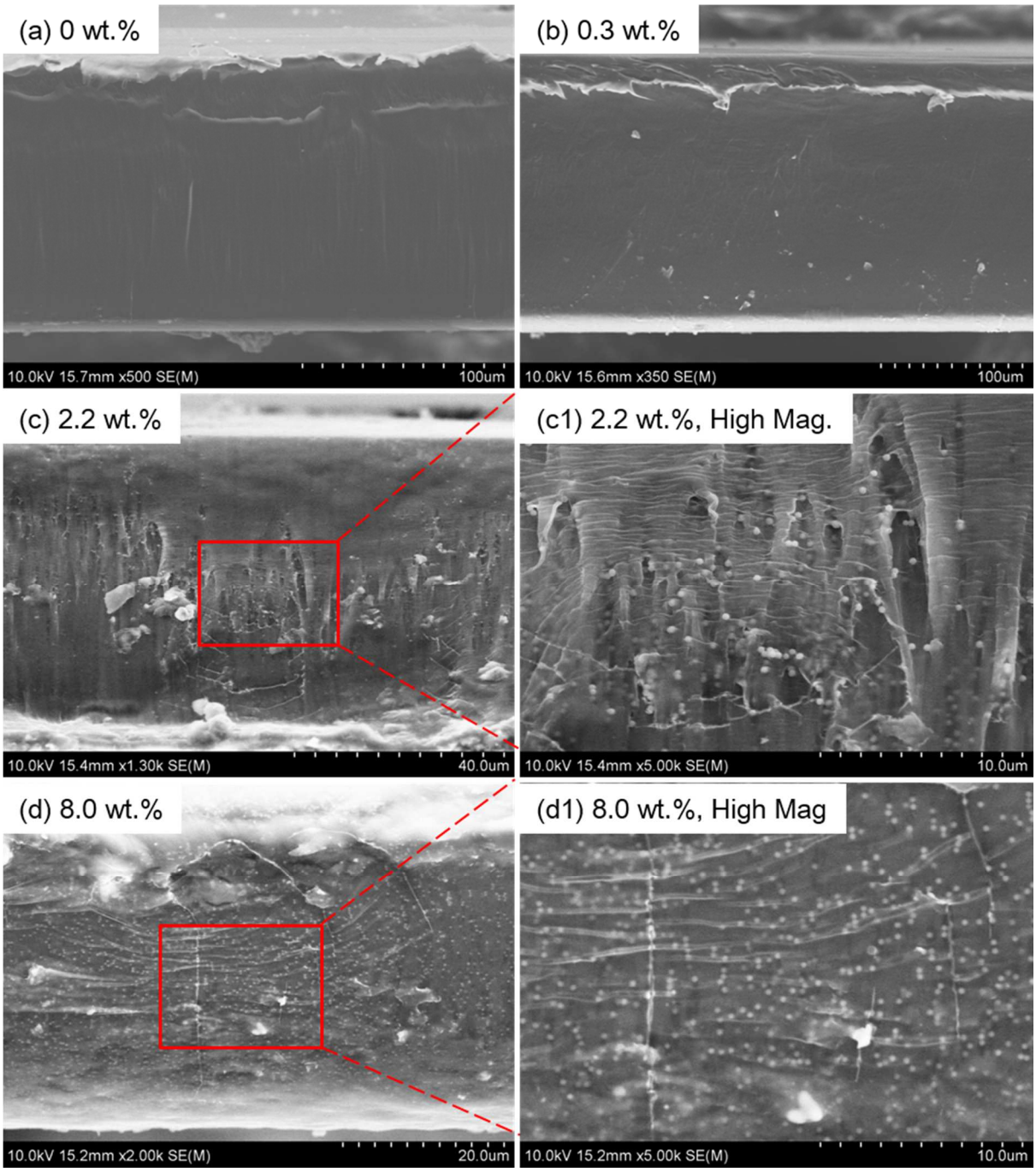

Figure 6-30. Cross section view of SEM images for PE films with different contents of SiO_2 particles: (a) 0 wt.%, (b) 0.3 wt.%, (c) 2.2 wt.%, (c1) 2.2 wt.% magnified, (d) 8.0 wt.%, and (d1) 8.0 wt.% magnified.

6.3.2.4. Test of dimension stability and thermal shrinkage

The separator should main dimensional stability over a wide temperature range because if it shrinks, the shutdown performance of the separator film will become very poor. Incorporation of inorganic nanoparticles such as SiO_2, TiO_2, Al_2O_3, MgO, and $CaCO_3$ with polymer separators ~~are~~ have been widely studied to enhance the dimension / thermal stability [104-108]. Lee's group coated polyethylene with closely packed SiO_2 or Al_2O_3 / poly(vinylidene fluoride-hexafluoropropylene) to enhance the dimension stability and thermal shrinkage [109, 110]. Kim et. al., used Al_2O_3 for ~~batter~~ improved cycling performance [111].

As mentioned in the foregoing, in micro/milli reactor system, SiO_2 is being used as the catalyst support and the polymer grows from the SiO_2. Thus, we can produce the HDPE as a separator that contains different amount of silica nanoparticles by controlling the polymerization activity.

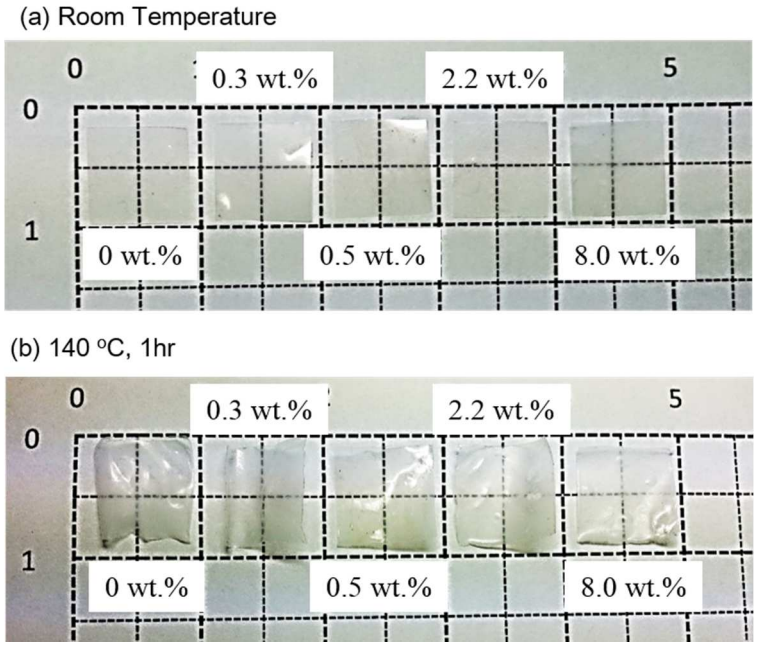

Figure 6-31. Dimension stability and thermal shrinkage of PE/SiO_2 samples: (a) before, and (b) after being stored at 140°C for 1hr.

As shown in Figure 6-31, a good dimension stability and thermal stability was obtained with increasing the amount of SiO_2 nanoparticle.

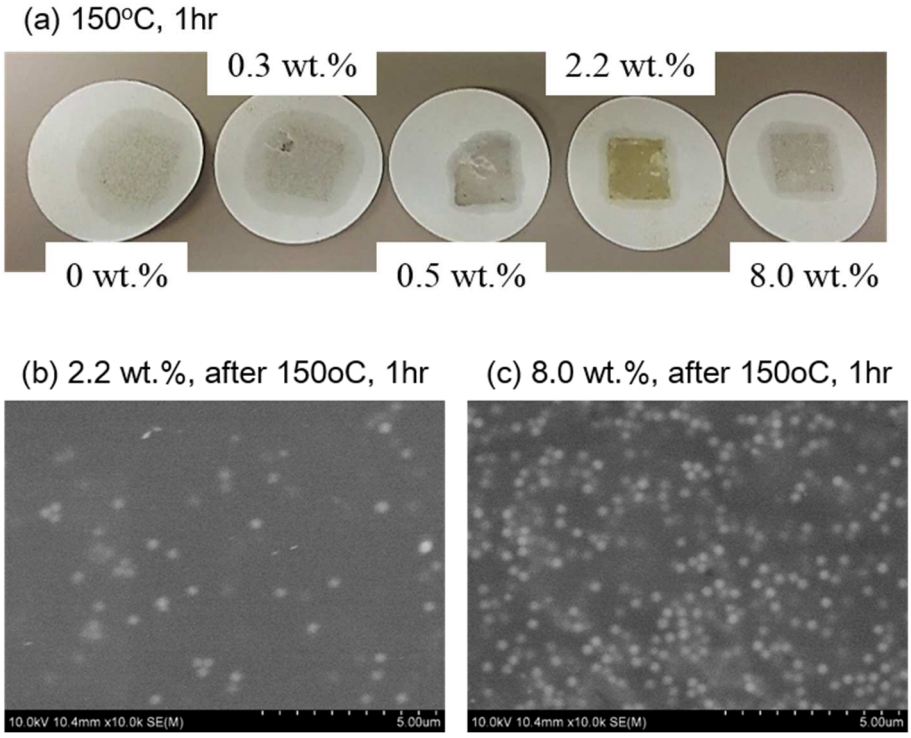

Figure 6-32. (a) Picture of PE/SiO_2 films, and SEM images of (b) 2.2 wt.% PE/SiO_2, (c) 8.0 wt.% of PE/SiO_2 after being stored at 150°C for 1hr.

The shutdown function of a separator is extremely important in preventing an explosion from thermal runaway that a battery may experience. The polymer must melt and block the pores while keeping shrinkage at a minimum. The shutdown test was performed at 150°C for 1hr. Figure 6-32 show the results. Some changes in the PE/SiO_2 films were observed after heating for 1hr at 150°C.

While at 0 wt% of SiO_2, the film melted and was absorbed by the filter paper, when the SiO_2 content increases, the films maintain the initial shape much better. In Figure 6-32(a), 0.5 ~ 8.0 wt.% PE/SiO_2 films almost maintain their initial shapes while some PE has melted and

absorbed into the filter paper. For a good separator, the film must maintain their shape and partially melt to prevent the thermal runaway. According to several requirement test, the PE with different amount of SiO_2 synthesized in micro/milli reactor has a good feasibility to be adopt as a battery separator.

6.3.2.5. DSC analysis

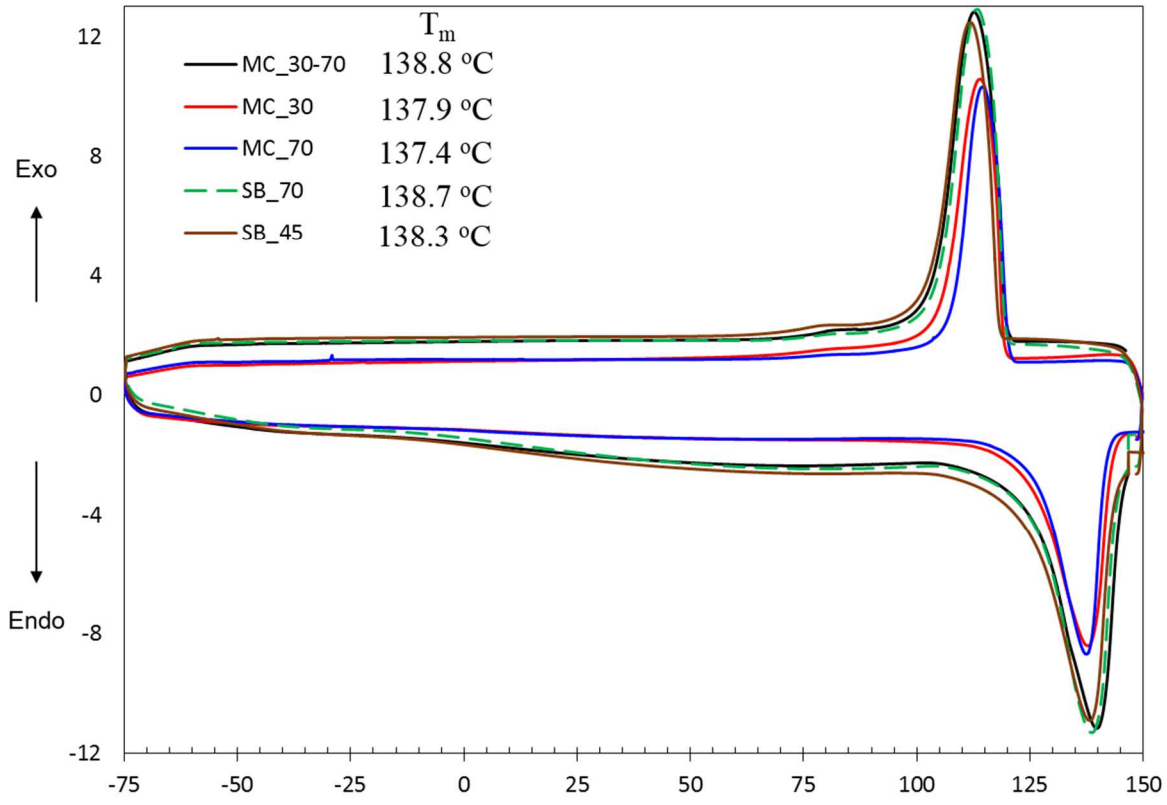

Figure 6-33. DSC data of PE synthesized in microreactor (MC), and semibatch (SB) reactor:

Figure 6-33 shows the DSC results of the PE produced with a micro/milli reactor (MC) and semi-batch reactor (SB). There is no significant difference in the melting point of PE that passed through both Zone 1 (30°C) / Zone 2 (70°C) (black), and the PE that passed through only

one temperature zone, 30°C (red) or 70°C (blue). Likewise, there is no significant difference in melting point between semi-batch PE (70°C-green, 45°C-brown) and micro/milli reactor PE.

6.3.3. Copolymerization in micro/mill reactor

Copolymers were produced using a micro-reactor with a side feed for the comonomer. The total pressure in the reactor was 35psig, T_1 and T_2 were set at 30°C and 70°C, respectively, 3.2 mg_{SiO2}/ml catalyst solution was added to the reactor at 56µl/min. The total flow rate in the reactor was 2ml/min. For the comonomer side injection, the 1-hexane/toluene mixture was fed between reactor 1 and reactor 2 at 50µl/min. For comparison, polyethylene was polymerized at the same condition without comonomer injection.

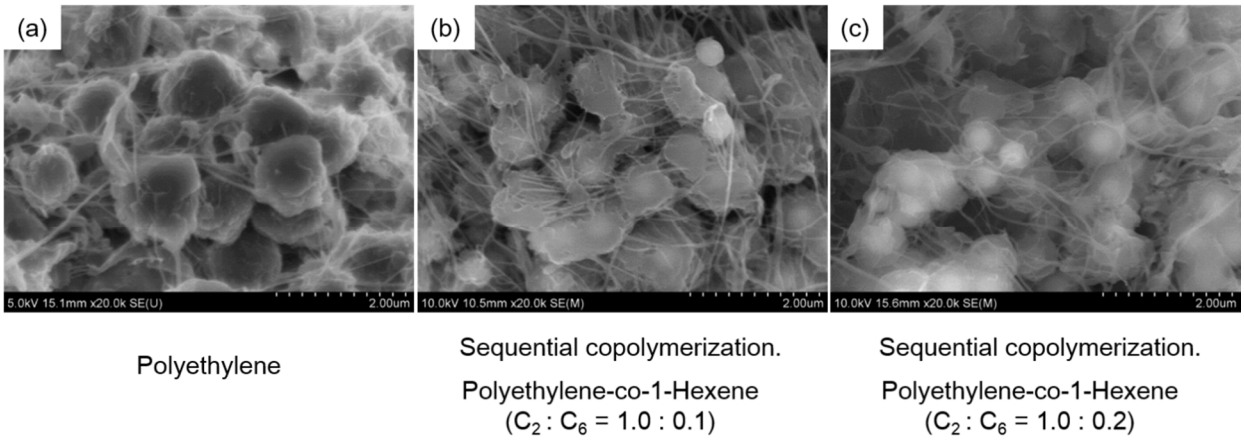

Figure 6-34. SEM images of (a) polyethylene, (b) PE-co-Hex (C_2:C_6=1.0:0.1), and (c) PE-co-Hex (C_2:C_6=1.0:0.2) synthesized in micro/milli reactor.

The SEM images in Figure 6-34 show polymers synthesized in a micro/milli reactor using the same reaction conditions. However, Figure 6-34(a) is polymerization of ethylene only, Figure 6-34(b) is the sequential copolymer with a 1:0.1 molar ratio of ethylene and 1-hexene, and the Figure 6-34(c) is the sequential copolymer of ethylene and 1-hexene at a 1:0.2 molar ratio.

The images taken at the same magnification show that as the ratio of 1-hexene increases, the polymer particle size decreases. Again, this is because the total activity is lowered by the addition of 1-hexene which has a low activity. Also, as the ratio-of 1-hexene to ethylene increases, the silica core of the polymer particle becomes more visible due to low packing density of polymer caused by the short butyl branches from 1-hexene.

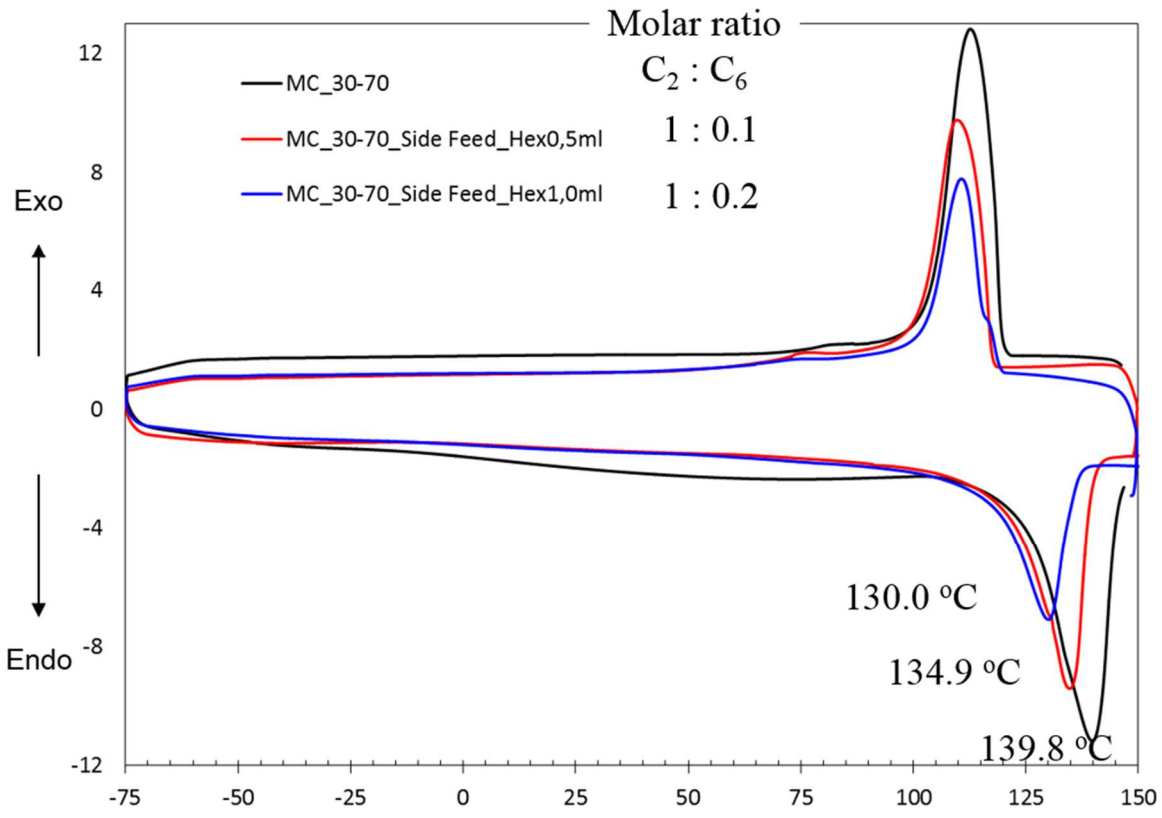

Figure 6-35. DSC data of polyethylene (Black), and PE-co-Hex (C_2:C_6=1.0:0.1, Red), (C_2:C_6=1.0:0.2, blue) synthesized in micro/milli reactor.

Figure 6-35 is the DSC data. The molar ratios of ethylene to 1-eexene were set at 1.0 : 0.1 and 1.0 : 0.2. As the concentration of 1-hexene increased, the T_m decreases from approximately 140°C to130°C. As already confirmed by SEM (Figure 6-34), due to the existence of hexane in

the chain, the packing density of the polymer decreased, and finally the melting temperature decreased.

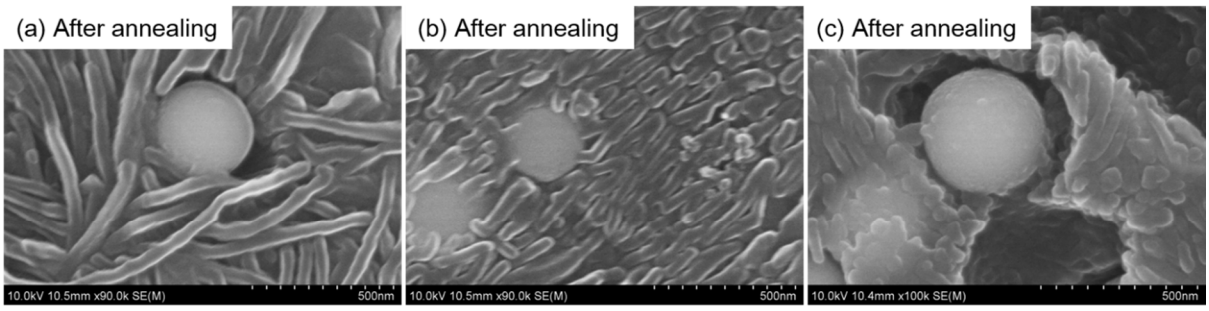

Figure 6-36. SEM images of (a) polyethylene, (b) PE-co-Hex (C_2:C_6=1.0:0.1), and (c) PE-co-Hex (C_2:C_6=1.0:0.2) after annealing

To check the effect of 1-hexene, each sample was annealed at 120 ºC for 1hr. The SEM images of the result are shown in Figure 6-36. PE sample (Figure 6-36(a)) shows that the PE has crystallized as fiber. Note that the diameter of fiber formed during crystallization is around 50 nm, which is quite similar to the PE nano fibrils formed during heterogeneous polymerization. Figure 6-36(b) shows that the ethylene-1-hexene copolymer with the C2/C6 ratio of 1.0/0.1 has shorter crystallized nano fibrils but with similar thickness. Figure 6-36(c) also shows the polyethylene fibrils with similar thickness but even shorter lengths. Even some ~~rods or~~ spherical shaped structures are seen. It is believed that increased amount of 1-hexene in the copolymer chain disrupts the polyethylene chains These phenomena mainly due to the hexene chain, which hinders the ethylene chains to be folded for the formation of crystalline structure.

6.4. Conclusions

The micro/mill reactor system for olefin polymerization with an air sensitive catalyst has been developed and some preliminary feasibility experimentations have been carried out. The reactor system evolved from the initial design through testing and we were able to develop a system where heterogeneous ethylene polymerization can be performed without serious plugging problem. The preliminary experimental test results indicate that the micro/milli reactor can be used for ethylene homo- and co-polymerization. The reactor system is equipped with side injection ports so that either comonomer or hydrogen or both can be injected into the tubular reactor to modify the polymer MWD properties. Setting up the reactor with various reaction conditions such as temperature zones and side injection positions (comonomer, H_2 gas) can be designed through a mathematical reactor modeling. Although the present work provides some technical data about the feasibility of the micro/milli reactor for ethylene polymerization, further experimental and modeling study will be needed to assess more quantitative aspects of the reactor system. For example, the maximum polymer yield and solid content (wt.% of polymer in the liquid phase) without causing reactor plugging need to be established

Chapter 7. Binder Free Si-CNT Anode with Surface Modified Current Collector for Li-ion Battery.

7.1. Abstract

The research is aimed at developing a binder free silicon anode system that consists of a modified Cu foil (Current collector), Si nanoparticles (SiNPs), and carbon nanotubes (CNTs). This anode system includes the nanostructured Cu surface layer as a hub for the Si nanoparticles that undergo deformation and fragmentation during the charge/discharge cycles. Si nanoparticles are deposited with Fe-Co bimetallic catalyst and CNTs are grown *in situ* at the catalyst sites. The surface layer of the Cu is modified via oxidation and reduction processes to have knife-like nanostructure with high void fraction. The SiNPs are deposited on/in to the nanostructured Cu foil without any binder. The CNTs growing at the SiNP surfaces serve as electron conductor as well as holder of the SiNP during the lithiation/delithiation cycles. Since Si/CNT particles are surrounded by thin protrusions on the surface of Cu current collector, the maximum connectivity between silicon and current collector can be obtained and excellent cycle stability of the battery can be maintained without any binder.

7.2. Introduction

High capacity, stable, and inexpensive energy storage devices such as Li-ion batteries are needed from small or microelectronic devices to large automotive electric vehicles, aircrafts, and military equipment and thus we can say that any advancement in Li-ion battery technology can make a significant and broad impact in industry and human life. Demand for Li-ion batteries is expected to reach a market value of $26 billion annually by 2023, with a particularly strong and growing demand from the automobile industries. The global competition for securing advanced manufacturing technology for superior Li-ion battery systems is fierce and recent scientific and technical journals are literally flooded with articles presenting new ideas and developments for improved Li-ion battery performances and economy. Indeed. Every major constitutive element of Li-ion batteries such as anode, cathode, electrolyte, and separator membrane I the subject of intense research and development worldwide because all these components contribute significantly to the overall performance of a battery. The major factors in developing an ideal battery include energy density, power density, safety, cycle life, calendar life, and cost.

Conventional Li-ion batteries typically have a carbon bases anode, which tends to limit the charging capacity of the batteries to about 372 mAh/g. Although Sn based anode can produce a higher charging capacity of about 990 mAh/g, silicon based anode have been known to have highest theoretical specific capacity of 4,200 mAh/g (based on the fully alloyed form of $Li_{4.4}Si$ at high temperature), which is almost ten times higher than that of graphite, with a low electrochemical potential vs. Li/Li^+ between 0 and 0.4V, and small initial irreversible capacity loss [112]. Therefore, silicon is believed to bring disruptive change in anode materials. However, silicon anode has a serious problem of losing the physical integrity during the service period of a battery. Most importantly, the large volume change (300~370%) during the repeated lithiation

and delithiation cycles eventually lead to stress-induced cracking, pulverization of Si film or particles and electrical disconnection between the active anode material and current collector (Cu foil), leading to a decay of battery performance.[113] Therefore, it is strongly needed that such mechanical degradation or breakdown of Si be prevented or reduced to extend the service life of a Li-ion battery. Many techniques have been developed to resolve this issue as documented in a large number of journal publication in recent year. The advanced Si anode systems reported in the open literature can be classified broadly into a few major approaches. They are: (i) to use nano-structured Si such as Si nanorods, nanowire arrays, nanotubes(core-shell), nano spheres(particle) [13, 16, 112, 114-118]; (ii) incorporation of inactive components into Si materials [116]; (iii) fixation of Si materials in a patterned current collector surface [119] ;(iv) caging of Si particles to minimize the loss of electrical connectivity due to pulverization of Si nano particles [120, 121]. The development of a patterned current collector is relatively new research direction in Si anode system. It is aimed at securing a large surface area for the reduction of the stress of volume expansion of Si and a few attempts of modifying the current collector surfaces have been reported in the literature. Some of the notable examples are: a microdome-patterned Si electrode using a polylactic acid(PLA) patterning technique [119]; trench-type patterns by combining a photo-lithography with a wet etching process with nanostructures CuO grown on the patterned Cu foil [122]. and honeycomb-patterned current collector [123]. Most of these surface patterning techniques require quite expensive and sophisticated processing steps.

The idea of using nano-structures Si is worthy of further discussion: it is based on the observations that when Si particles fracture and pulverize during the charge/discharge cycles, there exists a certain minimum size of Si fragment beyond which further fragmentation ceases.

Some of the nano-structured Si anodes have been shown to be effective in reducing the adverse effect of stress-induced Si volume charge and capacity fading. The most notable contribution to this technique was reported by Chan and coworkers [124]: they grew Si nanowires directly on the current collector to about 90nm in diameter. They showed that even with an increase in nanowire diameter after cycling, the Si nanowires anode remained attached to the current collector surface and allowed for efficient 1D electron transport down the length of every nanowire. Si nanowires directly grown on a current collector surface showed improved cycle stability since the pulverization of Si was effectively avoided as the stress from lithiation/delithiation cycles was well relaxed [125]. A free standing CNT-Si composite film was also fabricated as both anode active material and current collector by Cui et al. [126, 127].

The detachment between the current collector and Si electrode due to the pulverization of Si particles leads to the electrical disconnection. Composites of silicon and inactive material (carbons or conductive polymers) have been studied extensively to mitigate this problem. Some examples of such materials include Si/amorphous carbon, Si/graphene, Si/carbon fiber or nanotube composites, Si/conduction polymer composites. It has been reported that nano Si particles larger than 30nm in composite tend to aggregate during the charge/discharge cycles making it very difficult to uniformly coat carbon onto the Si nanoparticles, and the resulting anode performance was poor [128].

The formation of solid-electrolyte interphase (SEI) film on the Si surface is also a critical factor in cycle life and coulombic efficiency because it leads to irreversible loss of battery capacity. According to Kim et al. [128], the irreversible capacity loss decreases with an increase in nano Si particle size (5~20 nm range) because the formation of the nonconductor SEI is reduced as specific surface area decrease with larger nano Si particles.

The performance of Si anodes is known to depend on a number of parameters (e.g., silicon material, polymer binder, electrolyte system, etc.) and it might be impossible to take into account all these parameters into a single research study for the development of advanced anode systems. Moreover, economic factor is another important issue to be considered in developing a new battery technology because the widespread use of Li ion batteries in a variety of applications requires low-cost manufacturing technology. Although many of the anode systems reported in the literature demonstrate improved capacity and cycle stability, the fabrication of such anodes needs quite sophisticated and complex process. The tradeoff between the performance and cost needs to be considered in engineering advanced Li-ion battery systems.

In this chapter, binder free silicon anode system that consists of a modified Cu foil, Si nanoparticles (SiNPs), and catalytically grown carbon nanotubes (CNTs) on the SiNPs are studied. Cu foil was surface modified to enhance the contact area between active materials (Si) and current collector (Cu foil). Si nanoparticles were deposited with metal catalyst, and they were attached on/in to the nanostructured Cu foil without any binder. Finally, CNTs were grown *in situ* at the catalyst sites. The CNTs grown at the SiNPs surfaces serve as electron conductor as well as holder of the SiNPs during the lithiation/delithiation cycles. Due to the large 3D surface area of current collector and entanglement of CNT, excellent cycle stability of the battery can be maintained without any binder

7.3. Experiment

7.3.1. Materials

Silicon nanopowder (SiNP, <200 nm, ≥98% trace metals basis, Sigma Aldrich) was used as a catalyst support for CNT growth and anode material. Sulfuric acid (ACS plus, Fisher Scientific), hydrogen peroxide (30%), and hydrofluoric acid (50%) were used for the surface treatment of SiNP. A cobalt(II) acetate tetrahydrate(ACS reagent, ≥98.0%, Sigma Aldrich), iron(II) acetate (95%, Sigma Aldrich), conbalt(II) nitrate hexahydrate (ACS reagent, ≥98.0%, Sigma Aldrich), and iron(III) nitrate nonahydrate (ACS reagent, ≥98.0%, Sigma Aldrich) were used as a catalyst without further treatment. Sodium chlorite ($NaClO_2$), sodium hydroxide (NaOH), sodium phosphate tribasic dodecahydrate ($Na_3PO_4 \cdot 12H_2O$) were used to modify the surface of Cu foil (current collector).

7.3.2. Preparation of Binder Free Si/CNT Anode

The anode part of a conventional Li-ion battery is made with active material, carbon black, and binder. Carbon black works as an electron conductor and a binder helps the active material and carbon black to be attached on a current collector. Figure 7-1(a) illustrate the conventional method to prepare the anode part of Li-ion battery. Some researchers replace the carbon black to carbon nanofiber (CNF) or carbon nanotube (CNT) to enhance the conductivity of active materials and Figure 7-1(b) briefly shows their methods. Huang et.al. [129], ball-milled micron sized silicon powder and grew CNT on it, and they made electrodes with active materials (82 wt%), carbon black (10 wt%), and polyvinylidene fluoride (PVDF) as a binder (8wt%). Oh's group physically mixed micron sized silicon and CNT [130]. They also synthesized CNT on

micron silicon to fabricate the active material. Finally, the electrode was assembled with Si/CNT composite (80 wt%), carbon additive (Super P, 10 wt%), and PDVF (10 wt%) [130]. Yamamoto's group carbonized PVC on nano-Si powder and physically mixed it with CNF. The electrode was fabricated with 60~80 wt% of active materials, 10~20 wt% of acetylene black and 20 wt% of PVDF [131]. Yoon et.al. [132], used graphite and CNF (85 wt%) as an active material and 15 wt% of PVDF to assemble the electrode.

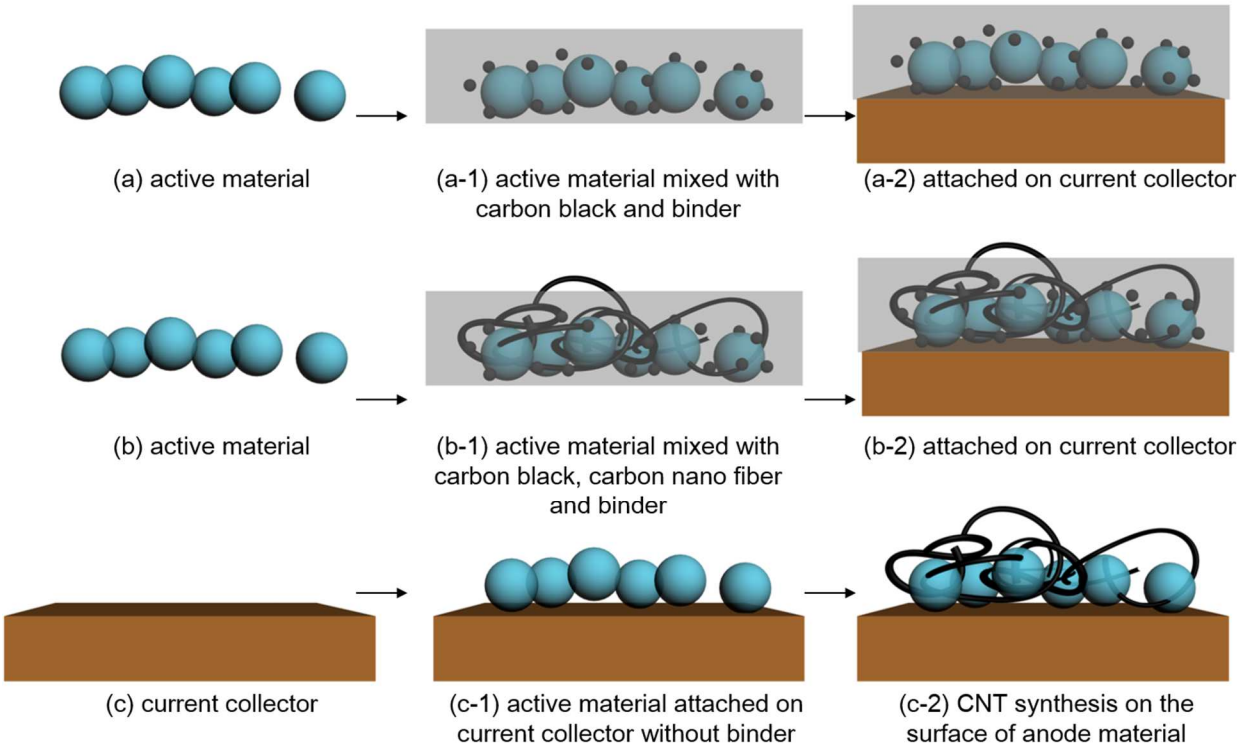

Figure 7-1. Method to fabricate an anode electrode: (a) conventional method, (b) current researchers' approach, (c) new approach for binder free electrode used in this work.

The current research is focused on the active materials. Ina typical anode, 10~20 wt% of conducting materials and similar amount of binder are used. The binder is essential part to attach active materials onto current collector. Some polymer materials such as PVDF and sodium carboxymethyl cellulose (CMC) are used for binder, and they are non-conducting materials. So

additional conducting materials (e.g. carbon black, acetylene black) must be added to make the active material/binder mixture electrically conductive. Although the binder helps active materials to be attached onto the current collector, they also work as an impurity. It hinders the movement of Li ion, which must move freely in anode electrode for a good battery performance.

The most commonly used binder in Li-ion battery is PVDF, which is flexible and chemically stable. It is also widely used in semiconductor, medical, chemical, and aerospace industries. However, due to the high chemical stability, strong solvent must be added to apply it. Usually, 5 wt% of PVDF is mixed with 95 wt% of N-Methyl-2-pyrrolidone (NMP) to cast the active materials onto current collector. Although NMP is a biodegradable material with low toxicity, it is on the list of Chemicals Known to the State to Cause Cancer or Preproductive Toxicity. Even some manufacturers are considering to use alternative solvents instead of NMP.

In this work, we found that binder free anode electrode for Li-ion battery can be easily fabricated. Figure 7-1(c) shows that active materials are attached directly onto a current collector, and CNTs are synthesized on the surface of active materials to enhance the conductivity and mechanical strength of anode electrode.

Silicon nanoparticles (SiNPs) are surface treated with acid piranha solution, which was prepared with mixture of 80 ml of concentrated H_2SO_4 and 30ml of 30% H_2O_2 for 30min at ambient temperature and washed with methanol thoroughly. Then, they were treated with 1%-HF aqueous solution for 30 min to remove the oxide which was formed during the piranha solution treatment. (Figure 7-2(a))

Figure 7-2(b) illustrates the catalyst anchoring on SiNP surface. A cobalt acetate and iron acetate precursor were used as a catalyst without further treatment. 2.5 wt.% of cobalt and iron

metals were dissolved in 20ml of methanol and then, the surface treated SiNPs were mixed with catalyst solution homogeneously under sonication for 24 hr at room temperature.

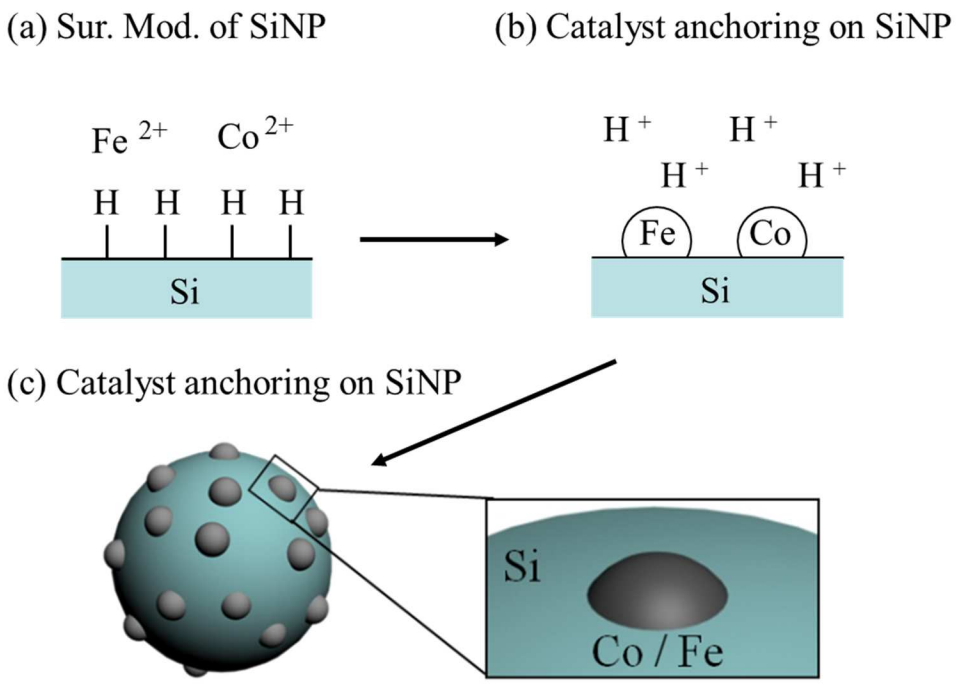

Figure 7-2. Scheme of (a) Surface modification of SiNP, (b),(c) Fe/Co bicatalyst anchoring on the surface of SiNP.

Some catalysts such as Fe-Co and Co-Mo are quite effective in growing single-walled carbon nanotubes. There bimetallic catalysts form smaller catalyst particles than single elemental catalysts and generate CNTs with higher efficiency [133-135]. For example, Fe-Co bimetallic catalyst impregnated in a zeolite support has been used to synthesize single-walled CNTs by catalytic chemical vapor deposition (CCVD) [133]. When only Co catalyst is used to grow CNTs on Si/SiO_2 surface, 7~20 nm Co catalyst particles were formed at the surface and then upon heating they penetrated into the SiO_2 layer. The subsequent CNT growth followed the root growth model. However, when Fe catalyst was used alone, a uniform catalyst layer with a thickness of about 10 nm was formed on the top of SiO_2 layer and little growth of CNT occurred

[134]. The idea of using Fe-Co bimetallic catalyst is that Fe in the Fe-Co bimetallic catalyst presents Co atoms from diffusing into SiO_2 and aggregating into larger particles, offering more effective catalytic sites for the surface growth of CNTs.

The premixed SiNPs/Fe-Co catalyst solution was spread on Cu foil at 80°C oven. After the solvent has been evaporated, SiNPs/Fe-Co catalyst was deposited on the surface of Cu foil without any binder (Figure 7-3(b)). The Cu foil/SiNPs/Fe-Co electrode was punched to ½ inch diameter as shown in Figure 7-3(c). Finally CNT was directly synthesized on the 1/2 inch anode disk as illustrated in Figure 7-3(d)

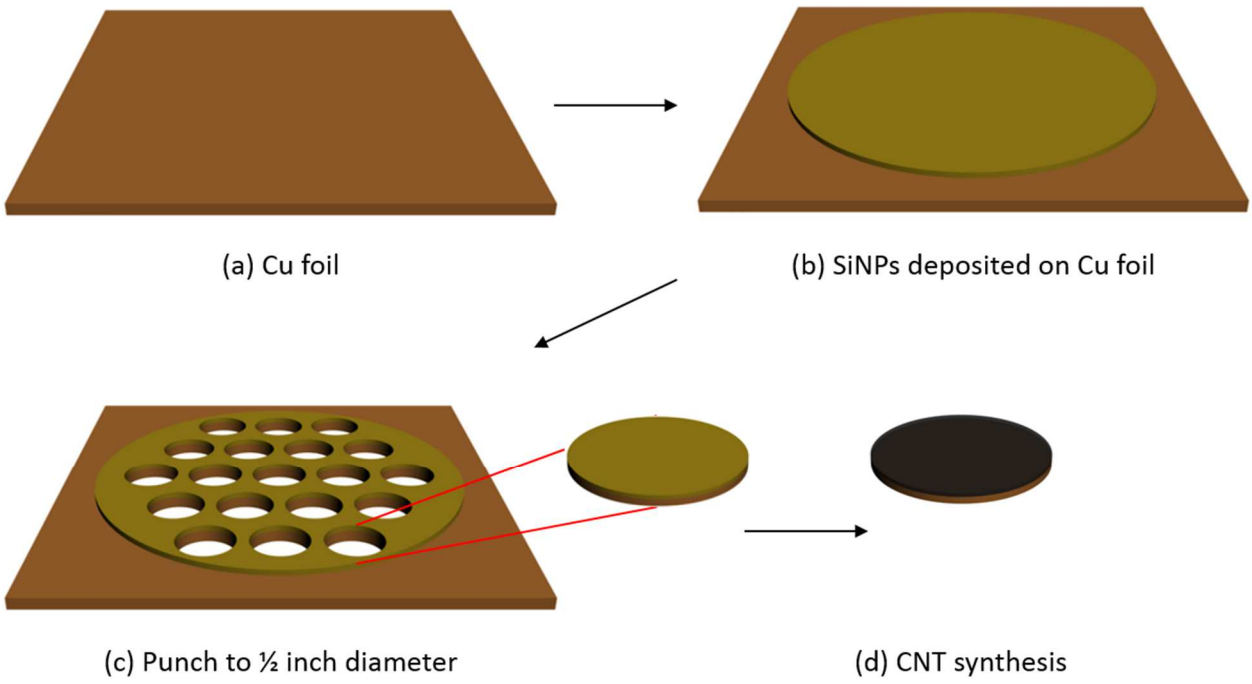

Figure 7-3. Picture of (b) SiNP attached Cu foil w/o binder, (c) after punch to 1/2 inch diameter, (d) after CNT growth on SiNP/Cu anode.

Figure 7-4(a) shows the chemical vapor deposition (CVD) reactor set-up. The CNT was grown over the Cu foil/SiNPs/Fe-Co electrode at 550~900°C for 2 min to 40 min by supplying an acetylene gas (12.5 ml/min) as a carbon source and a nitrogen gas (150 ml/min) as a carrier

gas. Figure 7-4(b) is the picture of actual furnace (Lindberg Blue M series, Thermo Scieentific.) and 1 inch quartz tube used in this experiments.

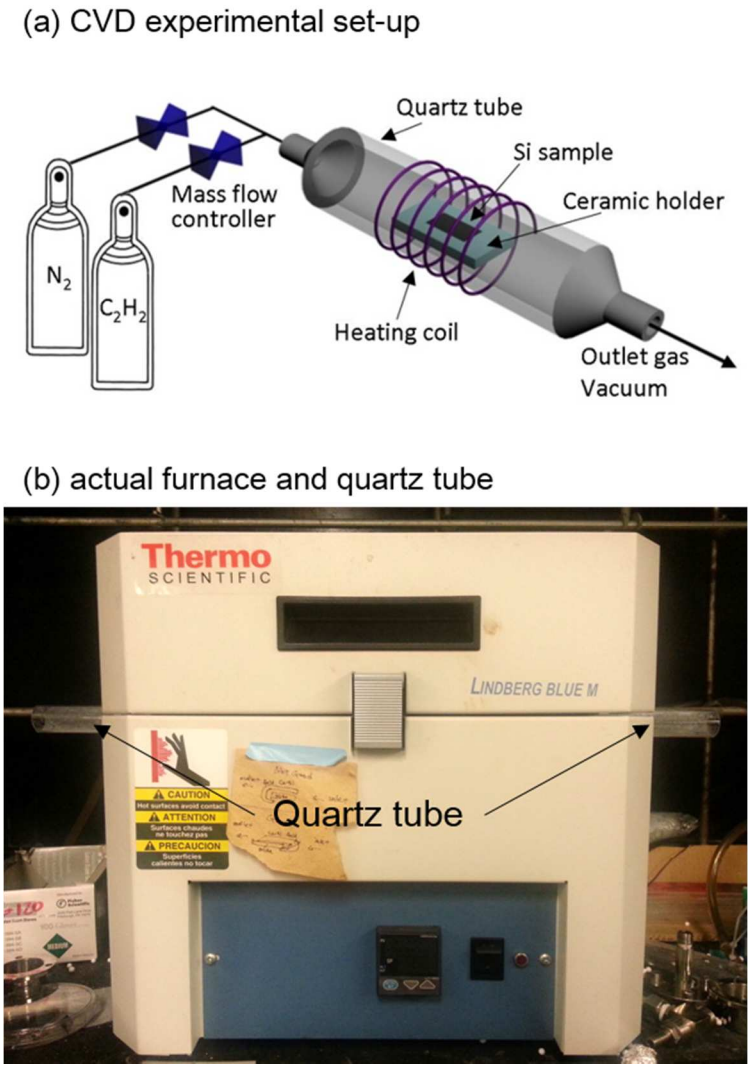

Figure 7-4. (a) Experimental scheme of CVD for CNT synthesis. (b) picture of actual furnace and quartz tube used in this experiments.

7.3.3. Modification of copper foil to nanostructured surface

Cu foil is widely used current collector and when Si particles coated onto it with a binder, the stress buildup by expansion of silicon particles causes them to crack and fracture and to be detached from the current collector surface, losing electrical connectivity.

Here, the copper foil surface (Figure 7-5(a)) is modified to a porous nanostructure or 'knife-like' structure (Figure 7-5(b)) where SiNP particles can be trapped securely (Figure 7-5(c)) during the lifetime of a battery during which they may undergo lithiation/delithiation and partial fragmentation. Finally, CNTs are grown on the surface of SiNP ((Figure 7-5(d)).

The main idea is that the surface layer of Cu can be chemically oxidized to CuO with a nanostructure [136]. And then it can be converted back to Cu by reduction reaction [137, 138]. The Cu foil was first cleaned in an ultrasonic bath with acetone and rinsed with ethanol, isopropyl alcohol, and deionized (DI) water. Then the film was immersed in a 2.0 M hydrochloric acid solution to remove the native oxide film on the surface and then it was rinsed with DI water. The Cu foil was dipped into an alkaline solution for various reaction temperature and time to form Cu_2O layer, which was reoxidized to sharp, knife-like CuO structures with a layer height of about 1μm.

The isothermal reduction of CuO was performed at 250^{o}C for 1hr under 5%-H_2 / 95%-Ar mixture and a flow rate of 200 ccm in a quartz tube furnace.

The SiNP/Fe/Co solution was spread on nanostructure-surfaced Cu foil at 80^{o}C oven. After the solvent was removed, SiNP/Fe-Co catalyst was firmly deposited onto the surface of modified Cu foil. The modified Cu foil/SiNP/Fe-Co electrode was punched to a ½ inch diameter disc and placed in the quartz tube furnace for CNT growth. The CNT was grown over the Cu

foil/Si electrode at 550~900ºC for 2 min to 40 min by supplying an acetylene gas (12.5 ml/min) as a carbon source and a nitrogen gas (150 ml/min) as a carrier gas.

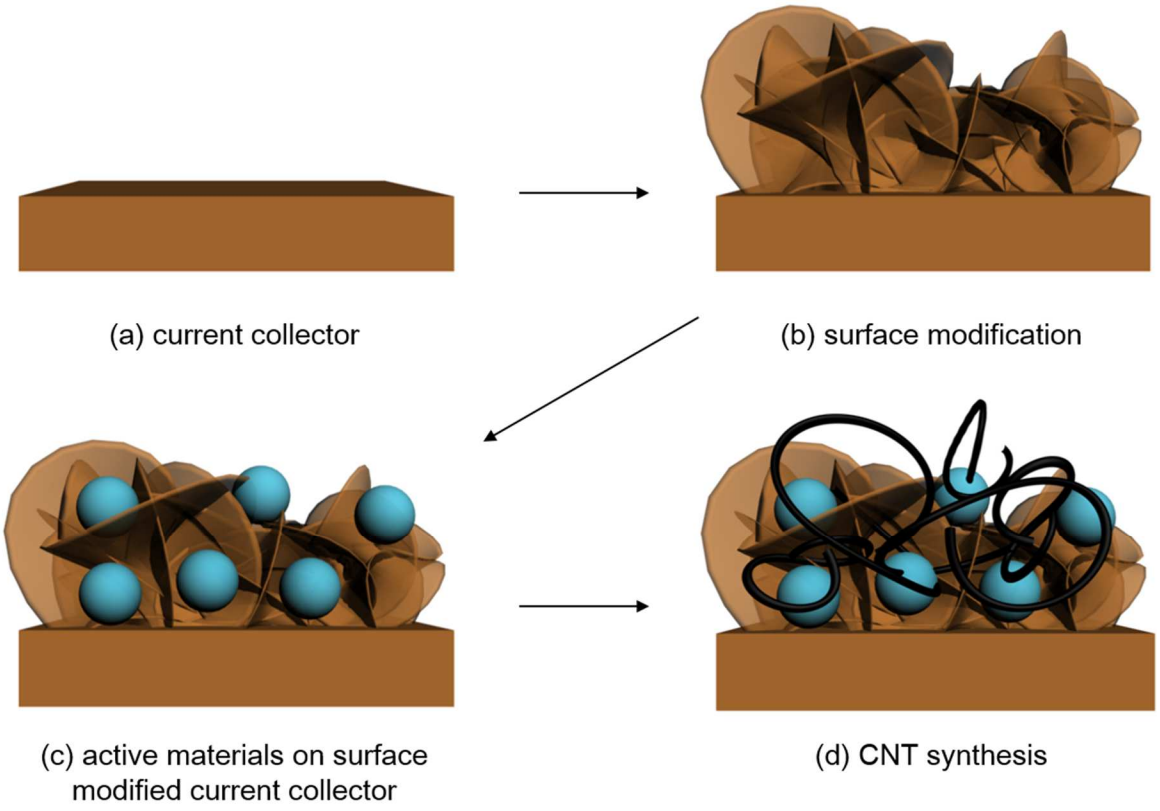

Figure 7-5. Illustration of surface modified current collector electrode.

7.4. Results and discussion

7.4.1. Morphology of catalytic growth of CNTs on Si nanoparticles.

CNTs in the Si/CNT anode system have two major function: (i) they provide pathway for electrons to a current collector, (ii) they mechanically hold or wrap expanding and fracturing SiNP to sustain the connectivity to current collector as Si particles expand and fragment. It was observed that the growth of CNTs and their morphologies are strongly dependent on the reaction conditions such as temperature, reaction time, catalyst, and carbon source flow rate.

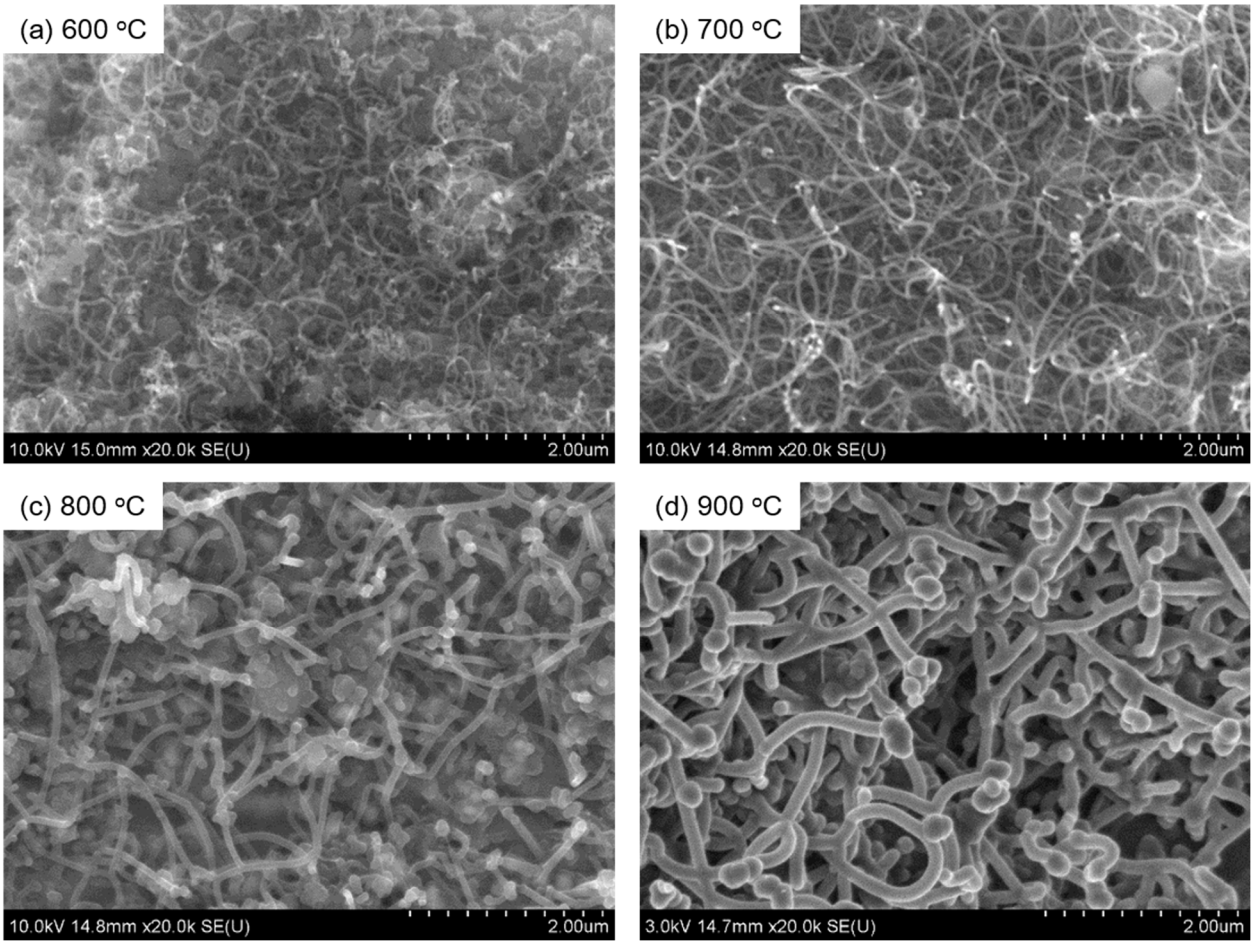

Figure 7-6. CNTs grown at different reaction temperature. (a) 600 oC, (b) 700 oC, (c) 800 oC, (d) 900 oC. Acetylene gas : 12.5 ccm, Nitrogen gas : 150 ccm, Reaction time : 3.5 min

Figure 7-6 shows the CNTs synthesized on Si surface at different temperature for 3.5 min. As the reaction temperature increased, thicker CNT has formed. Figure 7-7 also indicates thicker CNTs has synthesized as the reaction time has increased at same temperature. At high reaction temperature, the carbon sources are deformed and deposited on any surface. In this case, they deposited on the surface of CNT and make it thicker. After CNT synthesis at 900^{o}C, it is found that the inner layer of quartz tube becomes black due to the carbon sediments.

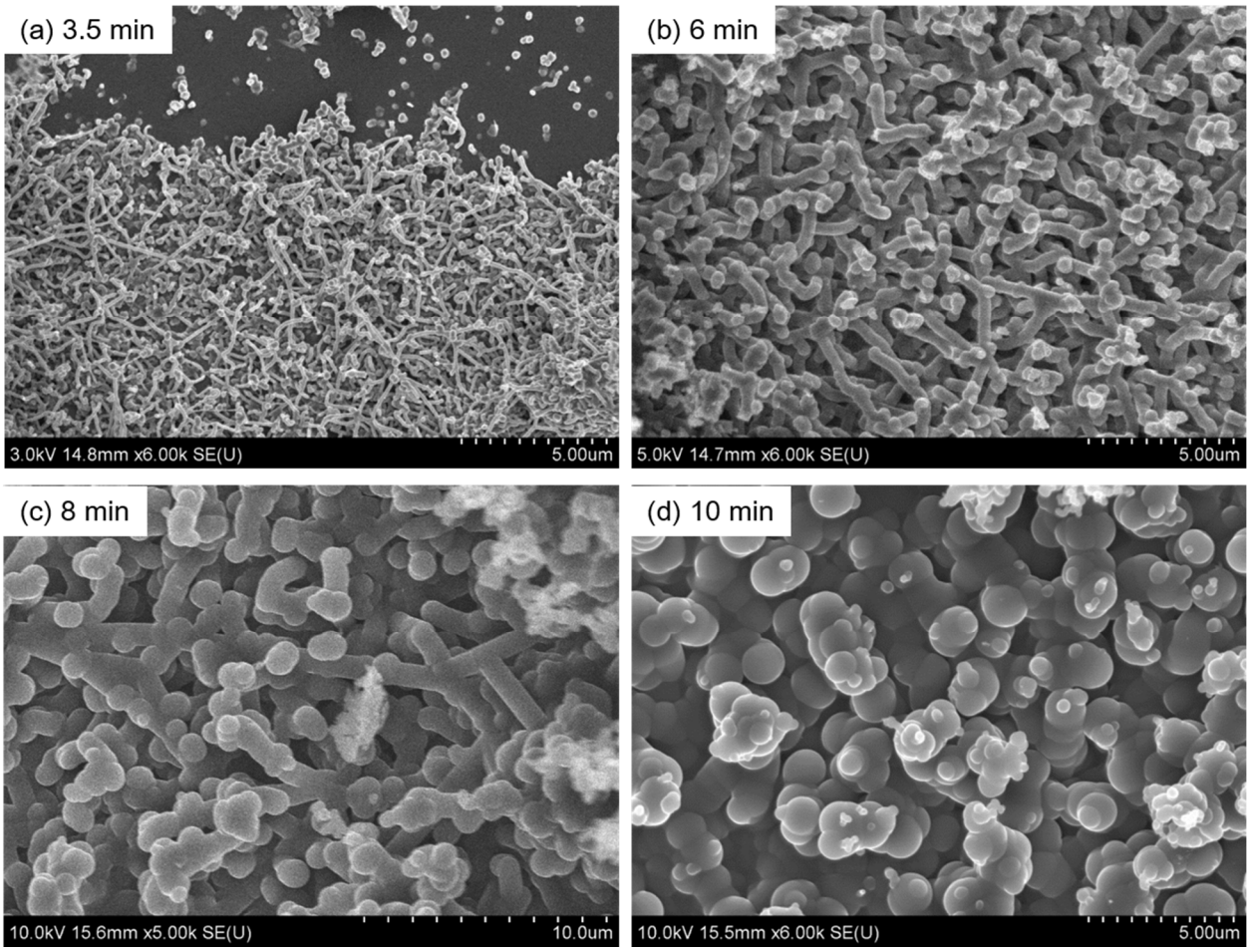

Figure 7-7. CNTs grown at different reaction time (a) 3.5 min, (b) 6 min, (c) 8min, (d) 10 min. Acetylene gas : 12.5 ccm, Nitrogen gas : 150 ccm, Reaction temperature : 900 oC

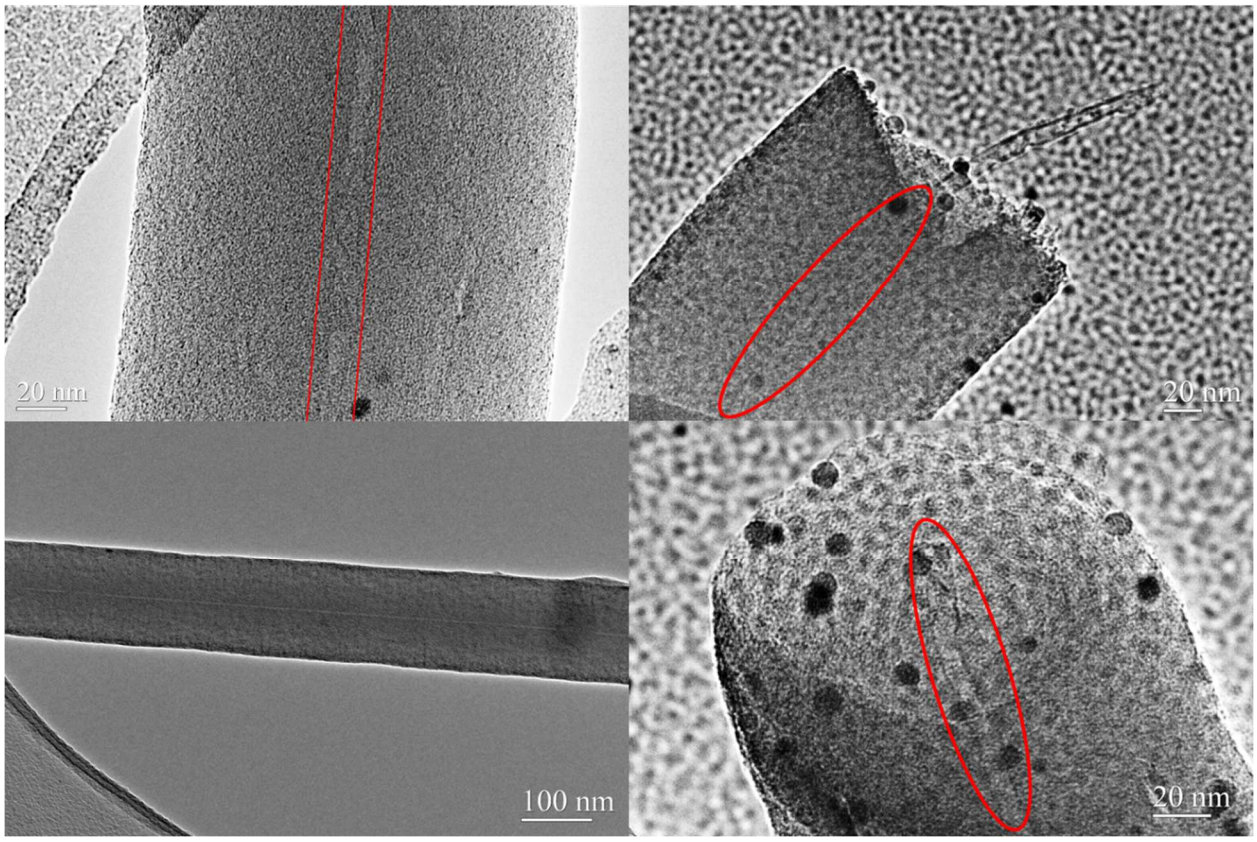

Figure 7-8. TEM images of CNTs grown at 700 oC for 5 min. Acetylene gas : 12.5 ccm, Nitrogen gas : 150 ccm.

Figure 7-8 are the TEM images of CNTs grown at 700 ^{o}C for 5 min. The flow rate of acetylene and nitrogen gas was 12.5, and 150 cm^3/min, respectively. These images confirm the existence of nanotube, which has a diameter around 10nm in the core of each CNTs. It seems like initially the 10nm CNTs are formed, and in the meantime, carbon sources are deformed and attached around the nanotubes so make the CNTs thicker. At higher temperature (Figure 7-6(a) vs. (d)) and longer reaction time (Figure 7-7(a) vs. (d)), the carbon sources become easier to degrade and have more chance to deposit around the thin nanotubes to make them thicker.

To warrant the no-loss of connectivity even with fragmented Si particles, it is important to have CNTs covalently attached to the Si surface. There are many of literature on the catalytic growth of CNTs with bimetallic catalysts but not much has been reported on the kinetics of CNT

growth reactions, which is essential to control the morphology of CNTs ideally suited for Li-ion battery applications.

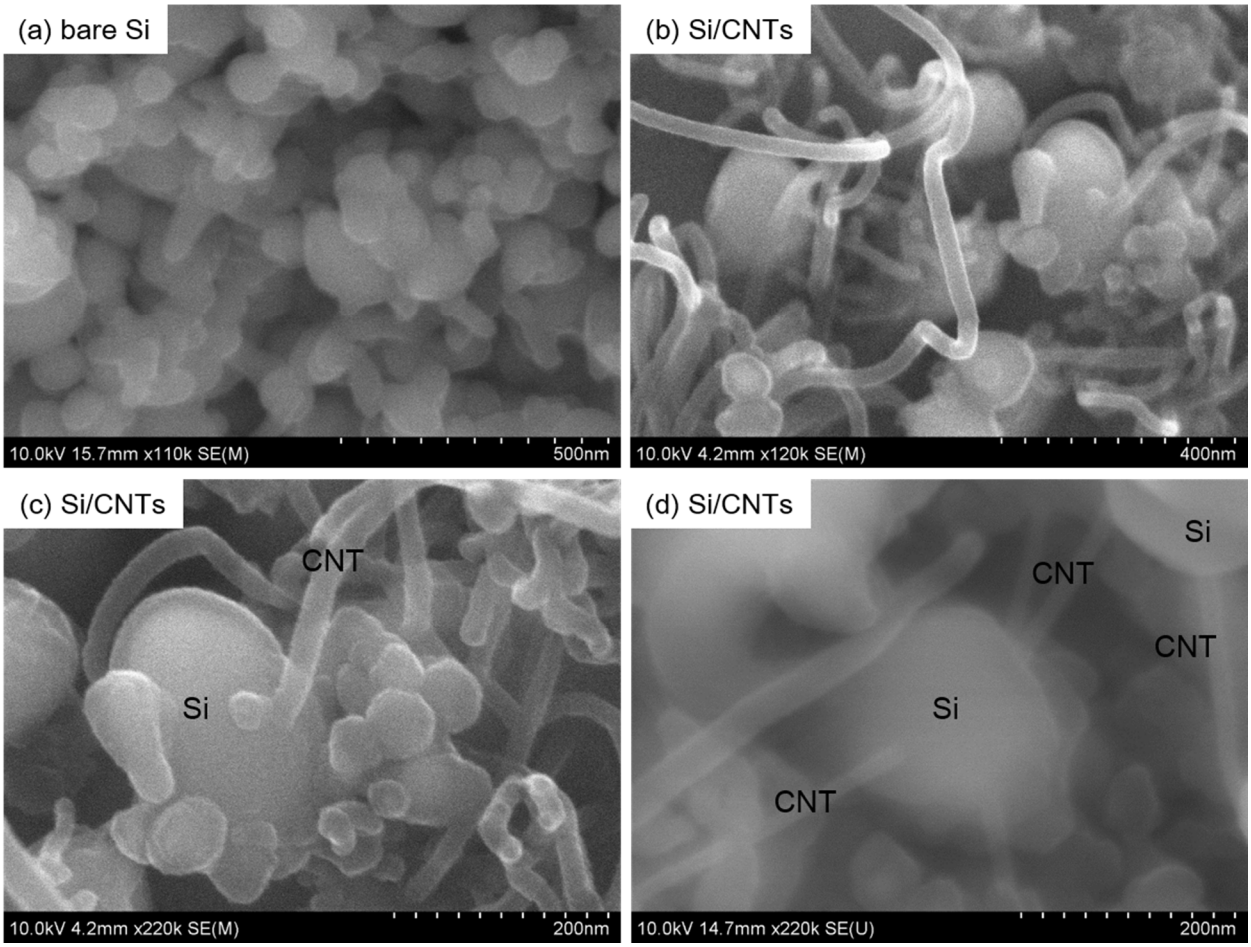

Figure 7-9. SEM images of (a) bare silicon nanoparticles, (b), (c), and (d) CNTs synthesized on Si.

Figure 7-9 shows the SEM images of bare SiNP used in this experiments (a), and CNTs synthesized on Si surface for 1.5 min at 700 ºC with flow rate of 12.5 ccm of acetyelene and 150 ccm of nitrogen (b), (c), and (d). Bare SiNPs used during this experiments have a broad size distribution with diameters less than 200 nm, and the diameter around 20~35 nm CNTs are stretched out from SiNP.

7.4.2. Morphology of catalytically grown CNTs on Binder Free Si/Cu electrode.

To use Si/CNTs composite, binder is necessary to attach Si/CNTs active materials onto current collector (Cu foil) as illustrate in Figure 7-10. Although binder is an essential material to attach active materials onto current collector for Li-ion battery, it is a non-conductive material so the additional conducing materials are required. And also it act as an impurity, which hinders/blocks the movement of Li ion. If binder is successfully removed, Li-ion can move freely inside of the cell.

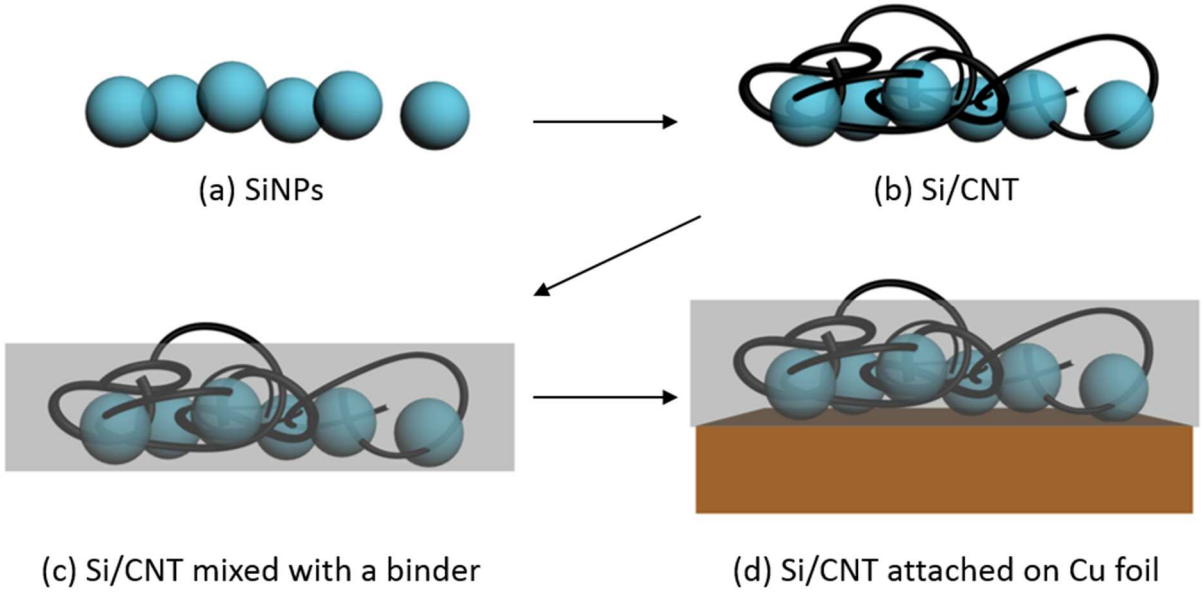

Figure 7-10. Illustration of procedure to apply Si/CNT active materials onto the current collector.

In this study, binder free electrode has been fabricated. The concept of binder free electrode is shown in Figure 7-1(c), and actual pictures of this process are shown in Figure 7-11. To fabricate binder free electrode, SiNPs were first mixed with metal catalyst solution, then it was spread onto Cu-foil. After the evaporation of the solvent, SiNPs were deposited well onto Cu-foil during the whole process of this experiments (Figure 7-11 (a)). Then it was punched to

1/2 inch diameter size for coin cell assembly (Figure 7-11 (b), (c)). Finally 1/2 inch Cu/Si unit is placed in a quartz tube reactor to synthesize CNT on the surface of SiNPs (Figure 7-11 (d)).

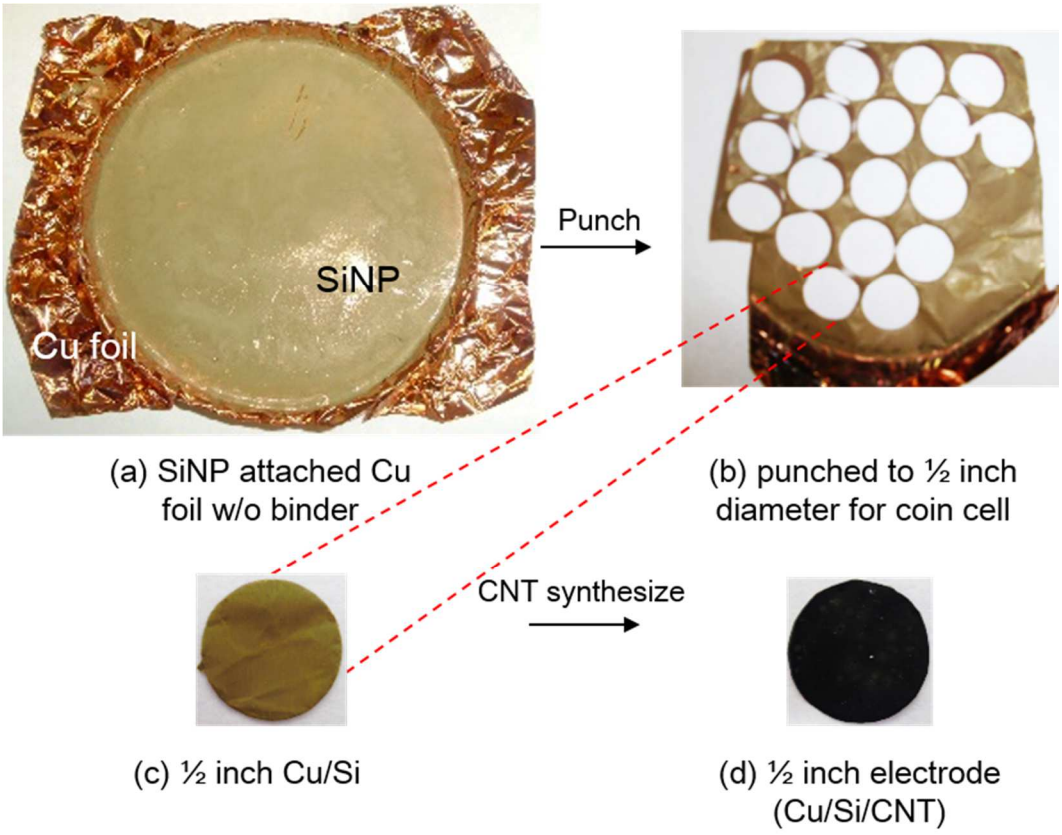

Figure 7-11. Experimental pictures: procedure for binder free electrode fabrication.

CNTs were synthesized for various reaction time at different reaction temperatures. Figure 7-12 represents the SEM images of binder free electrode. Figure 7-12(a) is a neat Cu foil, and Si deposited Cu foil is shown in Figure 7-12(b). CNTs were synthesized at 900^{o}C for 3.5 min (Figure 7-12(c)) and 8 min (Figure 7-12(d)). As it has already been confirmed at section 7.4.1 (page176), the thickness of CNT increased as reaction time.

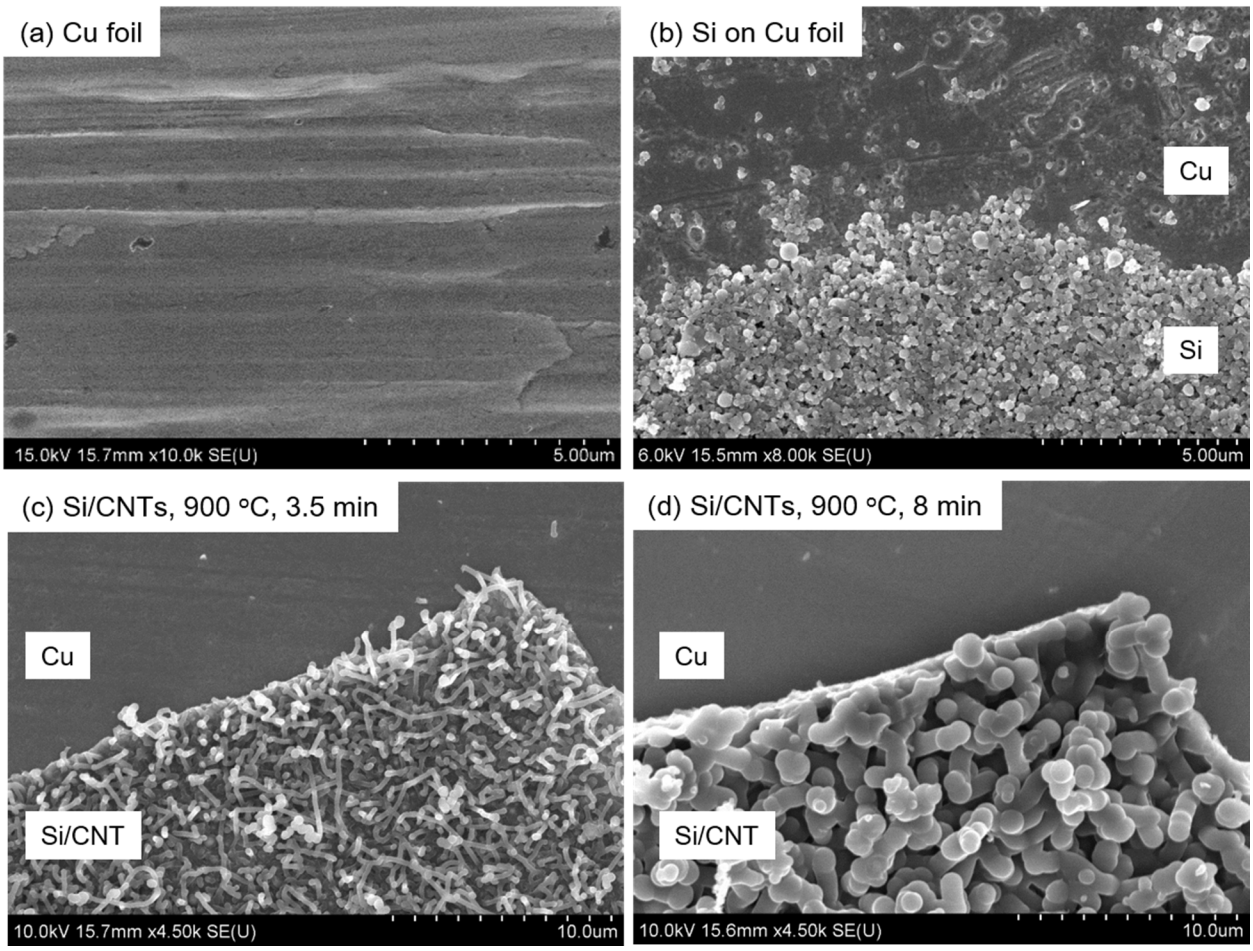

Figure 7-12. SEM images of binder free electrode. (a) Cu foil, (b) SiNP deposited onto Cu foil without binder, (c) after CNT growth at 900oC for 3.5 min, (d) after CNT growth at 900oC for 8 min.

Figure 7-13 is EDX mapping image of binder free Si/CNT anode (sample Figure 7-12(c)) (Blue-Cu, Green-Si, and Red-C), and it is figured out that the CNTs are grown from Si parts.

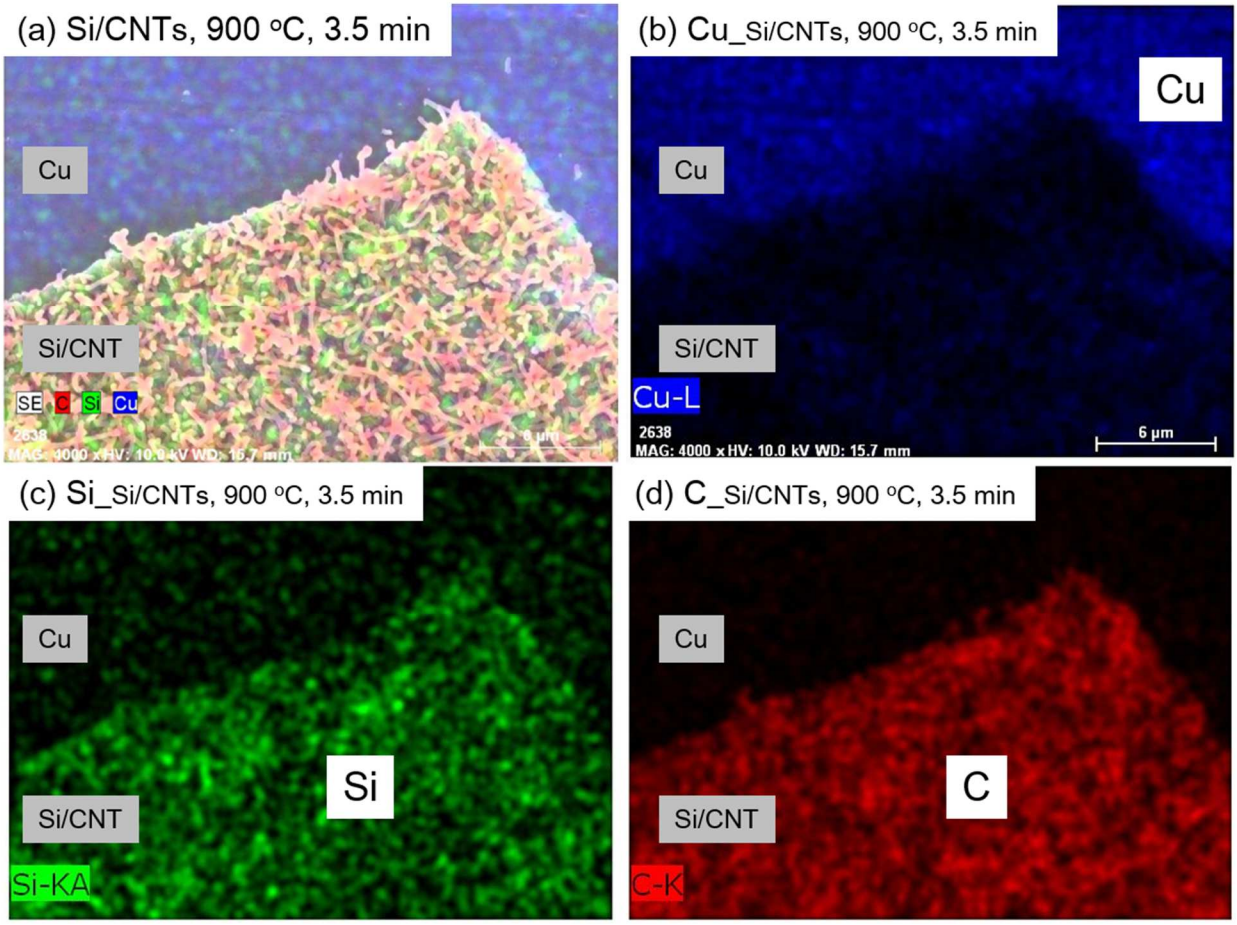

Figure 7-13. EDX mapping of (a) binder free Si/CNT anode (sample Figure 7-12(c)), (b) Cu element mapping, blue, (c) Si element mapping, green, (d) C element mapping, red.

Although, the CNTs were successfully synthesized at 900°C, longer and thinner CNTs were required to wrap the SiNPs effectively. So the reaction temperature was reduced to 500 ~ 700°C, and CNT synthesis was performed with an acetylene (12.5 ccm) and nitrogen gas (150 ccm) for 3.5 min. Figure 7-14 show the SEM images of the results. At 500°C (Figure 7-14(b)), no CNTs were formed on the Si surface because the reaction temperature was too low for the CNT formation. On the other hand, at 600°C and 700°C, CNTs were formed well especially at 700°C. Additional CNT synthesis studies were performed at 700°C for various reaction time.

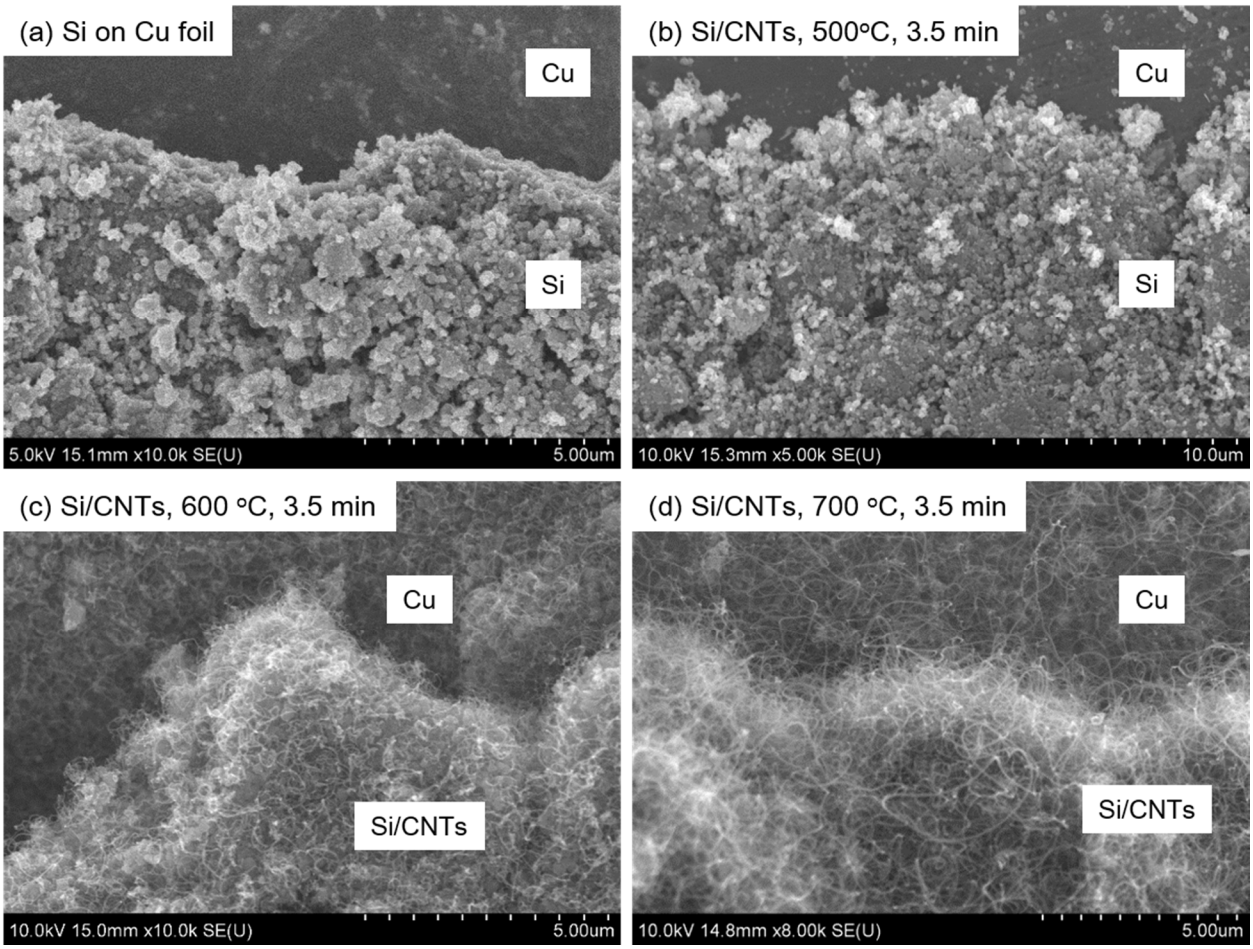

Figure 7-14. SEM images of (a) binder free Si on Cu foil, and CNTs synthesized condition at (b) 500oC, (c) 600oC, and (d) 700oC for 3.5min.

CNTs were synthesized at 700^{o}C for 5, 7, 10 min on binder free Si/Cu electrode. The left column of Figure 7-15 shows the SEM images of each binder free Si/CNTs. As reaction time increased, more CNTs and thicker CNTs are formed. However compared with 900^{o}C (Figure 7-7, Figure 7-12), the difference is small. This is mainly due to the reaction temperature, where at high temperature the carbon can deposit easily on the surface of CNTs, hindering the acetylene gas to diffuse into the inner layer of SiNPs. This means that at high reaction temperature, the carbon source degrade, and it becomes difficult to synthesize the CNTs inside of SiNPs layers due to the diffusion resistance. In other words, at high reaction temperature, CNTs are formed only at the top layer of SiNPs, which is not quite desirable. CNTs must be formed evenly and so that they can wrap as many SiNP as possible to work as an electron conductor.

The images on the right column of Figure 7-15 represent the cross sectional view of each sample. At 5 min reaction, around 1/3 upper portion has Si/CNTs and the rest is only Si. The Si/CNTs portion becomes larger as reaction time increased, and finally at 10 min reaction, Si/CNTs composites are dominant. Figure 7-16 illustrate this phenomena. Due to the reactor setting, the acetylene gas and nitrogen gas passes through the upper layer of Si/Cu binder free electrode. So the CNTs are first formed on the top surface of packed SiNPs, and as reaction time increased, acetylene gas can diffuse into the inner layer of packed SiNPs to form CNTs.

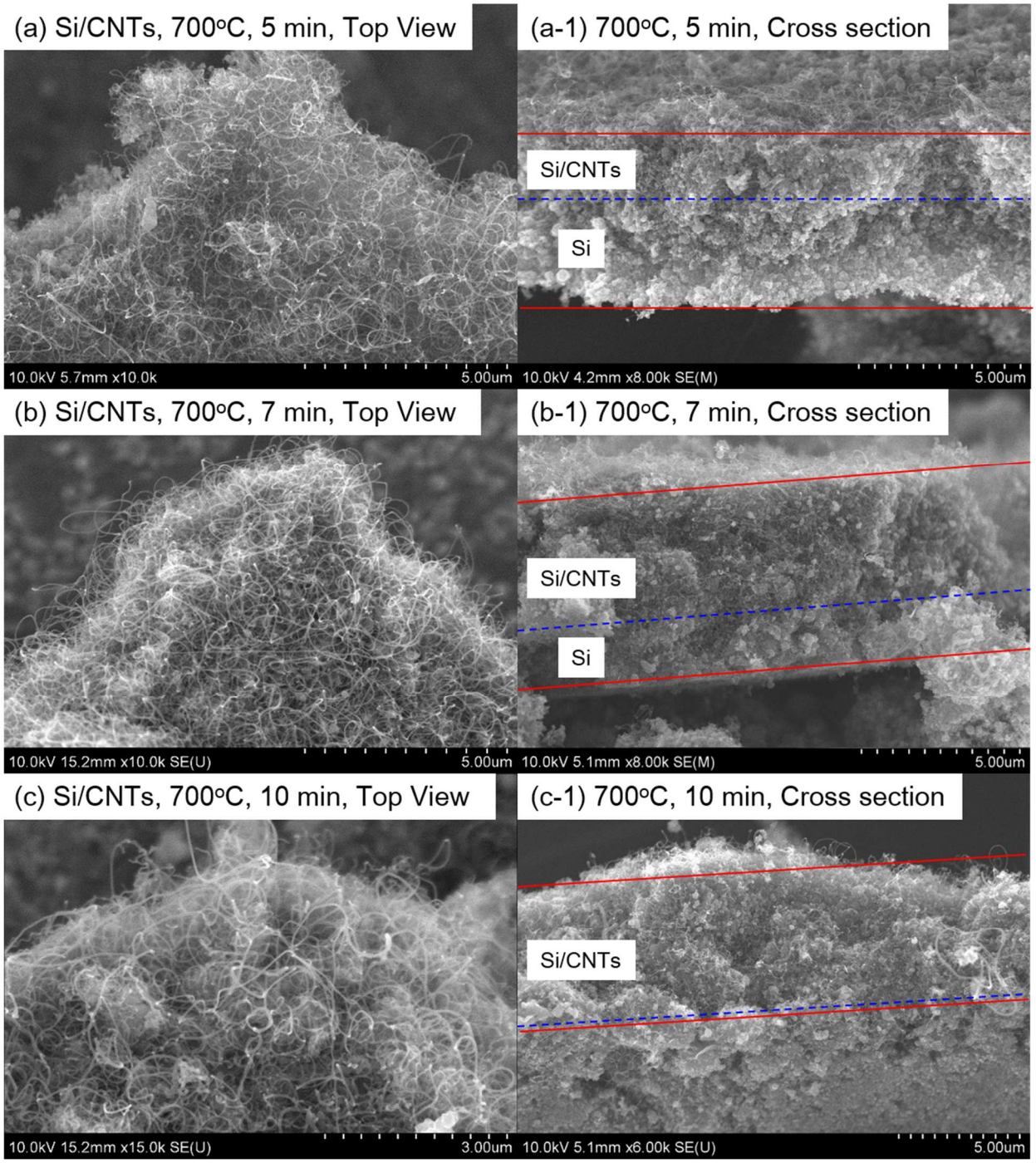

Figure 7-15. SEM images of binder free Si/CNT on Cu foil. CNTs synthesized at 700oC for (a) 5 min, (b) 7 min, (c) 10min. Left column : Top view, Right column : Cross section view.

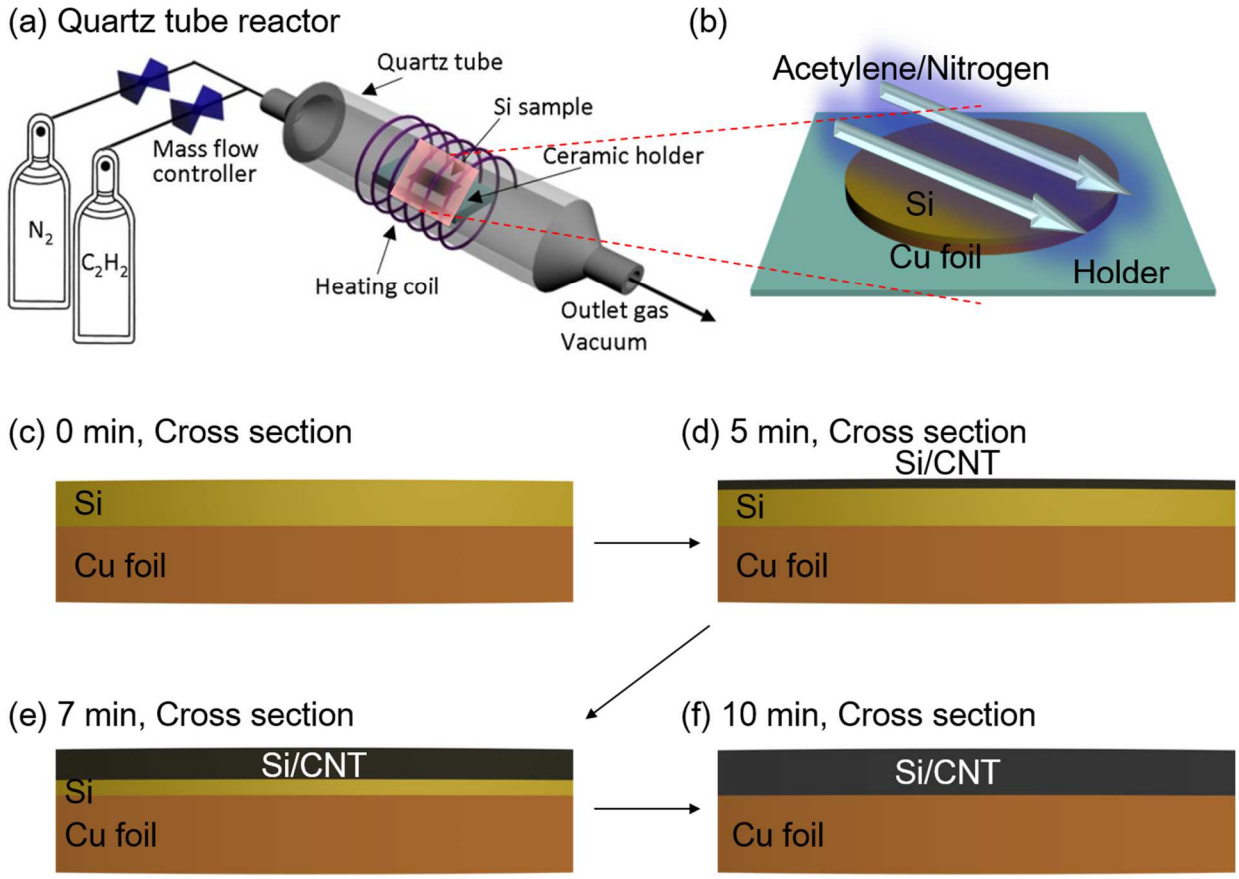

Figure 7-16. Illustration of cross section view of Figure 7-15 (right column).

7.4.3. Control of nano-structured and porous Cu surfaces

The severe volume change of silicon during lithiation / delithiation process leads to pulverization of Si to small particles. The pulverized Si particles lose electrical connectivity to current collector surfaces, and finally they don't function as an active material. To enhance a stability of Li-ion battery, Si particles must maintain the electrical connectivity. Cui's group used silicon nanowires to prevent the fragmentation of silicon [113, 124, 126]. Wang et al. coated silicon with carbon to make a high capacity silicon anode for Li-ion battery [120]. In the study, instead of modifying the silicon active material, the surface structure of a current collector was modified to make a large surface area. The surface modified current collector can simply increase the contact area between active materials and current collector to improve a stability of Li-ion battery.

The idea of this work was adopted from the work by Wang who studied superhydrophobic nanostructured surfaces to improve the heat transfer efficiency of heat exchanger [136]. They modified the surface of Cu pipe to nanostructured CuO as shown in Figure 7-17.

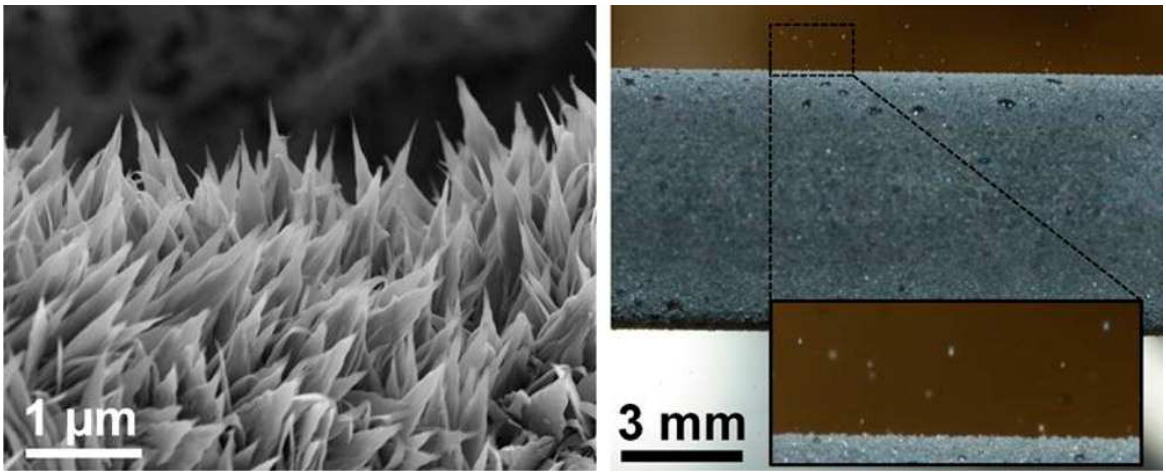

Figure 7-17. Nanostructured CuO tube. Image from research paper [136].

7.4.3.1. Surface Modification of Cu foil to nanostructured Cu foil

Sodium chlorite ($NaClO_2$), sodium hydroxide (NaOH), and sodium phosphate tribasic dodecahydrate ($Na_3PO_4 \cdot 12H_2O$) were used to modify the surface of Cu foil. The composition of alkaline solution and the reaction conditions for the oxidation of Cu foil are listed on Table 7-1.

Table 7-1. Composition of alkaline solution for current collector oxidation

Temperature (°C)	$NaClO_2$	NaOH	$Na_3PO_4 \cdot 12H_2O$	Water	Time
	Weight ratio				
20	3.6	5.0	10.0	160.0	3 hr ~ 24 hr
96	3.6	5.0	10.0	100.0	2min ~ 1 hr

Oxidation: $2Cu + O_2 \rightarrow 2CuO$

Direct Reduction (210~270°C): $CuO + H_2 \rightarrow Cu + H_2O$

Sequential Reduction (≥300°C): $2CuO + H_2 \rightarrow Cu_2O + H_2O$, $Cu_2O + H_2 \rightarrow 2Cu + H_2O$

Cu foil was oxidized at 96°C for 2, 5, 10, 15, 60 min. First of all, Cu foil was cleaned in an ultrasonic bath with acetone and rinsed with ethanol, isopropyl alcohol, and deionized (D.I.) water. Then the Cu foil was immersed into a 2.0 M hydrochloric acid solution to remove the native oxide film on the surface, and then it was rinsed with D.I. water. Given amount of $NaClO_2$, NaOH, and $Na_3PO_4 \cdot 12H_2O$ was mixed with D.I. water. Lastly cleaned Cu foil was dipped into the mixed alkaline solution for desired reaction time for oxidation.

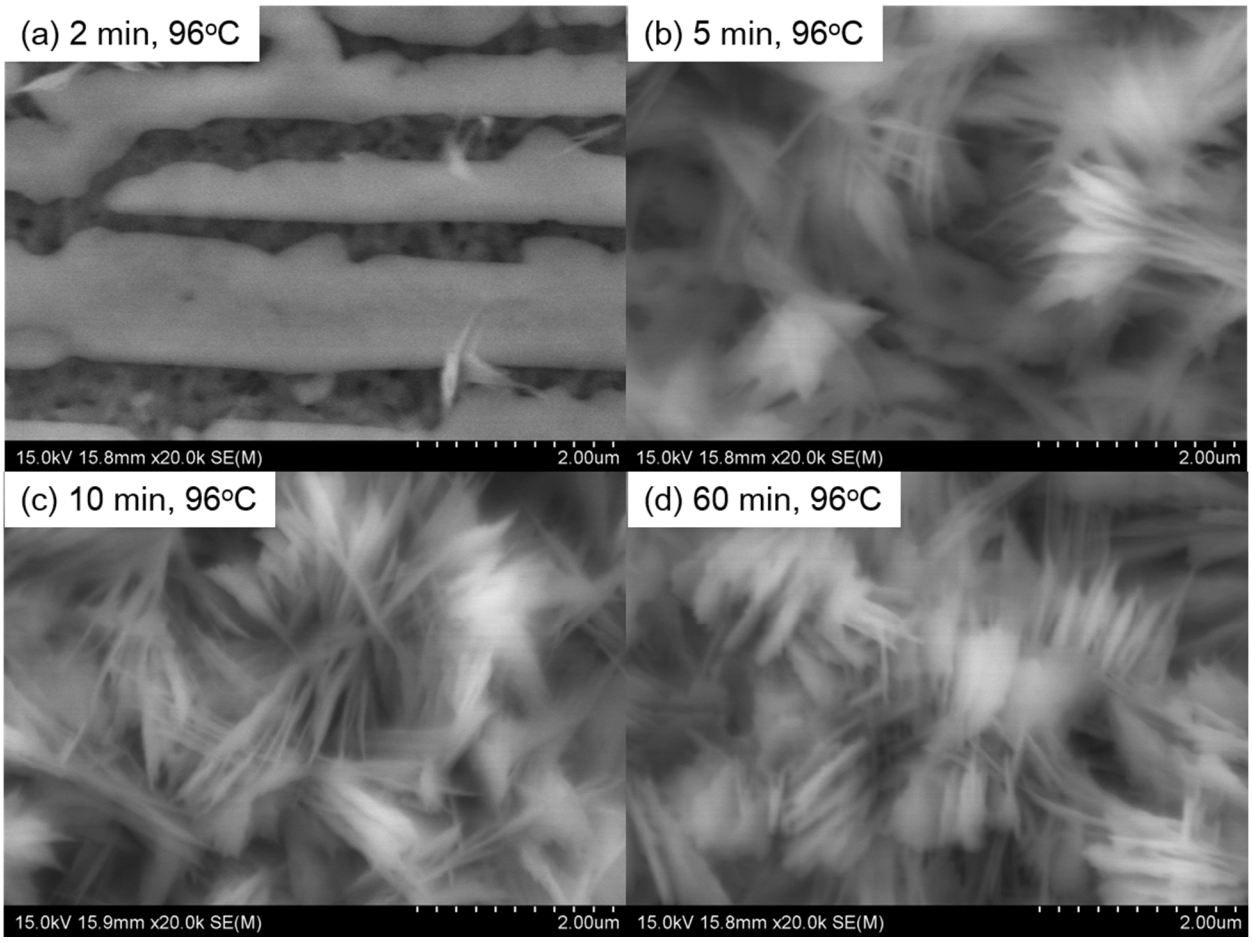

Figure 7-18. SEM images of nanostructured CuO foil. Modified at 96oC for (a) 2 min, (b) 5 min, (c) 10 min, and (d) 60 min.

After oxidation to CuO, the color of Cu foil turned to black (Figure 7-19(a1), (a2)), which is a color of CuO. Note that the color of Cu_2O is red. Figure 7-18 is SEM images of oxidized Cu foil at 96°C for various reaction temperature. It shows that CuO nanostructures are start to develop at about 5 min.

The isothermal reduction of CuO was performed at 250 °C for 1hr with 5%-H_2 / 95%-Ar mixture at a flow rate of 200 ccm. Figure 7-19 shows the pictures and SEM images of CuO (left column), and nanostructured Cu foil (right column), which is reduced from the CuO foil. Even after the reduction of nanostructured CuO foil to Cu foil, the main structure of knife-like

morphology still remains. And surprisingly, the structure becomes rougher, the main purpose of this work, due to the elimination of oxygen (Figure 7-19(b3), (b4)).

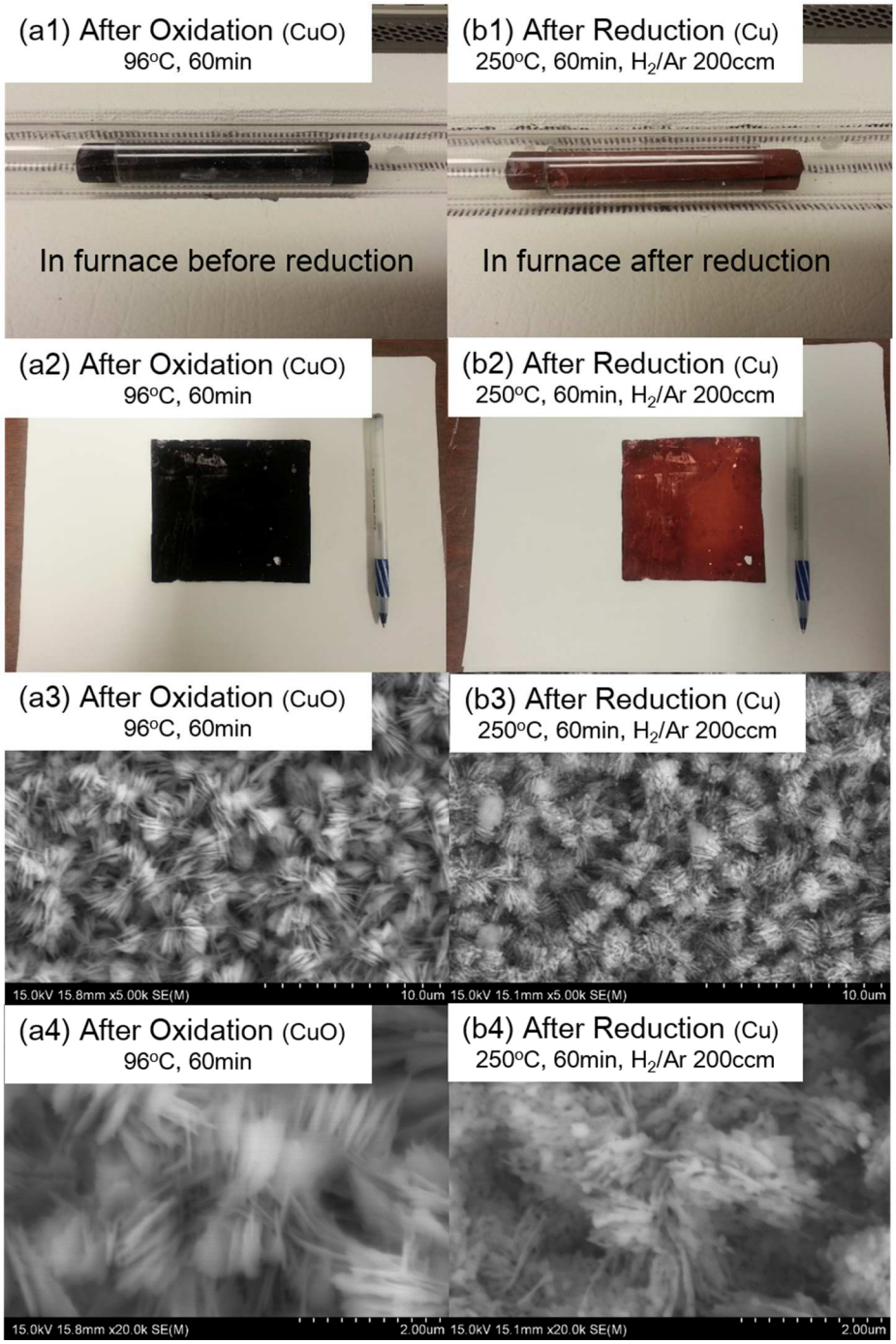

Figure 7-19. Left Column : pictures((a1), (a2)) and SEM images ((a3), (a4)) of CuO nanostructured foil. Right Column : pictures((b1), (b2)) and SEM images ((b3), (b4)) of Cu foil; reduced from CuO.

One problem of this nanostructured Cu foil is that it is so thin and it easily rolls up after CNT synthesis. To solve this problem, only one surface of the Cu foil was modified instead of both sides. When Cu foil was dipped into alkaline solution, both sides of the foil were oxidized. This problem was solved by placing the Cu foil in a petri dish and filling the alkaline solution in it. Figure 7-20 shows the experimental picture of one side oxidation of Cu foil for various time at 20^{o}C.

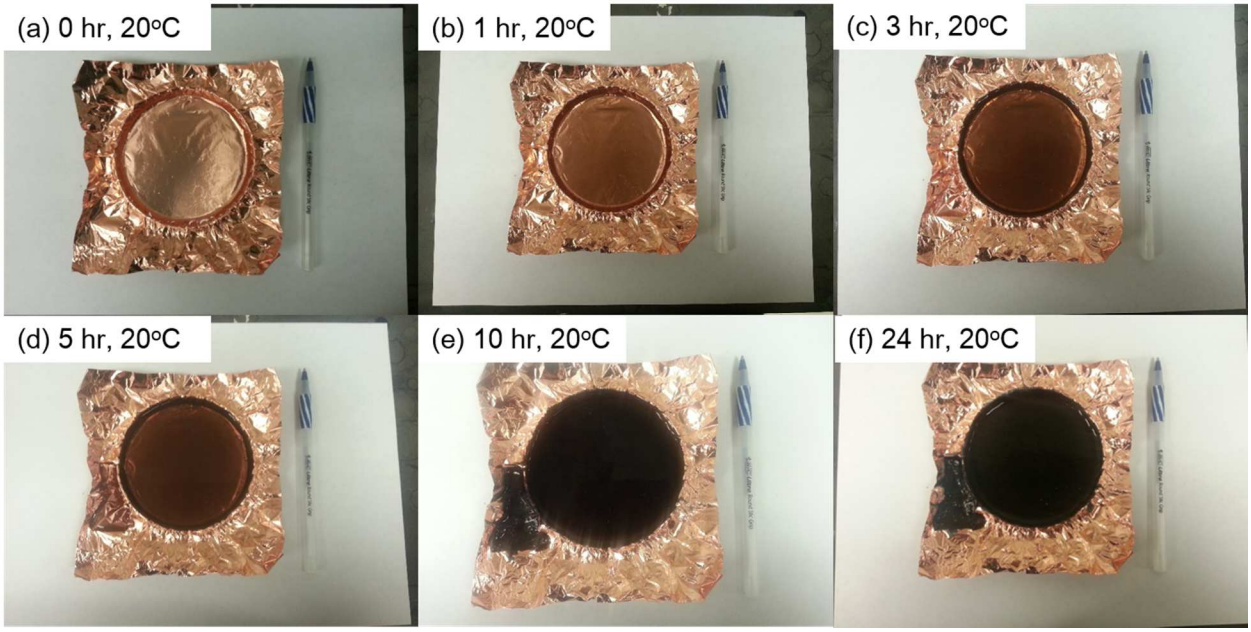

Figure 7-20. Experimental picture of Cu foil placed in a petri dish with alkaline solution at 20oC for (a) before reaction, (b) 1 hr, (c) 3 hr, (d) 5 hr, (e) 10 hr, and (f) 24 hr.

In Figure 7-20, the color change of Cu to CuO at 20^{o}C reaction is clearly displayed. It seems that the conversion of Cu to CuO has already taken at 10 hr. In contrast to 96^{o}C reaction, the rate of reaction is much slow because the reaction temperature was quite low. SEM was used check the morphology of modified Cu foil.

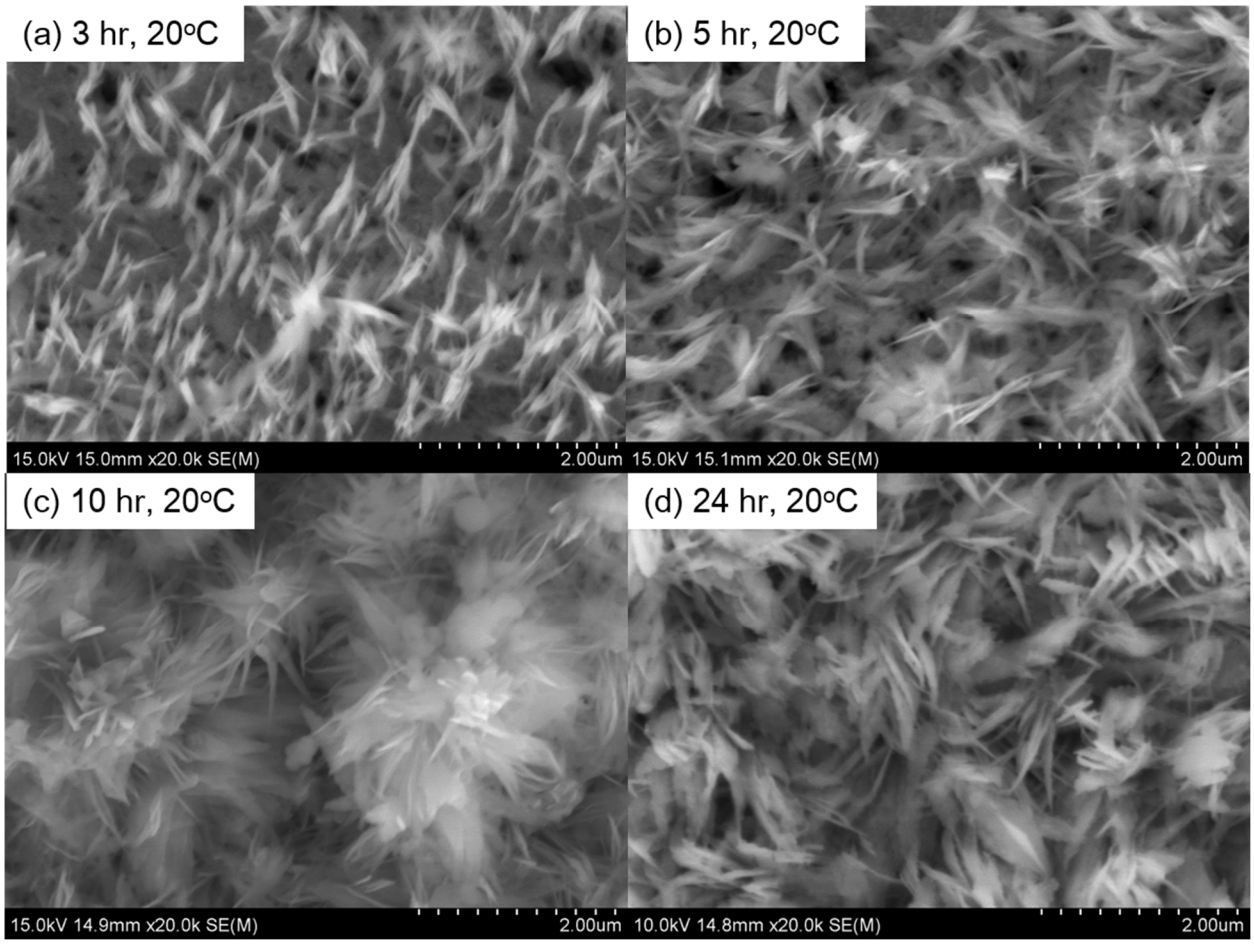

Figure 7-21. SEM images of nanostructured CuO foil. Modified at 20oC for (a) 3 hr, (b) 5 hr, (c) 10hr, and (d) 24 hr

Figure 7-21 are the SEM images of surface modified CuO foil for various reaction times at 20ºC. At 3 and 5 hr reaction, the bottom of Cu foil is still observed. As already seen in Figure 7-20, it takes about 10 hr to fully modify the surface of Cu foil to knife-like morphology (Figure 7-21(c)). The copper and oxygen atom percentage of modified CuO foil was monitored by EDX. Table 7-2 and Figure 7-22 show the EDX's elemental mapping results. EDX's results also confirm that after 10 hr of reaction, copper/oxygen ratio is almost 1:1 (Cu : O = 1.27 : 1), which means CuO is dominant.

Table 7-2. Atom percentage of CuO film for various reaction time.

Time (hr)	Cu (atom %)	O (atom %)	Cu/O
3	88.42	11.58	7.64
5	75.70	24.30	3.12
10	55.91	44.09	1.27
24	53.90	46.10	1.17

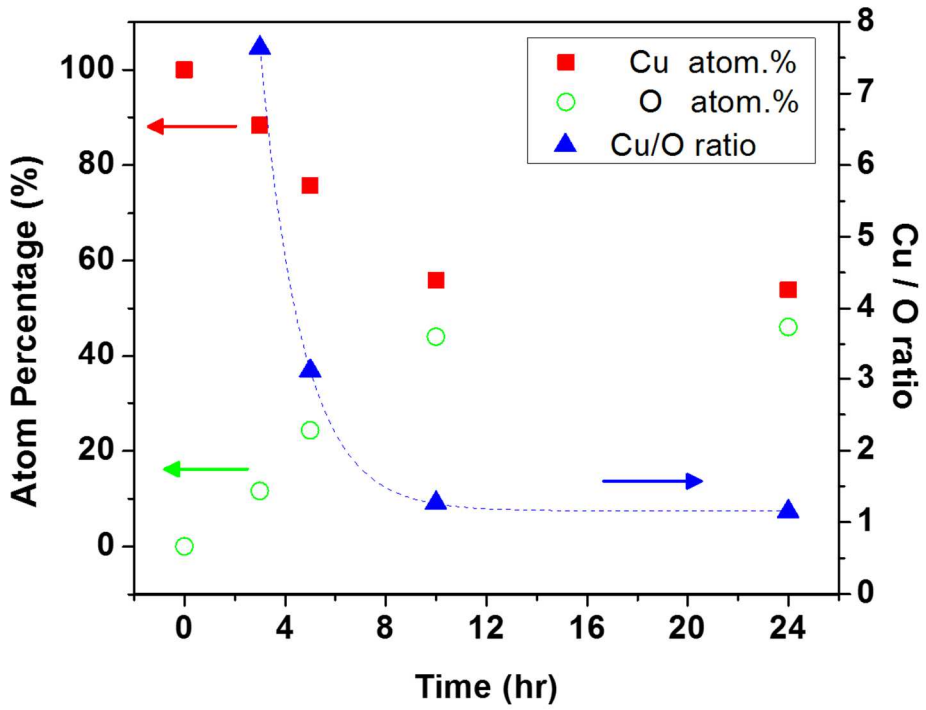

Figure 7-22. Atom percentage of CuO film (Red: Cu, Green: Oxygen), and Cu/O ratio (Blue).

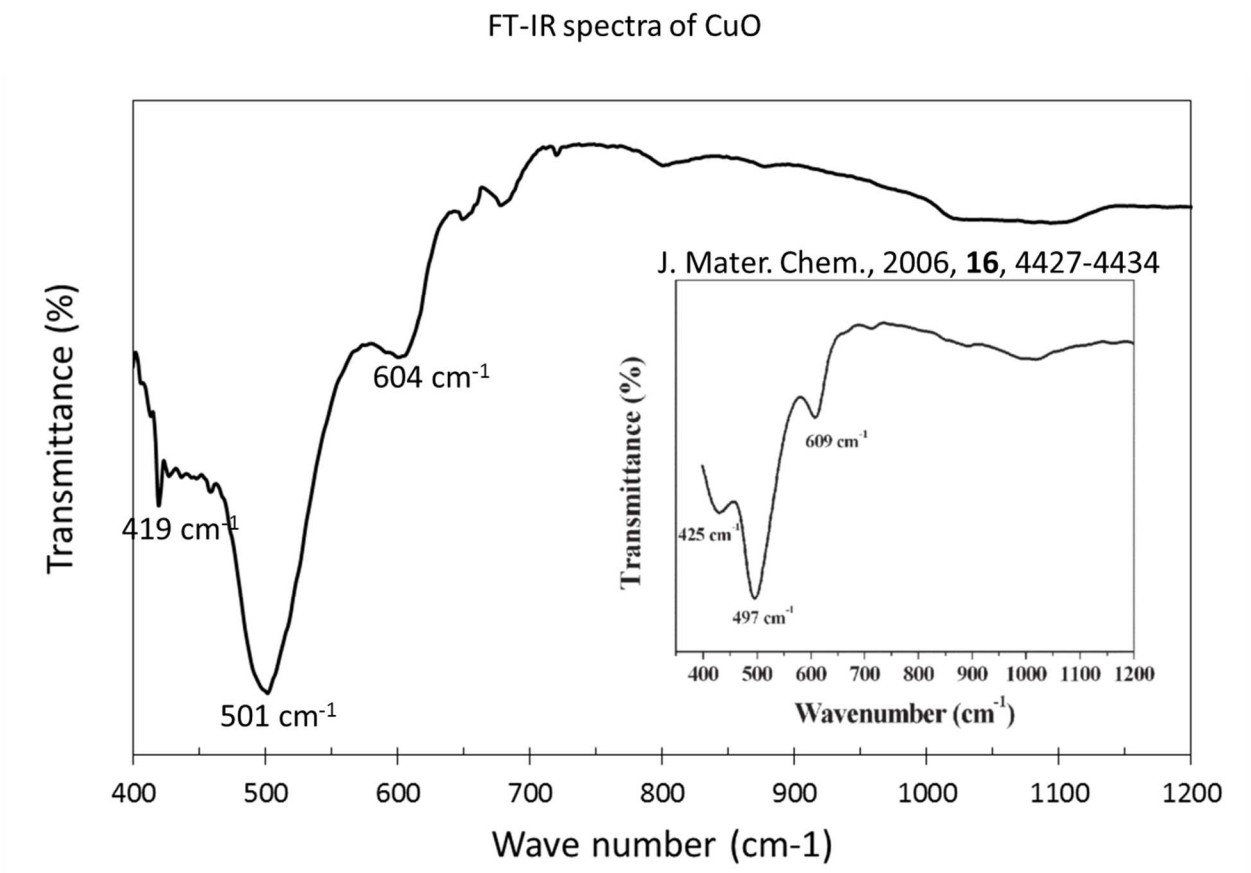

Figure 7-23. FT-IR spectra of nanostructured CuO. (Inside : data from research paper [139].)

The oxidized CuO foil for 24hr was examined by FT-IR analyses. As shown in Figure 7-23, the three main characteristic peaks were observed at around 419, 501, and 604 cm^{-1}. Also the similar spectra has been reported by Huang's group [139], and Qian's group [140]. The mode at ~604 cm^{-1} is a Cu-O stretching along the [-101] direction, and at ~501 cm^{-1} is Cu-O stretching vibration along the [101] direction [139, 140]. No active modes from Cu_2O and other impurities are observed.

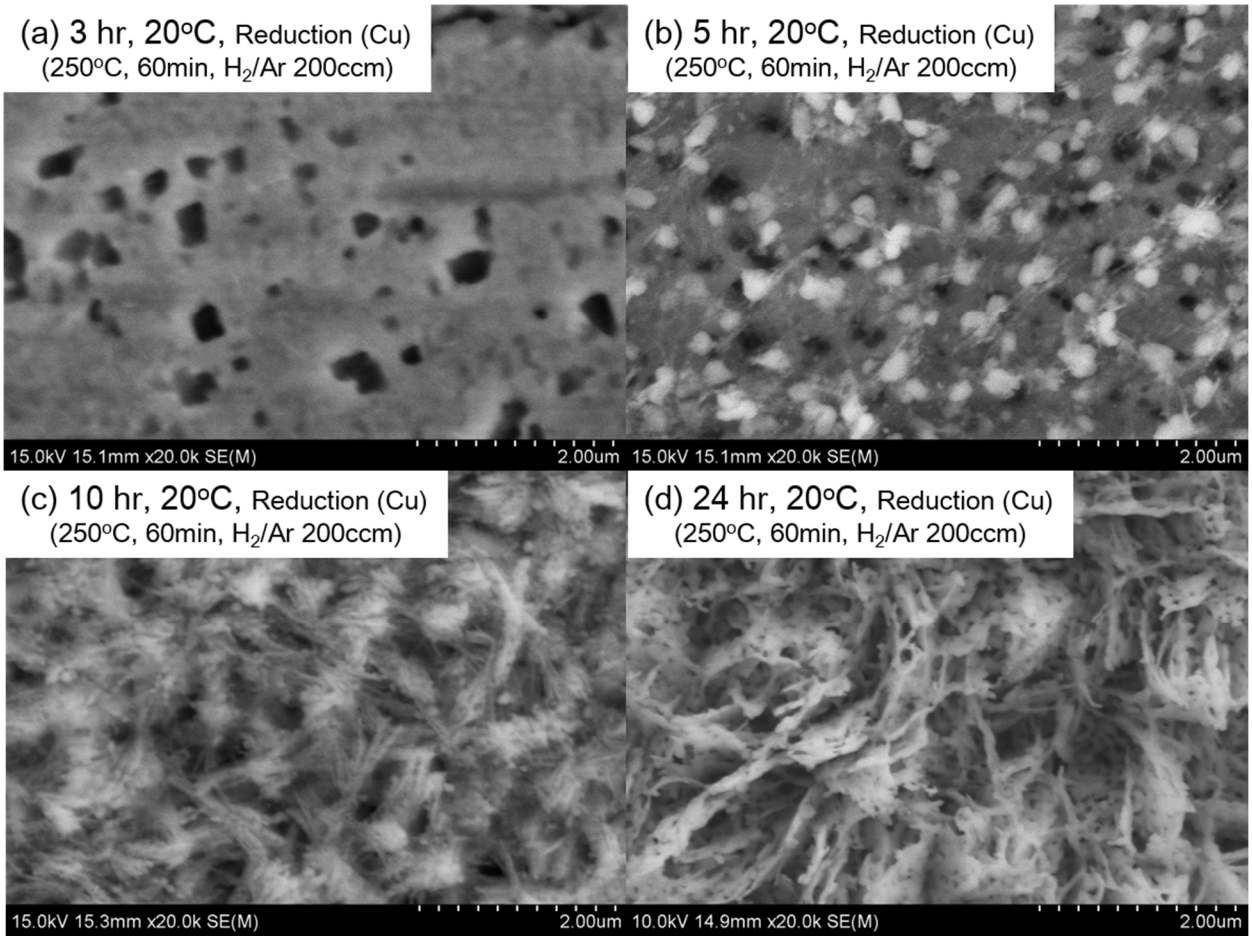

Figure 7-24. Surface modified Cu foil (reduced from CuO foil) at 250oC for 60 min.

Each 3, 5, 10, 24 hr CuO foils were reduced at 250°C for 1hr under 5%-H_2 / 95%-Ar mixture and a flow rate of 200 ccm. Figure 7-24 shows the morphology of surface modified Cu foil. In case of 3 hr and 5 hr sample (Figure 7-24(a), (b)), the nanostructures are not observed because the surfaces were not fully developed as it was already checked in Figure 7-21(a), (b)). Figure 7-24(d) shows rough surface area after reduction. SiNPs were deposited on/in this sample and CNTs were synthesized for further study of binder free electrode.

7.4.3.2. Deposit of SiNP on/in Surface Modified Cu foil and *in situ* Growth of CNTs

The surface modified Cu foil was used as a current collector, and SiNPs were deposited onto the modified Cu foil with the same technique as described in section 7.4.2 (page 180). Figure 7-25 show the SEM images of SiNPs in/on the modified Cu foil (Figure 7-25(c), (d)), and also the neat Cu foil (Figure 7-25(a)) and surface modified Cu foil (Figure 7-25(b)) were added for comparison. Figure 7-25(d) shows the SiNPs are well deposited in/on the modified Cu foil.

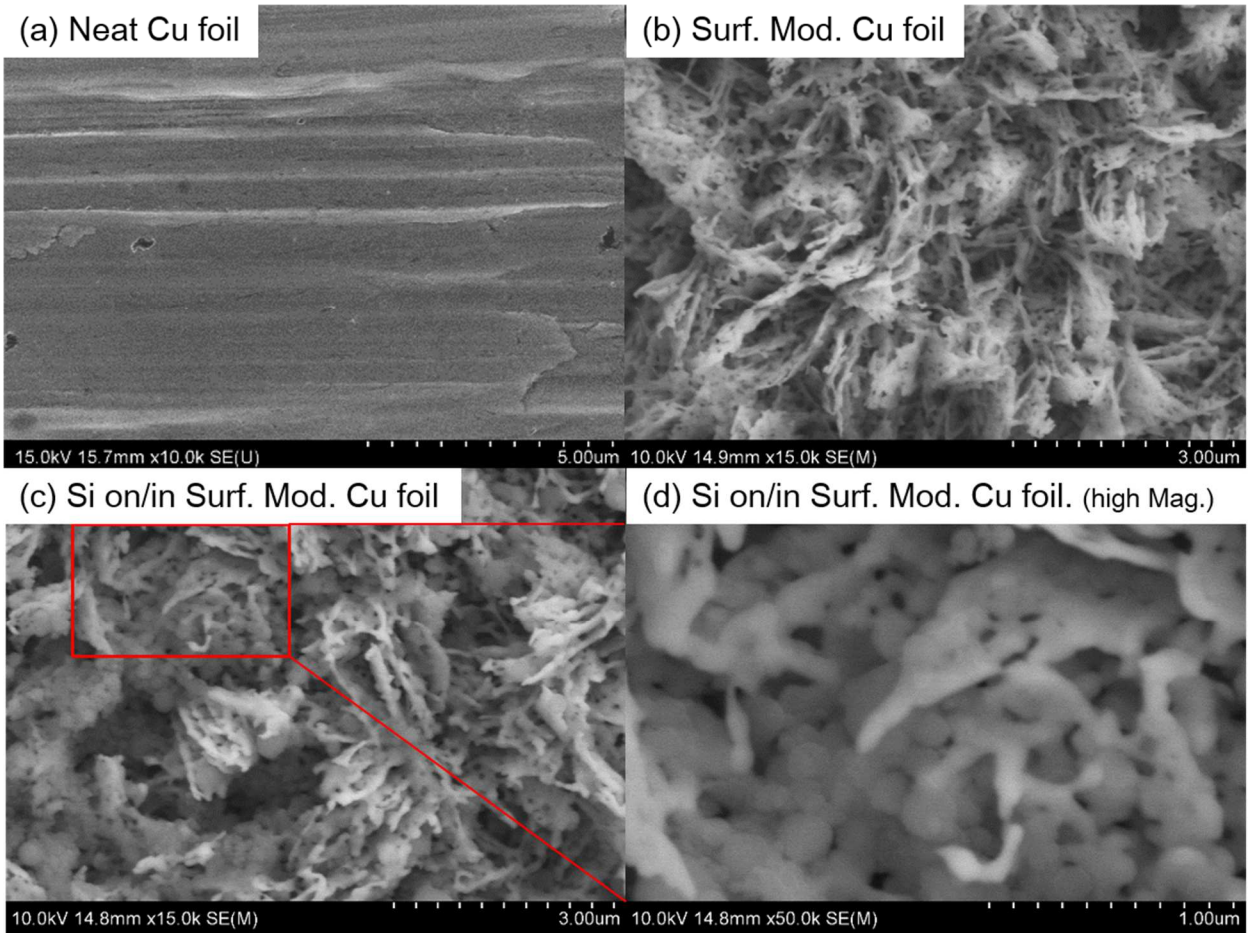

Figure 7-25. SEM image of (a) neat Cu foil, (b) surface modified Cu foil, (c) SiNPs on/in surface modified Cu-foil, and (d) high magnification of image (c).

EDX elemental mapping was taken to confirm the deposition of SiNPs on the surface modified Cu foil. Figure 7-26 shows the EDX mapping results, and it seems that the SiNPs are well dispersed in/on surface modified Cu foil.

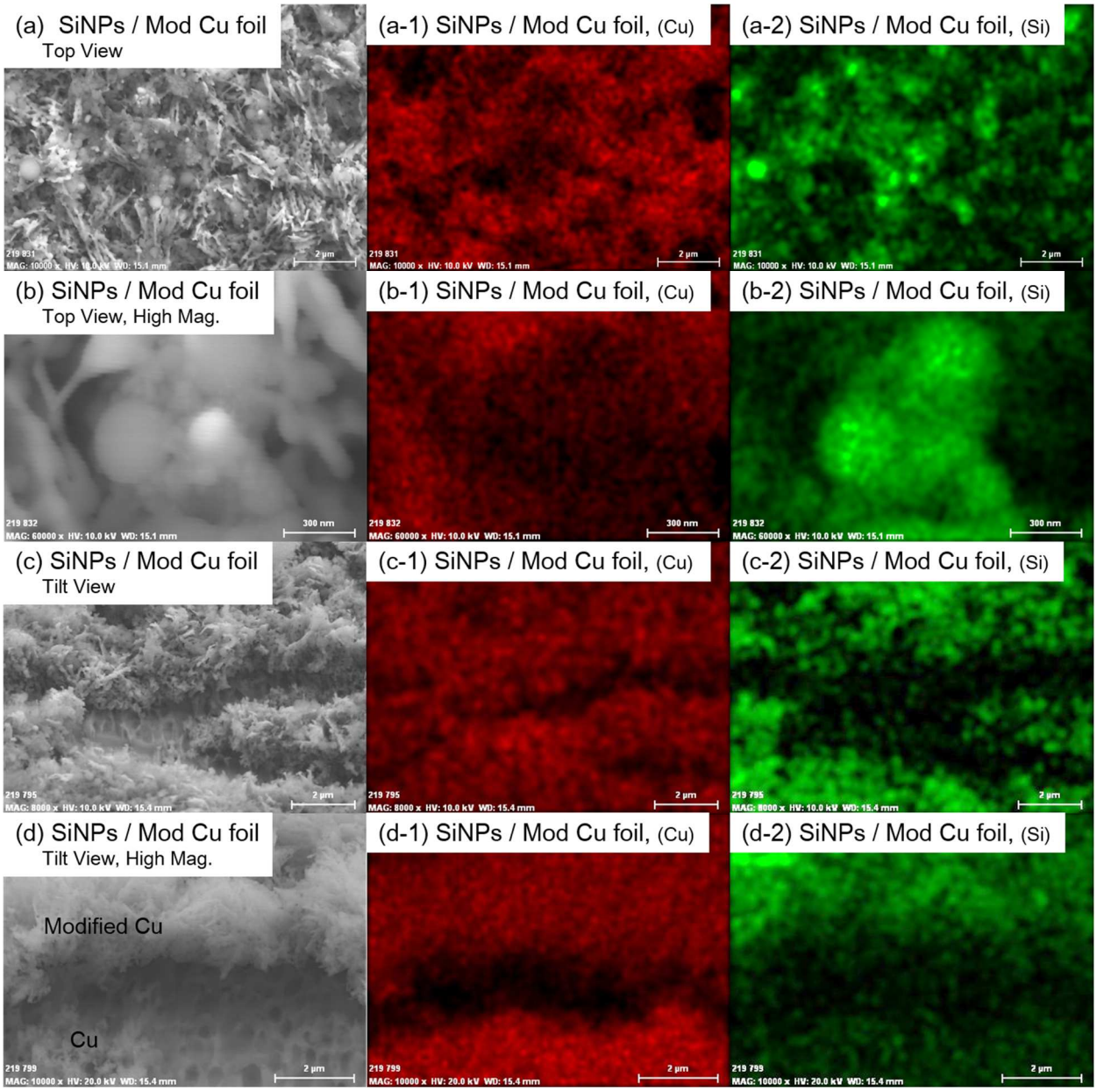

Figure 7-26. EDX elemental mapping of SiNP/Mod Cu foil (Red : Cu, Green : Si).

The final step to fabricate binder free SiNP/CNT electrode is the CNT synthesis over SiNPs deposited in/on modified Cu foil. The SiNPs deposited surface modified Cu foil was

punched to 1/2 inch diameter circular shape as described in Figure 7-11(page 181), and it was placed in the middle of the quartz tube reactor for CNT synthesis. The reactor was vacuumed for 30 min and filled with nitrogen gas with the flow rate of 150 ccm. Then after the reaction temperature has reached 700^{o}C, the acetylene gas and nitrogen gas was supplied at 12.5 ccm and 150 ccm, respectively.

The SEM and EDX images in Figure 7-27 show the CNTs grown not only on the top layer of SiNPs (Figure 7-27(b)) but also in the middle of SiNPs layers (Figure 7-27(c), (c3)). The nanostructured Cu surface layer is about 1 μm height and it is very well populated with CNTs. The top view of the surface shows that SiNPs are wrapped by CNTs. As seen in Figure 7-27(c-1), the modified Cu structure is clearly confirmed by EDX. Also, SiNPs are seen to be well dispersed in the nanostructured Cu foils (Figure 7-27(c-2)). The binder free CNTs/SiNPs/Mod Cu foil was used for anode electrode of Li-ion battery, and the cycle life test was performed.

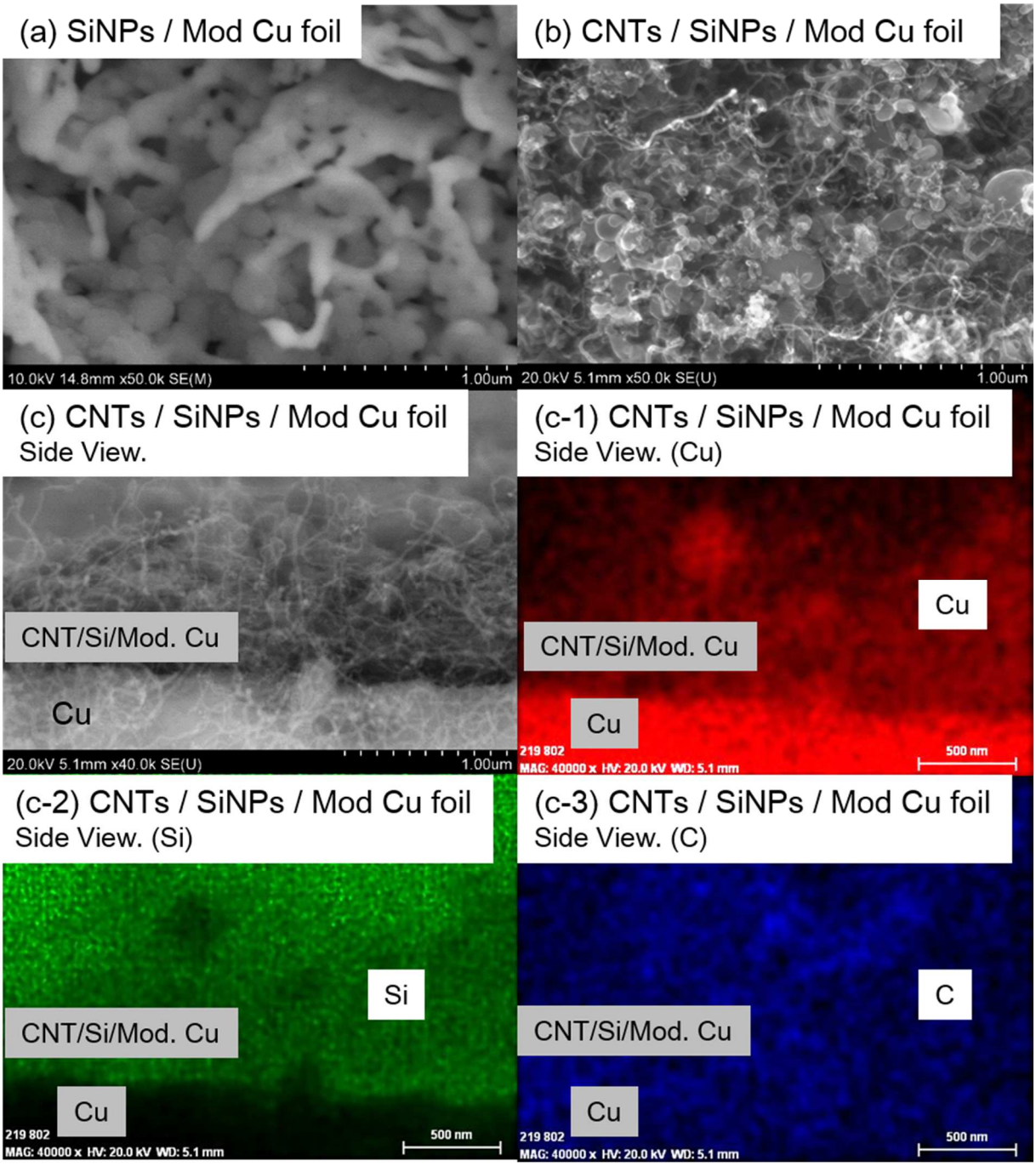

Figure 7-27. SEM images ; (a), (b), (c), and EDX elemental mapping images ; (c-1), (c-2), and (c-3), of binder free CNTs/SiNPs/Mod Cu foil electrode.

7.4.4. Cycle life test

7.4.4.1. Effect of CNTs and Surface Modified Cu foil on Cycle Life Test.

The coin cells of the Si anode were fabricated with Li metal as a cathode, and 1M $LiPF_6$ in a mixture of fluoroethylene carbonate–dimethyl carbonate (FEC-DMC, 1:1 by volume) as electrolyte with 500 mA/g. And they were tested by Arbin battery test station (BT2000, Arbin instruments, U.S.A.). Figure 7-28 shows the test results for the unmodified Cu/SiNP/CNT anode and the surface modified Cu/Si/CNT anode systems, also unmodified Cu/SiNP without CNT anode is included for the comparison of CNT function. In all these experiments, no external binder was used. The specific capacity vs. cycle number graph shows that the CNTs are very effective to maintain the stability of cycle life. Unmodified Cu/SiNP without CNT sample failed in about 10 cycles while CNT wrapped sample is stable more than 250 cycles. The modified Cu/SiNP/CNT anode system shows the capacity that is about 1.5~2 times higher than the anode system with unmodified Cu foil. However the stability of the modified Cu/SiNP/CNT system tends to decrease with cycyles. At 200 cycles, the capacity of modified Cu/SiNP/CNT system has dropped to ~65% of the original while unmodified Cu/SiNP/CNT has dropped to ~75%. And the overall capacity was not that high enough than the expectation.

To solve the problems of relatively low capacity and capacity fade of the anode system, several researches were conduct.

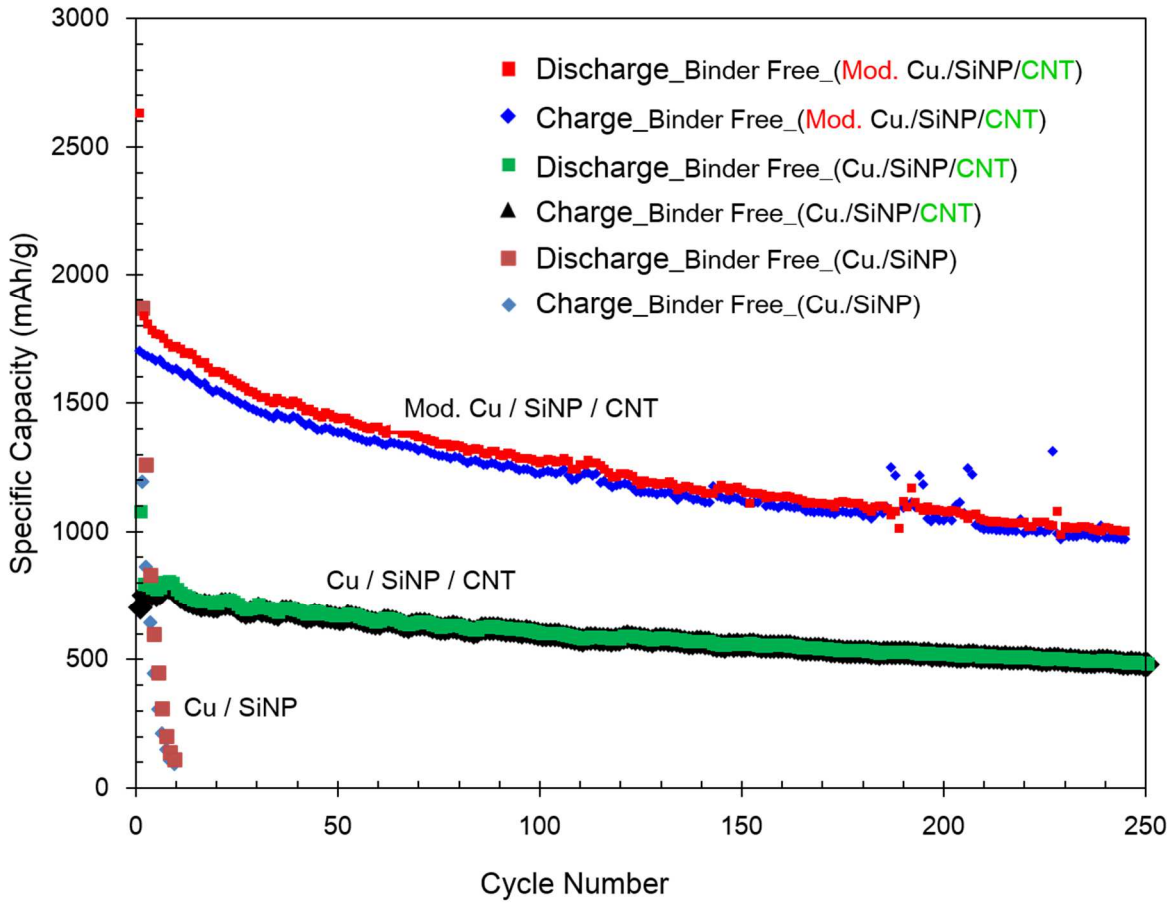

Figure 7-28. Cycle life test of Mod.Cu/SiNP/CNT, Cu/SiNP/CNT, and Cu/SiNP anode system.

7.4.4.2. Polyacrylonitrile (PAN) coating on Surf. Mod. Cu/SiNP/CNT system.

To enhance the stability of surface modified Cu/SiNP/CNT anode system during cycle life test, polyacrylonitrile (PAN) was coated on the anode system. PAN is usually used for electrospinning technique, which is relay on electrostatic forces drawing out a jet of polymeric solution, and the solution forms a thin nanofibers due to high extension [141-144]. Zental et.al.[145], coated TiO_2 nanorods with PAN to increase the stability of active materials. Biswal's group [146] also made freestanding silicon with PAN template for stable anode.

In this work, 80 mg of PAN was dissolved in 20 ml of *N*,*N*-dimethylformamide (DMF) and 2~3 drops of the mixture were dropped on the top of the surface modified Cu/SiNP/CNT

anode system. The DMF was removed in a vacuum oven at 50°C overnight. To carbonize the top layer of PAN, the anode was placed into the middle of tube furnace and stabilized at 250°C for 2 hr in an air atmosphere. Then the furnace was vacuumed and filled with argon gas at the flow rate of 200 ccm. The carbonization process of PAN was performed at 550°C for 4hr with heating rate of 5°C/min and argon flow rate of 200 ccm.

EDX elemental mapping results (Figure 7-29) confirms the silicon and carbon atoms are well dispersed on modified Cu surface. However, both CNT and carbonized PAN have a carbon atom, it is hard to separately divide CNT and PAN.

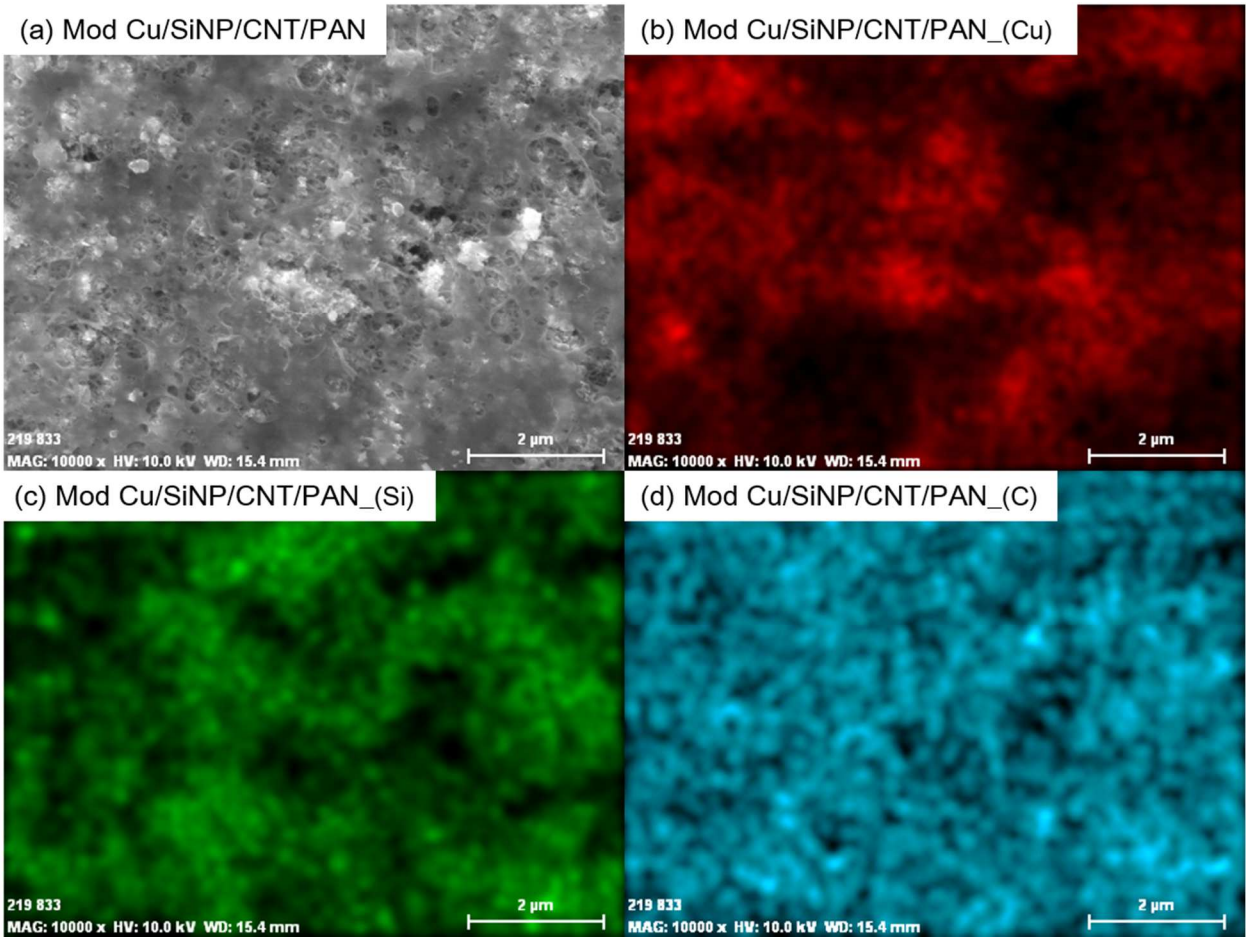

Figure 7-29. EDX elemental mapping of PAN covered electrode system.

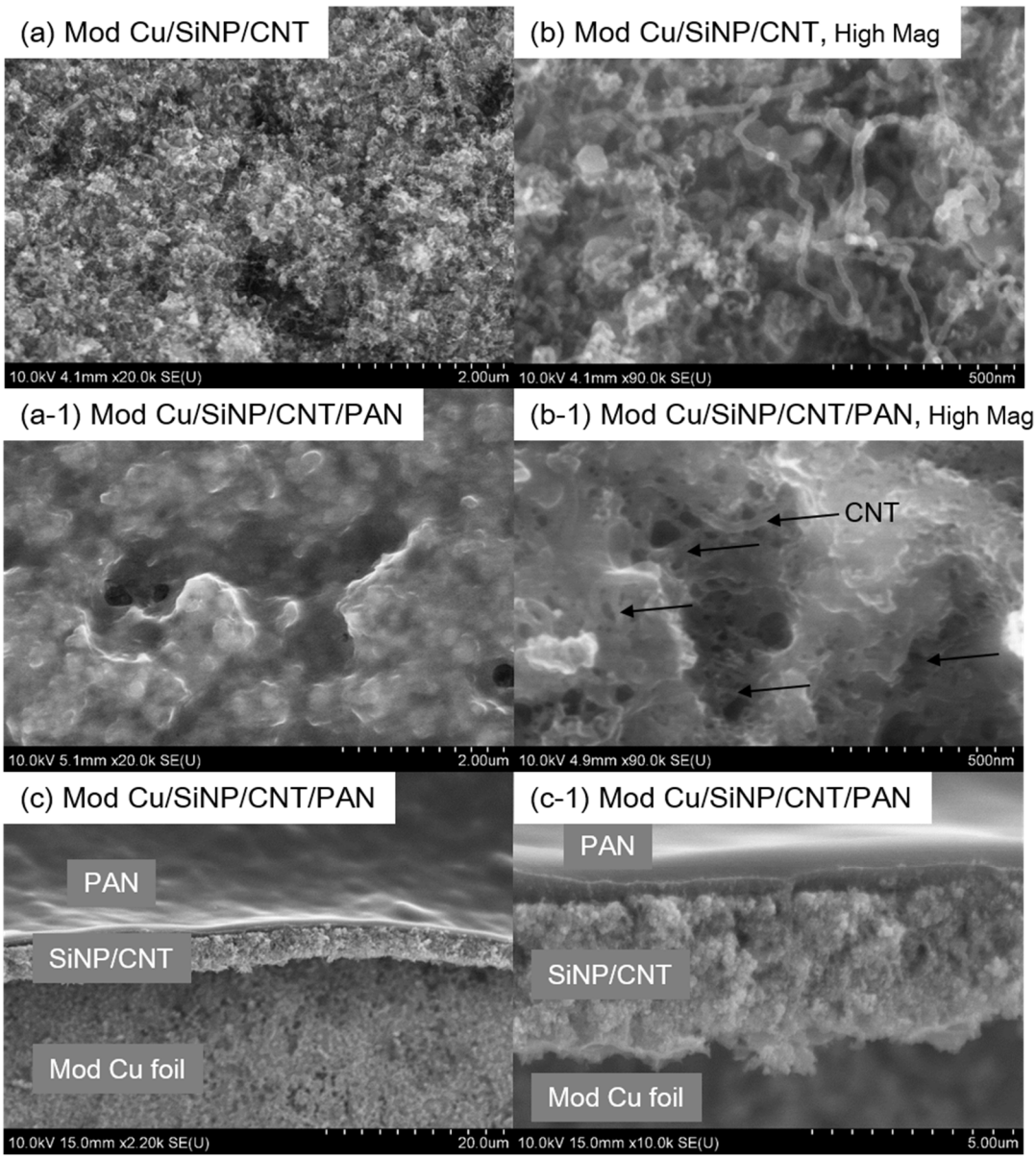

Figure 7-30. SEM image of (a), (b) mod. Cu/SiNP/CNT anode, (a-1), (b-1) PAN coated anode, and (c), (c-1) side view of PAN coated anode.

Figure 7-30 includes the SEM image of surface modified Cu/SiNP/CNT anode system before PAN coating and after PAN coating. Figure 7-30(a), (a-1), and Figure 7-30(b), (b-1) is in the same magnification, respectively, for easy comparison. The side view images (Figure 7-30(c), (c-1)) clearly shows the PAN is well covered on the top of the surface modified Cu/SiNP/CNT anode system.

Cycle life test was performed with fluoroethylene carbonate (FEC) as electrolyte at current rate of 500 mA/g. The test results of PAN coated modified Cu/SiNP/CNT electrode is shown in Figure 7-31, also the result of uncovered modified Cu/SiNP/CNT electrode has attached. In case of PAN coated electrode, the stability of the cycle life has improved however the specific capacity has decreased. The overall capacity trend and value is quite similar to Cu/SiNP/CNT anode system as already expressed in Figure 7-28. At this moment, I suspect the structure of modified Cu foil. To check this hypothesis, the morphology of surface modified Cu foil was studied at various temperature.

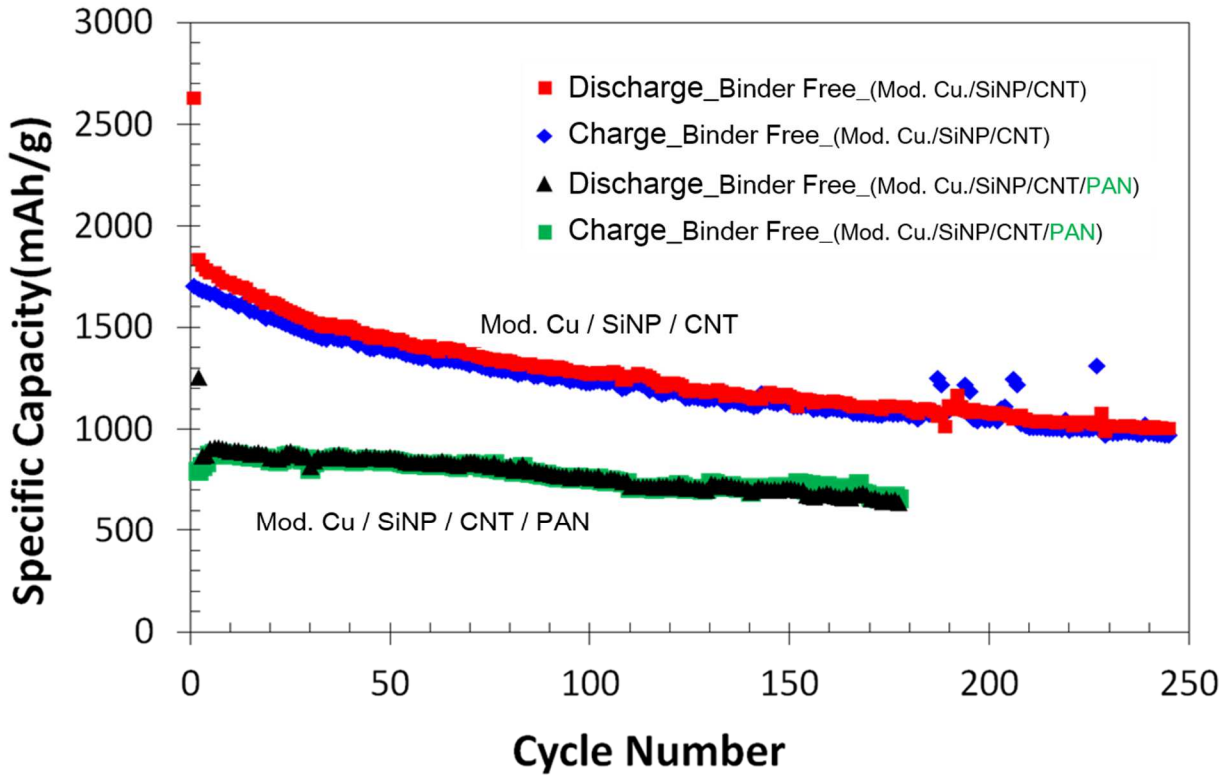

Figure 7-31. Cycle life test of Mod.Cu/SiNP/CNT, and Mod.Cu/SiNP/CNT/PAN anode system.

7.4.4.3. Effect of Temperature for degrade of Surf. Mod. Cu foil.

As mentioned in previous section, the morphology of surface modified Cu foil at elevate temperature was studied. It was counted that the shape of the knife-like nanostructured Cu foil remains stable during CNT growth and PAN carbonization. However as already checked in cycle life tests, the nanostructured Cu foil electrode was not that stable (Figure 7-28) and PAN coated nanostructured Cu foil electrode has lower specific capacity (Figure 7-31). These phenomena can be expressed by the deformation or elimination of nanostructured Cu foil during CNT synthesis and carbonization of PAN.

The knife-like surface modified Cu foil was placed in the middle of the furnace and vacuumed to remove the oxygen in the quartz tube. Then it was filled with nitrogen gas with the flow rate of 150 ccm. The temperature of the furnace was elevated to 700, 600, 575, and 550^{o}C for 30 min. This procedure is exactly same as CNT growth process except supplying acetylene gas as carbon source. The results are shown in Figure 7-32. For comparison, neat Cu foil and knife-like surface modified Cu foil has presented in Figure 7-32(a) and (b), respectively. The results in Figure 7-32 concludes that the structure of knife-like nanostructured Cu foils are deformed at the temperature above 550^{o}C. The minimum temperature was set up to 550^{o}C because CNT cannot be synthesized below 550^{o}C in this experiments.

According to Karabacak's group [147], and Takiya's group [148], the nanosized copper starts melting around 400^{o}C even the melting point of copper metal is 1048.6^{o}C. Among the heat treated Cu foils, 550^{o}C sample has the largest surface area. Since the main goal of this experiment is relied on large surface area current collector, the temperature of 550^{o}C was chosen for further CNT synthesis.

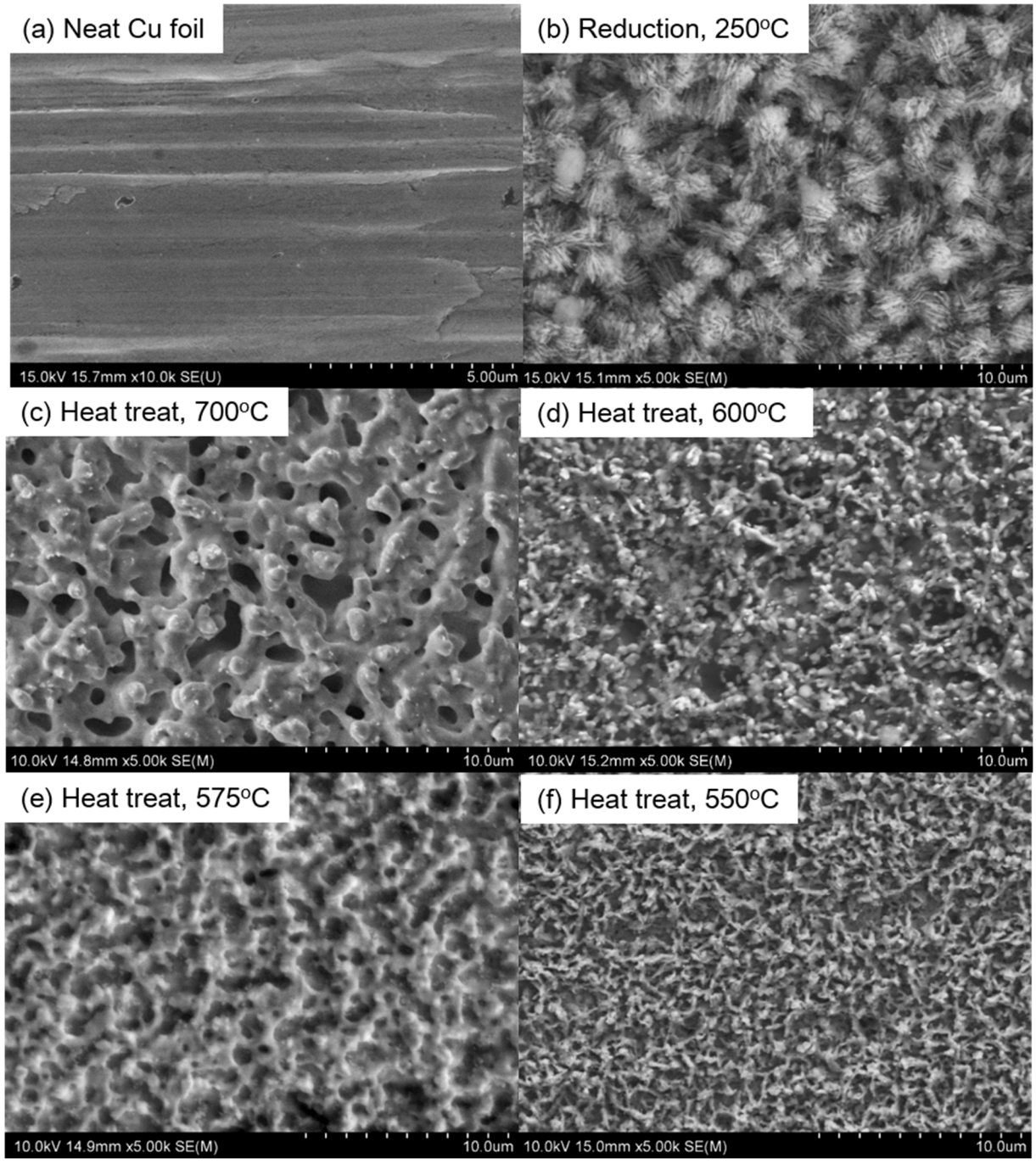

Figure 7-32. SEM image of surface modified Cu foil after heat treatments; (a) neat Cu foil, (b) after reduction at 250oC, heat treat at (c) 700oC, (d) 600oC, (e) 575oC, and (f) 550oC .

7.4.4.1. CNT synthesize at low temperature with minimal deformation of Surf. Mod. Cu foil

The reaction temperature about 700^{o}C is good for CTN growth, however, the structure of modified Cu foils are degrade at this temperature. It was reported that the nanostructured copper starts melting and fusing above 400^{o}C [147], [148], and CNTs are not synthesized below 400^{o}C. Because of this experimental restriction, 550^{o}C was chosen to minimize the structure deformation of the surface modified Cu foil and CNTs synthesis. To synthesize the CNT at relatively low temperature (550^{o}C), catalyst system was changed from Fe/Co acetate to Fe/Co nitrate system. The CNT synthesize procedure was same as described in section 7.4.2 (page 180). To achieve high and stable specific capacity, Cu foil was also switched from flat type Cu foil to rugged Cu foil. The surface of rugged Cu foil is expressed in Figure 7-33(a). It was oxidized (Figure 7-33(b)) and reduced (Figure 7-33 (c)) to make a knife-like nanostructured Cu foil with the same procedure. SiNPs are loaded on/in this foil, and it was placed in the middle of quartz tube reactor for the catalyst reduction at 250^{o}C. After the catalyst reduction process, CNTs are synthesized at 700^{o}C with acetylene flow rate of 12.5 ccm and nitrogen flow rate of 150 ccm. Before synthesis CNTs at 550^{o}C, the reaction temperature of 700^{o}C was used first to check the feasibility of Fe/Co nitrate catalyst system. Figure 7-33(d) shows the CNTs are well populated around the foil. Compare to Fe/Co acetate catalyst system, Fe/Co nitrate catalyst system has longer and thinner CNTs, which is an essential property for this research.

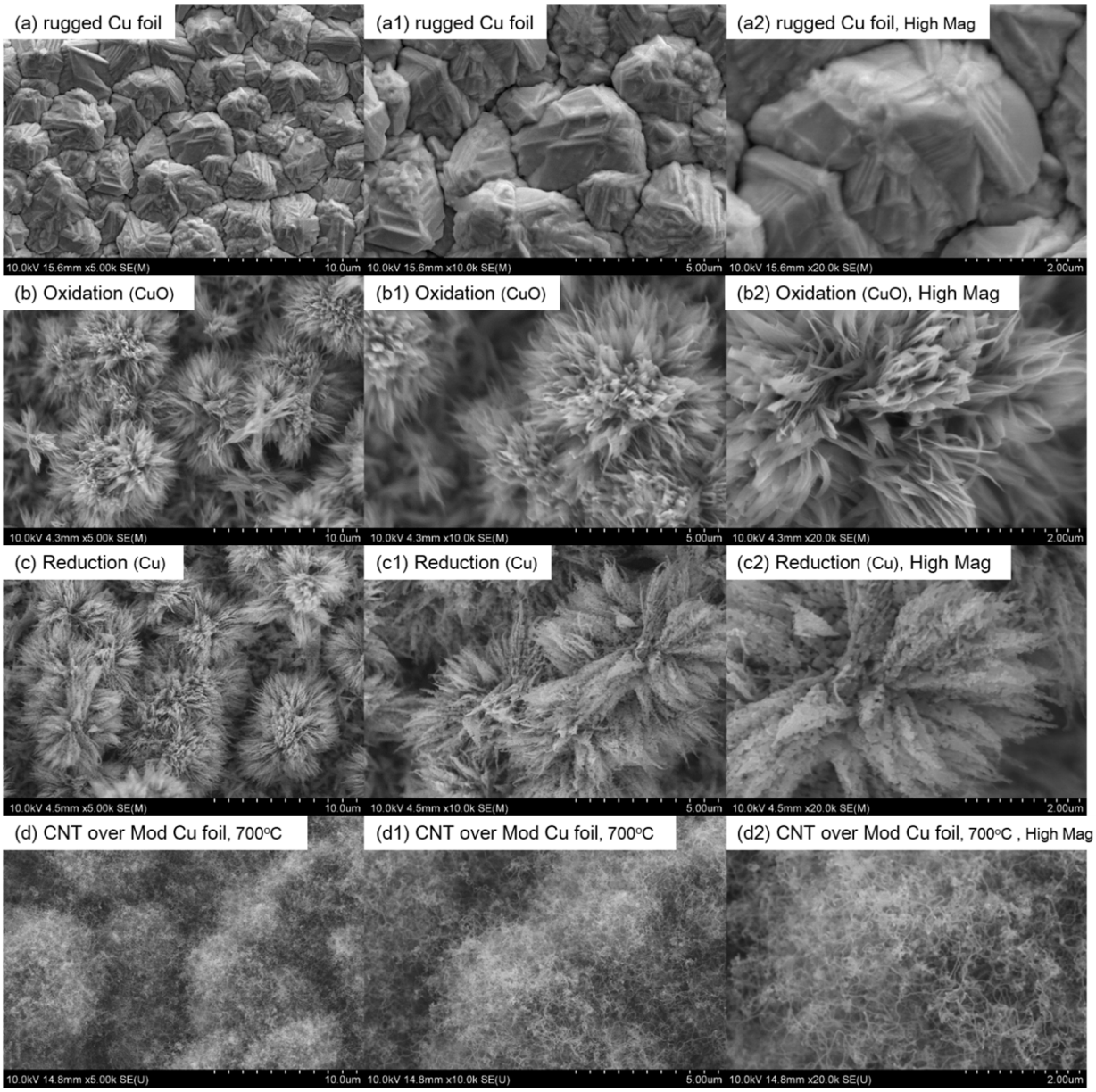

Figure 7-33 SEM images of (a), (a1), (a2) rugged Cu foil; (b), (b1), (b2) oxidation; (c), (c1), (c2) reduction; and (d), (d1), (d2) CNT synthesized at 700oC.

For minimal degrade of knife-like nanostructured Cu foil, CNTs were synthesized at 550^{o}C for various reaction time from 5 to 40 min. And the morphology check of grown CNT in/on modified Cu foil/SiNP was conducted by SEM. Figure 7-34 shows that the CNTs have grown well over modified Cu foil/SiNP for various reaction time at 550^{o}C. However due to the

low reaction temperature, the morphology like 700°C was hard to find. It is worthy to consider that the morphology of CNTs between 10 to 40 min are almost same while they are getting thicker as the reaction time increased at high temperature.

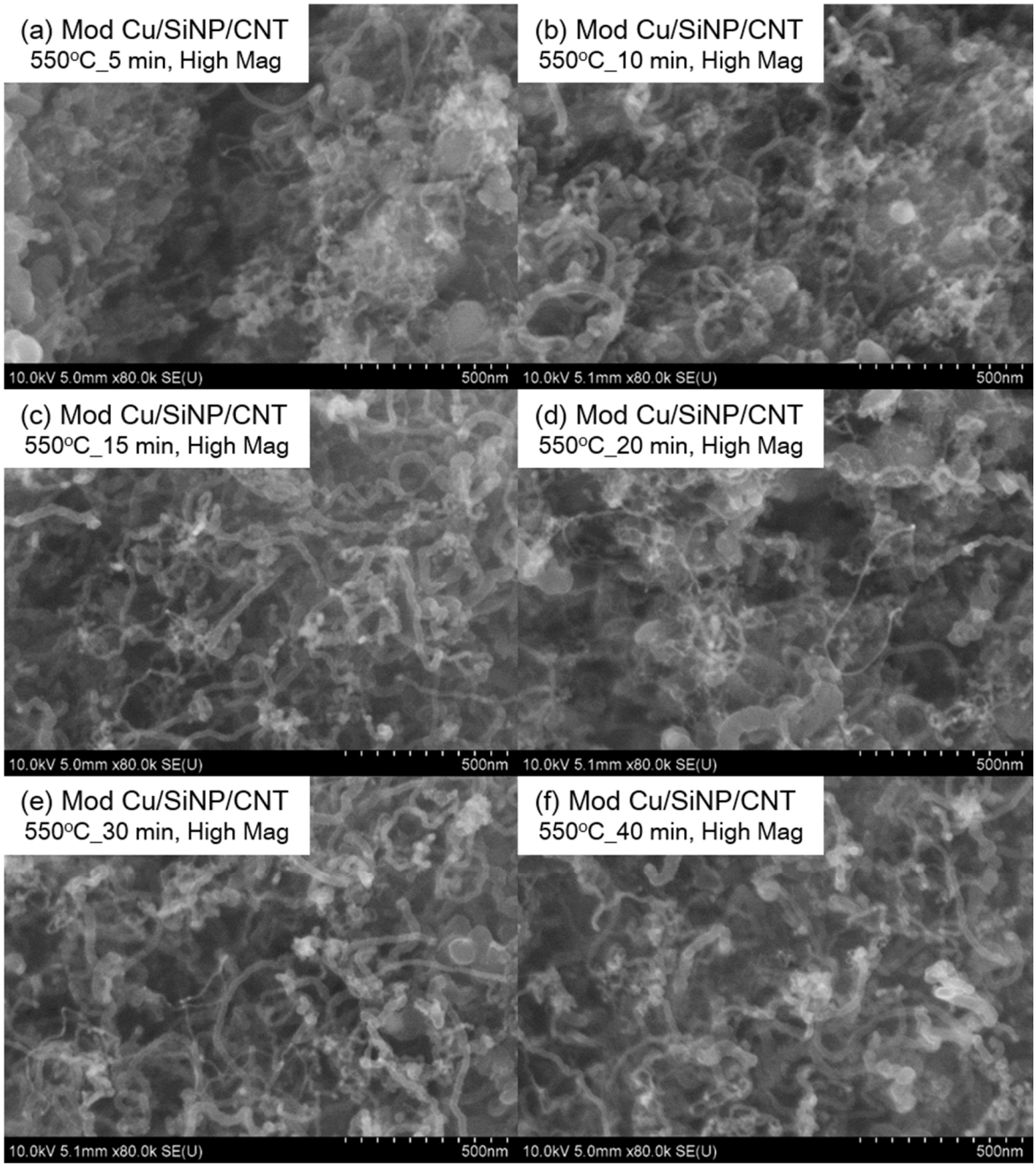

Figure 7-34. SEM images (high Mag., ×80,000) of CNTs synthesized on modified Cu foil/SiNP/CNT at 550oC for (a) 5 min, (b), 10 min, (c) 15 min, (d) 20 min, (e) 30 min, and (f) 40 min.

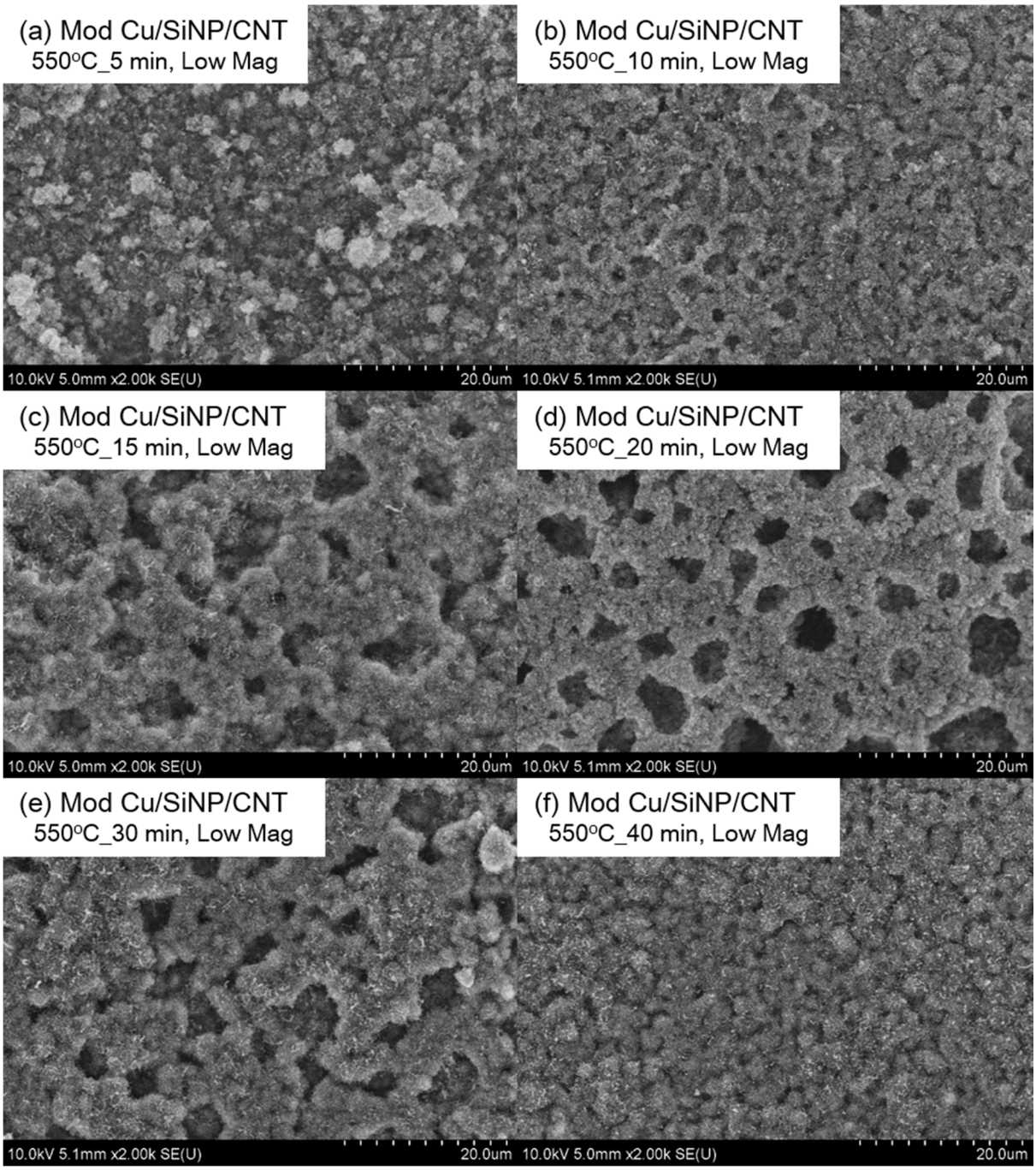

Figure 7-35. SEM images (low Mag., ×2,000) of CNTs synthesized on modified Cu foil/SiNP/CNT at 550oC for (a) 5 min, (b), 10 min, (c) 15 min, (d) 20 min, (e) 30 min, and (f) 40 min.

Figure 7-35 is low magnified SEM images of the same sample of Figure 7-34. Though, the morphology of CNTs in nano scale look almost same (10~40 min), it looks different in micro

scale. Initially CNTs on SiNP/Cu are also grown bumpy like Figure 7-35(a) due to the rugged surface of Cu foil. As the reaction time increased, acetylene gas diffused into the inner layer of SiNPs and formed CNTs, which push out the outer layer of SiNPs/CNTs composite. The further reaction push out more SiNPs/CNTs composite, and the outer layers fused each other as seen in Figure 7-35(c~e). Finally, after 40 min of reaction, the SiNPs/CNTs composite covers the Cu foil evenly.

The simple illustration of this situation is present at Figure 7-36. At high reaction temperature, the acetylene gas degrades and tends to deposit on the surface of CNT and forms thick CNTs. However at low temperature, 550^{o}C, there are no sign of this phenomena, which means the carbon source can diffuse deeply into the inner layer of SiNPs and form more CNTs in SiNP layers instead of making a thick CNTs.

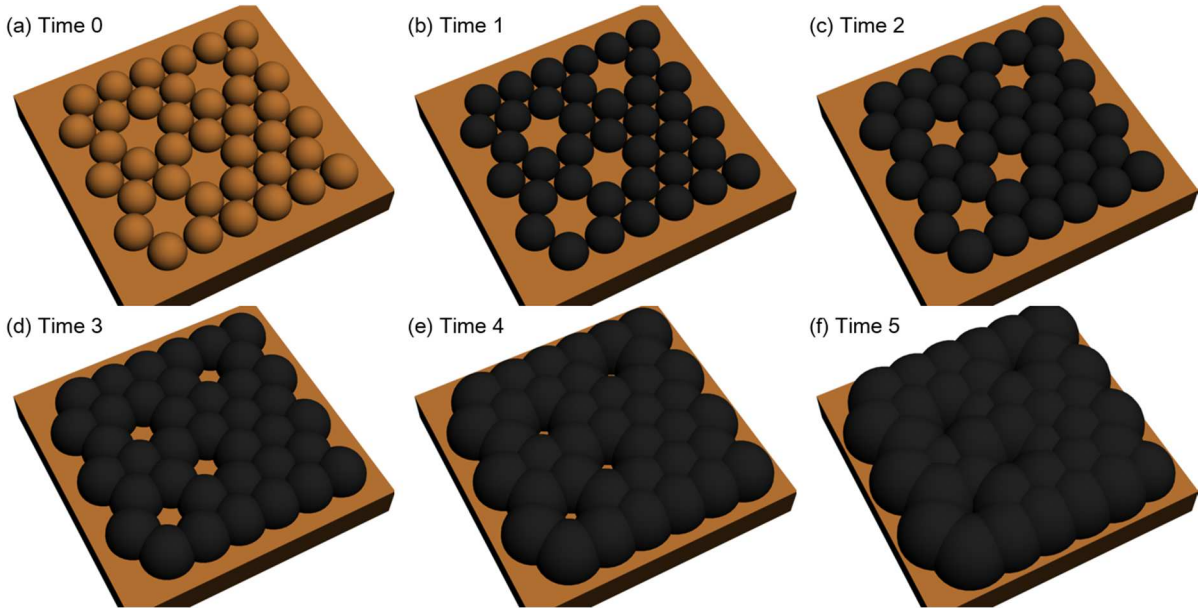

Figure 7-36. Illustration of Figure 7-35.

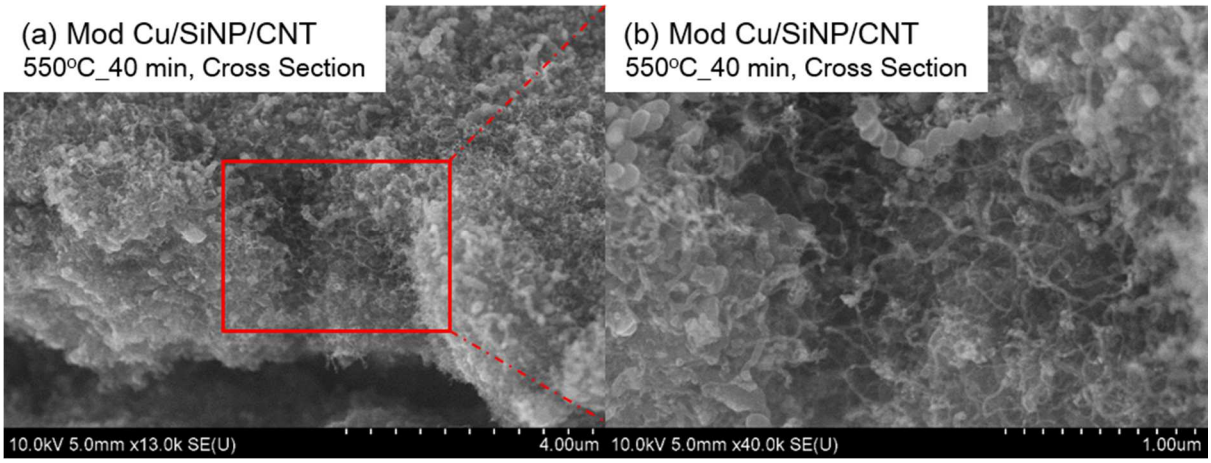

Figure 7-37. Cross section view of Mod.Cu/SiNP/CNT, 550oC, 40 min.

Figure 7-37 is cross sectional view of Mod.Cu/SiNP/CNT sample, which was made at 550°C for 40 min. It confirms that the CNTs are well grown and populated between inner layers of SiNPs.

The coin cell was assembled with Li metal as a cathode and 1 M $LiPF_6$ in a mixture of fluoroethylene carbonate-dimethyl carbonate (FEC-DMC, 1 : 1 by vol.) as the electrolyte, and Celgard® 3501 as the separator with current density of 200 mA/g and voltage window of 0.02 ~ 1.5 V. The cycle life test was performed using Arbin battery test station (BT2000, Arbin instruments, U.S.A.). Figure 7-38 shows the charge/discharge profiles of the Mod.Cu/SiNP/CNT electrode for first 5 cycles. In the first lithiation, the potential gradually decreased and shows long plateau around 0.8 V. The slope potential decrease in high potential area is mainly due to the lithiation of the CNT while the flat plateau ~0.08 V is a typical lithiation behavior of crystal Si [149]. After the first cycle, the charge/discharge curves show the typical electrochemical behavior of amorphous Si anodes at 0.5/0.2 V, respectively. The irreversible capacity is mainly due to the SEI formation, which consumes Li ions in cell, thus lowering the coulombic efficiency. The first cycle delivered a delithiation capacity of 3062 mAh/g and a reversible

capacity of 1991 mAh/g (coulombic efficiency: 65 %, typical value for Si-based coulombic efficiency). The coulombic efficiency jumped up to 97% at 4th cycle and stays around 98~99% for whole test, represents a good reversibility of the Mod. Cu/SiNP/CNT electrode.

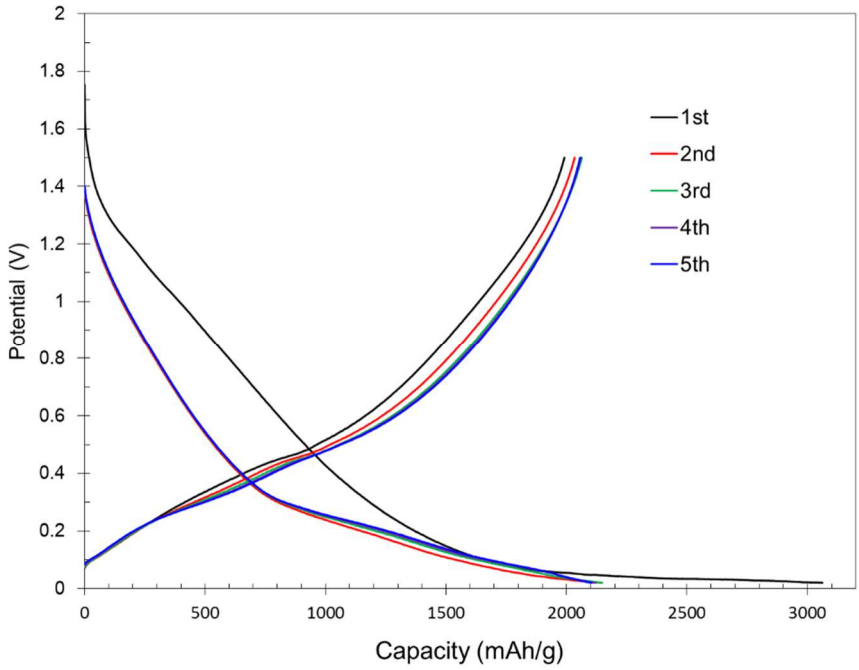

Figure 7-38. Charge / discharge profiles in the first five cycles of Mod.Cu/SiNP/CNT electrode.

Cycling stability of Mod. Cu/SiNP/CNT anode was tested at a current density of 500 mA/g and in the voltage range of 0.02 ~ 1.5 V. To compare the effect of surface modified Cu foil, unmodified Cu foil/SiNP/CNT electrode was fabricated binder freely and tested under the same conditions. The overall coulombic efficiency after first few cycles of Mod.Cu/SiNP/CNT electrode retains over 98~99% while unmodified Cu/SiNP/CNT has 97~98%. The capacity fade is mainly caused by the loss of electric connectivity of active materials. The specific capacity of unmodified Cu/SiNP/CNT starts decrease after ~50 cycles however Mod. Cu/SiNP/CNT is still stable. This is due to the morphology of nanostructured Cu foil, which provides large contact area between active materials and current collector.

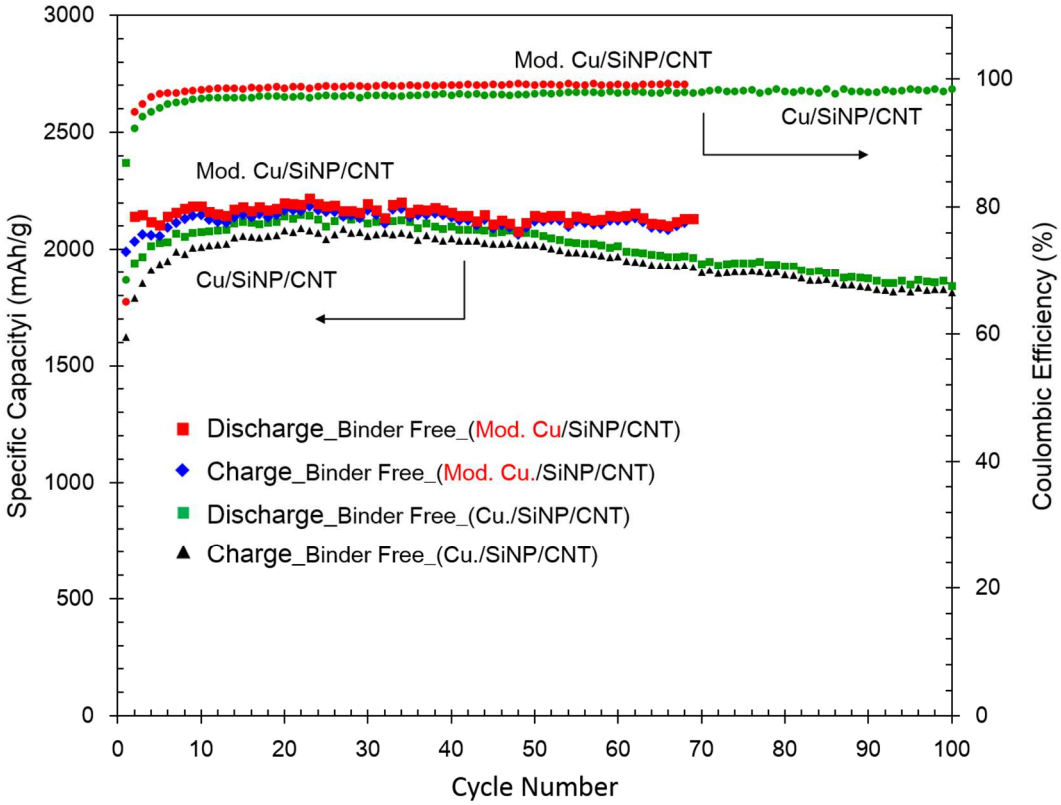

Figure 7-39. Cycling performance of Mod.Cu/SiNP/CNT and Cu/SiNP/CNT anode system.

7.5. Conclusions

In this chapter, the binder free Si/CNT anode material is introduced. Silicon nanoparticles were successfully deposited onto the surface of copper foil without any usage of binder. CNTs were synthesized on the silicon surface, and they work as an electron conducting materials also provides mechanical strength. CNT synthesis conditions were studied for various reaction temperatures and times. To enhance the cyclic performance of this electrode, the surface of current collector was modified to increase the contact area of active materials and current collector. The surface modified Cu foils were degraded and fused at CNT growth temperature. By adopting a Fe/Co nitrate catalyst system and relatively low CNT growth temperature, the deformation of surface modified Cu was minimal and CNT can be synthesized not only on the top layer of deposited SiNP but also in the middle of SiNP layers. The binder free surface modified Cu foil / SiNP / CNT electrode system has more than ~2100 mAh/g of capacity with coulombic efficiency about 98~99%. Compare to unmodified Cu foil / SiNP / CNT electrode system, modified electrode has better coulombic efficiency and cyclic stability.

Bibliography

1. Floyd, S.; Choi, K. Y.; Taylor, T. W.; Ray, W. H. Polymerization of olefins through heterogeneous catalysis. III. Polymer particle modelling with an analysis of intraparticle heat and mass transfer effects. *J. Appl. Polym. Sci.* **1986,** *32* (1), 2935-2960.
2. Niegisch, W. D.; Crisafulli, S. T.; Nagel, T. S.; Wagner, B. E. Characterization techniques for the study of silica fragmentation in the early stages of ethylene polymerization. *Macromolecules* **1992,** *25* (15), 3910-3916.
3. Hassan Nejad, M.; Ferrari, P.; Pennini, G.; Cecchin, G. Ethylene homo- and copolymerization over MgCl2-TiCl4 catalysts: Polymerization kinetics and polymer particle morphology. *J. Appl. Polym. Sci.* **2008,** *108* (5), 3388-3402.
4. Zheng, X.; Loos, J. Morphology Evolution in the Early Stages of Olefin Polymerization. *Macromol. Symp.* **2006,** *236* (1), 249-258.
5. Bonini, F.; Fraaije, V.; Fink, G. Propylene polymerization through supported metallocene/ MAO catalysts: Kinetic analysis and modelling. *J. Polym. Sci., Part A: Polym. Chem.* **1995,** *33* (14), 2393-2402.
6. Fink, G.; Steinmetz, B.; Zechlin, J.; Przybyla, C.; Tesche, B. Propene Polymerization with Silica-Supported Metallocene/MAO Catalysts. *Chem. Rev.* **2000,** *100* (4), 1377-1390.
7. Alexiadis, A.; Andes, C.; Ferrari, D.; Korber, F.; Hauschild, K.; Bochmann, M.; Fink, G. Mathematical Modeling of Homopolymerization on Supported Metallocene Catalysts. *Macromol. Mater. Eng.* **2004,** *289* (5), 457-466.
8. Luciani, C. V.; Choi, K. Y.; Han, J. J.; Jung, Y. Polymer particles with a pomegranate-like internal structure via micro-dispersive polymerization in a geometrically confined reaction space I. Experimental study. *Polymer* **2011,** *52* (4), 942-948.
9. Lee, S. Y.; Kim, S.-K.; Nguyen, T. M.; Chung, J. S.; Lee, S. B.; Choi, K. Y. Kinetics of Styrene Polymerization to Syndiotactic Polystyrene over Metallocene Catalyst on Flat Surface, Silica Nanotube Reactors and Porous Silica Particles. *Macromolecules* **2011,** *44* (6), 1385-1392.
10. Lee, S. Y.; Choi, K. Y. Kinetics and Growth of Polyethylene Nanofibrils over Metallocene Catalyst Supported on Flat Silica and Spherical Nano-Silica Particles. *Macromolecular Reaction Engineering* **2014,** *8* (11), 755-765.
11. Lee, S. Y.; Choi, K. Y. Polymerization of Ethylene over rac-Et(1-indenyl)2ZrCl2/MAO Catalyst Supported on Pseudo-Inverse Opal Silica Particles. *Industrial & Engineering Chemistry Research* **2012,** *51* (29), 9742-9749.
12. Lee, S.; Kim, S.-K.; Lee, S.; Choi, K. Y. Metallocene Catalyzed Ethylene Polymerization with Specially Designed Catalyst Supports and Reaction Systems. *Macromolecular Symposia* **2013,** *333* (1), 256-265.
13. Kasavajjula, U.; Wang, C.; Appleby, A. J. Nano- and bulk-silicon-based insertion anodes for lithium-ion secondary cells. *Journal of Power Sources* **2007,** *163* (2), 1003-1039.
14. Teki, R.; Datta, M. K.; Krishnan, R.; Parker, T. C.; Lu, T.-M.; Kumta, P. N.; Koratkar, N. Nanostructured Silicon Anodes for Lithium Ion Rechargeable Batteries. *Small* **2009,** *5* (20), 2236-2242.
15. Ng, S.-H.; Wang, J.; Wexler, D.; Konstantinov, K.; Guo, Z.-P.; Liu, H.-K. Highly Reversible Lithium Storage in Spheroidal Carbon-Coated Silicon Nanocomposites as Anodes for Lithium-Ion Batteries. *Angewandte Chemie International Edition* **2006,** *45* (41), 6896-6899.

16. Yang, Y.; McDowell, M. T.; Jackson, A.; Cha, J. J.; Hong, S. S.; Cui, Y. New Nanostructured Li2S/Silicon Rechargeable Battery with High Specific Energy. *Nano Letters* **2010,** *10* (4), 1486-1491.
17. Wang, W.; Kumta, P. N. Reversible high capacity nanocomposite anodes of Si/C/SWNTs for rechargeable Li-ion batteries. *Journal of Power Sources* **2007,** *172* (2), 650-658.
18. Kakugo, M.; Sadatoshi, H.; Yokoyama, M.; Kojima, K. Transmission electron microscopic observation of nascent polypropylene particles using a new staining method. *Macromolecules* **1989,** *22* (2), 547-551.
19. Kakugo, M.; Sadatoshi, H.; Sakai, J.; Yokoyama, M. Growth of polypropylene particles in heterogeneous Ziegler-Natta polymerization. *Macromolecules* **1989,** *22* (7), 3172-3177.
20. Nagel, E. J.; Kirillov, V. A.; Ray, W. H. Prediction of Molecular Weight Distributions for High-Density Polyolefins. *Industrial & Engineering Chemistry Product Research and Development* **1980,** *19* (3), 372-379.
21. Floyd, S.; Choi, K. Y.; Taylor, T. W.; Ray, W. H. Polymerization of olefins through heterogeneous catalysis. III. Polymer particle modelling with an analysis of intraparticle heat and mass transfer effects. *Journal of Applied Polymer Science* **1986,** *32* (1), 2935-2960.
22. Kittilsen, P.; McKenna, T. F.; Svendsen, H.; Jakobsen, H. A.; Fredriksen, S. B. The interaction between mass transfer effects and morphology in heterogeneous olefin polymerization. *Chemical Engineering Science* **2001,** *56* (13), 4015-4028.
23. Soares, J. B. P. Mathematical modelling of the microstructure of polyolefins made by coordination polymerization: a review. *Chemical Engineering Science* **2001,** *56* (13), 4131-4153.
24. Chiovetta, M. G.; Estenoz, D. A. Behavior of Active Sites in a Changing, Supported Metallocene Catalyst Particle: Modeling Monomer Transport and Kinetics. *Macromolecular Materials and Engineering* **2004,** *289* (11), 1012-1026.
25. Merquior, D. M.; Lima, E. L.; Pinto, J. C. Modeling of Particle Fragmentation in Heterogeneous Olefin Polymerization Reactions, 2. *Macromolecular Materials and Engineering* **2005,** *290* (6), 511-524.
26. Kanellopoulos, V.; Tsiliopoulou, E.; Dompazis, G.; Touloupides, V.; Kiparissides, C. Evaluation of the Internal Particle Morphology in Catalytic Gas-Phase Olefin Polymerization Reactors. *Industrial & Engineering Chemistry Research* **2007,** *46* (7), 1928-1937.
27. Ribeiro, M. R.; Deffieux, A.; Portela, M. F. Supported Metallocene Complexes for Ethylene and Propylene Polymerizations: Preparation and Activity. *Industrial & Engineering Chemistry Research* **1997,** *36* (4), 1224-1237.
28. Zurek, E.; Ziegler, T. Theoretical studies of the structure and function of MAO (methylaluminoxane). *Progress in Polymer Science* **2004,** *29* (2), 107-148.
29. Knoke, S.; Korber, F.; Fink, G.; Tesche, B. Early Stages of Propylene Bulk Phase Polymerization with Supported Metallocene Catalysts. *Macromolecular Chemistry and Physics* **2003,** *204* (4), 607-617.
30. Amgoune, A.; Krumova, M.; Mecking, S. Nanoparticle-Supported Molecular Polymerization Catalysts. *Macromolecules* **2008,** *41* (22), 8388-8396.
31. Chaichana, E.; Jongsomjit, B.; Praserthdam, P. Effect of nano-SiO2 particle size on the formation of LLDPE/SiO2 nanocomposite synthesized via the in situ polymerization with metallocene catalyst. *Chemical Engineering Science* **2007,** *62* (3), 899-905.
32. Zapata, P. A.; Quijada, R.; Lieberwirth, I.; Benavente, R. Polyethylene Nanocomposites Obtained by in situ Polymerization via a Metallocene Catalyst Supported on Silica Nanospheres. *Macromolecular Reaction Engineering* **2011,** *5* (7-8), 294-302.

33. Li, K.-T.; Ko, F.-S. Dimethylsilylbis(1-indenyl) zirconium dichloride/methylaluminoxane catalyst supported on nanosized silica for propylene polymerization. *Journal of Applied Polymer Science* **2008,** *107* (3), 1387-1394.
34. Li, K.-T.; Dai, C.-L.; Kuo, C.-W. Ethylene polymerization over a nano-sized silica supported Cp2ZrCl2/MAO catalyst. *Catalysis Communications* **2007,** *8* (8), 1209-1213.
35. Li, K.-T.; Li, C.-Y. Nano-sized silica supported Me2Si(Ind)2ZrCl2/MAO catalyst for ethylene polymerization. *Journal of Applied Polymer Science* **2012,** *123* (2), 1169-1175.
36. Smit, M. Heterogenization on silica of metallocene catalysts for olefin polymerization. Technische Universiteit Eindhoven, Ph.D. Thesis, 2005.
37. Carrero, A.; van Grieken, R.; Paredes, B. Ethylene polymerization with methylaluminoxane/(nBuCp)2ZrCl2 catalyst supported on silica and silica-alumina at different AlMAO/Zr molar ratios. *Journal of Applied Polymer Science* **2011,** *120* (1), 599-606.
38. dos Santos, J. H. Z.; Dorneles, S.; Stedile, F. C.; Dupont, J.; de Camargo Forte, M. M.; Baumvol, I. J. R. Silica supported zirconocenes and Al-based cocatalysts: surface metal loading and catalytic activity. *Macromolecular Chemistry and Physics* **1997,** *198* (11), 3529-3537.
39. dos Santos, J. H. Z.; Krug, C.; da Rosa, M. B.; Stedile, F. C.; Dupont, J. r.; de Camargo Forte, M. The effect of silica dehydroxylation temperature on the activity of SiO2-supported zirconocene catalysts. *Journal of Molecular Catalysis A: Chemical* **1999,** *139* (2–3), 199-207.
40. McKnight, A. L.; Waymouth, R. M. Ethylene/Norbornene Copolymerizations with Titanium CpA Catalysts. *Macromolecules* **1999,** *32* (9), 2816-2825.
41. Guttman, J. Y.; Guillet, J. E. Polymerization of Propylene on Single Crystals of α-Titanium Trichloride. *Macromolecules* **1968,** *1* (5), 461-463.
42. Naik, S. D.; Ray, W. H. Particle morphology for polyolefins synthesized with supported metallocene catalysts. *Journal of Applied Polymer Science* **2001,** *79* (14), 2565-2579.
43. Kakugo, M.; Sadatoshi, H.; Sakai, J. Morphology of nascent polypropylene produced by MgCl2 supported Ti catalyst. In *Catalytic Olefin Polymerization*, Keil, T.; Soga, K., Eds. Elservier: Tokyo, 1990; pp 345-354.
44. Fink, G.; Steinmetz, B.; Zechlin, J.; Przybyla, C.; Tesche, B. Propene Polymerization with Silica-Supported Metallocene/MAO Catalysts. *Chemical Reviews* **2000,** *100* (4), 1377-1390.
45. Ye, Z.; Zhu, S.; Wang, W.-J.; Alsyouri, H.; Lin, Y. S. Morphological and mechanical properties of nascent polyethylene fibers produced via ethylene extrusion polymerization with a metallocene catalyst supported on MCM-41 particles. *Journal of Polymer Science Part B: Polymer Physics* **2003,** *41* (20), 2433-2443.
46. Nair, S.; Naredi, P.; Kim, S. H. Formation of High-Stress Phase and Extrusion of Polyethylene due to Nanoconfinements during Ziegler−Natta Polymerization Inside Nanochannels. *The Journal of Physical Chemistry B* **2005,** *109* (25), 12491-12497.
47. Kageyama, K.; Tamazawa, J.-i.; Aida, T. Extrusion Polymerization: Catalyzed Synthesis of Crystalline Linear Polyethylene Nanofibers Within a Mesoporous Silica. *Science* **1999,** *285* (5436), 2113-2115.
48. Dong, X.; Wang, L.; Zhou, J.; Yu, H.; Sun, T. Preparation of nano-polyethylene fibres using TiCl4/MCM-41 catalytic system. *Catalysis Communications* **2006,** *7* (1), 1-5.
49. Dong, X.; Wang, L.; Jiang, G.; Zhao, Z.; Sun, T.; Yu, H.; Wang, W. MCM-41 and SBA-15 supported Cp2ZrCl2 catalysts for the preparation of nano-polyethylene fibres via in situ ethylene extrusion polymerization. *Journal of Molecular Catalysis A: Chemical* **2005,** *240* (1–2), 239-244.

50. Han, J. J. Kinetics and morphology of metallocene catalyzed syndiospecific polymerization of styrene in homogeneous and heterogeneous reaction systems. Univerisity of Maryland, College Park, 2008.
51. Somani, R. H.; Yang, L.; Zhu, L.; Hsiao, B. S. Flow-induced shish-kebab precursor structures in entangled polymer melts. *Polymer* **2005,** *46* (20), 8587-8623.
52. Schultz, J. M. *Polymer Crystallization: The Development of Crystalline Order in Thermoplastic Polymers*. Oxford University Press: New York, 2001.
53. Dong, X.; Wang, L.; Wang, W.; Jiang, G.; Chen, Y.; Zhao, Z.; Wang, J. Preparation of Nano-Polyethylene Fibers and Floccules by Extrusion Polymerization Under Atmospheric Pressure Using the SBA-15-Supported Cp2ZrCl2 Catalytic System. *Macromolecular Materials and Engineering* **2005,** *290* (1), 31-37.
54. Guttman, J. Y.; Guillet, J. E. Mechanism of Propylene Polymerization of Single Crystals of α-Titanium Trichloride. *Macromolecules* **1970,** *3* (4), 470-472.
55. Floyd, S.; Choi, K. Y.; Taylor, T. W.; Ray, W. H. Polymerization of olefins through heterogeneous catalysis IV. Modeling of heat and mass transfer resistance in the polymer particle boundary layer. *Journal of Applied Polymer Science* **1986,** *31* (7), 2231-2265.
56. Floyd, S.; Hutchinson, R. A.; Ray, W. H. Polymerization of olefins through heterogeneous catalysis—V. Gas-liquid mass transfer limitations in liquid slurry reactors. *Journal of Applied Polymer Science* **1986,** *32* (6), 5451-5479.
57. Grof, Z.; Kosek, J.; Marek, M. Modeling of morphogenesis of growing polyolefin particles. *AIChE Journal* **2005,** *51* (7), 2048-2067.
58. Zheng, X.; Smit, M.; Chadwick, J. C.; Loos, J. Fragmentation Behavior of Silica-Supported Metallocene/MAO Catalyst in the Early Stages of Olefin Polymerization. *Macromolecules* **2005,** *38* (11), 4673-4678.
59. Zheng, X.; Loos, J. Morphology Evolution in the Early Stages of Olefin Polymerization. *Macromolecular Symposia* **2006,** *236* (1), 249-258.
60. Goretzki, R.; Fink, G.; Tesche, B.; Steinmetz, B.; Rieger, R.; Uzick, W. Unusual ethylene polymerization results with metallocene catalysts supported on silica. *Journal of Polymer Science Part A: Polymer Chemistry* **1999,** *37* (5), 677-682.
61. Zechlin, J.; Steinmetz, B.; Tesche, B.; Fink, G. Development of a refined poly(propylene) growth model for silica supported metallocene catalyst systems. *Macromolecular Chemistry and Physics* **2000,** *201* (5), 515-524.
62. Alexiadis, A.; Andes, C.; Ferrari, D.; Korber, F.; Hauschild, K.; Bochmann, M.; Fink, G. Mathematical Modeling of Homopolymerization on Supported Metallocene Catalysts. *Macromolecular Materials and Engineering* **2004,** *289* (5), 457-466.
63. Collins, S.; Kelly, W. M.; Holden, D. A. Polymerization of propylene using supported, chiral, ansa-metallocene catalysts: production of polypropylene with narrow molecular weight distributions. *Macromolecules* **1992,** *25* (6), 1780-1785.
64. Quijada, R.; Rojas, R.; Alzamora, L.; Retuert, J.; Rabagliati, F. M. Study of metallocene supported on porous and nonporous silica for the polymerization of ethylene. *Catalysis Letters* **1997,** *46* (1-2), 107-112.
65. Hlatky, G. G. Heterogeneous Single-Site Catalysts for Olefin Polymerization. *Chemical Reviews* **2000,** *100* (4), 1347-1376.
66. Jongsomjit, B.; Kaewkrajang, P.; Shiono, T.; Praserthdam, P. Supporting Effects of Silica-Supported Methylaluminoxane (MAO) with Zirconocene Catalyst on Ethylene/1-Olefin

Copolymerization Behaviors for Linear Low-Density Polyethylene (LLDPE) Production. *Industrial & Engineering Chemistry Research* **2004,** *43* (24), 7959-7963.
67. Choi, K. Y.; Luciani, C. V.; Emdadi, L.; Lee, S. Y.; Baick, I. H.; Lim, J. S. Spherical Pseudo-Inverse Opal Silica with Pomegranate-Like Polymer Microparticles as Templates. *Macromolecular Materials and Engineering* **2012,** *297* (10), 1021-1027.
68. Han, J. J.; Lee, H. W.; Yoon, W. J.; Choi, K. Y. Rate and molecular weight distribution modeling of syndiospecific styrene polymerization over silica-supported metallocene catalyst. *Polymer* **2007,** *48* (22), 6519-6531.
69. Han, J. J.; Yoon, W. J.; Lee, H. W.; Choi, K. Y. Nascent morphology of syndiotactic polystyrene synthesized over silica-supported metallocene catalyst. *Polymer* **2008,** *49* (19), 4141-4149.
70. Malanga, M. Syndiotactic Polystyrene Materials. *Advanced Materials* **2000,** *12* (23), 1869-1872.
71. Schellenberg, J.; Leder, H.-J. Syndiotactic polystyrene: Process and applications. *Advances in Polymer Technology* **2006,** *25* (3), 141-151.
72. Silveira, F.; Alves, M. d. C. M.; Stedile, F. C.; Pergher, S. B.; Rigacci, A.; Santos, J. H. Z. d. Effect of the silica texture on the structure of supported metallocene catalysts. *Journal of Molecular Catalysis A: Chemical* **2009,** *298* (1–2), 40-50.
73. Choi, K. Y.; Han, J. J.; He, B.; Lee, S. B. Syndiotactic Polystyrene Nanofibrils in Silica Nanotube Reactors: Understanding of Synthesis with Ultrahigh Molecular Weight. *Journal of the American Chemical Society* **2008,** *130* (12), 3920-3926.
74. Thüne, P. C.; Loos, J.; de Jong, A. M.; Lemstra, P. J.; Niemantsverdriet, J. W. Planar model system for olefin polymerization: the Phillips CrO_{<i>x</i>}/SiO₂ catalyst. *Topics in Catalysis* **2000,** *13* (1), 67-74.
75. Thüne, P. C.; Loos, J.; Wouters, D.; Lemstra, P. J.; Niemantsverdriet, J. W. The CrOx/SiO2/Si(100) catalyst – a surface science approach to supported olefin polymerization catalysis. *Macromolecular Symposia* **2001,** *173* (1), 37-52.
76. Han, W.; Müller, C.; Vogt, D.; Niemantsverdriet, H.; Thüne, P. C. Introducing a Flat Model of the Silica-Supported Bis(imino)pyridyl Iron(II) Polyolefin Catalyst. *Macromolecular Rapid Communications* **2006,** *27* (4), 279-283.
77. van Kimmenade, E. M. E.; Loos, J.; Niemantsverdriet, J. W.; Th?e, P. C. The effect of temperature on ethylene polymerization over flat Phillips model catalysts. *Journal of Catalysis* **2006,** *240* (1), 39-46.
78. Andoni, A.; Chadwick, J. C.; Milani, S.; Niemantsverdriet, H.; Th?e, P. C. Introducing a new surface science model for Ziegler-Natta catalysts: Preparation, basic characterization and testing. *Journal of Catalysis* **2007,** *247* (2), 129-136.
79. Soga, K.; Nakatani, H. Syndiotactic polymerization of styrene with supported Kaminsky-Sinn catalysts. *Macromolecules* **1990,** *23* (4), 957-959.
80. Choi, K. Y.; Han, J. J.; He, B.; Lee, S. B. Syndiotactic Polystyrene Nanofibrils in Silica Nanotube Reactors:??Understanding of Synthesis with Ultrahigh Molecular Weight. *Journal of the American Chemical Society* **2008,** *130* (12), 3920-3926.
81. He, B.; Kim, S. K.; Son, S. J.; Lee, S. B. Shape-coded silica nanotubes for multiplexed bioassay: rapid and reliable magnetic decoding protocols. *Nanomedicine* **2010,** *5*, 77-88.
82. Yu, J.; Bai, X.; Suh, J.; Lee, S. B.; Son, S. J. Mechanical Capping of Silica Nanotubes for Encapsulation of Molecules. *Journal of the American Chemical Society* **2009,** *131* (43), 15574-15575.

83. Kim, S.-K.; Lee, S. B. Highly encoded one-dimensional nanostructures for rapid sensing. *Journal of Materials Chemistry* **2009,** *19* (10), 1381-1389.
84. Nan, A.; Bai, X.; Son, S. J.; Lee, S. B.; Ghandehari, H. Cellular Uptake and Cytotoxicity of Silica Nanotubes. *Nano Letters* **2008,** *8* (8), 2150-2154.
85. Bai, X.; Son, S. J.; Zhang, S.; Liu, W.; Jordan, E. K.; Frank, J. A.; Venkatesan, T.; Lee, S. B. Synthesis of superparamagnetic nanotubes as MRI contrast agents and for cell labeling. *Nanomedicine* **2008,** *3* (2), 163-174.
86. He, B.; Son, S. J.; Lee, S. B. Suspension Array with Shape-Coded Silica Nanotubes for Multiplexed Immunoassays. *Analytical Chemistry* **2007,** *79* (14), 5257-5263.
87. Son, S. J.; Lee, S. B. Controlled Gold Nanoparticle Diffusion in Nanotubes:??Platfom of Partial Functionalization and Gold Capping. *Journal of the American Chemical Society* **2006,** *128* (50), 15974-15975.
88. Son, S. J.; Reichel, J.; He, B.; Schuchman, M.; Lee, S. B. Magnetic Nanotubes for Magnetic-Field-Assisted Bioseparation, Biointeraction, and Drug Delivery. *Journal of the American Chemical Society* **2005,** *127* (20), 7316-7317.
89. Jayaraman, K.; Okamoto, K.; Son, S. J.; Luckett, C.; Gopalani, A. H.; Lee, S. B.; English, D. S. Observing Capillarity in Hydrophobic Silica Nanotubes. *Journal of the American Chemical Society* **2005,** *127* (49), 17385-17392.
90. Smit, M.; Zheng, X.; Loos, J.; Chadwick, J. C.; Koning, C. E. Effects of methylaluminoxane immobilization on silica on the performance of zirconocene catalysts in propylene polymerization. *Journal of Polymer Science Part A: Polymer Chemistry* **2005,** *43* (13), 2734-2748.
91. Ishihara, N.; Seimiya, T.; Kuramoto, M.; Uoi, M. Crystalline syndiotactic polystyrene. *Macromolecules* **1986,** *19* (9), 2464-2465.
92. Huang, B.; Cao, K.; Li, B.-G.; Zhu, S. Syndiospecific styrene polymerization with CpTiCl3/MAO: Effects of the order of reactant addition on polymerization and polymer properties. *Journal of Applied Polymer Science* **2004,** *94* (4), 1449-1455.
93. Steinbacher, J. L.; McQuade, D. T. Polymer chemistry in flow: New polymers, beads, capsules, and fibers. *Journal of Polymer Science Part A: Polymer Chemistry* **2006,** *44* (22), 6505-6533.
94. Iwasaki, T.; Yoshida, J.-i. Free Radical Polymerization in Microreactors. Significant Improvement in Molecular Weight Distribution Control. *Macromolecules* **2005,** *38* (4), 1159-1163.
95. Xu, C.; Wu, T.; Drain, C. M.; Batteas, J. D.; Beers, K. L. Microchannel Confined Surface-Initiated Polymerization. *Macromolecules* **2004,** *38* (1), 6-8.
96. Wu, T.; Mei, Y.; Cabral, J. T.; Xu, C.; Beers, K. L. A New Synthetic Method for Controlled Polymerization Using a Microfluidic System. *Journal of the American Chemical Society* **2004,** *126* (32), 9880-9881.
97. Wu, T.; Mei, Y.; Xu, C.; Byrd, H. C. M.; Beers, K. L. Block Copolymer PEO-b-PHPMA Synthesis Using Controlled Radical Polymerization on a Chip. *Macromolecular Rapid Communications* **2005,** *26* (13), 1037-1042.
98. Nielsen, C. A.; Chrisman, R. W.; LaPointe, R. E.; Miller, T. E. Novel Tubing Microreactor for Monitoring Chemical Reactions. *Analytical Chemistry* **2002,** *74* (13), 3112-3117.

99. Beigzadeh, D.; Nielsen, C. A. Study of Ethylene Polymerization Under Single Liquid Phase and Vapor-Liquid Phase Conditions in a Continuous-Flow Tubular Reactor. *Chemical Engineering & Technology* **2007,** *30* (8), 1088-1093.
100. Zhang, S. S. A review on the separators of liquid electrolyte Li-ion batteries. *Journal of Power Sources* **2007,** *164* (1), 351-364.
101. Fang, J.; Kelarakis, A.; Lin, Y.-W.; Kang, C.-Y.; Yang, M.-H.; Cheng, C.-L.; Wang, Y.; Giannelis, E. P.; Tsai, L.-D. Nanoparticle-coated separators for lithium-ion batteries with advanced electrochemical performance. *Physical Chemistry Chemical Physics* **2011,** *13* (32), 14457-14461.
102. Kang, S. M.; Ryou, M.-H.; Choi, J. W.; Lee, H. Mussel- and Diatom-Inspired Silica Coating on Separators Yields Improved Power and Safety in Li-Ion Batteries. *Chemistry of Materials* **2012,** *24* (17), 3481-3485.
103. Kim, M.; Kim, Y. S.; Lee, Y.-G.; Park, J. H. Solution processable silica thin film coating on microporous substrate with high tortuosity: application to a battery separator. *RSC Advances* **2013,** *3* (37), 16708-16713.
104. Prosini, P. P.; Villano, P.; Carewska, M. A novel intrinsically porous separator for self-standing lithium-ion batteries. *Electrochimica Acta* **2002,** *48* (3), 227-233.
105. Zhang, S. S.; Xu, K.; Jow, T. R. An inorganic composite membrane as the separator of Li-ion batteries. *Journal of Power Sources* **2005,** *140* (2), 361-364.
106. Takemura, D.; Aihara, S.; Hamano, K.; Kise, M.; Nishimura, T.; Urushibata, H.; Yoshiyasu, H. A powder particle size effect on ceramic powder based separator for lithium rechargeable battery. *Journal of Power Sources* **2005,** *146* (1–2), 779-783.
107. Park, J.-H.; Cho, J.-H.; Park, W.; Ryoo, D.; Yoon, S.-J.; Kim, J. H.; Jeong, Y. U.; Lee, S.-Y. Close-packed SiO2/poly(methyl methacrylate) binary nanoparticles-coated polyethylene separators for lithium-ion batteries. *Journal of Power Sources* **2010,** *195* (24), 8306-8310.
108. Kim, M.; Nho, Y.-C.; Park, J. Electrochemical performances of inorganic membrane coated electrodes for li-ion batteries. *J Solid State Electrochem* **2010,** *14* (5), 769-773.
109. Jeong, H.-S.; Lee, S.-Y. Closely packed SiO2 nanoparticles/poly(vinylidene fluoride-hexafluoropropylene) layers-coated polyethylene separators for lithium-ion batteries. *Journal of Power Sources* **2011,** *196* (16), 6716-6722.
110. Jeong, H.-S.; Hong, S. C.; Lee, S.-Y. Effect of microporous structure on thermal shrinkage and electrochemical performance of Al2O3/poly(vinylidene fluoride-hexafluoropropylene) composite separators for lithium-ion batteries. *Journal of Membrane Science* **2010,** *364* (1–2), 177-182.
111. Choi, J.-A.; Kim, S. H.; Kim, D.-W. Enhancement of thermal stability and cycling performance in lithium-ion cells through the use of ceramic-coated separators. *Journal of Power Sources* **2010,** *195* (18), 6192-6196.
112. Choi, N.-S.; Yao, Y.; Cui, Y.; Cho, J. One dimensional Si/Sn - based nanowires and nanotubes for lithium-ion energy storage materials. *Journal of Materials Chemistry* **2011,** *21* (27), 9825-9840.
113. Cui, L.-F.; Yang, Y.; Hsu, C.-M.; Cui, Y. Carbon−Silicon Core−Shell Nanowires as High Capacity Electrode for Lithium Ion Batteries. *Nano Letters* **2009,** *9* (9), 3370-3374.
114. Park, M.-H.; Kim, M. G.; Joo, J.; Kim, K.; Kim, J.; Ahn, S.; Cui, Y.; Cho, J. Silicon Nanotube Battery Anodes. *Nano Letters* **2009,** *9* (11), 3844-3847.

115. Green, M.; Fielder, E.; Scrosati, B.; Wachtler, M.; Moreno, J. S. Structured Silicon Anodes for Lithium Battery Applications. *Electrochemical and Solid-State Letters* **2003,** *6* (5), A75-A79.
116. Zhang, T.; Gao, J.; Zhang, H. P.; Yang, L. C.; Wu, Y. P.; Wu, H. Q. Preparation and electrochemical properties of core-shell Si/SiO nanocomposite as anode material for lithium ion batteries. *Electrochemistry Communications* **2007,** *9* (5), 886-890.
117. Liu, N.; Huo, K.; McDowell, M. T.; Zhao, J.; Cui, Y. Rice husks as a sustainable source of nanostructured silicon for high performance Li-ion battery anodes. *Sci. Rep.* **2013,** *3*.
118. Jung, D. S.; Ryou, M.-H.; Sung, Y. J.; Park, S. B.; Choi, J. W. Recycling rice husks for high-capacity lithium battery anodes. *Proceedings of the National Academy of Sciences* **2013,** *110* (30), 12229-12234.
119. Liu, X.; Jung, H.-G.; Kim, S.-O.; Choi, H.-S.; Lee, S.; Moon, J. H.; Lee, J. K. Silicon/copper dome-patterned electrodes for high-performance hybrid supercapacitors. *Scientific Reports* **2013,** *3*, 3183.
120. Guo, J.; Wang, C. A polymer scaffold binder structure for high capacity silicon anode of lithium-ion battery. *Chemical Communications* **2010,** *46* (9), 1428-1430.
121. Liu, B.; Soares, P.; Checkles, C.; Zhao, Y.; Yu, G. Three-Dimensional Hierarchical Ternary Nanostructures for High-Performance Li-Ion Battery Anodes. *Nano Letters* **2013,** *13* (7), 3414-3419.
122. Choi, S.; Lee, J.-I.; Park, S. Patterning of electrodes for mechanically robust and bendable lithium-ion batteries. *Journal of Materials Chemistry* **2012,** *22* (42), 22366-22369.
123. Park, M.-H.; Noh, M.; Lee, S.; Ko, M.; Chae, S.; Sim, S.; Choi, S.; Kim, H.; Nam, H.; Park, S.; Cho, J. Flexible High-Energy Li-Ion Batteries with Fast-Charging Capability. *Nano Letters* **2014,** *14* (7), 4083-4089.
124. Chan, C. K.; Peng, H.; Liu, G.; McIlwrath, K.; Zhang, X. F.; Huggins, R. A.; Cui, Y. High-performance lithium battery anodes using silicon nanowires. *Nat Nano* **2008,** *3* (1), 31-35.
125. Kim, H.; Lee, E.-J.; Sun, Y.-K. Recent advances in the Si-based nanocomposite materials as high capacity anode materials for lithium ion batteries. *Materials Today* **2014,** *17* (6), 285-297.
126. Cui, L.-F.; Ruffo, R.; Chan, C. K.; Peng, H.; Cui, Y. Crystalline-Amorphous Core−Shell Silicon Nanowires for High Capacity and High Current Battery Electrodes. *Nano Letters* **2009,** *9* (1), 491-495.
127. Cui, L.-F.; Hu, L.; Choi, J. W.; Cui, Y. Light-Weight Free-Standing Carbon Nanotube-Silicon Films for Anodes of Lithium Ion Batteries. *ACS Nano* **2010,** *4* (7), 3671-3678.
128. Kim, H.; Seo, M.; Park, M.-H.; Cho, J. A Critical Size of Silicon Nano-Anodes for Lithium Rechargeable Batteries. *Angewandte Chemie International Edition* **2010,** *49* (12), 2146-2149.
129. Shu, J.; Li, H.; Yang, R.; Shi, Y.; Huang, X. Cage-like carbon nanotubes/Si composite as anode material for lithium ion batteries. *Electrochemistry Communications* **2006,** *8* (1), 51-54.
130. Kim, T.; Mo, Y. H.; Nahm, K. S.; Oh, S. M. Carbon nanotubes (CNTs) as a buffer layer in silicon/CNTs composite electrodes for lithium secondary batteries. *Journal of Power Sources* **2006,** *162* (2), 1275-1281.
131. Si, Q.; Hanai, K.; Ichikawa, T.; Hirano, A.; Imanishi, N.; Takeda, Y.; Yamamoto, O. A high performance silicon/carbon composite anode with carbon nanofiber for lithium-ion batteries. *Journal of Power Sources* **2010,** *195* (6), 1720-1725.

132. Jang, S.-M.; Miyawaki, J.; Tsuji, M.; Mochida, I.; Yoon, S.-H.; Kang, F.-y. Preparation of a carbon nanofiber/natural graphite composite and an evaluation of its electrochemical properties as an anode material for a Li-ion battery. *New Carbon Materials* **2010,** *25* (2), 89-96.
133. Okamoto, A.; Shinohara, H. Control of diameter distribution of single-walled carbon nanotubes using the zeolite-CCVD method at atmospheric pressure. *Carbon* **2005,** *43* (2), 431-436.
134. Murakami, T.; Mitikami, K.; Ishigaki, S.; Matsumoto, K.; Nishio, K.; Isshiki, T.; Harima, H.; Kisoda, K. Catalytic mechanism of a Fe–Co bimetallic system for efficient growth of single-walled carbon nanotubes on Si/SiO2 substrates. *Journal of Applied Physics* **2006,** *100* (9), 094303.
135. Latorre, N.; Romeo, E.; Cazaña, F.; Ubieto, T.; Royo, C.; Villacampa, J. I.; Monzón, A. Carbon Nanotube Growth by Catalytic Chemical Vapor Deposition: A Phenomenological Kinetic Model. *The Journal of Physical Chemistry C* **2010,** *114* (11), 4773-4782.
136. Miljkovic, N.; Enright, R.; Nam, Y.; Lopez, K.; Dou, N.; Sack, J.; Wang, E. N. Jumping-Droplet-Enhanced Condensation on Scalable Superhydrophobic Nanostructured Surfaces. *Nano Letters* **2013,** *13* (1), 179-187.
137. Kim, J. Y.; Rodriguez, J. A.; Hanson, J. C.; Frenkel, A. I.; Lee, P. L. Reduction of CuO and Cu2O with H2: H Embedding and Kinetic Effects in the Formation of Suboxides. *Journal of the American Chemical Society* **2003,** *125* (35), 10684-10692.
138. Rodriguez, J.; Kim, J.; Hanson, J.; Pérez, M.; Frenkel, A. Reduction of CuO in H2: In Situ Time-Resolved XRD Studies. *Catalysis Letters* **2003,** *85* (3-4), 247-254.
139. Liu, J.; Huang, X.; Li, Y.; Sulieman, K. M.; He, X.; Sun, F. Hierarchical nanostructures of cupric oxide on a copper substrate: controllable morphology and wettability. *Journal of Materials Chemistry* **2006,** *16* (45), 4427-4434.
140. Zou, G.; Li, H.; Zhang, D.; Xiong, K.; Dong, C.; Qian, Y. Well-Aligned Arrays of CuO Nanoplatelets. *The Journal of Physical Chemistry B* **2006,** *110* (4), 1632-1637.
141. Chen, I. H.; Wang, C.-C.; Chen, C.-Y. Fabrication and Structural Characterization of Polyacrylonitrile and Carbon Nanofibers Containing Plasma-Modified Carbon Nanotubes by Electrospinning. *The Journal of Physical Chemistry C* **2010,** *114* (32), 13532-13539.
142. Ra, E. J.; An, K. H.; Kim, K. K.; Jeong, S. Y.; Lee, Y. H. Anisotropic electrical conductivity of MWCNT/PAN nanofiber paper. *Chemical Physics Letters* **2005,** *413* (1–3), 188-193.
143. Hou, H.; Reneker, D. H. Carbon Nanotubes on Carbon Nanofibers: A Novel Structure Based on Electrospun Polymer Nanofibers. *Advanced Materials* **2004,** *16* (1), 69-73.
144. Chronakis, I. S. Novel nanocomposites and nanoceramics based on polymer nanofibers using electrospinning process—A review. *Journal of Materials Processing Technology* **2005,** *167* (2–3), 283-293.
145. Oschmann, B.; Bresser, D.; Tahir, M. N.; Fischer, K.; Tremel, W.; Passerini, S.; Zentel, R. Polyacrylonitrile Block Copolymers for the Preparation of a Thin Carbon Coating Around TiO2 Nanorods for Advanced Lithium-Ion Batteries. *Macromolecular Rapid Communications* **2013,** *34* (21), 1693-1700.
146. Thakur, M.; Pernites, R. B.; Nitta, N.; Isaacson, M.; Sinsabaugh, S. L.; Wong, M. S.; Biswal, S. L. Freestanding Macroporous Silicon and Pyrolyzed Polyacrylonitrile As a Composite Anode for Lithium Ion Batteries. *Chemistry of Materials* **2012,** *24* (15), 2998-3003.

147. Karabacak, T.; DeLuca, J. S.; Wang, P.-I.; Ten Eyck, G. A.; Ye, D.; Wang, G.-C.; Lu, T.-M. Low temperature melting of copper nanorod arrays. *Journal of Applied Physics* **2006,** *99* (6), 064304.
148. Takiya, T.; Fukuda, N.; Umezu, I.; Sugimura, A.; Ueguri, S.; Yoshida, H.; Han, M. Low Temperature Bonding of Metals by Deposition of Nanoparticles at the Interface. *Applied Physics Research* **2012,** *4* (1), 42-47.
149. Xu, Y.; Zhu, Y.; Wang, C. Mesoporous carbon/silicon composite anodes with enhanced performance for lithium-ion batteries. *Journal of Materials Chemistry A* **2014,** *2* (25), 9751-9757.

Published Papers

1. Han, J. J.; Lee, S. Y.; Lee, S. B.; Choi, K. Y. Silica Nanotube Reactors for Catalytic Polymerization of Styrene and Olefins. *Macromolecular Symposia* **2010,** *289* (1), 25-32.

2. Emdadi, L.; Luciani, C. V.; Lee, S. Y.; Baick, I. H.; Choi, K. Y. Experimental and theoretical study of the reaction locus during the dispersion polymerization of methyl methacrylate in a nonpolar hydrocarbon solvent at low temperature. *Polymer Engineering & Science* **2011,** *51* (10), 1969-1986.

3. Lee, S. Y.; Kim, S.-K.; Nguyen, T. M.; Chung, J. S.; Lee, S. B.; Choi, K. Y. Kinetics of Styrene Polymerization to Syndiotactic Polystyrene over Metallocene Catalyst on Flat Surface, Silica Nanotube Reactors and Porous Silica Particles. *Macromolecules* **2011,** *44* (6), 1385-1392.

4. Luciani, C. V.; Emdadi, L.; Lee, S. Y.; Baick, I. H.; Choi, K. Y. Modeling of Phase Inversion and Particle Stability in the Dispersion Polymerization of Methyl Methacrylate in a Non-polar Hydrocarbon Solvent. *Macromolecular Reaction Engineering* **2011,** *5* (9-10), 340-351.

5. Choi, K. Y.; Luciani, C. V.; Emdadi, L.; Lee, S. Y.; Baick, I. H.; Lim, J. S. Spherical Pseudo-Inverse Opal Silica with Pomegranate-Like Polymer Microparticles as Templates. *Macromolecular Materials and Engineering* **2012,** *297* (10), 1021-1027.

6. Lee, S. Y.; Choi, K. Y. Polymerization of Ethylene over rac-Et(1-indenyl)2ZrCl2/MAO Catalyst Supported on Pseudo-Inverse Opal Silica Particles. *Industrial & Engineering Chemistry Research* **2012,** *51* (29), 9742-9749.

7. Lee, S. Y.; Kim, S.-K.; Lee, S.; Choi, K. Y. Metallocene Catalyzed Ethylene Polymerization with Specially Designed Catalyst Supports and Reaction Systems. *Macromolecular Symposia* **2013,** *333* (1), 256-265.

8. Lee, S. Y.; Choi, K. Y. Kinetics and Growth of Polyethylene Nanofibrils over Metallocene Catalyst Supported on Flat Silica and Spherical Nano-Silica Particles. *Macromolecular Reaction Engineering* **2014,** *8* (11), 755-765.

9. Lee, S. Y.; Choi, K. Y. Growth of Polyethylene Nanofibrils Over rac-Et(Indenyl)2ZrCl2/MAO Catalyst Supported on Silica Nanotubes. *Macromolecular Reaction Engineering* **2015,** DOI: 10.1002/mren.201500022